On the structure of metal oxalate anions: theory and experiment

Jenna Victoria Hamilton

Thesis submitted to the
Faculty of Graduate & Postdoctoral Studies
University of Ottawa
In partial fulfillment of the requirements for the
MSc. degree in the Ottawa-Carleton Chemistry Institute

Department of Chemistry
Faculty of Science
University of Ottawa

© Jenna Victoria Hamilton, Ottawa, Canada, 2015

TABLE OF CONTENTS

LIST OF FIGURES VI

LIST OF TABLES XVII

LIST OF EQUATIONS XXI

ACKNOWLEDGMENTS XXIII

ABSTRACT XXV

1 INTRODUCTION 1

1.1 METAL CATIONS 1

1.1.1 ELECTRONIC CONFIGURATIONS 1

1.1.2 ENERGIES 3

1.2 METAL ANIONS 4

1.3 CURRENT RESEARCH USING ATOMIC METAL ANIONS 6

1.4 OBJECTIVE 9

1.5 REFERENCES 10

2 EXPERIMENTAL METHODS 11

2.1 MASS SPECTROMETRY METHODS 11

2.1.1 Electrospray Ionization 13
2.1.2 Quadrupole 16
2.1.3 Time-of-Flight 17
2.1.4 Collision Induced Dissociation 19
2.2 Ion Mobility Spectrometry 19
2.2.1 Drift-time ion mobility spectrometry 19
2.2.2 Travelling-wave ion mobility spectrometry 21
2.3 Infrared Multiphoton Dissociation 24
2.3.1 Vibrational Frequencies 24
2.3.2 The Harmonic Oscillator and Anharmonic Oscillator 27
..... 28
2.3.3 The need for IRMPD 30
2.3.4 Theory behind IRMPD 32
2.3.5 Free-electron Laser 33
2.3.6 Fourier Transform Ion Cyclotron Resonance Mass Spectrometry 35
2.4 Computational Methods 39
2.4.1 Gaussian 09 Suite of Programs 39
2.4.2 Programs for collision cross-section determination 42
2.5 References 44

3 IRMPD AND THEORETICAL RESULTS 47

3.1 Methods 47
3.1.1 Experimental 47
3.1.2 Computational 47

3.2 METAL – $OX_2H_2^-$ COMPLEXES 49

3.2.1 $KOX_2H_2^-$ 50

3.2.2 $CSOX_2H_2^-$ 64

3.2.3 $AGOX_2H_2^{-1}$ 77

3.3 METAL – OX_2^{-1} COMPLEXES 86

3.3.1 $FEOX_2^{-1}$ 86

3.4 METAL – $OXCO_2^-$ COMPLEXES 95

3.4.1 $FEOXCO_2^{-1}$ 95

3.5 METAL –OX^- COMPLEXES 101

3.5.1 KOX^- 101

3.5.2 $CSOX^-$ 104

3.5.3 $AGOX^-$ 110

3.5.4 $FEOX^-$ 115

3.6 CONCLUSIONS 120

3.6.1 LEVELS OF THEORY 121

3.7 REFERENCES 123

4 COLLISION CROSS-SECTIONS OF METAL OXALATE COMPLEXES 124

4.1 THEORETICAL COLLISION CROSS-SECTION DETERMINATION: SIGMA OR MOBCAL? 124

4.2 METHODS 126

4.2.1 EXPERIMENTAL 126

4.2.2 COMPUTATIONAL 126

4.3 IRON – OXALATE COMPLEXES 127

4.3.1 HELIUM AS THE BUFFER GAS FOR IMS FOR COLLISION CROSS-SECTION DETERMINATION 128

4.3.2 NITROGEN AS THE BUFFER GAS FOR IMS FOR COLLISION CROSS-SECTION DETERMINATION 130
4.3.3 COMPARING EXPERIMENTAL AND THEORETICAL COLLISION CROSS-SECTIONS 132
4.4 SILVER-OXALATE COMPLEXES 138
4.4.1 NITROGEN AS THE BUFFER GAS FOR IMS COLLISION CROSS-SECTION DETERMINATION 139
4.4.2 COMPARING EXPERIMENTAL AND THEORETICAL COLLISION CROSS-SECTIONS 140
4.5 POTASSIUM-OXALATE COMPLEXES 142
4.5.1 NITROGEN AS THE BUFFER GAS FOR IMS FOR COLLISION CROSS-SECTION DETERMINATION 142
4.5.2 COMPARING EXPERIMENTAL AND THEORETICAL COLLISION CROSS-SECTIONS 144
4.6 CESIUM-OXALATE COMPLEXES 146
4.6.1 NITROGEN AS THE BUFFER GAS FOR IMS FOR COLLISION CROSS-SECTION DETERMINATION 147
4.6.2 COMPARING EXPERIMENTAL AND THEORETICAL COLLISION CROSS-SECTIONS 149
4.7 COLLISION CROSS-SECTION CONCLUSIONS 151
4.8 REFERENCES 153

5 CONCLUSIONS 154

6 CLAIM TO ORIGINAL RESEARCH 157

7 APPENDIX 158

7.1 OPTIMIZED "X" AND "Y" STRUCTURES FOR ALL LEVELS OF THEORY 158
7.2 IRMPD RESULTS 168
7.2.1 $KOX_2H_2^-$: UNIQUE "X" AND "Y" STRUCTURES 168
7.2.2 $KOX_2H_2^-$: SECOND ATTEMPT AT STRUCTURE DETERMINATION 172
7.2.3 $KOX_2H_2^-$: THIRD ATTEMPT AT STRUCTURE DETERMINATION 175

7.2.4 $CsOx_2H_2^-$: Unique "X" and "Y" structures 177

7.2.5 $CsOx_2H_2^-$: More attempts at structure determination 179

7.2.6 $AgOx_2H_2^-$: Unique "X" and "Y" structures 184

7.2.7 $AgOx_2H_2^-$: More attempts at structure determination 186

7.2.8 $FeOx_2^-$: Unique "X" and "Y" structures 189

7.2.9 $FeOx_2^-$: More attempts at structure determination 192

7.2.10 $FeOxCO_2^-$: Unique "X" and "Y" structures 197

7.2.11 $CsOx^-$: Unique "X" and "Y" structures 199

7.2.12 $AgOx^-$: Unique "X" and "Y" structures 201

7.2.13 $FeOx^-$: Unique "X" and "Y" structures 203

7.3 CID spectra to confirm species for collision cross-section determination 205

7.3.1 Silver 205

7.3.2 Cesium 207

LIST OF FIGURES

Figure 1-1: Electronic configurations and a Lewis dot diagram of potassium and chloride. 2

Figure 1-2: Electronic configurations of neutral iron, and iron with oxidation states +2 and +3 2

Figure 1-3: Mass spectrum of potassium oxalate dissociating resulting in a potassium anion. Reproduced from S. Curtis, J. Renaud, J. L. Holmes, P. M. Mayer, Old Acid, New Chemistry. Negative Metal Anions Generated from Alkali Metal Oxalates and Others. J Am Soc Mass Spectrom 2010, 21. 1944-1946, DOI: http://dx.doi.org/10.1016/j.jasms.2010.08.003 5

Figure 1-4: Atomic metal anions can react with A) PFP to form a negative PFP complex and a neutral metal and B) PFA to form a negative PFA complex and a neutral metal. Reproduced from: J. M. Butson, P. M. Mayer, Electron attachment to pentafluorophenol and pentafluoroaniline via reaction with atomic metal anions. Chemical Physics Letters 2014, 614. 186-191, DOI: http://dx.doi.org/10.1016/j.cplett.2014.09.026 7

Figure 1-5: Summary of the reaction scheme of atomic metal anions. Reproduced from: S. Curtis, J. DiMuzio, A. Mungham, J. Roy, D. Hassan, J. Renaud, P. M. Mayer, Reactions of atomic metal anions in the gas phase: competition between electron transfer, proton abstraction and bond activation. *J Phys Chem A* 2011, *115*. 14006-12, DOI: 10.1021/jp2086736. 7

Figure 1-6: Thirteen unique low energy structures of $KOx_2H_2^-$ 8

Figure 2-1: Schematic of a mass spectrometer (blue boxes) with examples of each component (in white boxes) 12

Figure 2-2: Schematic of a Waters Synapt G1. Reproduced from: http://www.genome.duke.edu/cores/proteomics/instrumentation/Synapt-G1-High-Definition-Mass-Spectrometer 12

Figure 2-3: Schematic of the electrospray ionization process in negative mode. 14

Figure 2-4: Schematic of the IEM theory. a) shows a charged analyte moving to the surface of the highly charged droplet and b) shows the small analyte ion ejected from the droplet. 15
Figure 2-5: The z-spray interface. a) Picture of a real spray where ions are guided downwards into the mass spectrometer entrance whereas other species are hitting the baffle. B) Schematic of the z-spray interface. Reproduced from J. Gross, in Mass Spectrometry. Springer Berlin Heidelberg, 2011, pp 561-620.[6] 15
Figure 2-6: Schematic of a quadrupole. A) shows a side view of a quadrupole with one pair of rods is highlighted in red while the other set is highlighted in blue. B) shows the rod pairs are along the same axis (one pair is along the x-axis while the another pair is along the y-axis). 17
Figure 2-7: Two different trajectories in a quadrupole. An ion with the correct m/z will travel through the quadrupole (black) while an ion with an incorrect m/z will hit one of the rods with opposite polarity (red) 17
Figure 2-8: Schematic of a reflectron TOF 18
Figure 2-9: Schematic of a TW-IMS. Reproduced from F. Lanucara, S. W. Holman, C. J. Gray, C. E. Eyers, The power of ion mobility-mass spectrometry for structural characterization and the study of conformational dynamics. *Nat Chem* 2014, *6*. 281-294, DOI: 10.1038/nchem.1889 [15] 22
Figure 2-10: Electric field and magnetic field waves propagating perpendicular to one another creating electromagnetic radiation 25
Figure 2-11: The electromagnetic spectrum. Reproduced from P. Atkins, J. d. Paula, Atkins' Physical Chemistry. 6 ed.; Oxford University Press: Great Britain, 2006; p 244 [19] 26
Figure 2-12: A mass on a spring representing a simple harmonic oscillator. The motion of the mass moving gives harmonic waves (sine/cosine). Bottom half shows half a cycle of the wave produced with different energy levels (v). 28

Figure 2-13: Difference between harmonic oscillator (left) and anharmonic oscillator (right) potentials and vibrational energy spacing. 30
Figure 2-14: Collision induced dissociation spectrum for iron (III) oxalate hexahydrate 31
Figure 2-15: Intramolecular vibrational energy redistribution. Part a) shows the first photon absorption and being transferred to other internal modes, allowing for another photon to be absorbed which can be seen in b). The process continues, and eventually there is enough energy put into the system that dissociation can occur via the lowest energy pathway as shown in part c). 33
Figure 2-16: Schematic of a FEL. Electrons are accelerated to relativistic speeds and then passed through an undulator which is a series of magnetics with alternating poles causing the electrons to wiggle through releasing monochromatic photons Reproduced from CLIO, What is a Free-Electron laser? http://clio.lcp.u-psud.fr/clio_eng/FEL.html.[33] 34
Figure 2-17: Motion of an ion in the presence of a magnetic field (B) known as the Lorentz force. Ions spin in a circular motion perpendicular to the magnetic field where ions of opposite charge spin in the opposite direction. 35
Figure 2-18: A cross-section of inside the ICR cell. Polarity alternates between the excitation plates resonant with the ion's cyclotron frequency allowing for the ion's orbit to increase for detection. (Trapping electrodes are within the plane of the page) 37
Figure 2-19: Components of an ICR cell. There are two trapping electrodes along the same plane as the magnetic field, two detection plates and two excitation plates orthogonal to each other. 37
Figure 2-20: Outline of the process to obtain mass spectra. Time-dependent raw data is obtained (A) and with the mathematical Fourier Transform process, frequencies are obtained (B) and converted to mass/charge ratios and calibrated allowing for mass spectra to be generated (C). 38
Figure 2-21: Importance of adding the d function in a basis set. It accounts for the polarization effect of the p-orbitals in the presence of d-orbitals. 41

Figure 2-22: An example of inner and outer orbitals for calculations. The outer orbitals are more diffuse than the inner orbitals. 41

Figure 3-1: Example of starting structures for complexes. Structure on the left is an “X” structure where ligands are on the same plane as the metal. The structure on the right is a “Y” structure where the ligands are above and below the plane of the metal. 48

Figure 3-2: Theoretical Structures (basis set : 6-311+gd) and Spectra for each unique $KOx_2H_2^-$ structure. The IRMPD spectrum (dotted) overlaps each theoretical spectra (green). Parts A-H are the “X” structures for B3lyp, B3pw91, B98, Bhandhlyp, M062x, Mpw1pw91 (“Y” structures B3pw91 and Mpw1pw91 are identical) , Pbe1pbe and MP2 respectively while Parts I-M are the “Y” structures for B3lyp, B98, Bhandhlyp (“Y” structure Pbe1pbe is identical), M062x and MP2 respectively..... 54

Figure 3-3 Theoretical spectra (basis set: 6-311+gd) of the three best matching structures from the 1600-1900 cm^{-1} range (green) compared to the IRMPD spectrum (dotted) for the range of 1000-2100 cm^{-1}. Parts A, B, and C are the “X” structures for M062x, Bhandhlyp and Pbe1pbe respectively. 56

Figure 3-4 Modified starting structures from the calculated "X" structure of M062x. 58

Figure 3-5: Theoretical spectrum (basis set: 6-311+gd) of the best M062x modified structure (green) compared to the IRMPD spectrum (dotted) for the range of 1000-2100 cm^{-1}. 59

Figure 3-6: Modified starting structures from structure in Figure 3-5 calculated with a 6-311+gd basis set and M062x level of theory. 60

Figure 3-7: Theoretical spectrum (basis set: 6-311+gd) of the best second round M062x modified structure (green) compared to the IRMPD spectrum (dotted) for the range of 1000-2100 cm^{-1}. 61

Figure 3-8: The dissociation of CO2 from the lowest energy structure of $KOx_2H_2^-$ 62

Figure 3-9: Theoretical Structures (with the lanl2dz basis set) and spectra for each unique $CsOx_2H_2^-$ structure. The IRMPD spectrum (dotted) overlaps each theoretical spectrum (green). Parts A-B are the “X” structures for Bhandhlyp (X-B3lyp, B3pw91, B98, Mpw1pw91, Pbe1pbe and MP2 are identical) and

M062x respectively while Parts C-F are the "Y" structures for B3pw91 (Y-B3lyp identical), B98, Bhandhlyp, M062x (Y-Mpw1pw91 and Pbe1pbe are identical), and MP2 respectively. 66

Figure 3-10: Theoretical spectra (basis set: lanl2dz) of the two best matching structures from the 1600-1900 cm^{-1} range where A) is the "X" structure and B) is the "Y" structure of the DFT method Bhandhlyp. 67

Figure 3-11: Modified starting structures with the Bhandhlyp level of theory 69

Figure 3-12: Theoretical spectrum (basis set: lanl2dz) of the best Bhandhlyp modified structure (green) compared to the IRMPD spectrum (dotted) for the range of 1000-2100 cm^{-1} 70

Figure 3-13: Modified starting structures from structure in Figure 3-12 calculated with a lanl2dz basis set at the Bhandhlyp level of theory. 71

Figure 3-14: Theoretical spectrum (basis set: lanl2dz) of the optimized structure of Figure 3-13C) overlapping the IRMPD spectrum for the range of 1000-2100 cm^{-1}. 72

Figure 3-16: Modified starting structures from the structure in Figure 3-14 calculated with a lanl2dz basis set at the Bhandhlyp level of theory. 73

Figure 3-15: Theoretical spectrum (basis set: lanl2dz) of the optimized structure of Figure 3-16B) overlapping with the IRMPD spectrum for the range of 100-2100cm^{-1}. 73

Figure 3-17: Theoretical spectrum (basis set: lanl2dz) of the best optimized Bhandhlyp level of theory structure overlapping the IRMPD spectrum (dotted) for the range of 1000-2100 cm^{-1}. 75

Figure 3-18: Modified starting structures from the optimized structure in Figure 3-15 calculated with a lanl2dz basis set at the Bhandhlyp level of theory. 75

Figure 3-19: Theoretical Structures (basis set: lanl2dz) and Spectra for each unique $AgOx_2H_2^-$ structure. The IRMPD spectrum (dotted) overlaps each theoretical spectra (green). Parts A-D are the "X" structures for B98 ("Y" structures B3lyp, B98, Mpw1pw91 are identical), Bhandhlyp ("X" structure of M062x is identical), Mpw1pw91 ("X" structures of B3lyp, B3pw91 and Pbe1pbe are identical), and MP2

respectively while Parts E-G are the "Y" structures for Bhandhlyp ("Y" structures of B3pw91 and Pbe1pbe are identical), M062x and MP2 respectively. 79

Figure 3-20: Theoretical spectra (basis set: lanl2dz) of the two best matching structures from the 1600-1900 cm^{-1} range (green) compared to the IRMPD spectrum (dotted) for the range of 1000-2100 cm^{-1}. Part A) is the "X" structure and part B) is the "Y" structure for the Bhandhlyp level of theory..... 81

Figure 3-21: Modified starting structures using the Bhandhlyp level of theory..... 83

Figure 3-22: A) The optimized structure from Figure 3-21D). B) The optimized structure from Figure 3-21E). 84

Figure 3-23: Theoretical Structures (basis set: 6-311+gd) and spectra for each unique $FeOx_2^{-1}$ structure. The IRMPD spectrum (dotted) overlaps each theoretical spectra (green). Parts A-D are the "X" structures for B98 ("X" structures of B3lyp, B3pw91, Mpw1pw91 and Pbe1pbe are identical), Bhandhlyp, M062x and MP2 respectively while E-I are the "Y" structures for B3pw91 ("Y" structures of B3lyp and B98 are identical), Bhandhlyp ("Y" structure of MP2 is identical), M062x, Mpw1pw91 and Pbe1pbe respectively. 89

Figure 3-24: Theoretical spectra (basis set: 6-311+gd) of the two best matching structures from the 1600-1900 cm^{-1} range (green) compared to the IRMPD spectrum (dotted) for the range of 1000-2100 cm^{-1}. Parts A and B are the "X" structure of Bhandhlyp and "Y" structure of Mpw1pw91 respectively. .. 90

Figure 3-25: Modified starting structures starting from the "X" structure of Bhandhlyp. 91

Figure 3-26: Theoretical spectrum (basis set: 6-311+gd) of the best Bhandhlyp modified structure (green) compared to the IRMPD spectrum (dotted) for the range 1000-2100cm^{-1}..... 92

Figure 3-27: Theoretical spectrum (basis set: 6-311+gd) of the Mpw1pw91 modified structure (green) overlapping the IRMPD spectrum (dotted) for the range of 1000-2100 cm^{-1}. 94

Figure 3-28: Theoretical Structures (basis set: 6-311+gd) and Spectra for each unique $FeOxCO_2^-$ structure. The IRMPD spectrum (dotted) overlaps each theoretical spectra (green). Parts A-D are the "X"

structures of B3pw91, Bhandhlyp ("X" structure of M062x is identical), Pbe1pbe ("X" structures of B3lyp, B98 and Mpw1pw91 are identical), and MP2 respectively while parts E-F are the "Y" structures of M062x ("Y" structures of Bhandhlyp and MP2 are identical) and Pbe1pbe ("Y" structures of B3lyp, B3pw91, B98 and Mpw1pw91 are identical) respectively..... 97

Figure 3-29: Theoretical spectra (basis set: 6-311+gd) for the two best matching structures from the 1600-1900 cm^{-1} range (green) compared to the IRMPD spectrum (dotted) for the range of 1000-2100 cm^{-1}. Part A is the "X" structure of Bhandhlyp and B is the "Y" structure for M062x. 98

Figure 3-30: Modified starting structures using the Mpw1pw91 level of theory..... 99

Figure 3-31: Theoretical spectra (basis set: 6-311+gd) of the modified structures (green) from Figure 3-30A and B compared to the IRMPD spectrum (dotted) for the range of 1000-2100 cm^{-1}. 100

Figure 3-32: Theoretical Structures (basis set: 6-311+gd) and Spectra for each unique KOx^- structure. The IRMPD spectrum (dotted) overlaps each theoretical spectra (green). Part A is the "X" structure for B98 and all of the other "X" structures and the "Y" structure of M062x are identical. Part B is the "Y" structure for Mpw1p91 and all other remaining "Y" structures are identical. 102

Figure 3-33: Theoretical spectra (basis set: 6-311+gd) of the two unique structures (green) compared to the IRMPD spectrum (dotted) for the range of 1000-2100 cm^{-1}. Part A is the "X" structure of B98 and part B is the "Y" structure of Mpw1pw91..... 103

Figure 3-34: Theoretical Structures (basis set: lanl2dz) and Spectra for each unique $CsOx^-$ structure. The IRMPD spectrum (dotted) overlaps each theoretical spectra (green). Parts A-C are the "X" structures for B3lyp, B3pw91 ("X" structures B98, Mpw1pw91, Pbe1pbe and "Y" structure of B3pw91 are identical), and Bhandhlyp ("X" structures of M062x, Mp2 and "Y" structures of B98, Bhandhlyp, M062x and MP2 are identical) respectively. Parts D-E are the "Y" structures of B3lyp and Mpw1pw91 ("Y" structure of Pbe1pbe is identical) respectively. 106

Figure 3-35: Theoretical spectra (basis set: lanl2dz) shown in green overlapping the IRMPD spectrum (dotted) for the 1000-2100 cm^{-1} range. Part A is the "X" structure of Bhandhlyp, B is the "Y" structure of B3lyp and C is the "Y" structure of Mpw1pw91. 107

Figure 3-36: Theoretical spectrum (basis set: lanld2dz) of the optimized Bhandhlyp modified structure (green) overlapping the IRMPD spectrum (dotted) for the range 1000-2100 cm^{-1}..... 109

Figure 3-37: Theoretical structures (basis set: lanl2dz) and spectra for different $AgOx^-$ structures. The IRMPD spectrum (dotted) overlaps each theoretical spectrum (green). Parts A-C are the "X" structures of Bhandhlyp ("X" structure of M062x is identical), Pbe1pbe ("X" structures of B3lyp, B3pw91, B98 and Mpw1pw91 are identical) and MP2 respectively. Parts D-F are the "Y" structures of B3pw91, B98 and Bhandhlyp ("Y" structures of B3lyp, M062x, Mpw1pw91, Pbe1pbe and MP2 are identical) respectively. 112

Figure 3-38: Theoretical spectra (basis set: lanl2dz) of the two best matching structures from the 1500-1800 cm^{-1} range (green) compared to the IRMPD spectrum (dotted) for the range 1000-2100 cm^{-1}. Part A is the optimized structure of "X" Bhandhlyp and part B is the optimized structure of "Y" Bhandhlyp.113

Figure 3-39: Theoretical Structures (basis set: 6-311+gd) and Spectra for each unique $FeOx^-$ spectra. The IRMPD spectrum (dotted) overlaps each theoretical spectra (green). Parts A-C are the "X" structures of Bhandhlyp, M062x ("X" structures of B3lyp, B3pw91, B98 and MP2 are identical) and Mpw1pw91 ("X" structure of Pbe1pbe is identical) respectively while parts D-G are the "Y" structures of B3lyp, B3pw91 ("Y" structure of Pbe1pbe is identical), Mpw1pw91 ("Y" structures of B98, Bhandhlyp, M062x are identical) and MP2 respectively..... 117

Figure 3-40: Theoretical spectra (basis set: 6-311+gd) of the three best matching structures from the 1600-1900 cm^{-1} range (green) compared to the IRMPD spectrum (dotted) for the range of 1000-2100 cm^{-1}. Parts A and B are the "X" structures of Bhandhlyp and M062x respectively while parts C and D are the "Y" structures of B3lyp and Mpw1pw91 respectively. 119

Figure 4-1: Schematic of $FeOx_2^-$ dissociating to $FeOx^-$. 127

Figure 4-2: CID spectrum for iron (III) hexahydrate. 128

Figure 4-3: Calibration set constructed from corrected drift times and collision cross-sections for PS using helium as the buffer gas. 129

Figure 4-4: Calibration set constructed from corrected drift times and collision cross-sections for PS with nitrogen as the buffer gas. 131

Figure 4-5: Calibration set with iron oxalate complexes. (Helium is the buffer gas). 136

Figure 4-6: Calibration set and iron oxalate complexes with natural logarithms removed. (Helium is the buffer gas). 137

Figure 4-7: CID spectrum for silver oxalate. 138

Figure 4-8: Calibration set constructed from corrected drift times and cross-sections for PS 139

Figure 4-9: CID spectrum for potassium oxalate. 142

Figure 4-10: Calibration set constructed from corrected drift-times and cross-sections for PS 143

Figure 4-11: CID spectrum for $CsOx_2H_2^-$. 146

Figure 4-12: CID spectrum for $CsOx^-$. 147

Figure 4-13: Calibration set constructed from correct drift times and cross-sections for PS 148

Figure 7-1: Optimized structures for $KOx_2H_2^-$. 159

Figure 7-2: Optimized structures for $CsOx_2H_2^-$. 160

Figure 7-3: Optimized structures for $AgOx_2H_2^-$. 161

Figure 7-4: Optimized structures for $FeOx_2^-$. 162

Figure 7-5: Optimized structures for $FeOxCO_2^-$ 163

Figure 7-6: Optimized structures for KOx^-. 164

Figure 7-7: Optimized structures for $CsOx^-$. 165

Figure 7-8: Optimized structures for $AgOx^-$. 166

Figure 7-9: Optimized structures for $FeOx^-$ 167

Figure 7-10: All unique optimized structures and theoretical spectra overlapping the IRMPD spectrum for the 1000-2000cm^{-1} range. 171

Figure 7-11: Starting structures for the second attempt at determining a plausible structure. 172

Figure 7-12: Optimized structures and spectra resulting from structures in Figure 7-11. 174

Figure 7-13: Starting structures for the third attempt at determining a plausible structure. 175

Figure 7-14: Optimized structures and spectra resulting from structures in Figure 7-13. 176

Figure 7-15: All unique optimized structures and theoretical spectra overlapping the IRMPD spectrum for the 1000-2000cm-1 range. 178

Figure 7-16: Starting structures for the second attempt at determining a plausible structure. 179

Figure 7-17: Starting structures for the third attempt at determining a plausible structure. 180

Figure 7-18: Starting structures for the fourth attempt at determining a plausible structure. 180

Figure 7-19: Starting structures for the fifth attempt at determining a plausible structure. 181

Figure 7-20: Optimized structures and spectra. Parts A-F are resulting from starting structures in Figure 7-16 respectively. Part E also resulted from Figure 7-17A, Figure 7-18A and Figure 7-19A. Parts G and H are the result from Figure 7-17B and C, while I and J are the results from Figure 7-18B and Figure 7-19B respectively. 183

Figure 7-21: All unique optimized structures and theoretical spectra overlapping the IRMPD spectrum for the 1000-2000cm-1 range. 185

Figure 7-22: Starting structures for more attempts at determining a plausible structure. 186

Figure 7-23: Optimized structures and spectra resulting from structures in Figure 7-22. 188

Figure 7-24: All unique optimized structures and theoretical spectra overlapping the IRMPD spectrum for the 1000-2000cm-1 range. 191

Figure 7-25: Starting structures for more attempts at determining a plausible structure. 193

Figure 7-26: Optimized structures and spectra resulting from structures in Figure 7-25. 196
Figure 7-27: All unique optimized structures and theoretical spectra overlapping the IRMPD spectrum for the 1000-2000cm-1 range. 198
Figure 7-28: All unique optimized structures and theoretical spectra overlapping the IRMPD spectrum for the 1000-2000cm-1 range. 200
Figure 7-29: All unique optimized structures and theoretical spectra overlapping the IRMPD spectrum for the 1000-2000cm-1 range. 202
Figure 7-30: All unique optimized structures and theoretical spectra overlapping the IRMPD spectrum for the 1000-2000cm-1 range. 204
Figure 7-31: CID spectrum of m/z 287 205
Figure 7-32: CID spectra of A) m/z 195 and B) m/z 197 206
Figure 7-33: CID of m/z 133. 207

LIST OF TABLES

Table 1-1: Ionization energies and electron affinities of certain elements. 3

Table 1-2: Electron affinities of certain atoms/molecules in kJ/mol 6

Table 3-1: Scaling factors used on computed frequencies. Note: scaling factors for basis set 6-311+gd were not listed so scaling factors for 6-311** were used for 6-311+gd. Levels of theory with a star were not listed and averages of similar levels of theory were therefore taken. MP2=full was used for Cs only. 49

Table 3-2: Relative energies (kJ/mol) of optimized structures from Figure 3-4. Calculations were performed with a 6-311+gd basis set at a M062x level of theory. 59

Table 3-3: Relative energies (kJ/mol) of optimized structures from Figure 3-6. Calculations were performed with a 6-311+gd basis set at a M062x level of theory. 61

Table 3-4: Vibrational assignments to corresponding frequencies. Note: Each vibration was doubly degenerate. 64

Table 3-5: Relative energies (kJ/mol) of optimized structures from Figure 3-11. Calculations were perfomed with a lanl2dz basis set at a Bhandhlyp level of theory. 69

Table 3-6: Relative energies (kJ/mol) of optimized structures from Figure 3-13. Calculations were performed with a lanl2dz basis set at a Bhandhlyp level of theory 71

Table 3-7: Relative energies (kJ/mol) of optimized structures from Figure 3-16. Calculations were performed with a lanl2dz basis set at a Bhandhlyp level of theory 74

Table 3-8: Relative energies (kJ/mol) of all optimized structures calculated at the Bhandhlyp level of theory with the lanl2dz basis set. 76

Table 3-9: Vibrational assignments to corresponding frequencies. 77

Table 3-10: Relative energies (kJ/mol) of optimized structures the “X” and “Y” structures of the Bhandhlyp level of theory and optimized structures from Figure 3-21. 84
Table 3-11: Vibrational assignments to corresponding frequencies. Note: Each vibration was doubly degenerate. 85
Table 3-12: Relative energies (kJ/mol) of optimized structures from Figure 3-25. Calculations were performed with a 6-311+gd basis set at a Bhandhlyp level of theory. 93
Table 3-13: Vibrational assignments to corresponding frequencies. Note: Each vibration had four generate modes (two on each oxalate). 94
Table 3-14: Vibrational assignments to corresponding frequencies. Note: vibrations denoted with a * are doubly degenerate. 101
Table 3-15: Vibrational assignments to corresponding frequencies. Note: Each vibration was doubly degenerate. 104
Table 3-16: Relative energies (kJ/mol) of optimized structures of the Bhandhlyp of theory. Calculations were performed with the lanl2dz basis set. 109
Table 3-17: Vibrational assignments to corresponding frequencies. Note: each vibration was doubly degenerate. 110
Table 3-18: Relative energies (kJ/mol) of optimized structures of the Bhandhlyp of theory. Calculations were performed with the lanl2dz basis set. 114
Table 3-19: Vibrational assignments to corresponding frequencies. Note: each vibration was doubly degenerate. 114
Table 3-20: Vibrational assignments to corresponding frequencies. Note: each vibration was doubly degenerate. 120
Table 3-21: Plausible structures of all metal-oxalate complexes. 122

Table 4-1: Energies and collision cross-sections for proposed low energy structures of glycine and diglycine. 125
Table 4-2: The drift times and cross-sections for polystyrene, used to build the calibration set 129
Table 4-3: Drift times and experimental collision cross-sections for iron oxalate complexes with helium as the buffer gas..... 130
Table 4-4: The drift times and collision cross-sections for PS, used to build the calibration set with nitrogen as the buffer gas..... 131
Table 4-5: Drift times and experimental collision cross-sections for iron oxalate complexes 132
Table 4-6: Comparison of collision cross-sections (Ω) of experimental results using helium gas and theoretical results for different levels of theory. 133
Table 4-7: Comparison of collision cross-sections (Ω) of experimental results using nitrogen gas and theoretical results for different levels of theory. 134
Table 4-8: The drift times and collision cross-sections for polystyrene, used to build the calibration set 139
Table 4-9: Drift times and experimental collision cross-sections for silver oxalate complexes. 140
Table 4-10: Comparison of collision cross-sections (Ω) of experimental results using nitrogen gas and theoretical results for different levels of theory. 141
Table 4-11: The drift-times and cross-sections for polystyrene, used to build the calibration set. 143
Table 4-12: Drift times and experimental collision cross-sections for potassium oxalate complexes. 144
Table 4-13: Comparison of collision cross-sections (Ω) of experimental results using nitrogen gas and theoretical results for different levels of theory. 145
Table 4-14: The drift times and cross-sections for polystyrene, used to build the calibration set 148
Table 4-15: Drift times and experimental collision cross-sections for cesium oxalate complexes 149

Table 4-16: Comparison of collision cross-sections (Ω) of experimental results using nitrogen gas and theoretical results for different levels of theory. 150

Table 4-17: Comparison of collision cross-sections (Ω) of experimental results and theoretical results for the IRMPD determined plausible structures. 152

Table 5-1: Plausible structures of all metal-oxalate complexes 156

LIST OF EQUATIONS

Equation 2-1: Relationship between TOF and m/z 18

Equation 2-2: Mobility of an ion 20

Equation 2-3: Reduced mobility of an ion 20

Equation 2-4: Relationship between mobility and collision-cross section 21

Equation 2-5: Corrected drift time for collision cross-section determination 23

Equation 2-6: Corrected collision cross-section 23

Equation 2-7: Relationship between corrected collision cross-section and corrected drift time 24

Equation 2-8: Equation resulting in plotting the natural logarithms of the corrected collision cross-section versus corrected drift time 24

Equation 2-9: Relationship between c, the speed of light; (m/s), λ, the wavelength (m); v, the frequency (s^{-1}). 25

Equation 2-10: Relationship of frequency and wavelength expressed in terms of $\tilde{\nu}$, wavenumber (usually expressed in cm^{-1}) 25

Equation 2-11: The energy of a photon, E_{photon} is defined by h, Plank's constant ($6.626X10^{-34}J/s$); c, the speed of light; and $\tilde{\nu}$, the vibrational wave number. The energy of a photon is also equal to $E_{molecule}$, the overall change in the molecule's energy. 27

Equation 2-12: Hooke's Law, the force of a spring (F) is proportionate to spring constant (k) and the mass' displacement (x) 28

Equation 2-13: Relationship between frequency (*v*) and force (F), where u is the reduced mass 28

Equation 2-14: Potential energy of the harmonic oscillator 29

Equation 2-15: The vibrational energy (E_{vib}), related to v (quantum number with integer values), *h* (Planck's constant) and *v* (vibrational frequency). 29

Equation 2-16: Morse potential of a diatomic molecule where h is Planck's constant, c is the speed of light, D_e the energy needed to dissociate from the curves minimum, a is a constant, R is the bond distance and R_e is the equilibrium bond distance..... 30
Equation 2-17: Anharmonic vibrational energy. X_e is the anharmonicity constant 30
Equation 2-18: Lorentz force where F is the force, q is the charge, **v** is the velocity and B is the magnetic field 36
Equation 2-19: Frequency of ion experiencing the Lorentz force where f is the frequency, q is the charge, B is the magnetic field, and m is the mass of the ion. 36
Equation 2-20: The angular frequency of an ion experiencing the Lorentz force where ω is the angular frequency. 36

ACKNOWLEDGMENTS

I would not have made it this far academically if it weren't for certain people in my life. I would like to thank my parents for all their support and encouragement throughout the years. I need to thank my fiancé Jordan Cuff as he has supported me in many ways throughout this endeavour. He always encouraged me, pushed me to be the best I can be and was always there when I needed him the most. I would also like to thank Jordan's family for everything they have done in the past few years to ensure my success.

My MSc. gave me an amazing opportunity to work with a fantastic group of people. Firstly I would like to thank Dr. Justin Renaud. For lack of better words, he was an exceptional colleague. Not only was he more than willing to guide and help me throughout the entire project, but was of great help when I was broke my ankle by covering TA duties and ensuring I got around campus safely. For that, I am incredibly grateful.

Secondly, I would like to thank Dr. Ameneh Gholami. I am thankful for her expertise in IRMPD and advice with the analysis of spectra. Working together allowed us to build a close friendship that will last a lifetime.

I am thankful for having the opportunity to work with other members of the Mayer research group: Dr. Barbara Francisco, Dr. Brandi West, Dr. Hauyu Xue, Eduardo Solano, Jeffery Butson, Jaleh Halvachizadeh, Melanie Ouelette, Peter Chen, Sabria Mohammad, Kevin Berland, Milène Nghiem Xuan, Nick Zinck, Samata Khan, Alicia Sit and Iden Djavani.

Members of the John Holmes Mass Spectrometry Centre, Dr. Sharon Curtis, Dr. Sander Mommers and Sean Overton, are extremely talented and knowledgeable when it comes to mass spectrometry. I am thankful for their assistance in trouble-shooting and advice.

Lastly and most importantly I would like to thank Dr. Paul Mayer. I am very fortunate to have been a graduate student in the Mayer research group. Not only do we get the chance to learn a great deal about mass spectrometry, but we are given constant support, feedback and ensured we are always prepared for success. With all the given opportunities presented to me throughout my MSc, I have gained skills and assets that will allow me to become successful in my future endeavours. For this, I am extremely thankful.

ABSTRACT

Anionic metal-oxalate complexes have been generated in the gas phase and an attempt at determining plausible structures were made. Two different experimental techniques were coupled to mass spectrometry: Infrared Multiphoton Dissociation (IRMPD) and ion mobility. Both techniques were compared to theoretical structures calculated using various levels of theory. With the use of IRMPD, frequencies were generated for each complex and compared to theoretical frequencies. Plausible structures for all complexes were found using the M-series of density functional levels of the theory when the 6-311+gd basis set was used and Bhandhlyp functional was appropriate for the lanl2dz basis set. Using ion mobility allowed for collision cross-sections to be calculated and compared to theoretical collision cross-sections of the various structures. Unfortunately no plausible structures were determined using this technique due to a lack of calibrants for the negative mode of ion mobility.

1 INTRODUCTION

1.1 Metal Cations

Since the first few lessons in high school chemistry, everyone learns that when metals become ionic, they are always in the cationic form. This section will briefly describe why this is the case.

1.1.1 Electronic Configurations

When looking at electronic configurations, it is important to remember the three rules: Pauli's principle (no more than two electrons can share the same orbital, and the two electrons must be of opposite spin), Hund's Rule (every orbital is singly occupied in a shell before a second electron can be added) and Aufbau's principle (orbitals must be filled from lowest energy to highest).[1]

In introductory chemistry class, everyone was taught noble gases are the most stable elements due to a having a full valence electron shell which is extremely difficult to react with and therefore inert.[2] When a valence shell becomes full it is stabilized. Other elements can gain full valence shells by either gaining or losing electrons. The alkali metals have only a single electron in their valence shell and to acquire a full valence, it is much easier to lose an electron than to gain seven. Therefore they lose an electron and become positively charged. Likewise with alkaline earth metals, it is easier to lose two electrons then gain six to have a full valence shell. Whereas, with non-metals, such as halogens, it is easier to gain an electron to fill their valence shell as oppose to losing many electrons. An example can be seen in Figure 1-1 where potassium and chloride are coming together to make a salt. Potassium has one valence electron whereas chlorine has seven. Chlorine steals the electron, forming an ionic bond, leaving potassium positively charged and chlorine negatively charged giving both ions full valence shells.

Neutral Configurations	K: [Ar]$4s^1$, Cl: [Ne]$3s^2 3p^5$
Charged Configurations	K: [Ar], Cl: [Ne]$3s^2 3p^6$
Lewis Diagram	

Figure 1-1: Electronic configurations and a Lewis dot diagram of potassium and chloride.

Transition metals also become cationic; however they do not necessarily gain a full valence shell. Main group metals, such as sodium, potassium and cesium only have the s-orbitals filled in the valence shell but with transition metals, d-orbitals contain electrons making it possible for metals to have more than one oxidation state. Looking at electronic configurations demonstrates how this is possible. An example is shown for iron, where common oxidation states are +2 and +3 (Figure 1-2). The 4s orbital is filled before the 3d orbitals and therefore in the case of iron, the 4s orbital is filled before the 3d orbitals (obeying Aufbau's principle). The d-orbitals all have at least one electron (Hund's rule) before a second electron is added to an orbital, and the d orbital containing two electrons have the electrons in opposite spin which is obeying Paul's principle. When electrons are being removed, they are removed from the highest subshell first, in this case being the 4s orbital. Therefore the electronic configuration of Fe^{2+} is [Ar]$3d^6$. Whereas with Fe^{3+}, three electrons are being removed and the first two are removed from the 4s orbital and one is removed from a 3d orbital making the electronic configuration [Ar]$3d^5$. When the d-orbitals are half filled, like in the case of Fe^{3+}, there is a stabilization effect. [2]

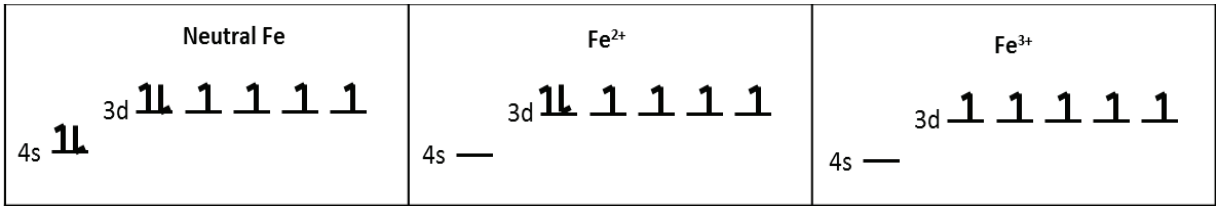


Figure 1-2: Electronic configurations of neutral iron, and iron with oxidation states +2 and +3

1.1.2 Energies

The previous section showed examples of electronic configurations of neutrals and cations and this section will demonstrate metals are positively charged based on energies. Ionization energy is the energy required to remove an electron from an element/molecule and electron affinity can be defined as the energy released when an electron is attached to an element or molecule. Positive energy values for electron affinity represent exothermic reactions (energy is released) and negative values represent endothermic reactions (energy is required to attach an electron).[3] Table 1-1 shows ionization energies and electron affinities of certain elements.[4] To demonstrate noble gases are in fact stable and inert, the ionization energies for helium and neon are very high, while to add an electron to the elements the electron affinities have negative values. When comparing metals listed and halogens, less energy is required to remove an electron from metals versus non-metals and the electron affinities of non-metals are much higher compared to metals making it more favourable for non-metals to accept electrons. Therefore, metals tend to be positive.

Table 1-1: Ionization energies and electron affinities of certain elements.

Element	Ionization energies (kJ/mol)	Electron Affinities (kJ/mol)
Na	495.8	59.8
K	418.8	52.9
Cs	375.5	45.5
Fe	762.2	14.6
F	1681	322
Cl	1251.1	348.7
He	2372.3	-21
Ne	2080.6	-29

1.2 Metal Anions

In the previous section it was demonstrated metals, when charged, are in the cationic form. However under special circumstances it is possible to generate metal anions.

There are methods to generate metal anions through laser photodetachment experiments where anionic beams undergo charge transfer and electron affinities can be determined. Two methods are extracting anions directly from a Penning source and generating anions from an initially positive beam of gas undergoing charge exchange to become negatively charged.[5] These methods work well for the main group of elements and a better method to determine the electron affinities for metals is to use a cesium ion sputtering source. [5-6] Photodetachment experiments are appropriate to determine electron affinities but another method is used to study the reactivity of atomic metal anions.

In 1983, Sallans *et al.* were able to generate Cr^{-1} with the use of a Fourier transform mass spectrometer and collision-induced dissociation experiments using metal carbonyl complexes which were then reacted with neutral species.[7] In 1985, Sallans *et al.* were able to generate atomic metal anions for V^-, Fe^-, Co^-, Mo^- and W^- again using carbonyl complexes.[8] To generate atomic metal anions, there is a neutral metal carbonyl complex which loses CO groups until there is nothing but the bare metal anion.[7-8]

Similar research has been done by Curtis *et al* using oxalic acid to generate bare metal anions.[9] Using a triple quadrupole mass spectrometer, metal-oxalate complexes were dissociated resulting in atomic metal anions. For example, Figure 1-3 shows the dissociation of potassium-oxalate losing a CO_2 group to generate KCO_2^- which then in turn loses CO_2 leaving K^-.[9a]

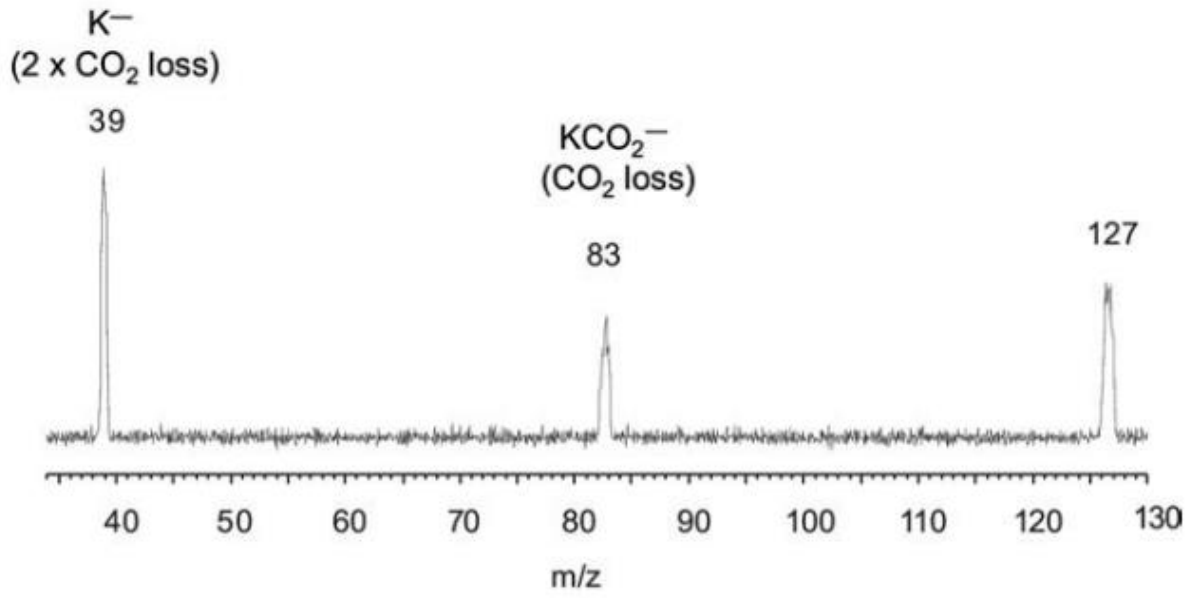


Figure 1-3: Mass spectrum of potassium oxalate dissociating resulting in a potassium anion. Reproduced from S. Curtis, J. Renaud, J. L. Holmes, P. M. Mayer, Old Acid, New Chemistry. Negative Metal Anions Generated from Alkali Metal Oxalates and Others. J Am Soc Mass Spectrom 2010, 21. 1944-1946, DOI: http://dx.doi.org/10.1016/j.jasms.2010.08.003

Table 1-2 lists electron affinities for certain atoms/molecules used to generate metal anions.[4, 9a] Even though metals are usually positively charged, in the case of metal-oxalate complexes, the metals have a higher electron affinity compared to that of CO_2. Due to carbon dioxide having a negative electron affinity, when the complexes are dissociating, the negative charge will stay on the metal thus generating bare metal anions.

Table 1-2: Electron affinities of certain atoms/molecules in kJ/mol

Atom/molecule	Electron Affinity (kJ/mol)
K	52.9
Cs	45.5
Fe	14.6
Ag	125.8
CO_2	-10.0

1.3 Current research using atomic metal anions

Studies have been done where the generated atomic metal anions were reacted with neutral organic species. Butson *et al.* generated atomic metal anions and reacted them with pentaflurophenol and pentafluroanaline.[10] Reactions were done using a triple quadrupole mass spectrometer in which the metal anion was mass selected in the first quadrupole and the pentaflurophenol (PFP) and pentafluoroanaline (PFA) were introduced to the hexapole (collision cell) containing argon where the reaction took place. With the use of bare metal anions, electrons can attach to PFP and PFA (Figure 1-4) making the complexes ionic and the metal neutralized.

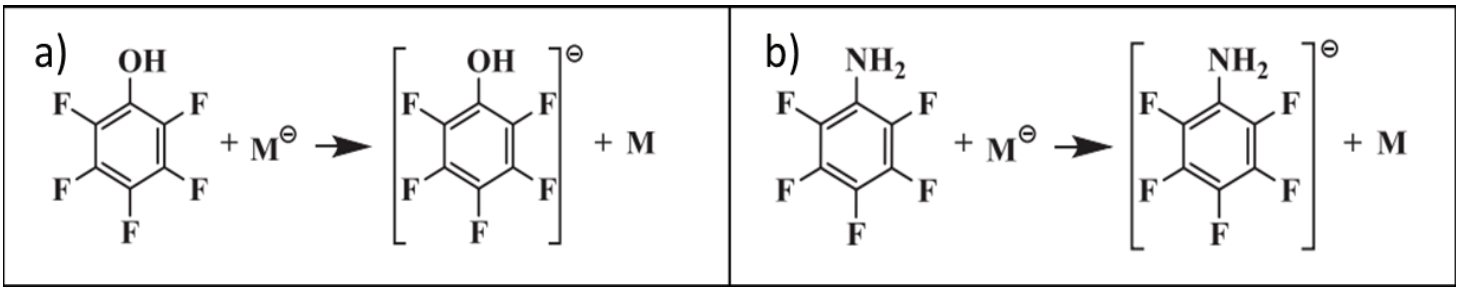


Figure 1-4: Atomic metal anions can react with A) PFP to form a negative PFP complex and a neutral metal and B) PFA to form a negative PFA complex and a neutral metal. Reproduced from: J. M. Butson, P. M. Mayer, Electron attachment to pentafluorophenol and pentafluoroaniline via reaction with atomic metal anions. Chemical Physics Letters 2014, 614. 186-191, DOI: http://dx.doi.org/10.1016/j.cplett.2014.09.026

Curtis *et al.* used metal anions to perform substitution reactions with organic species (CH_3Br, CH_3CH_2Cl, CH_3NO_2, and CH_3CN) where three different types of reactions were observed.[9b] They postulated the formation of halide, cyanide and nitride anions are due to the metal inserting itself into the complex. Hydrogen transfer between the organic and the metal is observed as well as direct electron transfer from the metal to the organic substrate. Thus, three different products can emerge from atomic metal anions reacting with neutral organic species and a summary of the process can be seen in Figure 1-5.

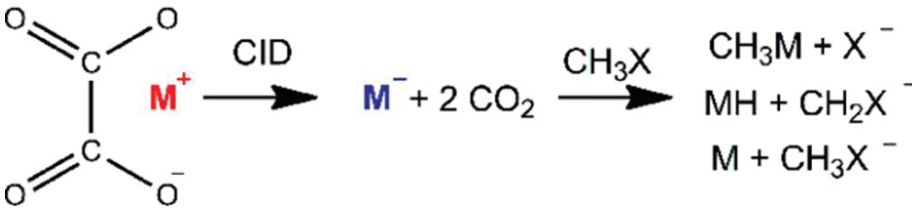


Figure 1-5: Summary of the reaction scheme of atomic metal anions. Reproduced from: S. Curtis, J. DiMuzio, A. Mungham, J. Roy, D. Hassan, J. Renaud, P. M. Mayer, Reactions of atomic metal anions in the gas phase: competition between electron transfer, proton abstraction and bond activation. *J Phys Chem A* 2011, *115*. 14006-12, DOI: 10.1021/jp2086736.

.

The research on atomic metal anions done by Butson and Curtis shows metal anions have the possibility to undergo many types of reactions and theory can help explain these reactions. However, before theory can be used, an appropriate level of theory is needed. Exploring different levels of theory has two benefits: it can allow a correct one to be determined and the metal-oxalate complexes to be characterized. When using different levels of theory, usually convergence will happen, where a low energy structure will be dominant. However, in the case of anionic metal complexes, convergence does not happen because different levels of theory gave many low energy structures. For example, when two different structures for $KOx_2H_2^-$ had optimization and frequency calculations performed using eight different levels of theory; thirteen unique low energy structures were generated (Figure 1-6). Therefore it is not possible to characterize these metal-oxalate complexes using theory alone, and in order to fully understand the behaviour of these complexes theory must be compared to experimental results.

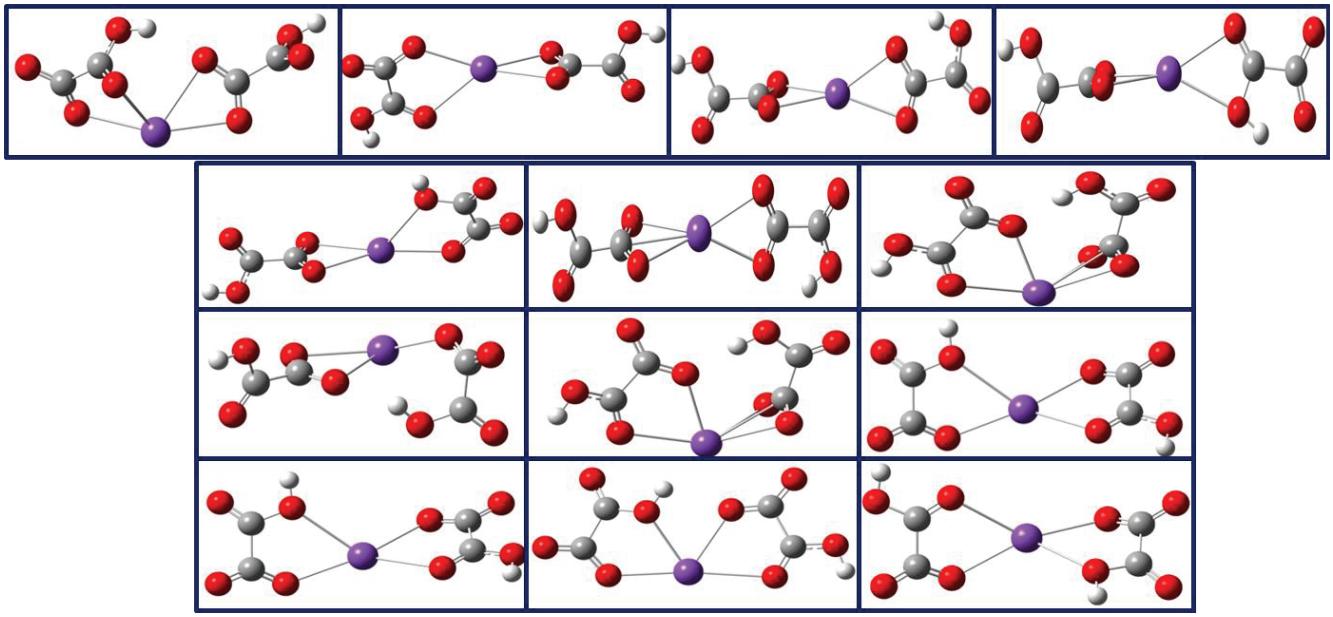


Figure 1-6: Thirteen unique low energy structures of $KOx_2H_2^-$

1.4 Objective

Bare metal anions can be generated in the gas phase with the use of mass spectrometry. In recent years, the lab has been interested in studying properties of these metal anions that can be generated from metal-oxalate complexes. However, the structures of these complexes are still unknown. With the use of computational methods, infrared multiphoton dissociation and ion mobility spectroscopy coupled to mass spectrometry, an attempt on structure determination will be made.

1.5 References

1. P. Atkins, J. d. Paula, *Atkins' Physical Chemistry*. 6 ed.; Oxford University Press: Great Britain, 2006; p 337-341.
2. R. H. Petrucci, *General chemistry principles and modern applications*. Pearson/Prentice Hall: Upper Saddle River, N.J., 2007.
3. P. Atkins, J. d. Paula, *Atkins' Physical Chemistry*. 6 ed.; Oxford University Press: Great Britain, 2006; p 342-343.
4. (a) P. Atkins, J. d. Paula, *Atkins' Physical Chemistry*. 6 ed.; Oxford University Press: Great Britain, 2006; p 1010. (b) D.G. Leopold, W.C. Lineberger, A study of the low-lying electronic states of Fe_2 and CO_2 by negative ion photoelectron spectroscopy. *The Journal of Chemical Physics* 1986, *85*. 51-55, DOI: http://dx.doi.org/10.1063/1.451630
5. H. Hotop, W. C. Lineberger, Binding Energies in Atomic Negative Ions: II. *Journal of Physical and Chemical Reference Data* 1985, *14*. 731-750, DOI: doi:http://dx.doi.org/10.1063/1.555735.
6. R. Middleton, A versatile high intensity negative ion source. *Nuclear Instruments and Methods in Physics Research* 1984, *220*. 105-106, DOI: http://dx.doi.org/10.1016/0167-5087(84)90416-2.
7. L. Sallans, K. Lane, R. R. Squires, B. S. Freiser, Preparation and reactions of chromium(1-) ion. The chromium-hydrogen bond strength. *Journal of the American Chemical Society* 1983, *105*. 6352-6354, DOI: 10.1021/ja00358a049.
8. L. Sallans, K. R. Lane, R. R. Squires, B. S. Freiser, Generation and reaction of atomic metal anions in the gas phase. Determination of the heterolytic and homolytic bond energies for the vanadium, chromium, iron, cobalt, and molybdenum hydrides VH, CrH, FeH, CoH, and MoH. *Journal of the American Chemical Society* 1985, *107*. 4379-4385, DOI: 10.1021/ja00301a002.
9. (a) S. Curtis, J. Renaud, J. L. Holmes, P. M. Mayer, Old Acid, New Chemistry. Negative Metal Anions Generated from Alkali Metal Oxalates and Others. *Journal of the American Society for Mass Spectrometry* 2010, *21*. 1944-1946, DOI: http://dx.doi.org/10.1016/j.jasms.2010.08.003; (b) S. Curtis, J. DiMuzio, A. Mungham, J. Roy, D. Hassan, J. Renaud, P. M. Mayer, Reactions of atomic metal anions in the gas phase: competition between electron transfer, proton abstraction and bond activation. *Journal of Physical Chemistry A* 2011, *115*. 14006-12, DOI: 10.1021/jp2086736.
10. J. M. Butson, P. M. Mayer, Electron attachment to pentafluorophenol and pentafluoroaniline via reaction with atomic metal anions. *Chemical Physics Letters* 2014, *614*. 186-191, DOI: http://dx.doi.org/10.1016/j.cplett.2014.09.026.

2 EXPERIMENTAL METHODS

2.1 Mass Spectrometry Methods

Mass Spectrometry (MS) is an extremely versatile and useful analytical instrument with an endless number of applications of which some examples include the pharmaceutical industry for drug analysis, forensic analysis, food and drug quality control, identifying unknown substances, proteomic studies and drug testing in athletes.[1] Mass spectrometry can achieve this since it allows for ions in the gas phase to be detected based on their mass to charge ratios (m/z). It measures the exact mass of species, not an averaged mass, thus in a mass spectrum (intensity of ions vs. m/z), different peaks of an analyte can appear due to the different isotopes allowing for reliable complex identification. Fragmenting the ion of interest (parent ion) can also help confirm the complex's identity.[1a]

In order for the mass spectrometer to give a spectrum it requires a sample inlet (to introduce the sample), an ion source (to get the ions into the gas phase), a mass analyzer (allowing for m/z to be separated), a detector (measures the ions electronically), and a data system (usually a computer).[1a] A schematic of a Waters Synapt G1 is shown in Figure 2-2. Figure 2-1 shows typical components of a mass spectrometer and examples of each component that are relevant to the research done present in this thesis. Sub-chapters 2.1.1-2.1.3 will explain how the relevant ion source and mass analyzers work.

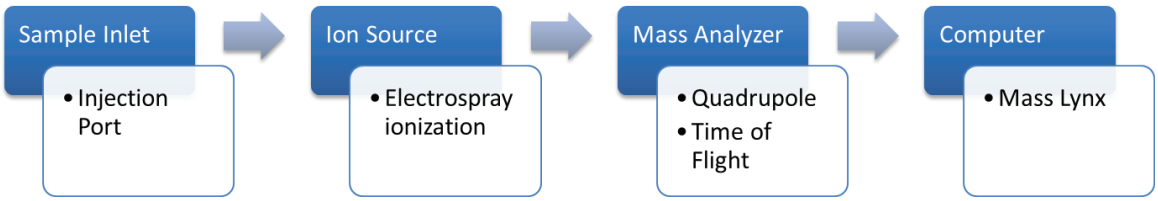


Figure 2-1: Schematic of a mass spectrometer (blue boxes) with examples of each component (in white boxes)

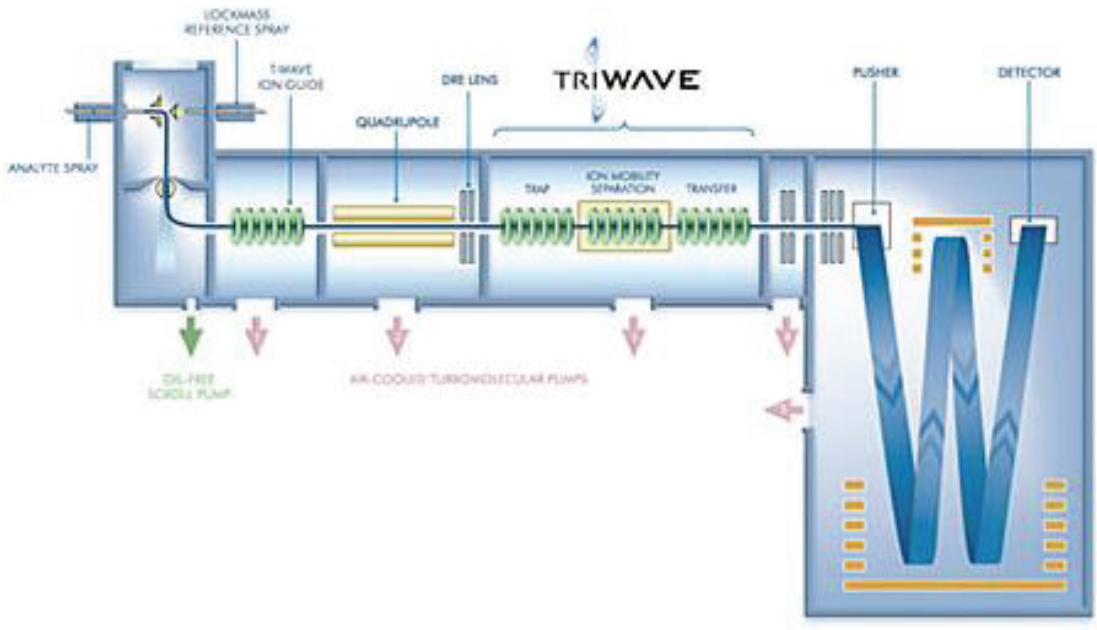


Figure 2-2: Schematic of a Waters Synapt G1. Reproduced from:

http://www.genome.duke.edu/cores/proteomics/instrumentation/Synapt-G1-High-Definition-Mass-Spectrometer

2.1.1 Electrospray Ionization

The electrospray ionization (ESI) technique began with Dole, however became really popular after Fenn improved the technique as a soft ionization technique for biological macromolecules.[2] Electrospray ionization allows for intact compounds to go from the solution phase directly to the gas phase. The overall steps of the ESI process is to create highly charged droplets which shrink due to solvent evaporation, and continue to shrink until there is a highly charged droplet creating a gas phase ion.[3] This is achieved by applying a voltage on the capillary to which the liquid is flowing through at atmospheric pressure. There also needs to be a counter electrode (around 0.3-2 cm away from the capillary) in which a potential difference of three to six kilovolts is applied between it and the capillary. This allows for an accumulation of charge to be built up on the surface of a liquid causing a disruption and creating charged droplets.[4] These droplets can either be positively or negatively charged depending on the polarity and are directed into the mass spectrometer by the electric field through the counter electrode.[4-5] To achieve a continuous spray for mass spectral analysis, a Taylor cone must be created. Whenever there is an electric field applied to the capillary, the liquid at the end of the capillary is spherical in shape, however at a certain voltage, the shape will change from a sphere into a cone allowing for the solution to be ejected into a stream of droplets.[6] Due to the droplets being highly charged, they begin to break apart as the solvent evaporates due to Coulombic repulsion and will continue to do so until there is a gas phase ion (as shown in Figure 2-3).

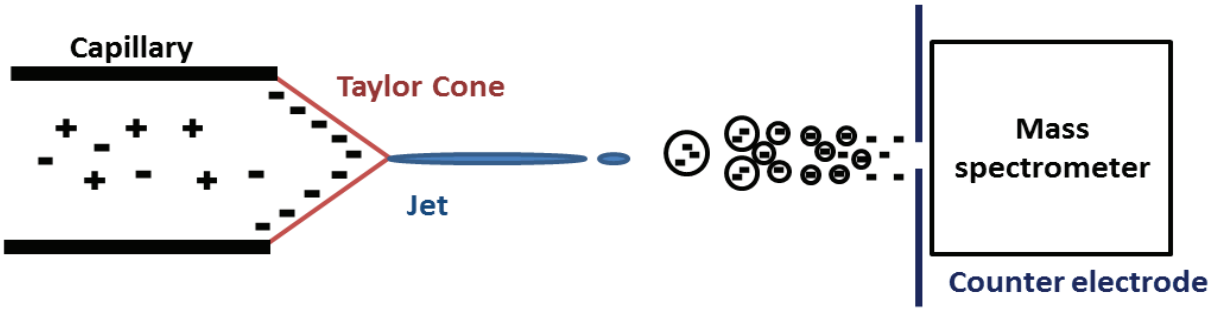


Figure 2-3: Schematic of the electrospray ionization process in negative mode.

There are two theories of how the gas phase ions are created: the charged-residue model (CRM) and the ion evaporation model (IEM).[6-7] The first theory, CRM, believes gas phase ions are created by droplets shrinking due to solvent evaporation while the charge on the droplet remains constant. At a certain point, the surface tension is equal to the electrostatic repulsion causing the droplet to break into smaller droplets. When the surface tension is equal to the electrostatic repulsion on the smaller drops, they break up into even smaller droplets and the process repeats until there is nothing left but one charged analyte per droplet where eventually all solvent disappears leaving a gas phase ion.[6-7] This process is shown in the schematic of the ESI source (Figure 2-3). The second theory, IEM, believes the ions become desolvated by the analyte directly evaporating from the surface of the highly charged droplet and a schematic can be seen in Figure 2-4.[6-7]

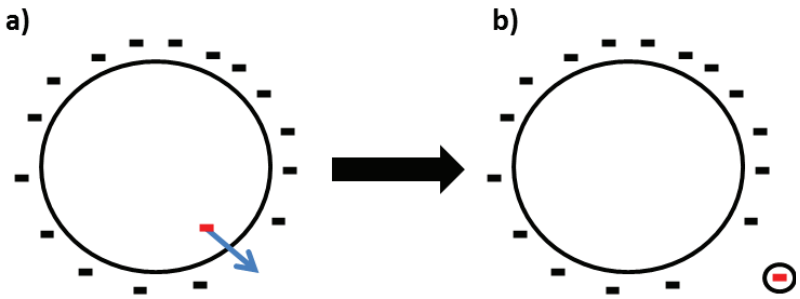


Figure 2-4: Schematic of the IEM theory. a) shows a charged analyte moving to the surface of the highly charged droplet and b) shows the small analyte ion ejected from the droplet.

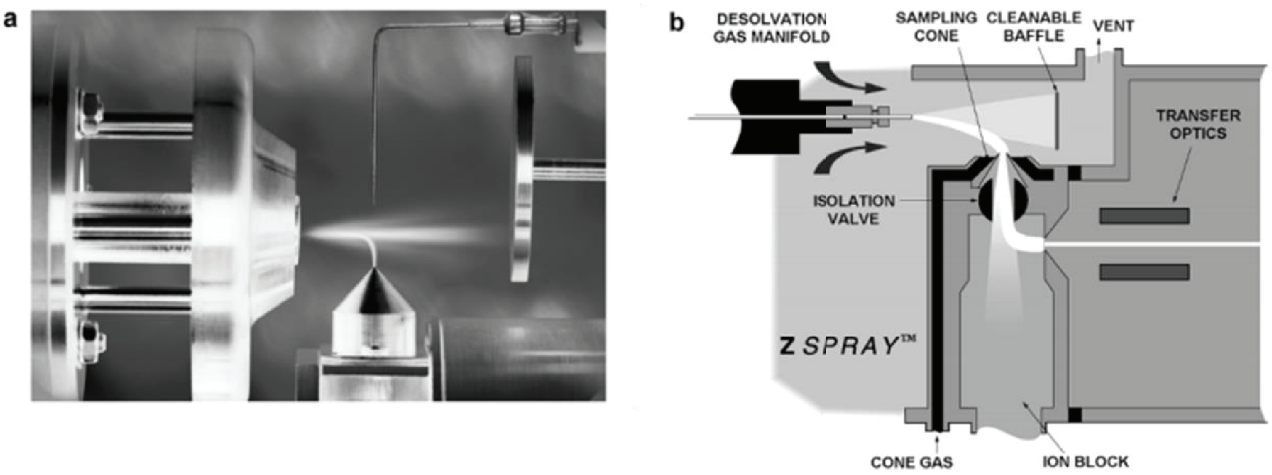


Figure 2-5: The z-spray interface. a) Picture of a real spray where ions are guided downwards into the mass spectrometer entrance whereas other species are hitting the baffle. B) Schematic of the z-spray interface. Reproduced from J. Gross, in Mass Spectrometry. Springer Berlin Heidelberg, 2011, pp 561-620.[6]

In some instruments, the ESI source has been improved by changing the position of the capillary to be at a right angle of the entrance of the mass spectrometer, known as a z-spray interface (Figure 2-5).[6] The purpose for this geometry is to help remove possible contamination that could affect the spray or block capillaries such as neutrals and buffer salts, as they are not attracted to the electric field at that angle and miss the entrance that guide the ions into the mass spectrometer.[6]

2.1.2 Quadrupole

Quadrupoles can be used as a mass analyzer but they can also be used as a filter to isolate ions for tandem mass spectrometry (MS/MS) experiments. A quadrupole consists of four parallel rod electrodes placed in a square orientation to which direct current (DC) and alternating current (AC) are applied to guide the ions.[8] The quadrupole can be thought of having two sets of rods; two in one plane and two in another plane. When the DC and AC voltages are applied, it creates a positive polarity in one set of rods, and a negative polarity in the other set. The polarity is constantly switching between the two sets causing the ions to travel in a circular like fashion through the quadrupole (as they are attracted to one polarity and move towards a rod with the desired polarity, and as soon as it switches, it moves to the next rod) and eventually is guided towards the end of the quadrupole (Figure 2-6). However, by playing with the DC and AC voltage settings it is possible to allow only ions with a certain m/z to pass through the quadrupole while the other ions do not have a correct trajectory, crash onto a rod of opposite polarity and therefore do not make it through the quadrupole (Figure 2-7).[9]

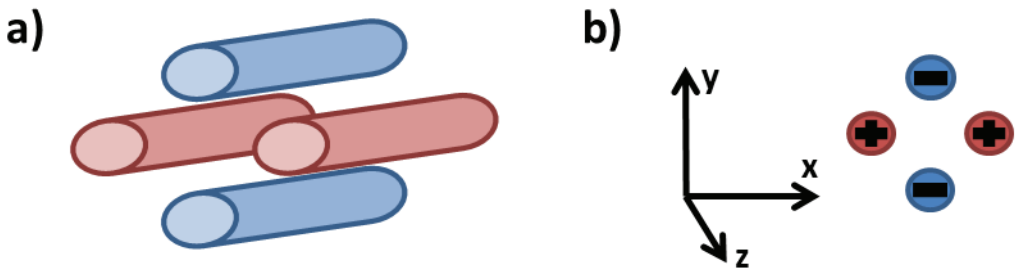


Figure 2-6: Schematic of a quadrupole. A) shows a side view of a quadrupole with one pair of rods is highlighted in red while the other set is highlighted in blue. B) shows the rod pairs are along the same axis (one pair is along the x-axis while the another pair is along the y-axis).

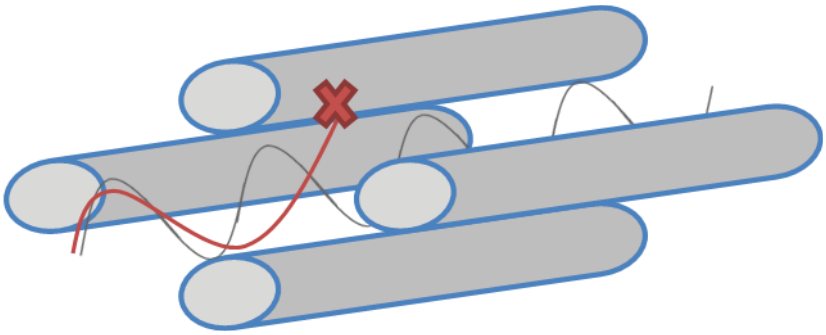


Figure 2-7: Two different trajectories in a quadrupole. An ion with the correct m/z will travel through the quadrupole (black) while an ion with an incorrect m/z will hit one of the rods with opposite polarity (red).

2.1.3 Time-of-Flight

Time-of-Flight (TOF) mass analyzers have higher mass resolution than a quadrupole mass analyzer giving better advantages at better identifying different ions with the same nominal mass, separating isotopic peaks and giving better signal to noise ratios.[10] There are a couple of different TOFs that are used: linear and with a reflectron. [11] In both cases, it measures the amount of time the ions are in the tube, or how long they are "in flight" and can convert the data to m/z values with the use of Equation 2-1 where m is the mass, z is the charge, e is the electron charge, E is the electric field, t is the time the ion spends in

the TOF and D is the distance it travels. On the right hand side of the equation, everything will be the same for every ion with the exception of time. Therefore it is possible to relate the time directly to the m/z, and thus separate ions based on their m/z values.[11]

$$\frac{m}{z} = 2eEs\left[\frac{t}{D}\right]^2$$

Equation 2-1: Relationship between TOF and m/z

The benefit of a reflectron TOF (where there is an ion mirror causing it to reflect) is it increases the distance the ions travel which increases the separation capability because it allows more time to correct for the initial energy of the ions when they first enter the TOF.[10] A schematic of a reflectron TOF can be seen in Figure 2-8 where the ions travel perpendicular from their initial ion trajectory due to the applied electric field, hit the ion mirror causing them to reflect and hit the detector.[10, 12]

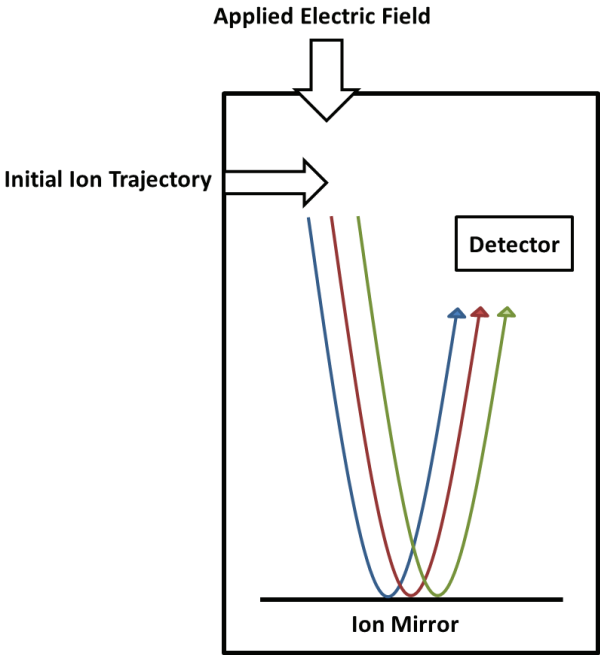


Figure 2-8: Schematic of a reflectron TOF

2.1.4 Collision Induced Dissociation

Collision induced dissociation (CID) experiments have the ability to confirm identities of ions by causing the parent ion to fragment and looking at those fragments can confirm the ion of interest is in fact that ion and not an artifact of the spectrum. For CID to occur there is a collision between an ion and a neutral gas phase molecule (such as argon).[13] Ions have kinetic energy and when they collide with a neutral molecule, the energy is transferred into internal energy. After multiple collisions, the internal energy is high enough in the ion for it to dissociate and thus it fragments.[14]

2.2 Ion Mobility Spectrometry

Ion mobility spectrometry (IMS) is a separation technique similar to chromatography for gas phase ions and is becoming popular in many fields, such as airport security where they use ion mobility to detect explosives.[15-16] There are different types of ion mobility that exist such as drift-time ion mobility, travelling-wave ion mobility and field-asymmetric ion mobility.[15] For the purpose of this thesis however, the only types will be discussed are drift-time and travelling wave.

2.2.1 Drift-time ion mobility spectrometry

Ions are released in packets at specific intervals and the time it takes the ions to get from one end of the drift tube to the other is called the mobility or drift time measured in milliseconds. Mobility separation happens where there is an electrostatic potential pushing the ions through the drift tube and a neutral buffer gas (nitrogen or helium) travelling in the opposite direction which impedes the ions. The overall velocity resulting from the electrostatic potential push and retardation of the buffer gas is the uniform velocity.[16] Showing the mobility mathematically can be seen in Equation 2-2 where K is the mobility, v_D is the uniform velocity and E is the electrostatic field.[17]

$$K = \frac{v_D}{E}$$

Equation 2-2: Mobility of an ion

Smaller ions reach the end of the tube first because they experience fewer collisions with the neutral buffer gas whereas larger ions experience more collisions and are slowed down. The amount of buffer gas present in the drift tube will have an effect on the mobility of an ion (since more buffer gas means more collisions) and therefore it is better to express the mobility as a reduced mobility which can be defined as the mobility relative to the number density of the neutral buffer gas.[17] Equation 2-3 shows the reduced mobility of an ion where K_o is the reduced mobility, L is the length of the drift tube, t_D is the drift time, V is the voltage in the drift tube, T is the temperature of the gas, and p is the pressure of the gas.[17]

$$K_o = \frac{L^2}{t_D V} \times \frac{273.2}{T} \times \frac{p}{760}$$

Equation 2-3: Reduced mobility of an ion

An advantage of using ion mobility is to obtain structural information of ions. When an ion hits a buffer gas molecule, a collision cross-section can be determined and when there is more than one collision, an average collision cross-section can be measured.[15, 17] It is important to consider an average collision-cross section since ions are not perfect spheres and thus a buffer gas can hit them in many possible ways. The relationship between mobility and collision cross-section can be seen in Equation 2-4 where K is the ion mobility, m is the mass of the ion, m_b is the mass of the buffer gas, z is the charge of the ion, e is the elementary charge (in Coulombs), k_B is Boltzmann's constant, T is the temperature of the gas and Ω_{avg} is the average collision cross-section.

$$K = \frac{(18\pi)^{1/2}}{16}\left[\frac{1}{m} + \frac{1}{m_b}\right]^{1/2} \frac{ze}{(k_B T)^{1/2}\Omega_{avg}} \frac{1}{N}$$

Equation 2-4: Relationship between mobility and collision-cross section

The size of an ion is not the only thing that can affect its mobility time. Charge also has an effect on the mobility because the more charge an ion has, the stronger it will feel the electrostatic potential and the faster it will travel the length of the drift tube.

Drift-tube IMS has limitations when it comes to resolution as sometimes it can be difficult to resolve two ions with similar shape and determining collision-cross sections by themselves are not enough information to confirm species.[15, 17] A way to solve these limitations is to couple ion mobility to a mass spectrometer.

2.2.2 Travelling-wave ion mobility spectrometry

Ion mobility can be coupled to mass spectrometry to add another degree of separation to the ions. With the addition of ion mobility, not only can ions be separated based on their m/z ratios, they can be separated by their shapes as well. This can deem especially useful with isobaric ions. However, the benefit of coupling IMS to MS for the research present in this thesis is the ability to determine averaged collision cross-sections.

The ion mobility coupled to mass spectrometers is different than that of a straight-drift tube which was described in Section 2.2.1. Instead of a drift tube that has a constant electrostatic potential pushing the ions straight through, there are a series of ring electrodes in which the voltage is travelling along called travelling-wave ion mobility spectrometry (TW-IMS).[15] The TW-IMS works by having two series of voltages, RF and DC. There are RF voltages applied to the rings where the polarities alternate

throughout the rings confining the ions. The DC voltage is applied to each ring in stepwise fashion, creating a "travelling wave" allowing the ions to be guided through the TW-IMS in a wave like fashion. Smaller ions are stuck in the "valleys" between the waves and reach the end of the mobility cell quicker whereas the larger ions are "riding" on top of the waves resulting in a longer mobility times. A schematic of the TW-IMS can be seen in Figure 2-9. Playing with the voltages can either increase or decrease the wave height as well as increase or decrease how fast the waves are travelling which can be optimized to maximize separation.[15]

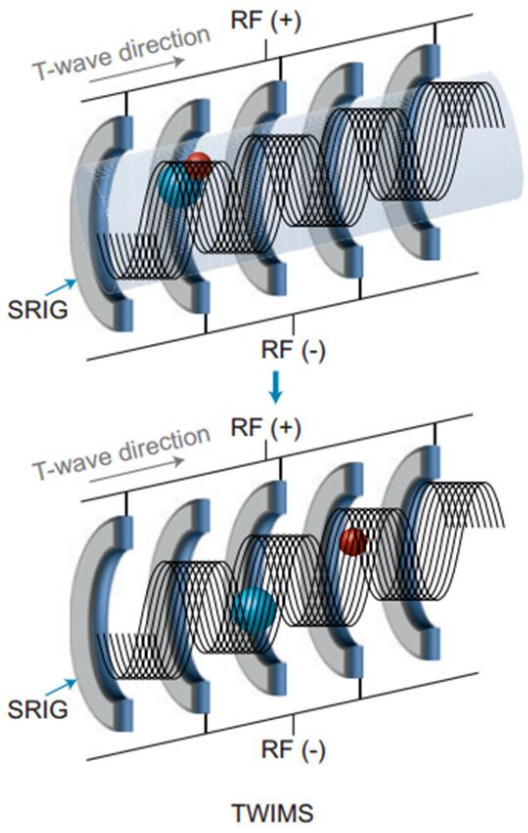


Figure 2-9: Schematic of a TW-IMS. Reproduced from F. Lanucara, S. W. Holman, C. J. Gray, C. E. Eyers, The power of ion mobility-mass spectrometry for structural characterization and the study of conformational dynamics. *Nat Chem* 2014, *6*. 281-294, DOI: 10.1038/nchem.1889 [15]

Due to the complexity of the TW-IMS, determining collision cross-sections directly is not possible and a calibration curve from a set of calibrants with well-defined collision cross-sections is needed.[15] Before the construction of the calibration curve can begin, calibrant drift times must be corrected from mass and charge effects. Equation 2-5 shows the correction for drift time where t'_D is the corrected drift time, t_D is the drift time, c is the Enhanced Duty Cycle delay coefficient (unique to each instrument), m is the mass of the ion and z is the charge of the ion.[18]

$$t'_D = t_D - \frac{\sqrt[c]{\frac{m}{z}}}{1000}$$

Equation 2-5: Corrected drift time for collision cross-section determination

Collision cross-sections must also be corrected for the calibrants and Equation 2-6 shows the corrected collision cross-section where Ω_c is the corrected collision cross-section, Ω is the literature cross-section, z is the charge of the ion, m is the mass of the ion and M_G is the mass of the neutral buffer gas. [18]

$$\Omega_C = \frac{\Omega}{\sqrt[z]{\frac{1}{m} + \frac{1}{M_G}}}$$

Equation 2-6: Corrected collision cross-section

Once the collision cross-sections and mobility times are corrected for the calibrants, construction of the calibration set can begin. The relationship between collision cross-section and mobility time is shown in Equation 2-7 where A and X are derived constants that are based on experimental parameters. These values can be determined by plotting the natural logarithms of the corrected collision cross-section versus corrected drift time. The equation from this plot is a straight line shown in Equation 2-8 where X is the slope and A is the y-intercept.

$$\Omega_C = At_d^X$$

Equation 2-7: Relationship between corrected collision cross-section and corrected drift time

$$\ln(\Omega_C) = Xln(t_D') + A$$

Equation 2-8: Equation resulting in plotting the natural logarithms of the corrected collision cross-section versus corrected drift time

Once the calibration set is complete and the linear equation is obtained (Equation 2-8), it is possible to determine experimental collision cross-sections of analyte ions by correcting their drift times using Equation 2-5 and putting them in Equation 2-8 to obtain Ω_c values. When the corrected collision-cross section is known it is possible to determine the true collision cross-section by solving for Ω in Equation 2-6.[18]

2.3 Infrared Multiphoton Dissociation

This section will go into the theory behind Infrared Multiphoton Dissociation (IRMPD), why this technique is used in the gas phase and the necessary instrumentation to generate spectra. Before IRMPD can be discussed, Section 2.3.1 will explain why vibrational frequencies are used and Section 2.3.2 will discuss the harmonic and anharmonic oscillators.

2.3.1 Vibrational Frequencies

IRMPD uses the infrared range in the electromagnetic spectrum, in which vibrational frequencies can be studied. The electromagnetic field consists of an electric field and a magnetic field [19] where electromagnetic radiation is created when the two fields are oscillating perpendicular to one another (shown in Figure 2-10).[20] The result is a wave (sine or cosine like) travelling at the speed of light (2.997 X 10^8 m/s).[21] The relationship between speed, frequency and wavelength can be seen in Equation 2-9 and shows the higher the frequency, the shorter the wavelength will be. Another way to express this

relationship is to look at it in terms of wavenumbers (how many full wavelengths happen per specified distance i.e. cm^{-1}) as shown in Equation 2-10 which is typically used in IRMPD spectra.[21]

$$\lambda v = c$$

Equation 2-9: Relationship between c, the speed of light; (m/s), λ, the wavelength (m); v, the frequency (s^{-1}).

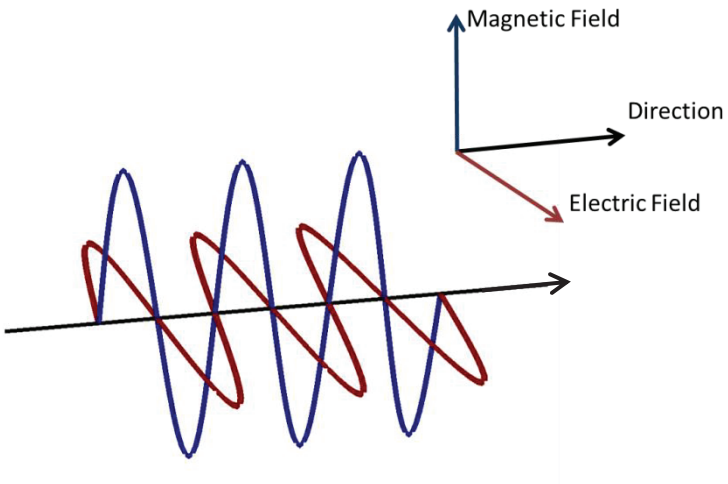


Figure 2-10: Electric field and magnetic field waves propagating perpendicular to one another creating electromagnetic radiation

$$\tilde{\nu} = \frac{v}{c} = \frac{1}{\lambda}$$

Equation 2-10: Relationship of frequency and wavelength expressed in terms of ν̃, wavenumber (usually expressed in cm^{-1})

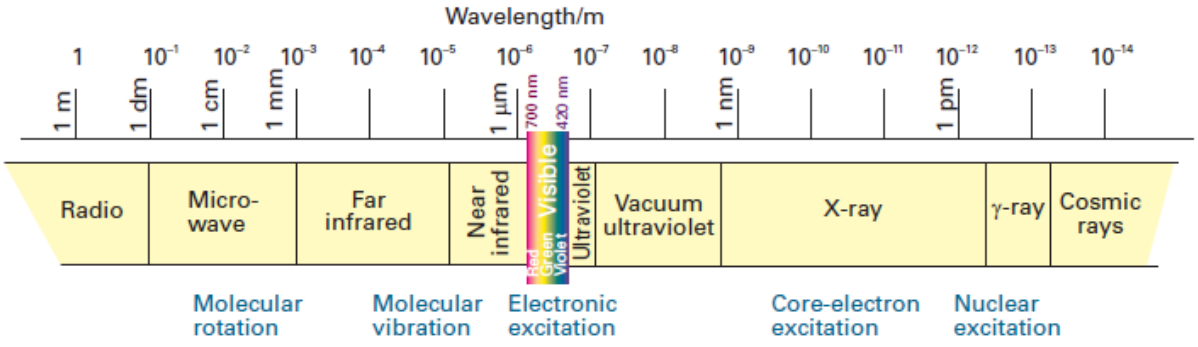


Figure 2-11: The electromagnetic spectrum. Reproduced from P. Atkins, J. d. Paula, Atkins' Physical Chemistry. 6 ed.; Oxford University Press: Great Britain, 2006; p 244 [19]

Understanding the relationship between frequency and wavelength can be extremely useful. Depending on wavelength, different parts of molecules can be studied, i.e. translation, vibrations, rotations and excitations. The electromagnetic spectrum (Figure 2-11) shows what can be studied at different wavelengths and as mentioned earlier, IRMPD uses the infrared region since this region has the same frequency range as molecular vibrations. Thus, if a specific frequency is needed to study a particular vibration, with the use of Equation 2-9 and Equation 2-10, it is possible to determine what wavelength is needed to study that vibrational mode.

If an external wavelength source has the correct frequency required for a molecular vibration to occur, a photon can be absorbed. The energy of a photon is shown in Equation 2-11, where E_{photon} is the energy of the photon, h is Plank's constant, c is the speed of light, and $\tilde{\nu}$ is the wave number. The energy of a photon is also equal to the change in the molecule's energy ($\Delta E_{molecule}$) due to the vibration. If the overall change is positive, then absorption will occur.[22]

$$E_{photon} = hc\tilde{\nu} = \Delta E_{molecule}$$

Equation 2-11: The energy of a photon, E_{photon} is defined by h, Plank's constant ($6.626X10^{-34}$J/s); c, the speed of light; and $\tilde{\nu}$, the vibrational wave number. The energy of a photon is also equal to $E_{molecule}$, the overall change in the molecule's energy.

For a molecule to be able to absorb a photon, frequencies of external wavelength and molecular vibration must be in sync. When they are in resonance with one another, a photon can be absorbed which increases the vibrational energy giving the vibration higher amplitude. However, when the frequencies are not in sync, a photon cannot be absorbed therefore there is no increase in vibrational energy and no difference in amplitude. [22]

2.3.2 The Harmonic Oscillator and Anharmonic Oscillator

When a single photon is absorbed, the vibrational mode can behave like a harmonic oscillator. If a mass is on a weightless spring, was pulled and released, it would oscillate back and forth. Tracking the displacement would show harmonic (sine or cosine) waves being produced which is related to the vibrational frequency (the reciprocal of the wave's period), and Figure 2-12 shows half a cycle of the harmonic wave with stretching in one direction and compression in the other.[22-23] Equation 2-12 shows the force (F) of the spring is negatively proportionate to the displacement of the mass (x) due to the spring constant (k) which is the amount of force per displacement unit (Hooke's Law).[23] In order for the spring to go back to equilibrium once it is extended (direction is +x), the force needs to act in the opposite direction to bring it back (negative), likewise to go back to equilibrium once the spring is compressed (direction is –x), the force acts on the opposite direction (positive) to bring it back to equilibrium. Therefore the relationship is F= -kx.[23]

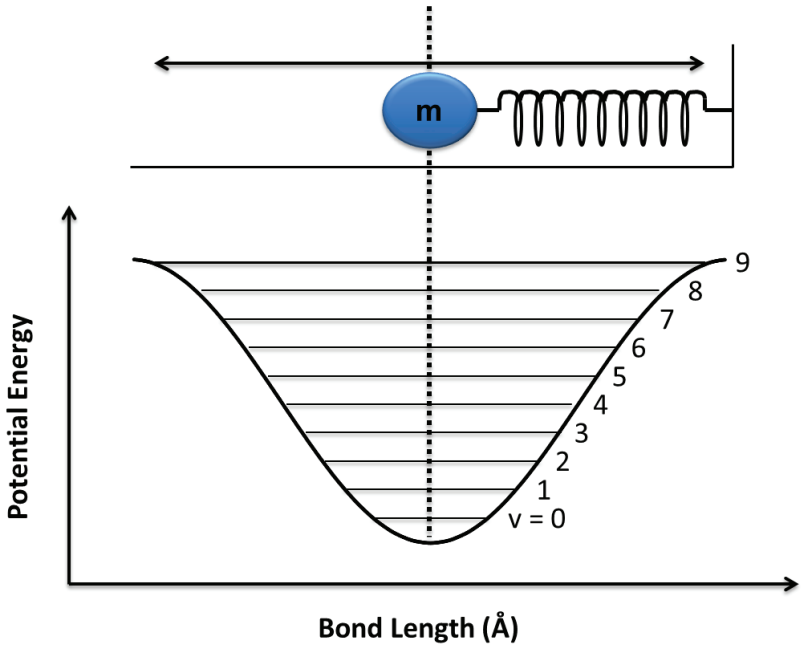


Figure 2-12: A mass on a spring representing a simple harmonic oscillator. The motion of the mass moving gives harmonic waves (sine/cosine). Bottom half shows half a cycle of the wave produced with different energy levels (v).

$$F = -kx$$

Equation 2-12: Hooke's Law, the force of a spring (F) is proportionate to spring constant (k) and the mass' displacement (x).

The relationship between the vibration and the force can be seen in Equation 2-13 for a diatomic molecule.[22] The vibration's frequency is directly proportional to the force and inversely proportional to the reduced mass. Therefore, stronger bonds and smaller masses will give higher frequencies. These differences will allow for very similar complexes to have unique frequencies.

$$v = \frac{1}{2\pi}\sqrt{\frac{F}{u}}$$

Equation 2-13: Relationship between frequency (*v*) and force (F), where u is the reduced mass.

The potential energy of the harmonic oscillator can be thought of classically where it is proportional to the force constant and the square of the displacement, thus giving it a parabolic shape. [23]

$$E_{potential} = \frac{1}{2}kx^2$$

Equation 2-14: Potential energy of the harmonic oscillator

However, it is important to keep in mind at the molecular level, energy is quantized and thus the vibrational energy must be looked at quantum mechanically instead of classically. Equation 2-15 shows the quantum vibrational energy has discreet energy levels (since v has integer values only). In Figure 2-12, discreet energy values are shown with equal spacing with different values of v.

$$E_{vib} = \left(\mathrm{v} + \frac{1}{2}\right)hv$$

Equation 2-15: The vibrational energy (E_{vib}), related to v (quantum number with integer values), *h* (Planck's constant) and *v* (vibrational frequency).

The harmonic oscillator only works for lower vibrational quantum numbers because in reality, at certain energy, bonds will break. To account for this, the anharmonic oscillator (in which the force is not proportional to the displacement) is a better approximation. [22, 24] The potential energy can be described using the Morse potential (Equation 2-16) and when plotted, is similar looking to a molecular potential energy surface where dissociation can occur.[24] The vibrational energy spacing is no longer equal and is calculated by solving the Schrödinger equation for the Morse potential (Equation 2-17).[22, 24] The difference between the two oscillators' potential energy and vibrational energy spacing is shown in

Figure 2-13 where on the left-hand side, the harmonic oscillator is shown and on the right-hand side is the anharmonic oscillator.

$$E_{potential} = hcD_e\left[1 - e^{-a(R-R_e)}\right]^2$$

Equation 2-16: Morse potential of a diatomic molecule where h is Planck's constant, c is the speed of light, D_e the energy needed to dissociate from the curves minimum, a is a constant, R is the bond distance and R_e is the equilibrium bond distance.

$$E_{vib} = hcv\left(\mathrm{v} + \frac{1}{2}\right) - hcx_e\left(\mathrm{v} + \frac{1}{2}\right)^2$$

Equation 2-17: Anharmonic vibrational energy. X_e is the anharmonicity constant

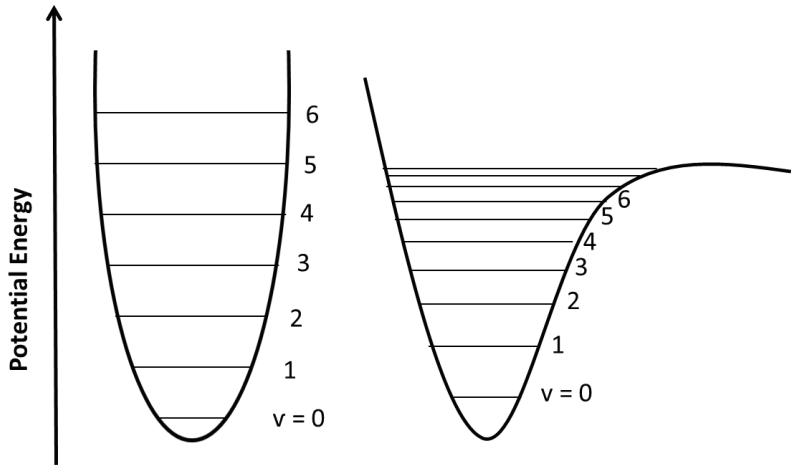


Figure 2-13: Difference between harmonic oscillator (left) and anharmonic oscillator (right) potentials and vibrational energy spacing.

2.3.3 The need for IRMPD

IRMPD uses both mass spectrometry and infrared techniques for structure determination, but these methods on their own are not sufficient. With the use of collision induced dissociation experiments, mass spectrometry allows for structures to be identified but does not give enough information about what the structure could look like. For example, Figure 2-14 shows the results from a CID spectrum of

iron (III) oxalate hexahydrate. The spectrum confirms there is an iron oxalate complex since it loses CO_2 until there is nothing left but a bare metal anion. However it does not give any information of where the CO_2 groups are located respective to the metal. Thus mass spectrometry alone does not provide enough information to determine the anionic complexes' structure.

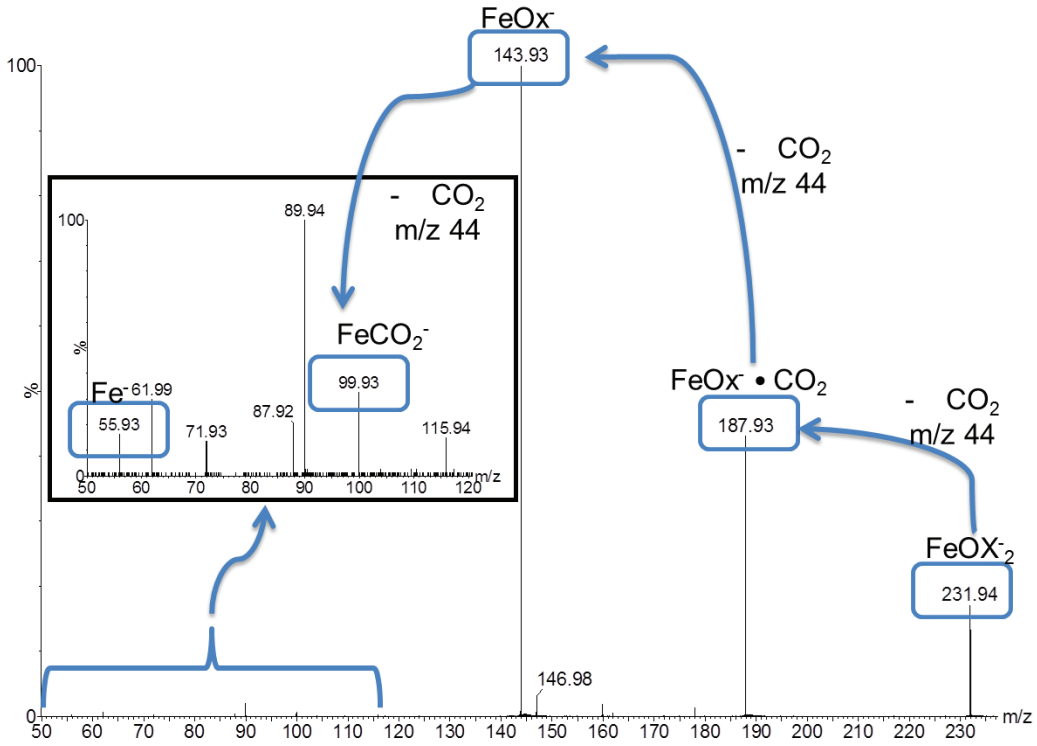


Figure 2-14: Collision induced dissociation spectrum for iron (III) oxalate hexahydrate

Traditional vibrational studies of molecules use infrared spectroscopy in which molecules can be studied in any phase (solid, liquid, gas).[25] When a wavelength passes that has the correct frequency a photon can be absorbed and spectra can be recorded. IR spectroscopy is especially useful when studying molecules that have CO, OH, or NH groups that are sensitive to hydrogen bonding which can be extremely helpful when determining structure.[26] This method is suitable for neutrals but becomes problematic when studying ions in the gas phase due to repulsion creating a low ion density. A typical IR direct absorption spectroscopy experiment requires about 10^{10} molecules/cm^3 to be able to obtain a

reliable spectrum. However due to repulsion, it is not possible to achieve the desired amount of ions within the cell and thus with very little ions, it becomes difficult to record a direct spectrum using traditional IR spectroscopy.[27] It will be shown in the next sub-chapters how IRMPD can overcome the problems presented and how this technique can obtain spectra.

2.3.4 Theory behind IRMPD

When a wavelength of the correct frequency is passed over a gas-phase ion, a photon can be absorbed via the v = 0 to v = 1 transition. [28] Due to anharmonicity, photons cannot be continued to absorb since the frequency of the external source will no longer be resonant. However, more than one photon can be absorbed due to the intramolecular vibrational energy redistribution (IVR) process.[26, 28] IVR happens when there is enough anharmonic coupling between the absorbing mode and other modes (all vibrational degrees of freedom). When there is sufficient anharmonic coupling, the photon can be quickly depopulated from the v=1 state into other modes of the ion, leaving the v=0 to v=1 transition free for another photon to be absorbed. This process repeats and can require tens to hundreds of photons until there is enough energy in the system to dissociate the ion via the lowest energy pathway.[26, 28] The diagram in Figure 2-15 illustrates this process.

IRMPD spectra look at the fragmentations of the parent ion that underwent the IVR process and dissociated. This is known as consequence spectroscopy since it is relying on dissociation and not the intensity of absorption from photons. [29] With the use of mass spectrometry, the ion of interest can be selected, trapped, and with a use of a laser can be fragmented. Since mass spectrometry is very sensitive, low ion density is no longer problematic.[30]

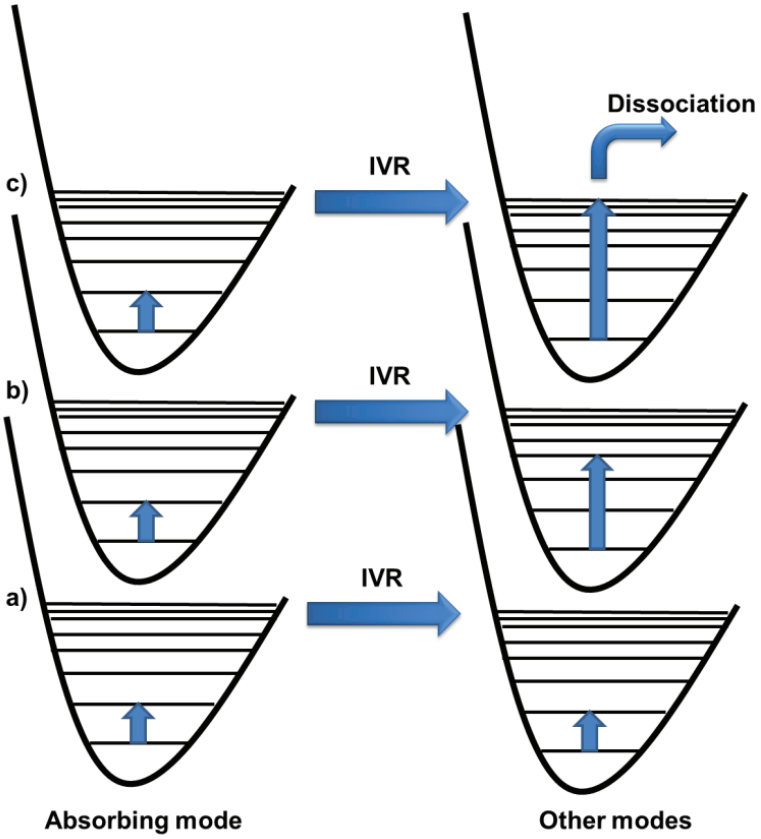


Figure 2-15: Intramolecular vibrational energy redistribution. Part a) shows the first photon absorption and being transferred to other internal modes, allowing for another photon to be absorbed which can be seen in b). The process continues, and eventually there is enough energy put into the system that dissociation can occur via the lowest energy pathway as shown in part c).

2.3.5 Free-electron Laser

The free-electron laser (FEL) is a high powered monochromatic laser that is highly tuneable and can be used to study species in the infrared range.[31] What is unique about a FEL is it uses electrons that are accelerated to relativistic speeds having energy in the 10-50-MeV range as opposed to bound, atomic or molecular states as its lasing medium.[32] A schematic of a FEL can be seen in Figure 2-16. Once the electrons are accelerated to relativistic speeds, they pass through an endulator, where there are a series

of magnetics with alternating poles causing the electrons to “wiggle” through. This “wiggling” allows for monochromatic photons to be released, and the mirrors allow for the light to pass back and forth creating more intense and coherent light.[32] Changing the distance between magnets in the undulator allows for different wavelengths being produced making the FEL highly tunable. [31]

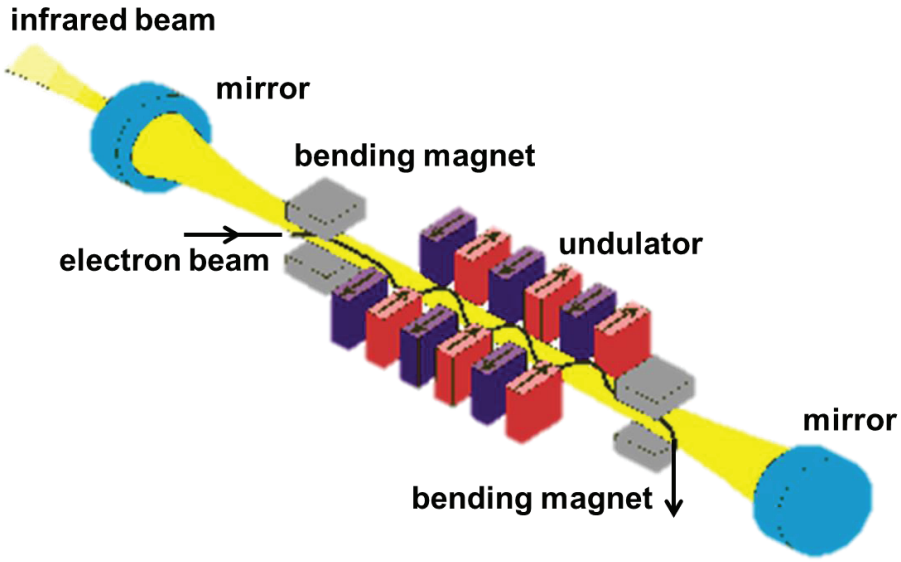


Figure 2-16: Schematic of a FEL. Electrons are accelerated to relativistic speeds and then passed through an undulator which is a series of magnetics with alternating poles causing the electrons to wiggle through releasing monochromatic photons Reproduced from CLIO, What is a Free-Electron laser? http://clio.lcp.u-psud.fr/clio_eng/FEL.html.[33]

Due to size and cost, there are only two facilities housing a FEL in the IR range, FELIX (FOM-Institute for Plasma Physics in the Netherlands) and CLIO (Centre Laser Infrarouge Orsay).[31-32] The FEL at CLIO has great tunability in the IR region giving intense radiation in the range of 3 to 120µm with a usable range of around 700 to 2000cm^{-1} allowing for complexes to be studied in the mid-infrared range.[34]

2.3.6 Fourier Transform Ion Cyclotron Resonance Mass Spectrometry

IRMPD uses a Fourier transform ion cyclotron resonance mass spectrometer (FT-ICR-MS) since it has the capability of trapping ions, in which the laser can be introduced. Ions are electrosprayed and are guided into a trap where ion cyclotron motion is created when there is a uniform magnetic field acting upon the ion.[35] Recall, in Section 2.3.1, the electric and magnetic fields are perpendicular to one another, thus when a magnetic field is introduced, and a part of the ion's velocity is perpendicular to the magnetic field, the ion (electric charge) will orbit perpendicular to the magnetic field. The magnetic field causes the ion path to bend in a circular motion which is known as the Lorentz force(Figure 2-17).[35] Equation 2-9 shows the Lorentz force and the frequency related to the travelling ion in circular motion (cyclotron frequency) can be seen in Equation 2-19.[36] To simplify, it is possible to look at the frequency as the angular frequency which can be seen in Equation 2-20 showing the frequency of the ion is related to the magnetic field, mass and charge. Therefore, since the magnetic field is uniform, it is possible to separate ions based on their different mass to charge ratios as they will have different frequencies.[35-36]

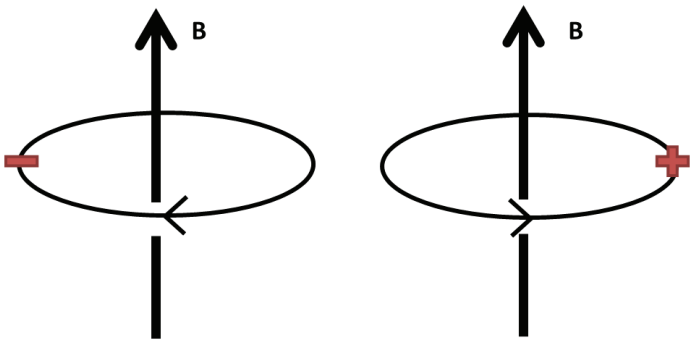


Figure 2-17: Motion of an ion in the presence of a magnetic field (B) known as the Lorentz force. Ions spin in a circular motion perpendicular to the magnetic field where ions of opposite charge spin in the opposite direction.

$$F = q\vec{v} \times B$$

Equation 2-18: Lorentz force where F is the force, q is the charge, $\vec{v}$ is the velocity and B is the magnetic field

$$f = \frac{qB}{2\pi m}$$

Equation 2-19: Frequency of ion experiencing the Lorentz force where f is the frequency, q is the charge, B is the magnetic field, and m is the mass of the ion.

$$\omega = \frac{qB}{m}$$

Equation 2-20: The angular frequency of an ion experiencing the Lorentz force where ω is the angular frequency.

A Penning Trap (the ICR cell) can allow ions to be trapped for periods of time allowing for the FEL to be introduced and irradiate the parent ion. There are different components of this trap that allows for this to occur. To ensure no ions escape along the axis where the magnetic field is applied, there is an electrostatic potential (around 1V) in the trapping electrodes.[35, 37] There are two plates known as the excitation and detection plates which are placed orthogonal to one another.[37] A schematic of a trap can be seen in Figure 2-19. When ions are orbiting with their cyclotron frequencies, the orbits are too small for detection, thus excitation plates are needed to increase the radius of the orbit for detection purposes.[36] This works by changing the radio frequency (alternating polarity) on the plates to be resonant with the cyclotron frequency of the ion which causes the orbit to increase to a detectable size and all ion orbits to be in sync with one another (but all ions have their unique cyclotron frequencies).[35-36] The excitation plates can also cause all unwanted ions to exit the cell by making the orbital too large, making it impossible to detect.[35] A cross section of the ICR cell can be seen in Figure 2-18.

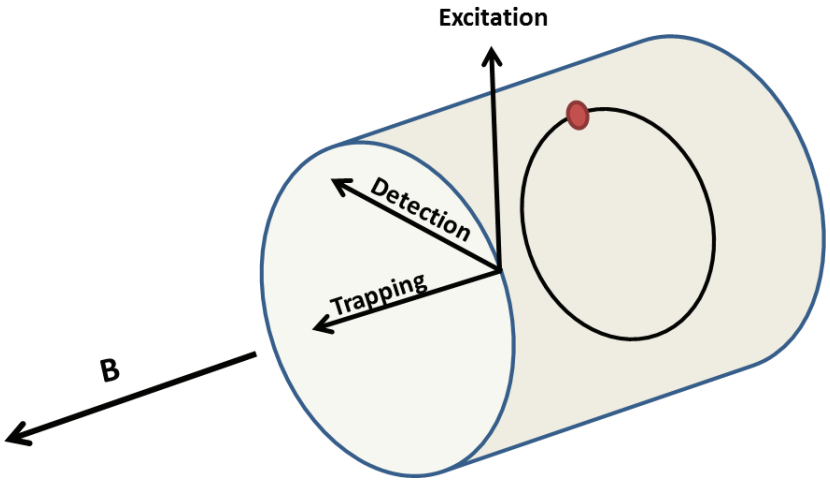


Figure 2-19: Components of an ICR cell. There are two trapping electrodes along the same plane as the magnetic field, two detection plates and two excitation plates orthogonal to each other.

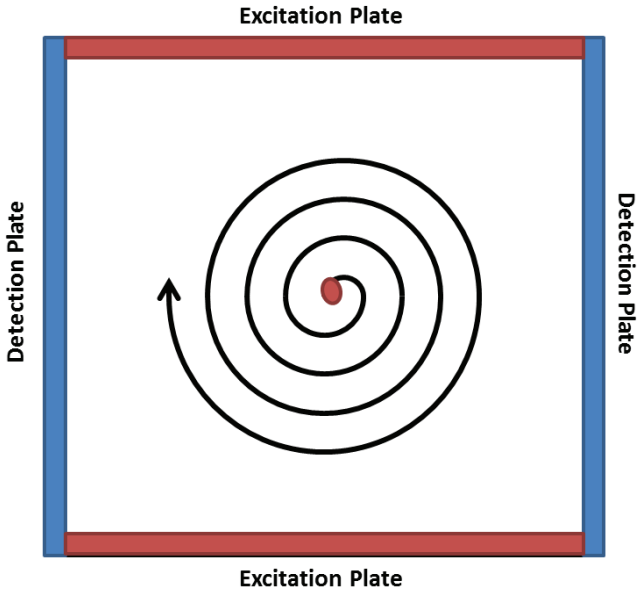


Figure 2-18: A cross-section of inside the ICR cell. Polarity alternates between the excitation plates resonant with the ion's cyclotron frequency allowing for the ion's orbit to increase for detection. (Trapping electrodes are within the plane of the page)

Once an ion's orbit reaches a radius that is detectable, it passes the two detection plates creating a charge in the plates which is used to counter the effect of the ion charge. The charges are recorded as a function of time and how close they are to the detector. As they move away from the detector, the signal is less intense and the raw data is recorded as free induction decay (FID).[36] All ions are detected at the same time but can be separated based on their individual cyclotron frequencies. The separation is possible by using a Fourier Transform (FT), which is a mathematical application that extracts frequencies from raw data.[36] Spectrums can be generated with intensity plotted versus frequencies, and with the use of Equation 2-19 and Equation 2-20, m/z spectra can be determined based on frequencies and plotted versus intensity. However, it is important to note, calibration is needed to obtain mass spectra which can be done internally with a known sample, or externally, where the standard is imported into experimental data.[36] Figure 2-20 outlines the process required to obtain mass spectra.

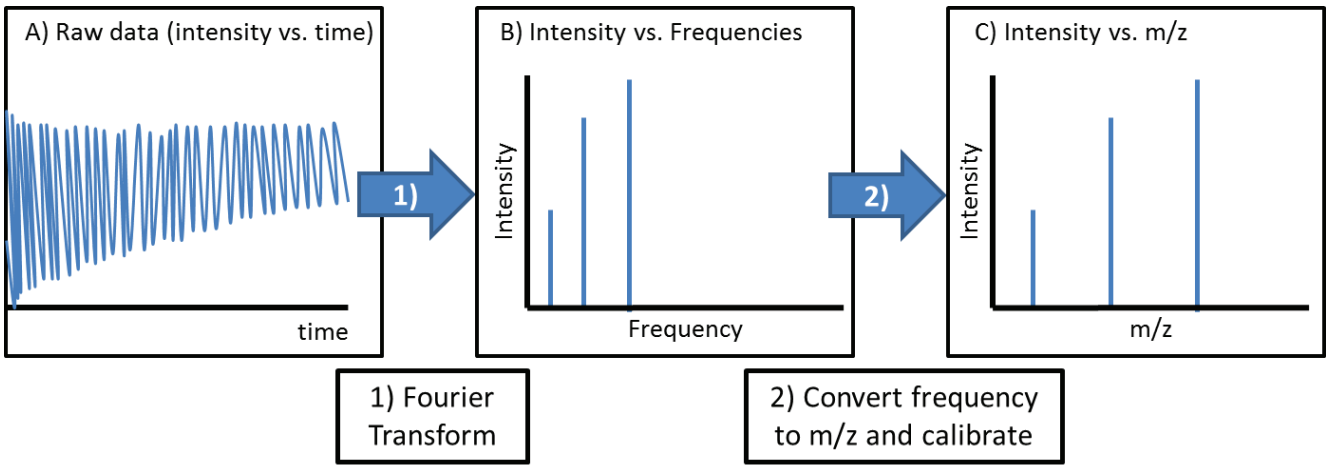


Figure 2-20: Outline of the process to obtain mass spectra. Time-dependent raw data is obtained (A) and with the mathematical Fourier Transform process, frequencies are obtained (B) and converted to mass/charge ratios and calibrated allowing for mass spectra to be generated (C).

2.4 Computational Methods

This section will explain different theoretical methods used to compare experimental results. Gaussian calculations were used compare both collision cross-sections and frequencies to experimental results, whereas Sigma Plot and Mobcal are programs used for collision cross-section determination only.

2.4.1 Gaussian 09 Suite of Programs

The Gaussian 09 Suite of Programs allows for low energy structures to be determined which is important because they are the ones that exist in the gas phase.[38] Starting structures with initially guessed geometries can be submitted to Gaussian where optimization calculations are performed on the system. Optimization calculations try to find a low energy structure by looking for a minimum in the potential energy surface and once the calculation is complete it is possible to determine if the calculation found a minimum by looking at the complex's frequencies. If there are no negative frequencies (which represent imaginary ones), then it has found a minimum; if there was one imaginary frequency, it has found a saddle point.[39] Thus, by having all real frequencies, the structure is in a minimum and can be used to compare to experimental results.

In order to perform optimization calculations, a basis set and level of theory are required. Both basis sets and level of theories are very complex and therefore only a brief description of each will be mentioned. Depending on the methods chosen, the calculations can either be very accurate but extremely time consuming, or done fairly quickly but not as accurate. Thus, usually a balance between the two is made. The level of theory is the method that is chosen, such as ab initio, density functional theory, semi empirical and molecular mechanics. Ab Initio is the most time consuming since it solves the Schrödinger equation for energy and wave functions (which is used to calculate electron distribution), whereas on the opposite side of the spectrum, molecular mechanics is the quickest since it uses a ball and spring model.[40] In between these methods, there is the semi empirical method which is

similar to ab initio methods but there are more approximations to solving the Schrödinger equation thus reducing calculation time and lastly, density functional theory (DFT) which uses the Kohn Sham equations to calculate electron density as a whole.[40] For the study of anionic metal complexes, DFT functionals were chosen (B3lyp, B3wp91, B98, Bhandhlyp, Mpw1pw91 and Pbe1pbe) since they are a nice compromise between speed and accuracy. A slower, ab initio method, MP2 was chosen as well.

The basis set is an important aspect of theoretical calculations as it calculates atomic and molecular orbitals as a linear function that are usually centered on the nucleus of atoms.[41] For studying chemical systems that have atoms past the first row of elements, it is important to add a d function which takes into consideration polarization that can arise from the d-orbitals polarizing the p-orbitals (as shown in Figure 2-21) since it moves the electron density based on polarization affecting the minimum energy. [42] Another way basis sets can simulate a realistic electron distribution is to split the valence functions into outer and inner shell functions where the outer functions are more diffuse allowing for more flexibility with the electron distribution (Figure 2-22). It is also possible to split a valence shell three ways with an inner, middle and outer orbital. A relatively accurate basis set that can do this is the 6-311+gd basis set where the valence shell is split into three with three Gaussian functions in the inner shell and single Gaussian functions in the middle and outer shells while the core shell has a basis function of six Gaussian functions.[42] For anionic complexes, adding a plus sign (representing a diffuse function) is ideal as it allows the heavier atom's electron density (everything except hydrogen and helium) to have larger distances away from the nucleus.[42] Therefore the 6-311+gd basis set is an appropriate basis set for anionic metal complexes.

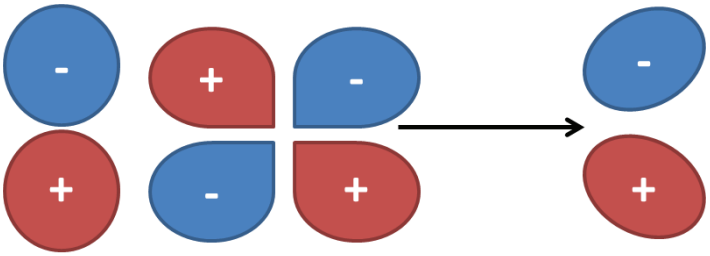


Figure 2-21: Importance of adding the d function in a basis set. It accounts for the polarization effect of the p-orbitals in the presence of d-orbitals.

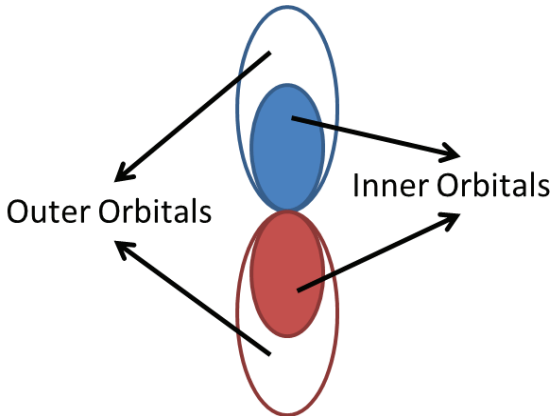


Figure 2-22: An example of inner and outer orbitals for calculations. The outer orbitals are more diffuse than the inner orbitals.

The 6-311+gd basis set works well with anionic metal complex systems, however it is not available for heavier metals that are lower in the periodic table, for example, silver, cesium and cobalt. Thus, another basis set able to handle heavier metals is needed and a suitable choice is the LANL2DZ set which was created by Hay *et al*.[43] It gets difficult and time consuming to calculate transition metals in lower rows because of the electron-electron repulsion occurring between core and valence electrons. This basis set uses something known as an effective core potential which minimizes the electron repulsion integrals by

adding a one-electron operator (Fock) that simplifies the core orbitals into a way that combines the core electrons into one repulsion on the valence electrons since they do not have an effect on bonding anyway, thus reducing time and the difficulty.[42]

Therefore with appropriate levels of theory and basis sets it is possible to determine reliable theoretical structures for metal anionic complexes.

2.4.2 Programs for collision cross-section determination

There are two different programs, Sigma (created by Bower *et al.*) and Mobcal (created by Jarrold *et al.*) that can be used to determine theoretical collision cross-sections computationally and each will be briefly described.

The Sigma program uses something known as the projection method for collisions between an ion and a neutral buffer gas.[44] The program randomly chooses a plain in space and a circle is drawn as a collision radius for the ion and for the buffer gas. Then there are points that are randomly chosen within a square area of collision radius of the ion or the buffer gas. If the points are inside one or both radii, it is considered in the overall average collision cross section. However, if a point is outside both collision radii, it is rejected. This process is repeated until the average collision cross-section has a value within the acceptable values of error. The average collision cross section is determined by the ratio of accepted points versus total and multiplied by the square area of the projected ion.[44]

The Mobcal program uses different techniques for collision cross-section determination than that of Sigma. It has three different methods: the projection approximation, exact sphere scattering and the trajectory method. However, the only method discussed will be the trajectory method since it was the method of interest for this project. The trajectory method can be deemed the most accurate out of the three as it considers each atom individually through a 12-6-4 Lennard-Jones potential and a scattering angle. A scattering angle can be defined as the trajectory angle of where the buffer gas hits the ion and

leaves the ion. To obtain a scattering angle, the potentials of each atom in the ionic complex are summed and made into an effective potential to which trajectories are run. Scattering angles are determined from all possible ion-buffer gas collisions and are averaged to give an average collision cross-section.[16, 45]

2.5 References

1. (a) J. Gross, in *Mass Spectrometry*. Springer Berlin Heidelberg, 2011, pp 1-20; (b) W. Schänzer, P. Delahaut, H. Geyer, M. Machnik, S. Horning, Long-term detection and identification of metandienone and stanozolol abuse in athletes by gas chromatography-high-resolution mass spectrometry. *Journal of Chromatography B: Biomedical Sciences and Applications* 1996, *687*. 93-108, DOI: http://dx.doi.org/10.1016/S0378-4347(96)00187-9.
2. (a) M. Dole, R. L. Hines, L. L. Mack, R. C. Mobley, L. D. Ferguson, M. B. Alice, Gas Phase Macroions. *Macromolecules* 1968, *1*. 96-97, DOI: 10.1021/ma60001a017; (b) M. Yamashita, J. B. Fenn, Electrospray ion source. Another variation on the free-jet theme. *The Journal of Physical Chemistry* 1984, *88*. 4451-4459, DOI: 10.1021/j150664a002; (c) J. Fenn, M. Mann, C. Meng, S. Wong, C. Whitehouse, Electrospray ionization for mass spectrometry of large biomolecules. *Science* 1989, *246*. 64-71, DOI: 10.1126/science.2675315.
3. P. Kebarle, L. Tang, From ions in solution to ions in the gas phase - the mechanism of electrospray mass spectrometry. *Analytical Chemistry* 1993, *65*. 972A-986A, DOI: 10.1021/ac00070a001.
4. R. D. Smith, J. A. Loo, C. G. Edmonds, C. J. Barinaga, H. R. Udseth, New developments in biochemical mass spectrometry: electrospray ionization. *Analytical Chemistry* 1990, *62*. 882-899, DOI: 10.1021/ac00208a002.
5. A. T. Blades, M. G. Ikonomou, P. Kebarle, Mechanism of electrospray mass spectrometry. Electrospray as an electrolysis cell. *Analytical Chemistry* 1991, *63*. 2109-2114, DOI: 10.1021/ac00019a009.
6. J. Gross, in *Mass Spectrometry*. Springer Berlin Heidelberg, 2011, pp 561-620.
7. L. Konermann, E. Ahadi, A. D. Rodriguez, S. Vahidi, Unraveling the Mechanism of Electrospray Ionization. *Analytical Chemistry* 2012, *85*. 2-9, DOI: 10.1021/ac302789c.
8. K. Miseki. Google Patents, 1993.
9. R. E. March, J. F. J. Todd, in *Quadrupole Ion Trap Mass Spectrometry*. John Wiley & Sons, Inc., 2005, pp 1-33.
10. I. V. Chernushevich, A. V. Loboda, B. A. Thomson, An introduction to quadrupole–time-of-flight mass spectrometry. *Journal of Mass Spectrometry* 2001, *36*. 849-865, DOI: 10.1002/jms.207.
11. J. C. Robert, in *Time-of-Flight Mass Spectrometry*. American Chemical Society, 1993, vol. 549, pp 16-48.
12. C. B. Ronald, in *Time-of-Flight Mass Spectrometry*. American Chemical Society, 1993, vol. 549, pp 49-60.
13. A. K. Shukla, J. H. Futrell, in *Encyclopedia of Spectroscopy and Spectrometry*, ed. J. C. Lindon. Elsevier: Oxford, 1999, pp 954-963.
14. S. A. McLuckey, Principles of collisional activation in analytical mass spectrometry. *Journal of The American Society for Mass Spectrometry* 1992, *3*. 599-614, DOI: http://dx.doi.org/10.1016/1044-0305(92)85001-Z.
15. F. Lanucara, S. W. Holman, C. J. Gray, C. E. Eyers, The power of ion mobility-mass spectrometry for structural characterization and the study of conformational dynamics. *Nat Chem* 2014, *6*. 281-294, DOI: 10.1038/nchem.1889.
16. M. F. Mesleh, J. M. Hunter, A. A. Shvartsburg, G. C. Schatz, M. F. Jarrold, Structural Information from Ion Mobility Measurements: Effects of the Long-Range Potential. *The Journal of Physical Chemistry* 1996, *100*. 16082-16086, DOI: 10.1021/jp961623v.
17. D. E. Clemmer, M. F. Jarrold, Ion Mobility Measurements and their Applications to Clusters and Biomolecules. *Journal of Mass Spectrometry* 1997, *32*. 577-592, DOI: 10.1002/(sici)1096-9888(199706)32:6<577::aid-jms530>3.0.co;2-4.

18. I. Michaelevski, N. Kirshenbaum, M. Sharon, T-wave ion mobility-mass spectrometry: basic experimental procedures for protein complex analysis. *Journal of Visualized Experiments* 2010. DOI: 10.3791/1985.
19. P. Atkins, J. d. Paula, *Atkins' Physical Chemistry*. 6 ed.; Oxford University Press: Great Britain, 2006; p 244.
20. P. Atkins, J. d. Paula, *Atkins' Physical Chemistry*. 6 ed.; Oxford University Press: Great Britain, 2006; p 490.
21. P. Atkins, J. d. Paula, *Atkins' Physical Chemistry*. 6 ed.; Oxford University Press: Great Britain, 2006; p 983.
22. N. B. Colthup, L. H. Daly, S. E. Wiberley, in *Introduction to Infrared and Raman Spectroscopy (Third Edition)*, ed. N. B. Colthup, L. H. Daly, S. E. Wiberley. Academic Press: San Diego, 1990, pp 1-73.
23. G. C. King, *Vibrations and waves*. Hoboken, NJ : Wiley: 2009; p 1-32.
24. P. Atkins, J. d. Paula, *Atkins' Physical Chemistry*. 6 ed.; Oxford University Press: Great Britain, 2006; p 455.
25. P. R. Griffiths, in *Handbook of Vibrational Spectroscopy*. John Wiley & Sons, Ltd, 2006.
26. N. C. Polfer, J. Oomens, Vibrational spectroscopy of bare and solvated ionic complexes of biological relevance. *Mass Spectrometry Reviews* 2009, *28*. 468-494, DOI: 10.1002/mas.20215.
27. J. Oomens, B. G. Sartakov, G. Meijer, G. von Helden, Gas-phase infrared multiple photon dissociation spectroscopy of mass-selected molecular ions. *International Journal of Mass Spectrometry* 2006, *254*. 1-19, DOI: http://dx.doi.org/10.1016/j.ijms.2006.05.009.
28. T. D. Fridgen, Infrared consequence spectroscopy of gaseous protonated and metal ion cationized complexes. *Mass Spectrometry Reviews* 2009, *28*. 586-607, DOI: 10.1002/mas.20224.
29. L. I. Yeh, M. Okumura, J. D. Myers, J. M. Price, Y. T. Lee, Vibrational spectroscopy of the hydrated hydronium cluster ions H3O+·(H2O)n (n=1, 2, 3). *The Journal of Chemical Physics* 1989, *91*. 7319-7330, DOI: doi:http://dx.doi.org/10.1063/1.457305.
30. O. P. Balaj, C. Kapota, J. Lemaire, G. Ohanessian, Vibrational signatures of sodiated oligopeptides (GG–Na+, GGG–Na+, AA–Na+ and AAA–Na+) in the gas phase. *International Journal of Mass Spectrometry* 2008, *269*. 196-209, DOI: http://dx.doi.org/10.1016/j.ijms.2007.10.004.
31. R. Prazeres, F. Glotin, C. Insa, D. A. Jaroszynski, J. M. Ortega, Two-colour operation of a Free-Electron Laser and applications in the mid-infrared. *The European Physical Journal D* 1998, *3*. 87-93, DOI: 10.1007/s100530050151.
32. W. B. Colson, E. D. Johnson, M. J. Kelley, H. A. Schwettman, Putting free-electron lasers to work. *Physics Today* 2002, *55*. 35-41, DOI: 10.1063/1.1457263.
33. CLIO, What is a Free-Electron laser? *http://clio.lcp.u-psud.fr/clio_eng/FEL.html* 2012.
34. T. D. Fridgen, L. MacAleese, P. Maitre, T. B. McMahon, P. Boissel, J. Lemaire, Infrared spectra of homogeneous and heterogeneous proton-bound dimers in the gas phase. *Physical Chemistry Chemical Physics* 2005, *7*. 2747-2755, DOI: 10.1039/b504926a.
35. A. G. Marshall, C. L. Hendrickson, G. S. Jackson, Fourier transform ion cyclotron resonance mass spectrometry: A primer. *Mass Spectrometry Reviews* 1998, *17*. 1-35, DOI: 10.1002/(sici)1098-2787(1998)17:1<1::aid-mas1>3.0.co;2-k.
36. M. P. Barrow, W. I. Burkitt, P. J. Derrick, Principles of Fourier transform ion cyclotron resonance mass spectrometry and its application in structural biology. *Analyst* 2005, *130*. 18-28, DOI: 10.1039/b403880k.
37. V. H. Vartanian, J. S. Anderson, D. A. Laude, Advances in trapped ion cells for Fourier transform ion cyclotron resonance mass spectrometry. *Mass Spectrometry Reviews* 1995, *14*. 1-19, DOI: 10.1002/mas.1280140102.
38. M. J. Frisch, G. W. Trucks, H. B. Schlegel, G. E. Scuseria, M. A. Robb, J. R. Cheeseman, G. Scalmani, V. Barone, B. Mennucci, G. A. Petersson, H. Nakatsuji, M. Caricato, X. Li, H. P. Hratchian, A. F.

Izmaylov, J. Bloino, G. Zheng, J. L. Sonnenberg, M. Hada, M. Ehara, K. Toyota, R. Fukuda, J. Hasegawa, M. Ishida, T. Nakajima, Y. Honda, O. Kitao, H. Nakai, T. Vreven, J. A. Montgomery Jr., J. E. Peralta, F. Ogliaro, M. J. Bearpark, J. Heyd, E. N. Brothers, K. N. Kudin, V. N. Staroverov, R. Kobayashi, J. Normand, K. Raghavachari, A. P. Rendell, J. C. Burant, S. S. Iyengar, J. Tomasi, M. Cossi, N. Rega, N. J. Millam, M. Klene, J. E. Knox, J. B. Cross, V. Bakken, C. Adamo, J. Jaramillo, R. Gomperts, R. E. Stratmann, O. Yazyev, A. J. Austin, R. Cammi, C. Pomelli, J. W. Ochterski, R. L. Martin, K. Morokuma, V. G. Zakrzewski, G. A. Voth, P. Salvador, J. J. Dannenberg, S. Dapprich, A. D. Daniels, Ö. Farkas, J. B. Foresman, J. V. Ortiz, J. Cioslowski, D. J. Fox. Gaussian, Inc.: Wallingford, CT, USA, 2013.

39. P. Hobza, J. Šponer, T. Reschel, Density functional theory and molecular clusters. *Journal of Computational Chemistry* 1995, *16*. 1315-1325, DOI: 10.1002/jcc.540161102.

40. E. Lewars, in *Computational Chemistry*. Springer Netherlands, 2011, pp 1-7.

41. E. Lewars, in *Computational Chemistry*. Springer Netherlands, 2011, pp 85-173.

42. E. Lewars, in *Computational Chemistry*. Springer Netherlands, 2011, pp 175-390.

43. (a) P. J. Hay, W. R. Wadt, Ab initio effective core potentials for molecular calculations. Potentials for K to Au including the outermost core orbitals. *The Journal of Chemical Physics* 1985, *82*. 299-310, DOI: doi:http://dx.doi.org/10.1063/1.448975; (b) W. R. Wadt, P. J. Hay, Ab initio effective core potentials for molecular calculations. Potentials for main group elements Na to Bi. *The Journal of Chemical Physics* 1985, *82*. 284-298, DOI: doi:http://dx.doi.org/10.1063/1.448800; (c) P. J. Hay, W. R. Wadt, Ab initio effective core potentials for molecular calculations. Potentials for the transition metal atoms Sc to Hg. *The Journal of Chemical Physics* 1985, *82*. 270-283, DOI: doi:http://dx.doi.org/10.1063/1.448799.

44. (a) T. Wyttenbach, G. von Helden, J. Batka, D. Carlat, M. Bowers, Effect of the long-range potential on ion mobility measurements. *Journal of The American Society for Mass Spectrometry* 1997, *8*. 275-282, DOI: 10.1016/s1044-0305(96)00236-x; (b) G. von Helden, M. T. Hsu, N. Gotts, M. T. Bowers, Carbon cluster cations with up to 84 atoms: structures, formation mechanism, and reactivity. *The Journal of Physical Chemistry* 1993, *97*. 8182-8192, DOI: 10.1021/j100133a011.

45. A. A. Shvartsburg, M. F. Jarrold, An exact hard-spheres scattering model for the mobilities of polyatomic ions. *Chemical Physics Letters* 1996, *261*. 86-91, DOI: http://dx.doi.org/10.1016/0009-2614(96)00941-4.

3 IRMPD AND THEORETICAL RESULTS

3.1 Methods

3.1.1 Experimental

Experiments were performed at CLIO (Centre de Laser Infra-rouge D'Orsay) in France using a Fourier Transform Ion Cyclotron Resonance (FT-ICR) mass spectrometer with a 7 tesla magnet (Apex Qe, Bruker). Solutions of metal oxalate complexes were prepared with methanol as the solvent and then ions were introduced into the FT-ICR mass spectrometer via electrospray ionization. Once the parent ion was trapped and isolated in the ICR cell, a FEL was introduced for 0.78 seconds over the range of 1000 to 2000cm^{-1} with intervals of 20.8 cm^{-1}. When the frequency of the FEL was resonant with a vibrational mode, photons were absorbed until there was enough energy for dissociation to occur and a mass spectrum was recorded. In order to plot IRMPD spectra, first IRMPD efficiency must be calculated by taking the negative of the normalized parent ion intensity's natural logarithm. It is then plotted versus the frequency of the laser.

3.1.2 Computational

To determine structural conformations of metal-oxalic acid anionic complexes, optimization and frequency calculations were done with different density functionals (B3lyp, B3pw91, B98, Bhandhlyp, M062x, Mpw1pw91 and Pbe1pbe) and MP2 calculations with either a 6-311+gd (Fe, K) or lanl2dz (Cs, Ag) basis set for each complex using the Gaussian 09 Suite of programs.[1] For each level of theory, two starting structures were generated per complex in order to start exploring different possible structural conformations. The first type of starting structure will be known as an "X" structure where the ligands are along the same plane as the metal and the second structure will be known as a "Y" structure where the ligands are above and below the plane (Figure 3-1).

Once the “X” and “Y” structures of each level of theory for each complex were optimized and had their frequencies calculated, theoretical spectra could be generated with intensity vs. frequency. However, the computed frequencies required scaling factors to account for inaccuracy of the method since they are calculated harmonically.[2] Scaling factors used are from the NIST database and are listed in Table 3-1.[3] Once the theoretical frequencies were scaled, they were plotted, and compared to the IRMPD experimental spectrum.

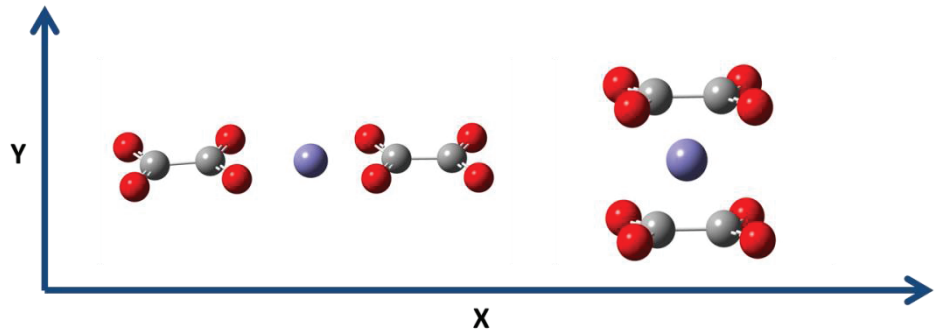


Figure 3-1: Example of starting structures for complexes. Structure on the left is an “X” structure where ligands are on the same plane as the metal. The structure on the right is a “Y” structure where the ligands are above and below the plane of the metal.

Table 3-1: Scaling factors used on computed frequencies. Note: scaling factors for basis set 6-311+gd were not listed so scaling factors for 6-311 were used for 6-311+gd. Levels of theory with a star were not listed and averages of similar levels of theory were therefore taken. MP2=full was used for Cs only.**

Level of Theory	6-311+gd Scaling Factors	Lanl2dz Scaling Factors
B3lyp	0.967	0.961
B3pw91	0.963	0.957
B98*	0.960	0.969
Bhandhlyp*	0.960	0.969
M062x*	0.957	0.950
Mpw1pw91	0.957	0.950
Pbe1pbe*	0.991	0.965
MP2	0.950	0.963
MP2=full	--	0.950

3.2 Metal – $Ox_2H_2^-$ complexes

As mentioned in the computational methods section, for theoretical calculations there were two starting structures ("X" and "Y") generated per level of theory to explore different structural conformations. After optimization, there were many different low energy structures generated from different levels of theory. Since there was no consistency between different levels of theory it is impossible to assign a gas phase structure to each metal complex using theoretical structures alone. This section will go through each complex and compare the IRMPD spectrum to each unique theoretical structure's spectrum in a methodical fashion. Once a plausible structure is determined, frequencies will be assigned.

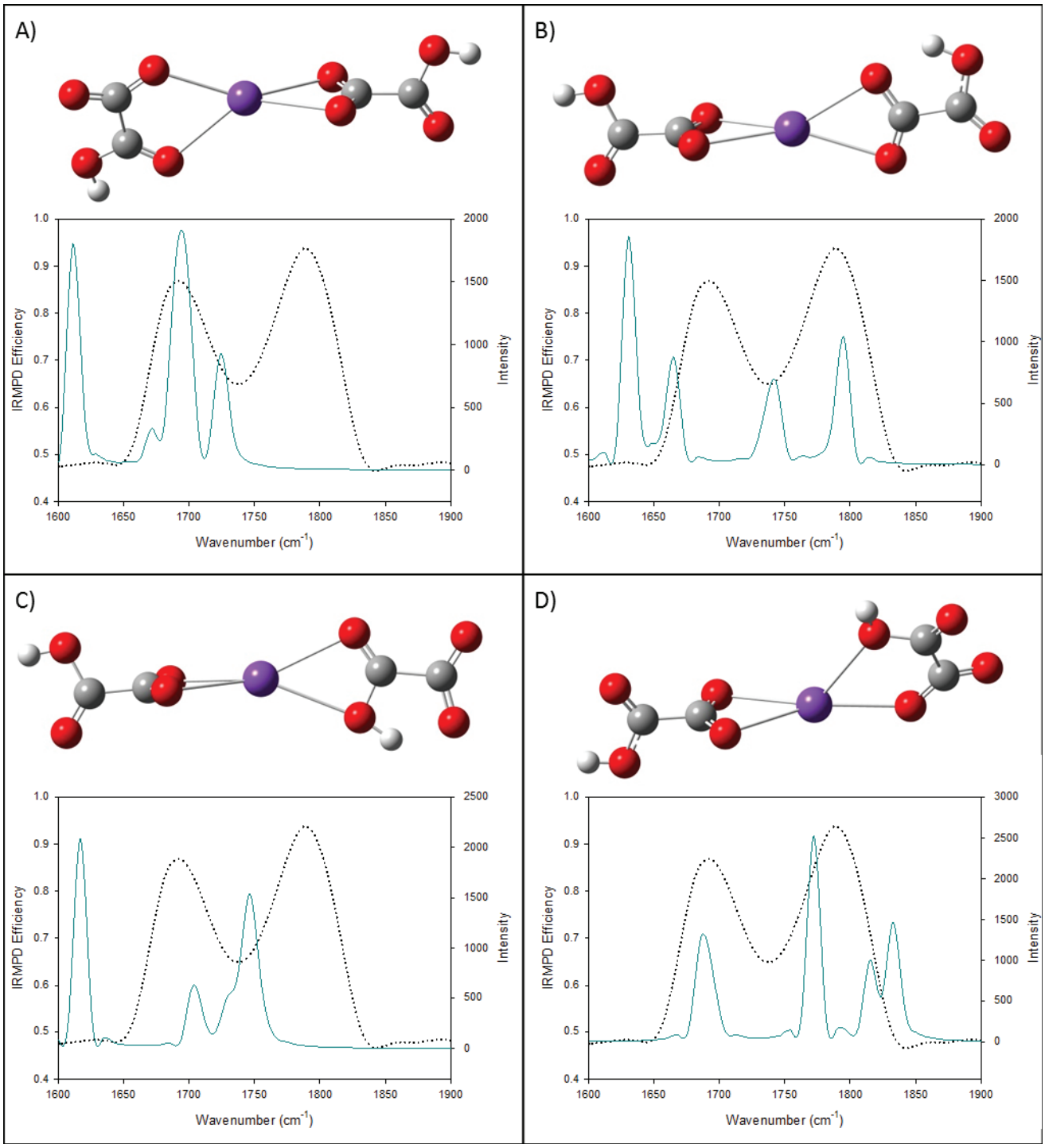
3.2.1 $KOx_2H_2^-$

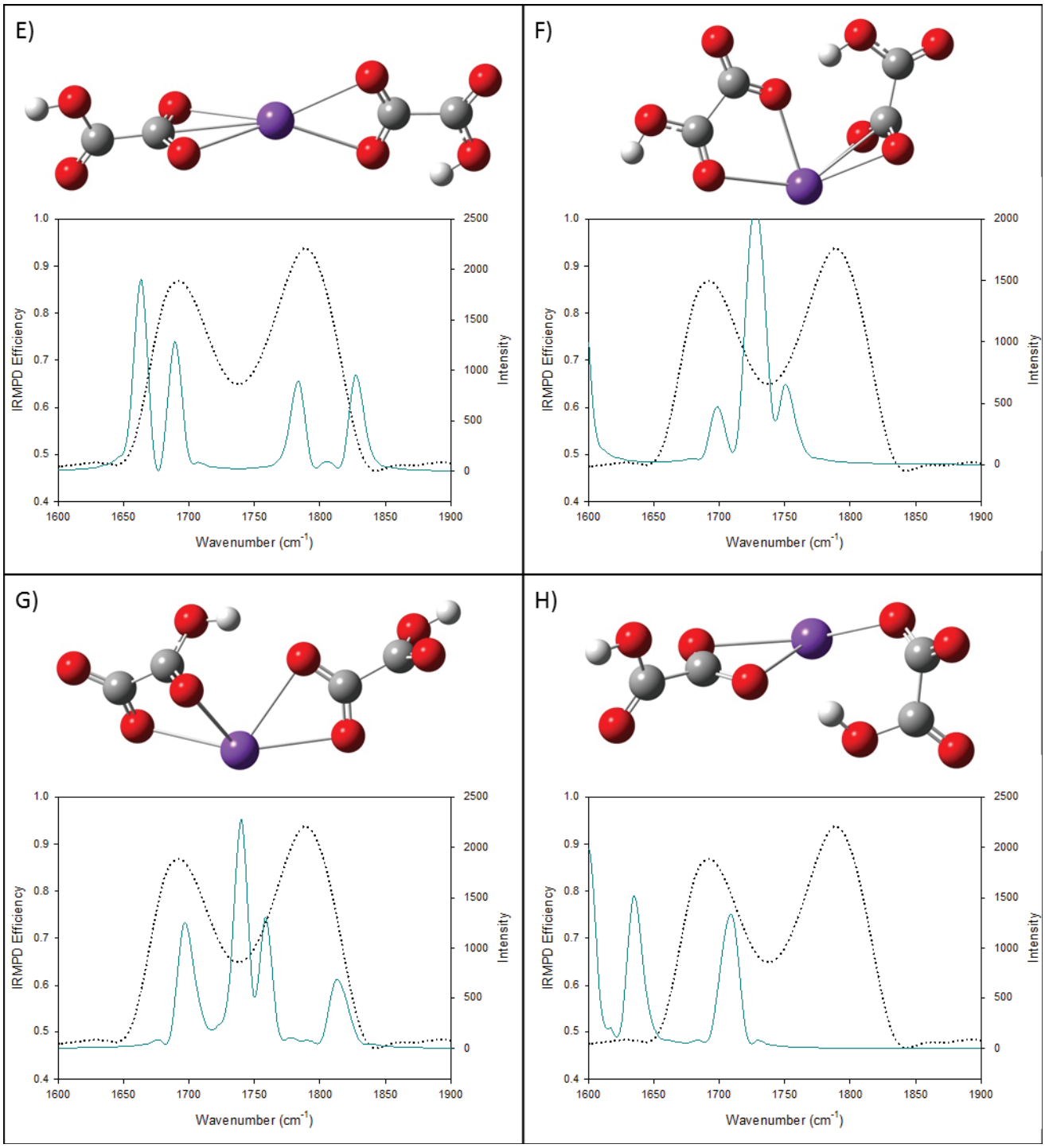
3.2.1.1 1600-1900 cm^{-1} Range

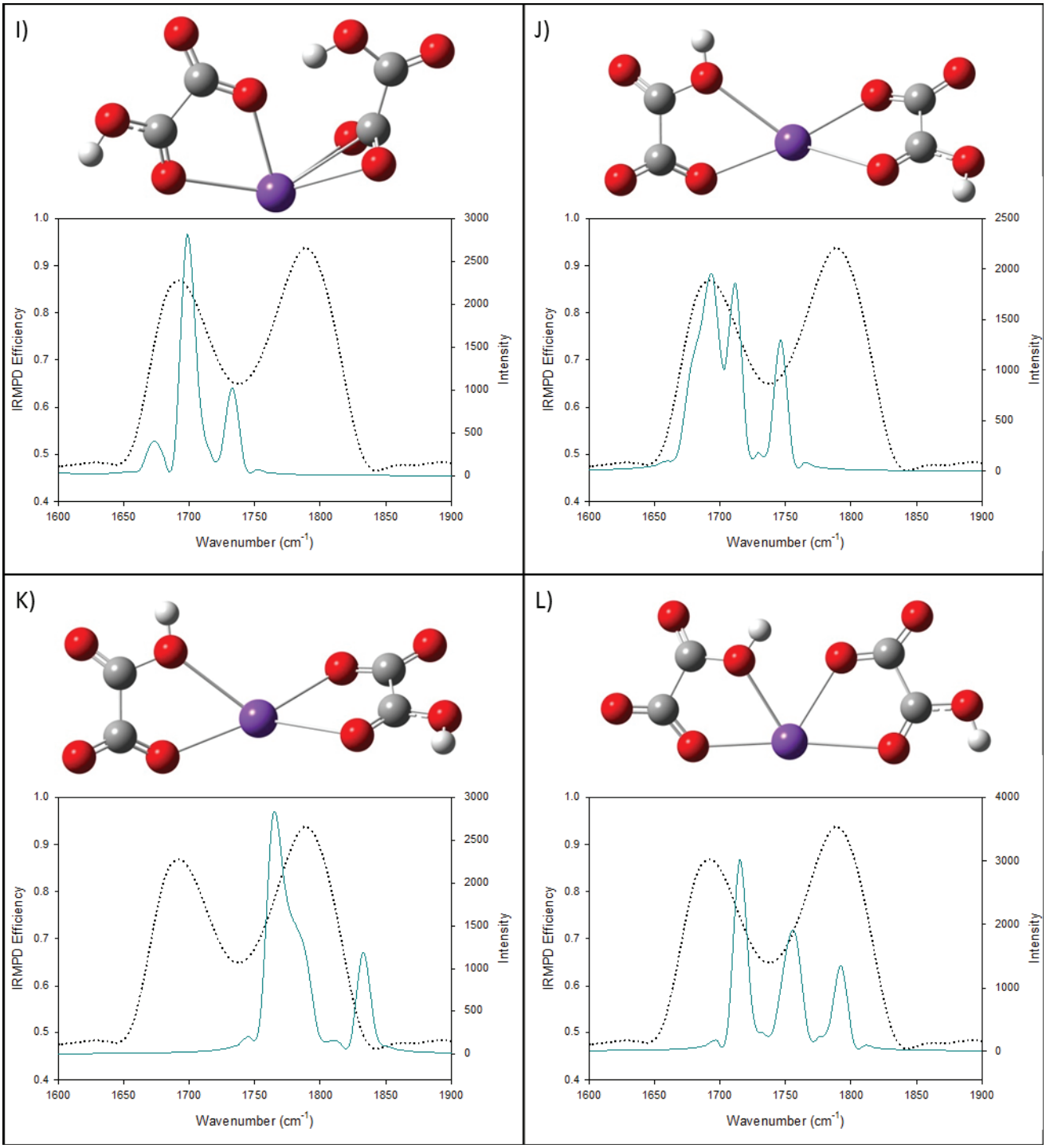
When optimization frequency calculations were done on $KOx_2H_2^-$, thirteen unique structures were generated. Each structure with its theoretical spectrum overlapped with the IRMPD spectrum can be seen in Figure 3-2.

Figure 3-2 shows the different structures that were generated from the "X" and "Y" structures of various levels of theory. Comparing the theoretical spectra to the IRMPD spectrum, structures can be eliminated immediately. Structures in Figure 3-2 parts A, B, C, F, H, I, J, K and L all have theoretical frequencies too different than that of the experimental spectrum. Thus, the remaining possible structures are in Figure 3-2 parts D, E and G with Figure 3-2E being the closest match for the range of 1600-1900 cm^{-1}.

The "X" structure of Bhandhlyp is represented in Figure 3-2D). There are four peaks in the 1600-1900 cm^{-1} range appearing around 1685 cm^{-1}, 1775 cm^{-1}, 1815 cm^{-1} and 1835 cm^{-1} where peaks 1685 cm^{-1}, 1815 cm^{-1} and 1835 cm^{-1} are close to IRMPD peaks . Figure 3-2E) shows the "X" structure of M062x with frequencies at approximately 1165 cm^{-1}, 1690 cm^{-1}, 1785 cm^{-1} and 1825 cm^{-1} with peaks 1690cm^{-1} and 1785 cm^{-1} being very close to experimental frequencies. The "X" structure for Pbe1pbe is shown in Figure 3-2G). There are four theoretical peaks appearing around 1700 cm^{-1}, 1740 cm^{-1}, 1755 cm^{-1} and 1815 cm^{-1} with the first and last peaks similar to the IRMPD peaks.


A)
B)
C)
D)
IRMPD Efficiency
Intensity
Wavenumber (cm-1)
1600
1650
1700
1750
1800
1850
1900


E)
F)
G)
H)
IRMPD Efficiency
Intensity
Wavenumber (cm-1)
1600
1650
1700
1750
1800
1850
1900
0.4
0.5
0.6
0.7
0.8
0.9
1.0
0
500
1000
1500
2000
2500


I)
J)
K)
L)
IRMPD Efficiency
Intensity
Wavenumber (cm-1)

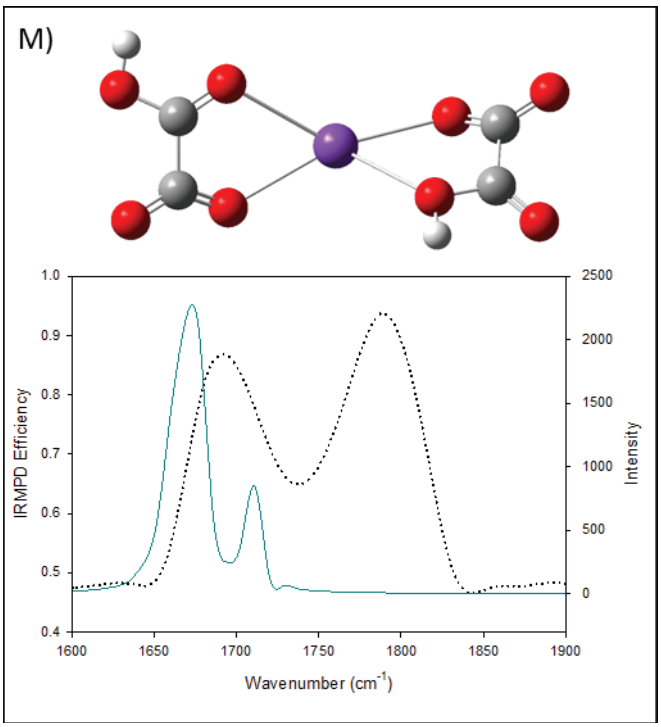


Figure 3-2: Theoretical Structures (basis set : 6-311+gd) and Spectra for each unique $KOx_2H_2^-$ structure. The IRMPD spectrum (dotted) overlaps each theoretical spectra (green). Parts A-H are the "X" structures for B3lyp, B3pw91, B98, Bhandhlyp, M062x, Mpw1pw91 ("Y" structures B3pw91 and Mpw1pw91 are identical) , Pbe1pbe and MP2 respectively while Parts I-M are the "Y" structures for B3lyp, B98, Bhandhlyp ("Y" structure Pbe1pbe is identical), M062x and MP2 respectively.

3.2.1.2 1000-2100 cm^{-1} Range

The theoretical structures that best matched the experimental IRMPD spectrum were Figure 3-2D,E and G for the range of 1600-1900 cm^{-1}However the IRMPD spectrum was observed from the 1000-2000cm^{-1} range. Figure 3-3 shows the three theoretical spectra compared to the IRMPD spectrum for the full range. There are two other peaks in the IRMPD spectrum around 1355 cm^{-1} and 1410 cm^{-1} and all three theoretical spectra have peaks in this area. The structure that has the most peaks matching up with the experimental data is Figure 3-3A.

In all three spectra in Figure 3-3 there is at least one peak below 1200 cm^{-1} with the major vibrational mode corresponding to a COH bend and a CO stretch happening simultaneously within the same CO group. This is problematic because in the IRMPD spectrum there are no peaks in this range. There could be two possibilities for the difference in theoretical and experimental spectra: the vibrational mode was too high in energy and could not absorb enough photons for dissociation to occur, or more probable, there is another structure that could exist in the gas phase. Therefore other structures must be explored.

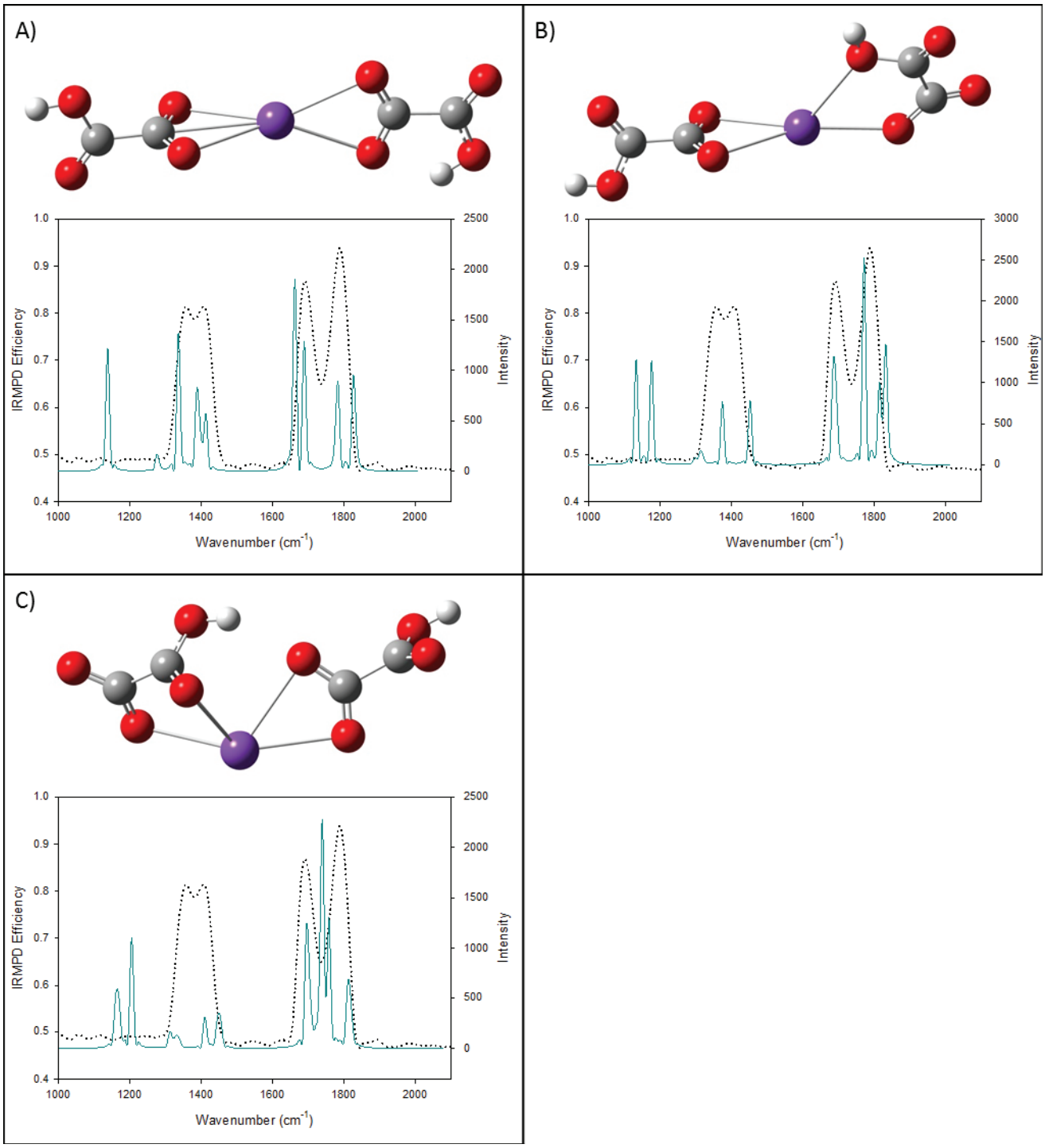


Figure 3-3 Theoretical spectra (basis set: 6-311+gd) of the three best matching structures from the 1600-1900 cm^{-1} range (green) compared to the IRMPD spectrum (dotted) for the range of 1000-2100 cm^{-1}. Parts A, B, and C are the "X" structures for M062x, Bhandhlyp and Pbe1pbe respectively.

3.2.1.3 Second attempt of structure determination for the 1000-2100 cm^{-1} range

At the first attempt of finding the correct structure existing in the gas phase, the best structure that matched up with the IRMPD data was the "X" structure for the DFT level of theory, M062x. Since the major vibrational mode corresponding to the peak below 1200 cm^{-1} involves hydrogen moving, the best solution is to move the protons around to see if the peak will disappear from the theoretical spectrum. Figure 3-4 shows the different starting structures from the optimized M062x structure.

When analyzing different computed structures with the same level of theory and basis set, it is possible to compare relative energies. The lowest energy structure in theory should also be the structure which has its theoretical IR spectrum matching most closely to the experimental results, since ions in the gas phase dissociate via the lowest energy pathway.

The relative energies from the optimized modified structures can be seen in Table 3-2. The structure which had the lowest energy by roughly 30 kJ/mol was structure F) corresponding to the optimized structure of Figure 3-4F). This structure also had the best matching frequencies to the IRMPD spectrum (Figure 3-5). The theoretical spectrum matches well with the exception of a peak around 1600 cm^{-1} (a CO_2 asymmetrical stretch for the protonated CO_2 group bound to potassium) that is not present in the experimental results suggesting a plausible structure has not yet been found.

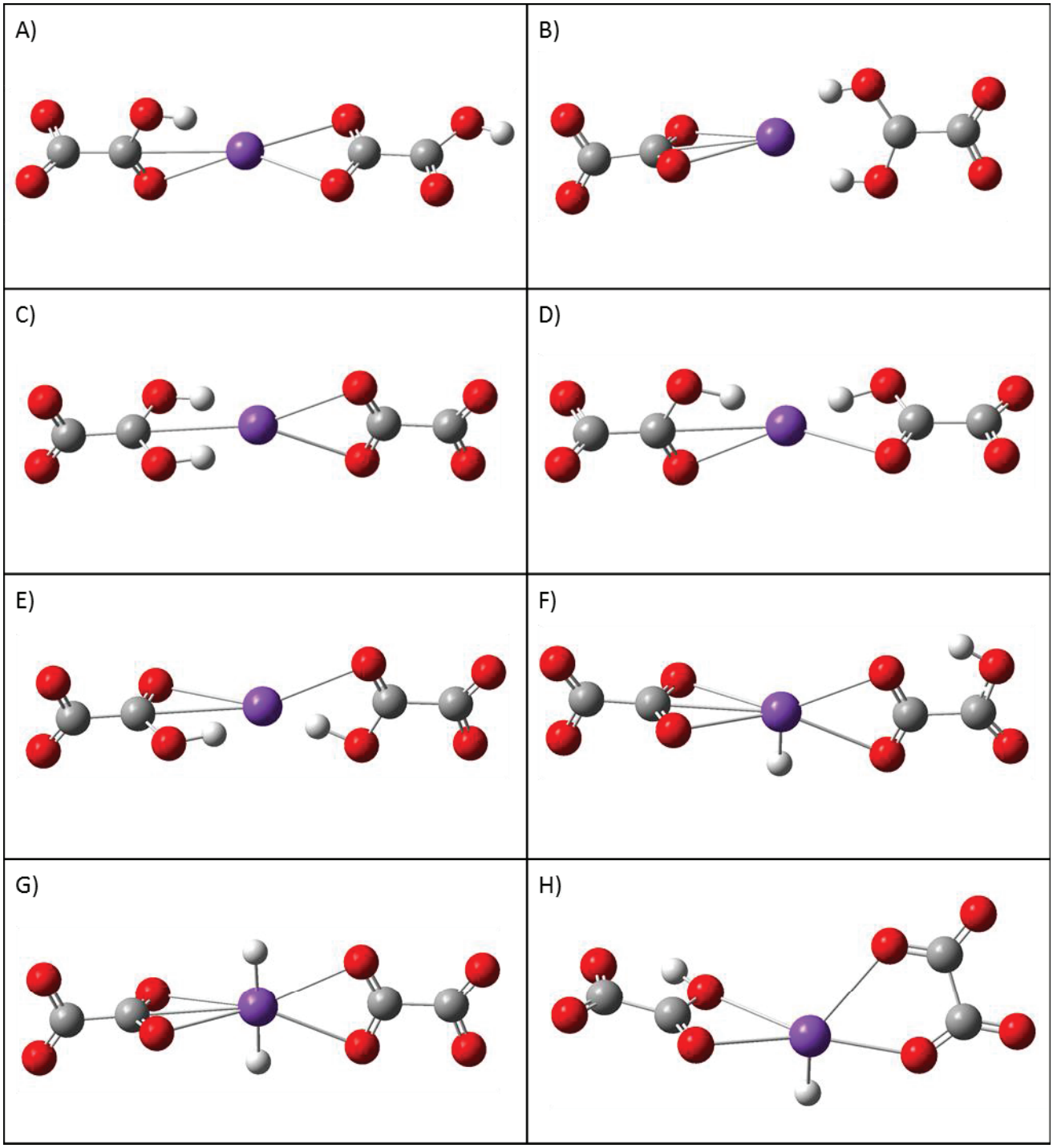


Figure 3-4 Modified starting structures from the calculated "X" structure of M062x.

Table 3-2: Relative energies (kJ/mol) of optimized structures from Figure 3-4. Calculations were performed with a 6-311+gd basis set at a M062x level of theory.

Structure	Relative Energy (kJ/mol)
A)	90.86
B)	84.82
C)	103.30
D)	100.86
E)	106.24
F)	**0.00**
G)	--
H)	31.13

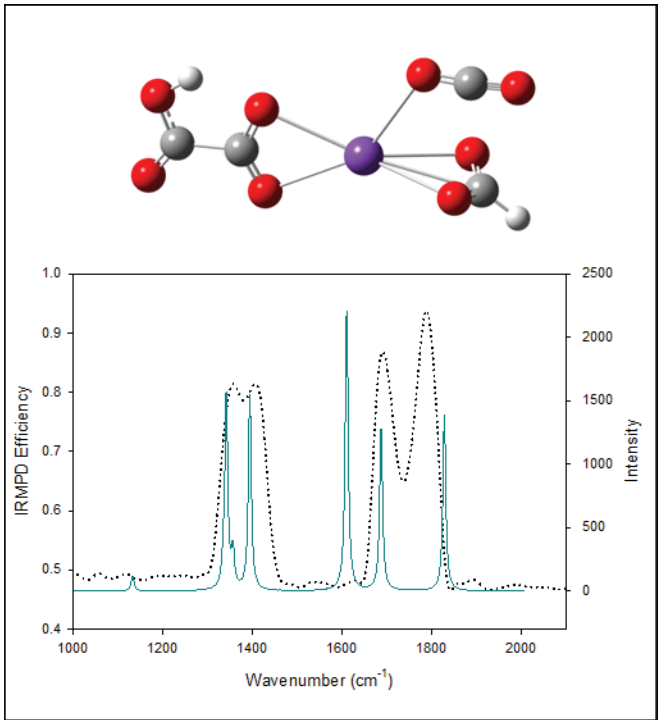


Figure 3-5: Theoretical spectrum (basis set: 6-311+gd) of the best M062x modified structure (green) compared to the IRMPD spectrum (dotted) for the range of 1000-2100 cm^{-1}.

3.2.1.4 Third attempt of structure determination for the 1000-2100 cm^{-1} range

Figure 3-5 shows the structure currently agreeing best with experimental data. To try and eliminate the peak around 1600cm^{-}, another attempt of structure determination can be made by altering the position of the proton and the CO_2 group it was bound too. Three new modified structures were generated – two in which the proton was moved to the complete oxalate in which one structure had the two CO_2 groups bound to potassium (Figure 3-6A) and the other had two intact oxalates (Figure 3-6B). The third modified structure had the intact oxalate and its proton duplicated to the other side of potassium (Figure 3-6B).

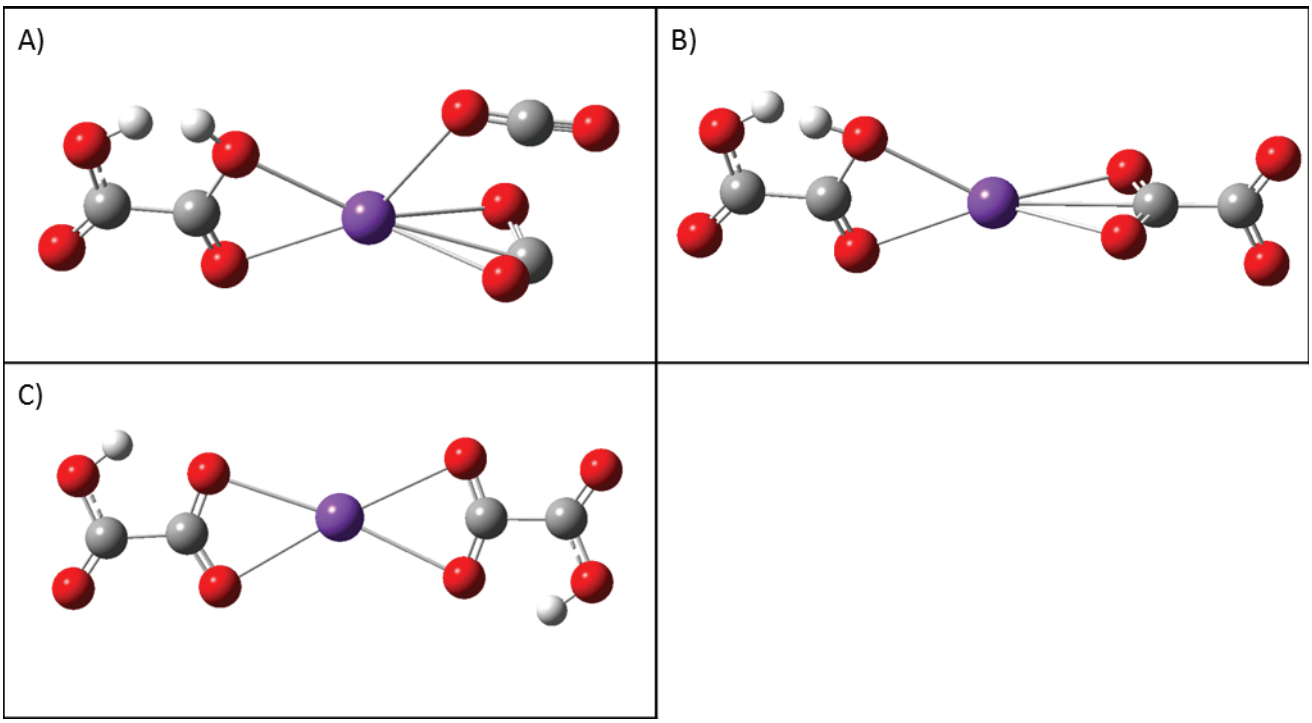


Figure 3-6: Modified starting structures from structure in Figure 3-5 calculated with a 6-311+gd basis set and M062x level of theory.

The energies were compared to the previous low energy structure (Table 3-3). The first two optimized structures that resulted from parts A) and B) in Figure 3-6 had theoretical spectra that did not match up as nicely to the IRMPD spectrum and had energies higher than the previous structure. Thus, these two

structures can be ruled out as a possibility. However the structure that resulted from optimization of Figure 3-6C) had a theoretical spectrum that matched well with experimental results (Figure 3-7) and is a strong candidate for the structure that exists in the gas phase.

Table 3-3: Relative energies (kJ/mol) of optimized structures from Figure 3-6. Calculations were performed with a 6-311+gd basis set at a M062x level of theory.

Structure	Relative Energy (kJ/mol)
A)	476.02
B)	64.74
C)	28.49

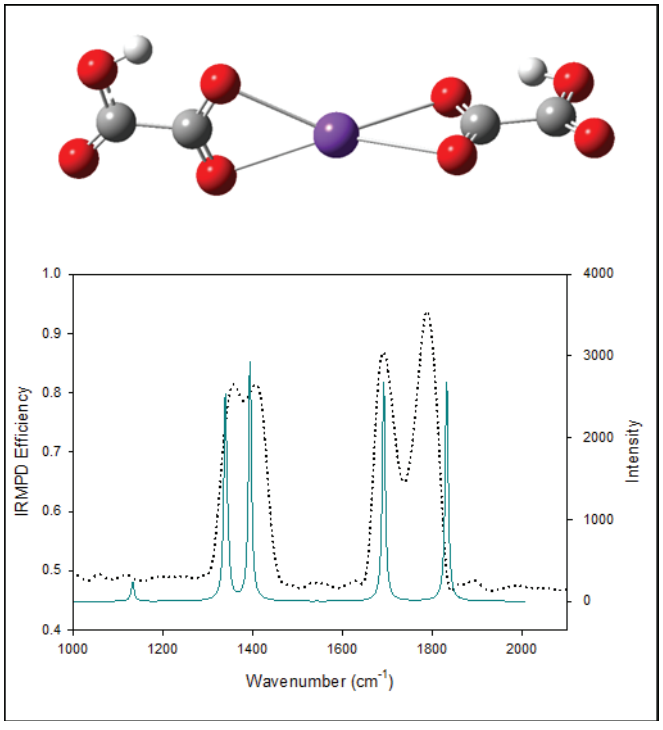
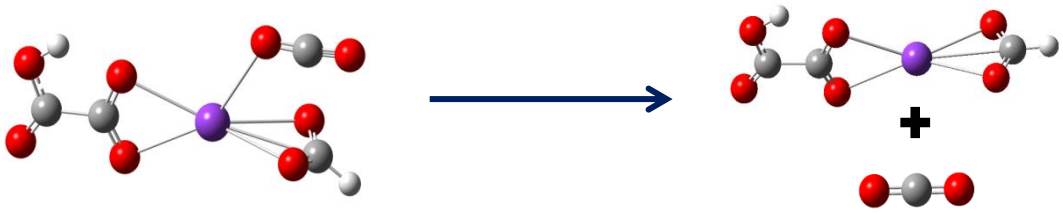


Figure 3-7: Theoretical spectrum (basis set: 6-311+gd) of the best second round M062x modified structure (green) compared to the IRMPD spectrum (dotted) for the range of 1000-2100 cm^{-1}.

Even though the structure in Figure 3-7 has the best match to experimental results, it is higher in energy than the structure in Figure 3-5. A potential explanation could be the structure in Figure 3-5 has a carbon dioxide dissociating immediately, leaving the structure in Figure 3-7 the lowest intact energy structure in the gas phase. Optimization calculations were performed on the structure in Figure 3-5 without the CO_2 group and then a lone CO_2 group in order to determine the energy required for dissociation. The optimized structures of carbon dioxide and $KOxCO_2^-$ are shown in Figure 3-8. Approximately 29 kJ/mol is required for CO_2 to dissociate which is around the energy difference between the two structures in Figure 3-5 and Figure 3-7. If the energy required for dissociation was much lower, then most likely, the carbon dioxide would dissociate readily in the source thus leaving the other structure as the lowest intact energy structure. However since the transition state energies are unknown, this could still be plausible.



Energy required for dissociation: 28.87 kJ/mol

Figure 3-8: The dissociation of CO2 from the lowest energy structure of $KOx_2H_2^-$

3.2.1.5 $KOx_2H_2^-$ Conclusions

To summarize the process of structure determination of $KOx_2H_2^-$, two starting structures were generated for each level of theory. After optimization and frequency calculations, the closest match ended up being the "X" structure of the M062x level of theory (Figure 3-3A). There was a peak around 1140 cm^{-1} that did not appear in the IRMPD spectrum corresponding to a proton vibration. Further structures were explored where the proton was moved to different positions in hopes of eliminating the theoretical peak. Figure 3-5 shows the best optimized structure that resulted from further exploration. The theoretical spectrum matched quite well with the exception of a peak around 1600cm^{-1} which was a CO_2 asymmetrical stretch for the protonated CO_2 group bound to potassium. Three more altered structures were optimized and Figure 3-7 shows a structure that matched quite well with the IRMPD spectrum. However, it was approximately 30 kJ/mol higher in energy than the structure in Figure 3-5. The possibility of the structure in Figure 3-5 having a CO_2 dissociate readily is plausible even though the energy required is roughly the same as the difference between the two lowest energy structures since the transition state energies are unknown.

Even though, the structure in Figure 3-7 is higher in energy, it matches best with the IRMPD spectrum. Computational chemistry is not always enough to determine structure alone so it is important to compare it to an experimental method, such as IRMPD. Therefore it is the best plausible structure that exists in the gas phase with its frequencies assigned in Table 3-4.

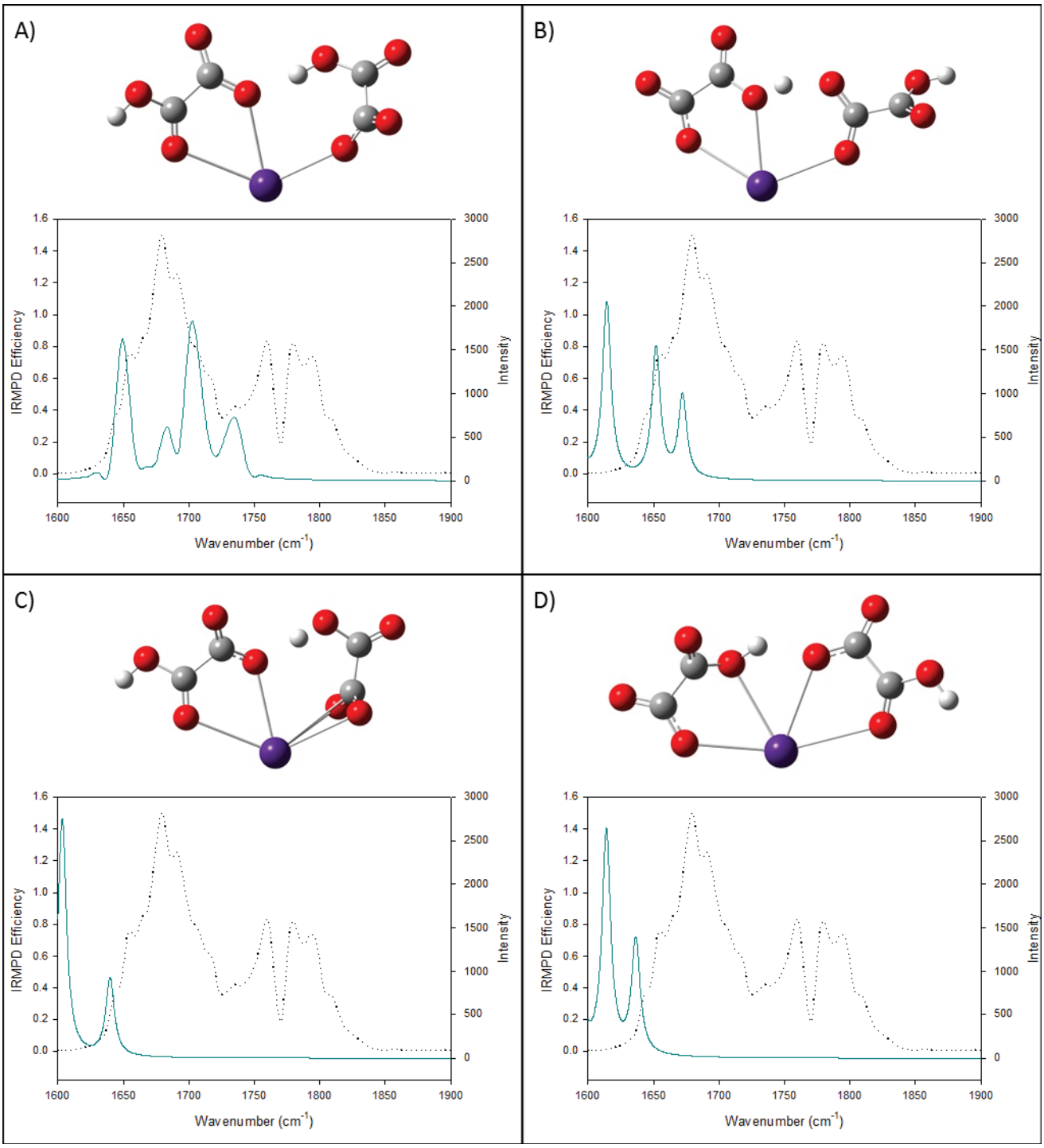
Table 3-4: Vibrational assignments to corresponding frequencies. Note: Each vibration was doubly degenerate.

Theoretical Frequencies (cm^{-1})	Experimental Frequencies (cm^{-1})	Assignment
1135	--	•H-bonded CO Stretch •H-bonded COH Bend
1340	1360	•Bound symmetrical CO_2 Stretch •H-bonded COH Bend
1395	1405	•Bound CO Stretch •H-bonded CO Stretch •H-bonded COH Bend
1695	1690	•Bound asymmetrical CO_2 Stretch •H-bonded asymmetrical CO_2 Stretch •H-bonded COH Bend
1835	1790	•CO Stretch •H-bonded COH Bend

3.2.2 $CsOx_2H_2^-$

3.2.2.1 1600-1900 cm^{-1} Range

When optimization and frequency calculations were performed on $CsOx_2H_2^-$, seven unique low energy structures were generated and each structure with its theoretical spectrum can be seen overlapping the IRMPD spectrum in Figure 3-9. Like in the case of the $KOx_2H_2^-$, structures can be ruled out immediately as those in Figure 3-9 parts B,C,D,F,G,H all have theoretical spectra too different than the experimental results. Thus, the closest structures to matching the IRMPD spectrum are in Figure 3-9 parts A and E, both having peaks in the 1645-1760 cm^{-1} range matching well experimental results. However both are missing a peak around the 1800 cm^{-1} range suggesting the structure existing in the gas phase has not yet been found.


A)
B)
C)
D)
IRMPD Efficiency
Intensity
Wavenumber (cm-1)
1600
1650
1700
1750
1800
1850
1900
0.0
0.2
0.4
0.6
0.8
1.0
1.2
1.4
1.6
0
500
1000
1500
2000
2500
3000

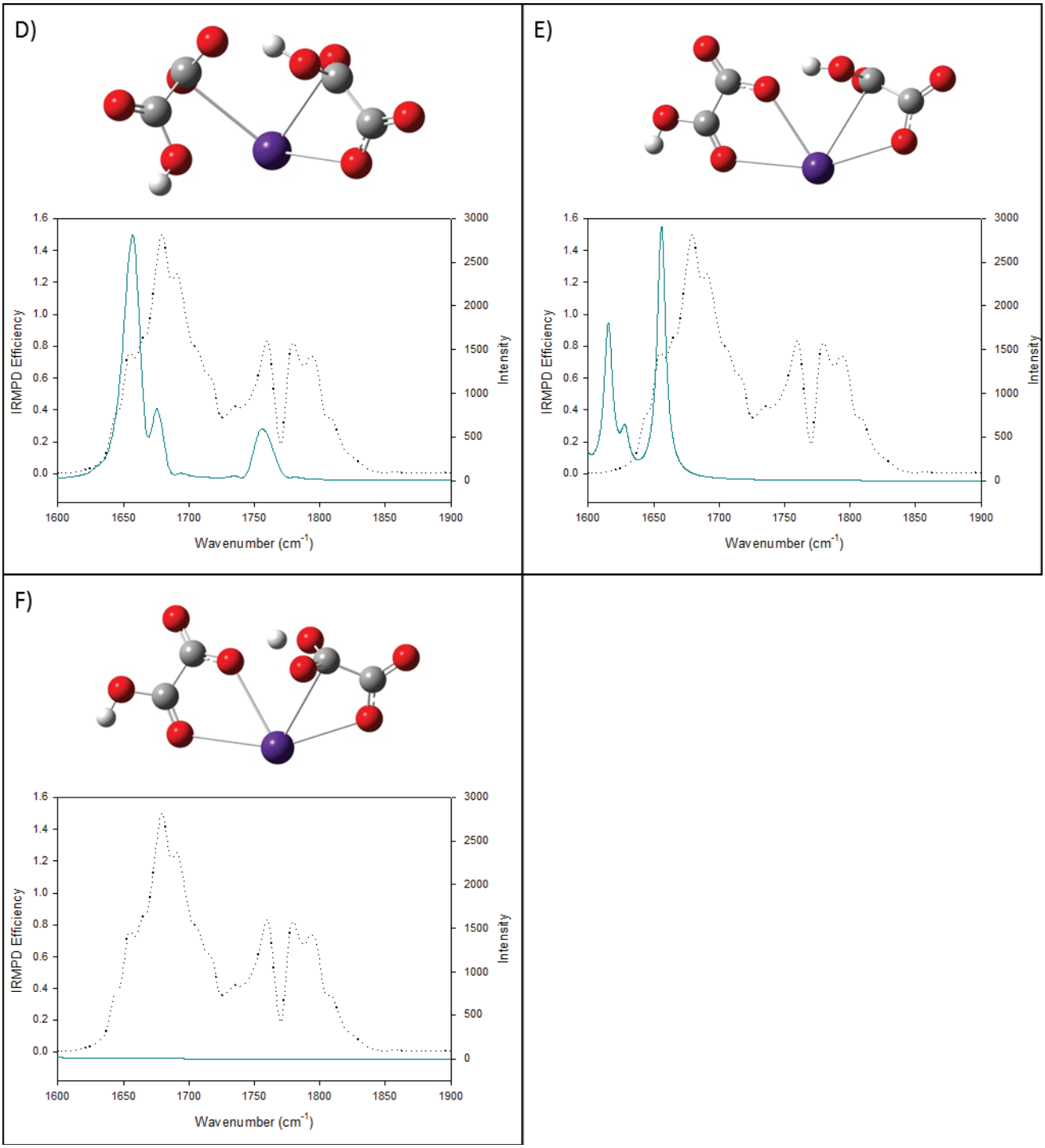


Figure 3-9: Theoretical Structures (with the lanl2dz basis set) and spectra for each unique $CsOx_2H_2^-$ structure. The IRMPD spectrum (dotted) overlaps each theoretical spectrum (green). Parts A-B are the "X" structures for Bhandhlyp (X-B3lyp, B3pw91, B98, Mpw1pw91, Pbe1pbe and MP2 are identical) and M062x respectively while Parts C-F are the "Y" structures for B3pw91 (Y-B3lyp identical), B98, Bhandhlyp, M062x (Y-Mpw1pw91 and Pbe1pbe are identical), and MP2 respectively.

3.2.2.2 1000 – 2100 cm^{-1} Range

Looking at the 1600-1900 cm^{-1} range for the "X" and Y" structure of Bhandhlyp already suggests the correct structure has not yet been found. When looking at the overall range the IRMPD spectrum was acquired, it is evident the structure existing in the gas phase has not been determined as there are peaks for both structures around the 1200 cm^{-1} range which are absent in experimental results (shown in Figure 3-10) due to vibration of protons. Therefore more structures need to be explored.

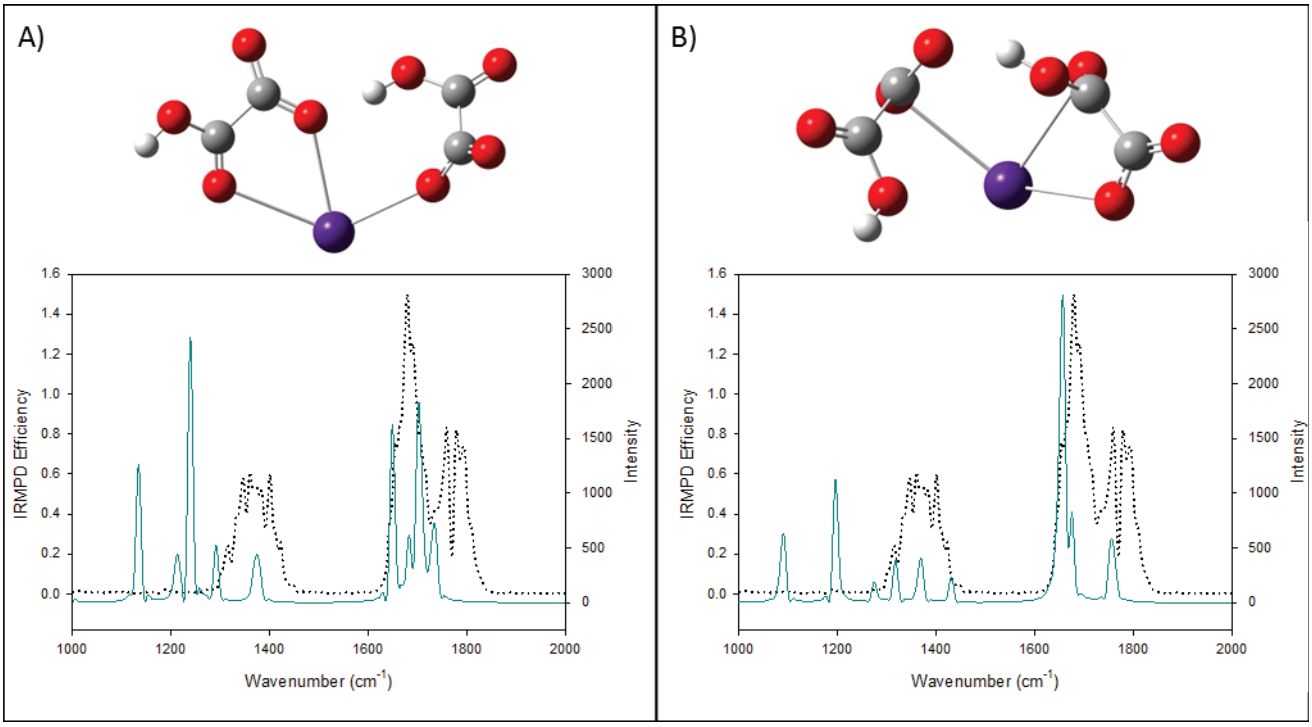


Figure 3-10: Theoretical spectra (basis set: lanl2dz) of the two best matching structures from the 1600-1900 cm^{-1} range where A) is the "X" structure and B) is the "Y" structure of the DFT method Bhandhlyp.

3.2.2.3 Second attempt of structure determination for the 1000-2100 cm^{-1} range

At the first attempt of finding a plausible structure that could exist in the gas phase, Bhandhlyp structures ended up matching the best with the experimental results therefore that level of theory was used for further structural exploration. At the second attempt of structure determination, there were six different starting structures (Figure 3-11) which alter the positions of the oxalates and the locations of the protons to remove theoretical peaks from the 1200 cm^{-1} range (vibrations due to protons) and to try and obtain peaks in the 1800 cm,$^{-1}$ range. The first three structures in Figure 3-11 did not have theoretical spectra agreeing with the IRMPD spectrum and were discarded as plausible structures. Figure 3-11D) was the optimized final structure for $KOx_2H_2^{-1}$ and was similar to the IRMPD spectrum which had a peak in the 1800 cm^{-1} range but missing a couple of peaks that were present in the IRMPD spectrum (appendix). However, by moving the positions of the protons as shown in Figure 3-11E) and F) a theoretical spectrum generated was very close to the experimental spectrum (part E) and its spectrum can be seen overlapping the IRMPD spectrum in Figure 3-12.

Relative energies in kJ/mol for the six optimized structures can be seen in Table 3-5. Structures A) – C) had the highest energies confirming they can be disregarded as plausible structures. The two lowest energy structures are D) and E) which matched best with the IRMPD spectrum. Structure E) is 30.7 kJ/mol higher than D) but a closer match to experimental results. However there is a theoretical peak around 1250 cm^{-1} where none exists in the IRMPD spectrum suggesting a plausible structure has not yet been found.

Table 3-5: Relative energies (kJ/mol) of optimized structures from Figure 3-11. Calculations were perfomed with a lanl2dz basis set at a Bhandhlyp level of theory.

Structure	Relative Energy (kJ/mol)
A)	87.28
B)	319.38
C)	78.12
D)	**0.00**
E)	30.70
F)	62.52

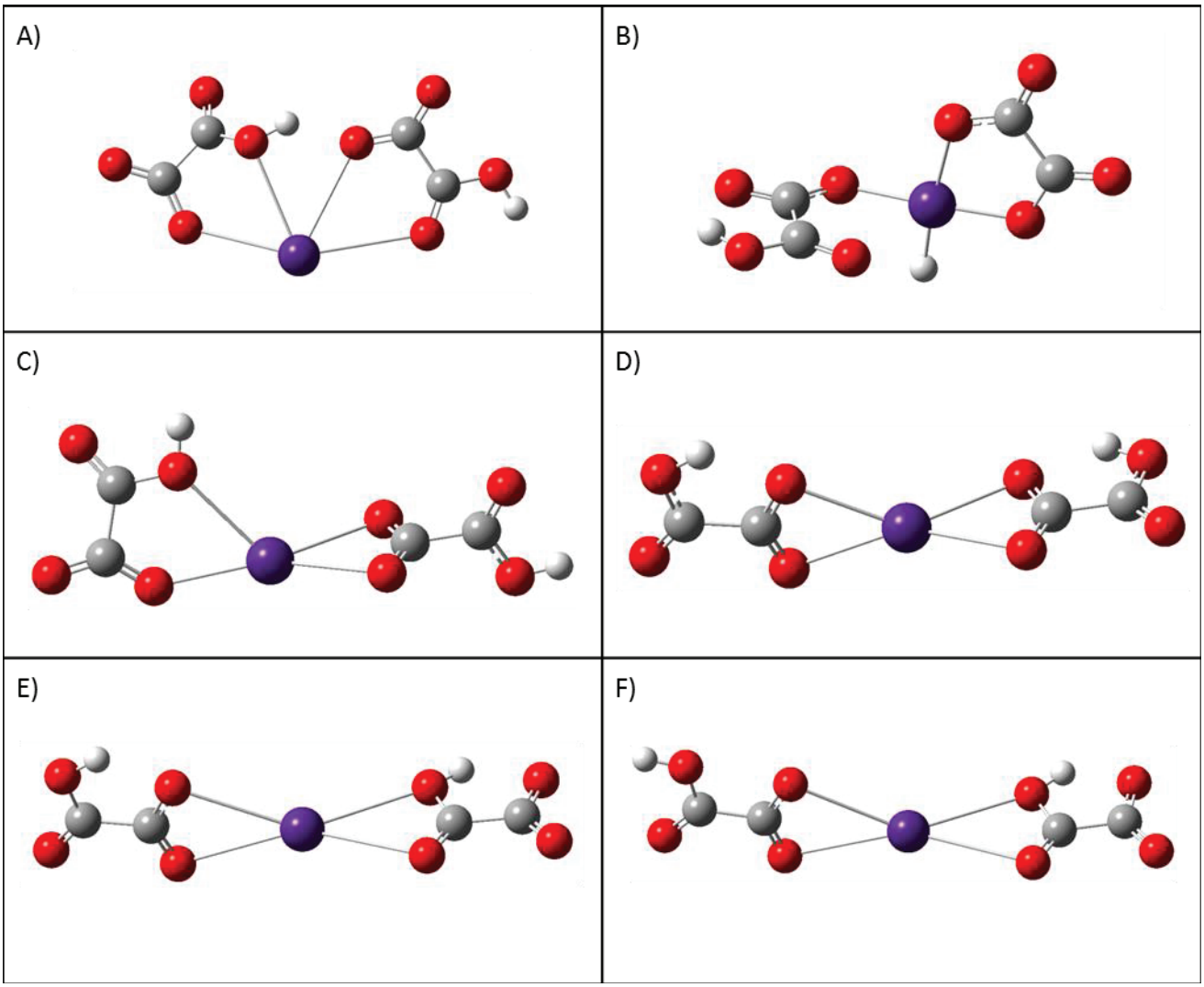


Figure 3-11: Modified starting structures with the Bhandhlyp level of theory

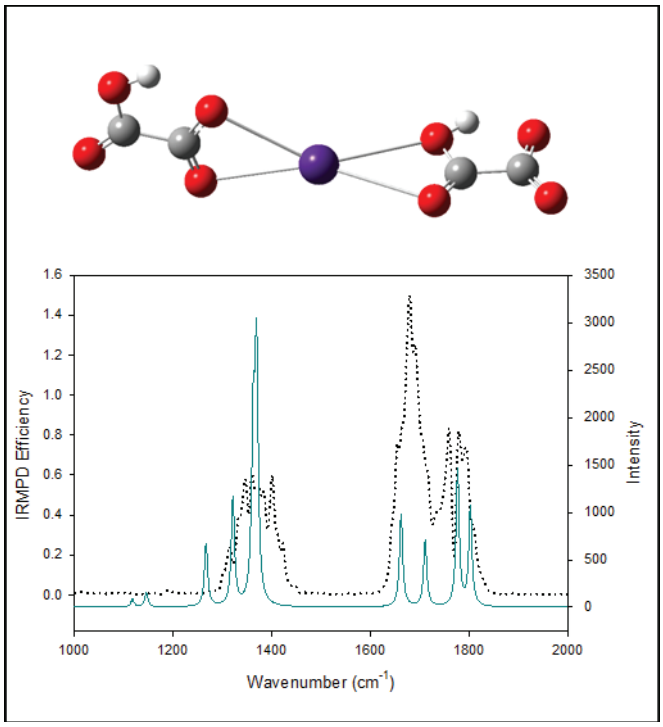


Figure 3-12: Theoretical spectrum (basis set: lanl2dz) of the best Bhandhlyp modified structure (green) compared to the IRMPD spectrum (dotted) for the range of 1000-2100 cm^{-1}

3.2.2.4 More attempts at structure determination for the 1000-2100cm^{-1} range

After a second attempt on structure determination, Figure 3-12 shows the currently best plausible structure. To try and eliminate the peak around 1250 cm^{-1}, the structure was modified and three new starting structures were generated (Figure 3-13). Structure A) optimized to the same structure, whereas structure B) optimized to degenerate oxalates minimizing the number of peaks making the calculated spectrum less like the IRMPD spectrum and structure C) had theoretical peaks where there was none present in the experimental spectrum. The relative energies of the structures can be seen in Table 3-6 and shows the structure A) to be the lowest energy but all are very close to one another. However, since

structures B) and C) did not match the IRMPD spectrum as nicely, they can be ruled out as plausible structures. Thus, further structural exploration is still needed.

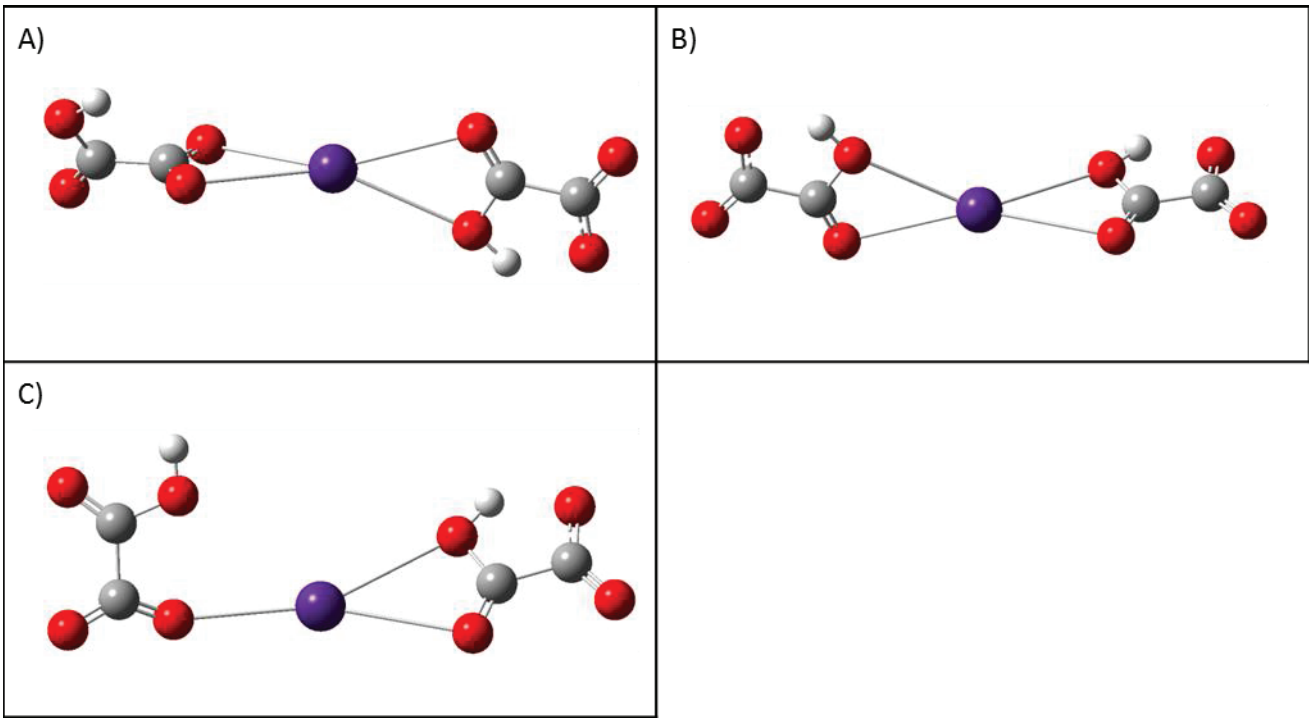


Figure 3-13: Modified starting structures from structure in Figure 3-12 calculated with a lanl2dz basis set at the Bhandhlyp level of theory.

Table 3-6: Relative energies (kJ/mol) of optimized structures from Figure 3-13. Calculations were performed with a lanl2dz basis set at a Bhandhlyp level of theory.

Structure	Relative Energy (kJ/mol)
A)	**0.00**
B)	33.82
C)	44.69

The next step in determining a plausible structure was modifying the optimized structure of Figure 3-13C) shown in Figure 3-14. The theoretical spectrum looks similar to the experimental results, but there are peaks around 1180cm^{-1} and 1270cm^{-1} resulting from vibrational modes from the proton to the left of the metal. To try and eliminate these peaks, two more starting structures were generated by moving the proton to different positions on the oxalate where Figure 3-16 A) has the proton located on the same oxygen, however rotated closer to the metal whereas B) has the proton moved to oxygen above. The first optimized structure gave the same structure as in Figure 3-12 and the second structure resulted in a new low energy structure shown in Figure 3-15. The relative energies of the two structures can be seen in Table 3-7 where the second optimized structure was slightly lower in energy by 7 kJ/mol. This structure looks very similar to the IRMPD spectrum, however only has one peak in the 1310-1425 cm^{-1} range whereas the IRMPD spectrum has many. Thus, more structures were explored.

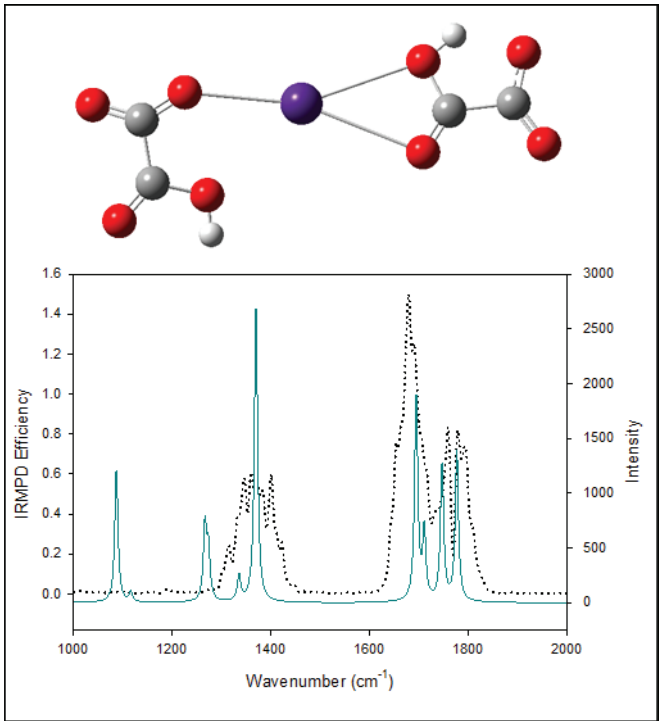


Figure 3-14: Theoretical spectrum (basis set: lanl2dz) of the optimized structure of Figure 3-13C) overlapping the IRMPD spectrum for the range of 1000-2100 cm^{-1}.

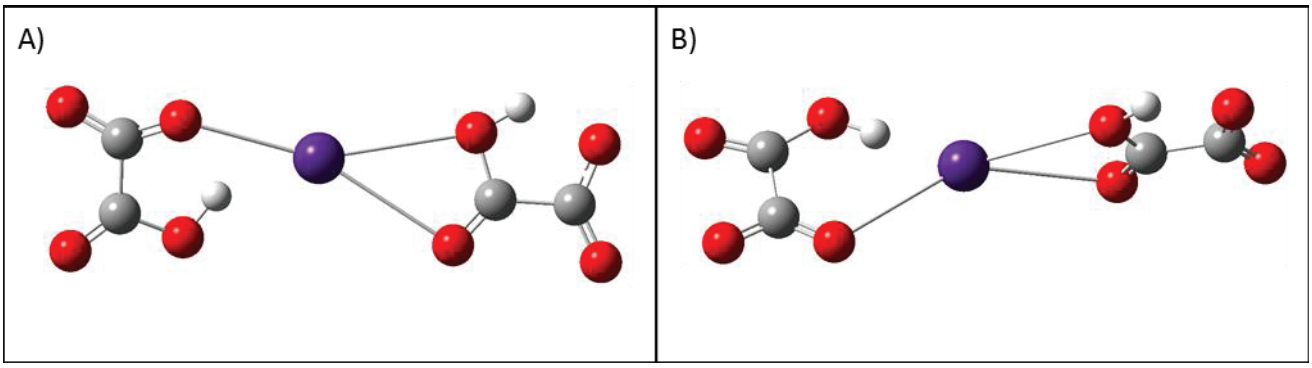


Figure 3-16: Modified starting structures from the structure in Figure 3-14 calculated with a lanl2dz basis set at the Bhandhlyp level of theory.

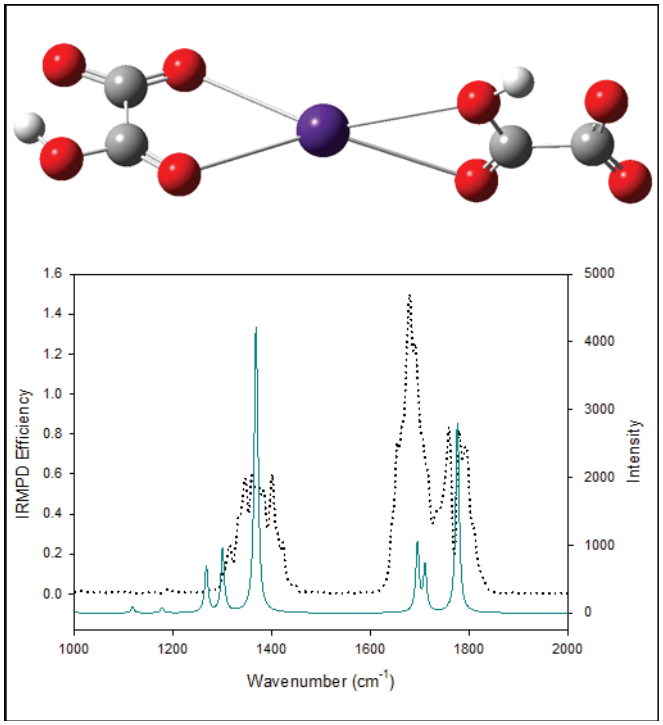


Figure 3-15: Theoretical spectrum (basis set: lanl2dz) of the optimized structure of Figure 3-16B) overlapping with the IRMPD spectrum for the range of 100-2100cm^{-1}.

Table 3-7: Relative energies (kJ/mol) of optimized structures from Figure 3-16. Calculations were performed with a lanl2dz basis set at a Bhandhlyp level of theory.

Structure	Relative Energy (kJ/mol)
A)	6.69
B)	**0.00**

A last attempt at structure determination was made for $CsOx_2H_2^{-1}$, where two more starting structures were generated based on the optimized structure seen in Figure 3-15. To try and obtain more vibrational modes in the 1310-1425 cm^{-1} range, the protons on the oxalates were rearranged. In Figure 3-18A) the oxalate to the left of the metal had the proton moved to a carbon closer to the metal whereas in B) the proton to the right of the metal moved to an oxygen atom away from the metal. In both cases, more theoretical peaks were generated in the desired range, giving theoretical spectra close to the experimental results where the only difference being the optimized structure of A) gave a peak just below the desired range, while the optimized structure of B) had all peaks overlapping the IRMPD spectrum. The optimized structure of Figure 3-18B) is shown in Figure 3-17 with the theoretical spectrum overlapping the IRMPD spectrum and it is the most plausible structure that could exist in the gas phase. To confirm this assumption, this structure had the lowest energy out of all the structures generated with the Bhandhlyp level of theory (Table 3-8).

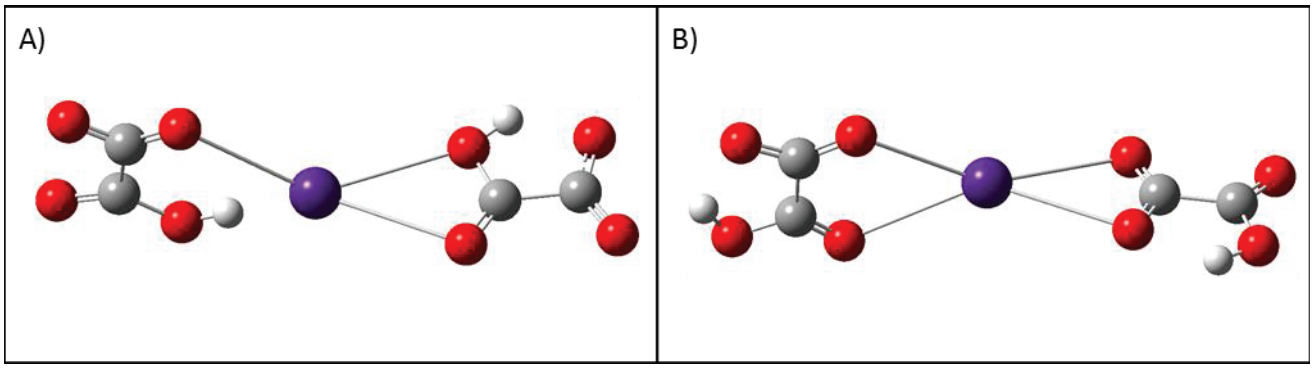


Figure 3-18: Modified starting structures from the optimized structure in Figure 3-15 calculated with a lanl2dz basis set at the Bhandhlyp level of theory.

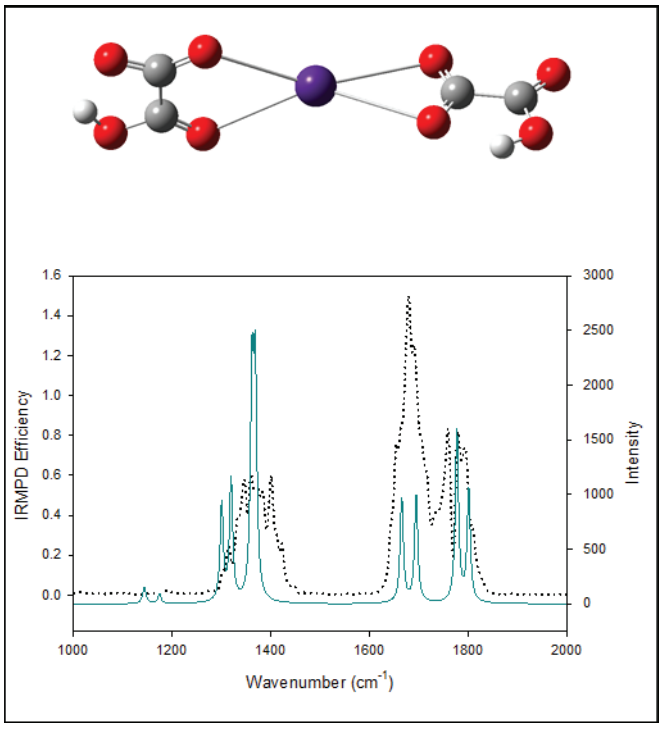


Figure 3-17: Theoretical spectrum (basis set: lanl2dz) of the best optimized Bhandhlyp level of theory structure overlapping the IRMPD spectrum (dotted) for the range of 1000-2100 cm-$^{-1}$.

Table 3-8: Relative energies (kJ/mol) of all optimized structures calculated at the Bhandhlyp level of theory with the lanl2dz basis set.

Structure	Relative Energy (kJ/mol)
"X"structure	110.23
"Y"structure	109.81
Figure 3-11A)	93.12
B)	325.22
C)	83.96
D)	5.84
E)	36.53
F)	68.36
Figure 3-13A)	36.53
B)	70.35
C)	81.22
Figure 3-16A)	36.53
B)	29.84
Figure 3-17A)	36.53
B)	**0.00**

3.2.2.5 $CsOx_2H_2^{-1}$ Conclusions

To summarize the process of determining a plausible low energy structure of $CsOx_2H_2^{-1}$ that could exist in the gas phase, two starting structures were generated per level of theory. After optimization and frequency calculations, the level of theory that gave a closest match was Bhandhlyp (Figure 3-10). However, further structures needed to be explored as there was a theoretical peak missing in the 1800 cm^{-1} range and theoretical peaks appearing around and below 1200cm^{-1} where none was present in the IRMPD spectrum. After many attempts at determining a plausible structure, the structure that matched best with the IRMPD spectrum and had the lowest energy, was the structure shown in Figure 3-17 and its frequencies are assigned in Table 3-9.

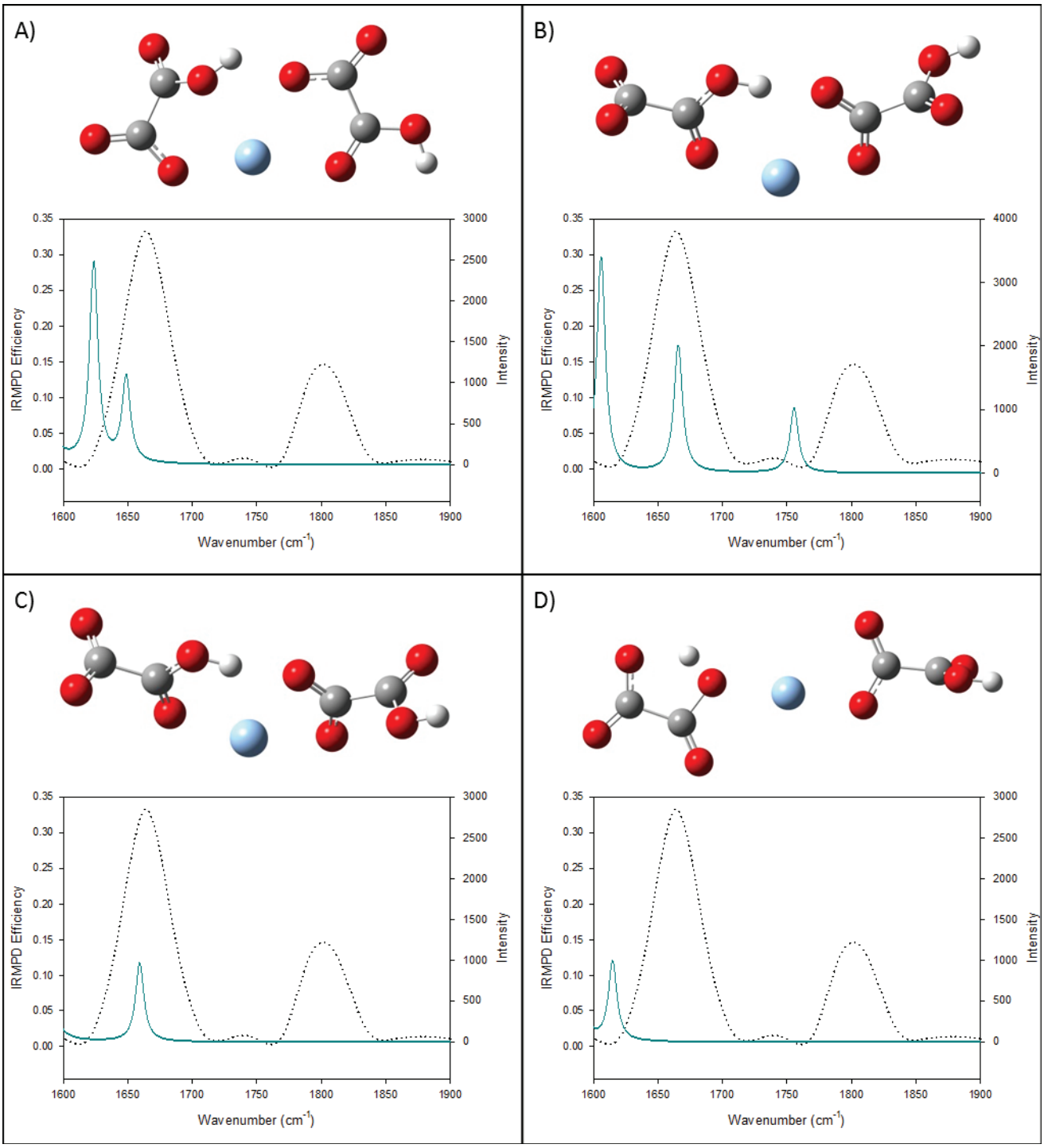
Table 3-9: Vibrational assignments to corresponding frequencies.

Theoretical Frequencies (cm^{-1})	Experimental Frequencies (cm^{-1})	Assignment
1150	--	• H-bonded CO Stretch • H-bonded COH Bend
1175	--	• H-bonded CO Stretch • H-bonded COH Bend
1300	1315	• Bound symmetrical CO_2 Stretch • H-bonded COH bend
1320	1315	• Bound symmetrical CO_2 Stretch •H-bonded COH Bend
1365	1365	• Bound CO Stretch • H-bonded CO Stretch • H-bonded COH Bend
1660	1680	• Bound asymmetrical CO_2 Stretch • H-bonded asymmetrical CO_2 Stretch • H-bonded COH Bend
1700	1680	• Bound asymmetrical CO_2 Stretch • H-bonded asymmetrical CO_2 Stretch • H-bonded COH Bend
1775	1480	• Bound CO Stretch • H-bonded COH Bend
1800	1790	• CO Stretch • H-bonded COH Bend

3.2.3 $AgOx_2H_2^{-1}$

3.2.3.1 1600-1900 cm^{-1} Range

When optimization and frequency calculations were performed on $AgOx_2H_2^{-1}$, seven unique structures were generated. Each structure with its theoretical spectrum overlapped with the IRMPD spectrum can be seen in Figure 3-19.


A)
B)
C)
D)
IRMPD Efficiency
Intensity
Wavenumber (cm-1)
0.35
0.30
0.25
0.20
0.15
0.10
0.05
0.00
3000
2500
2000
1500
1000
500
0
4000
1600
1650
1700
1750
1800
1850
1900

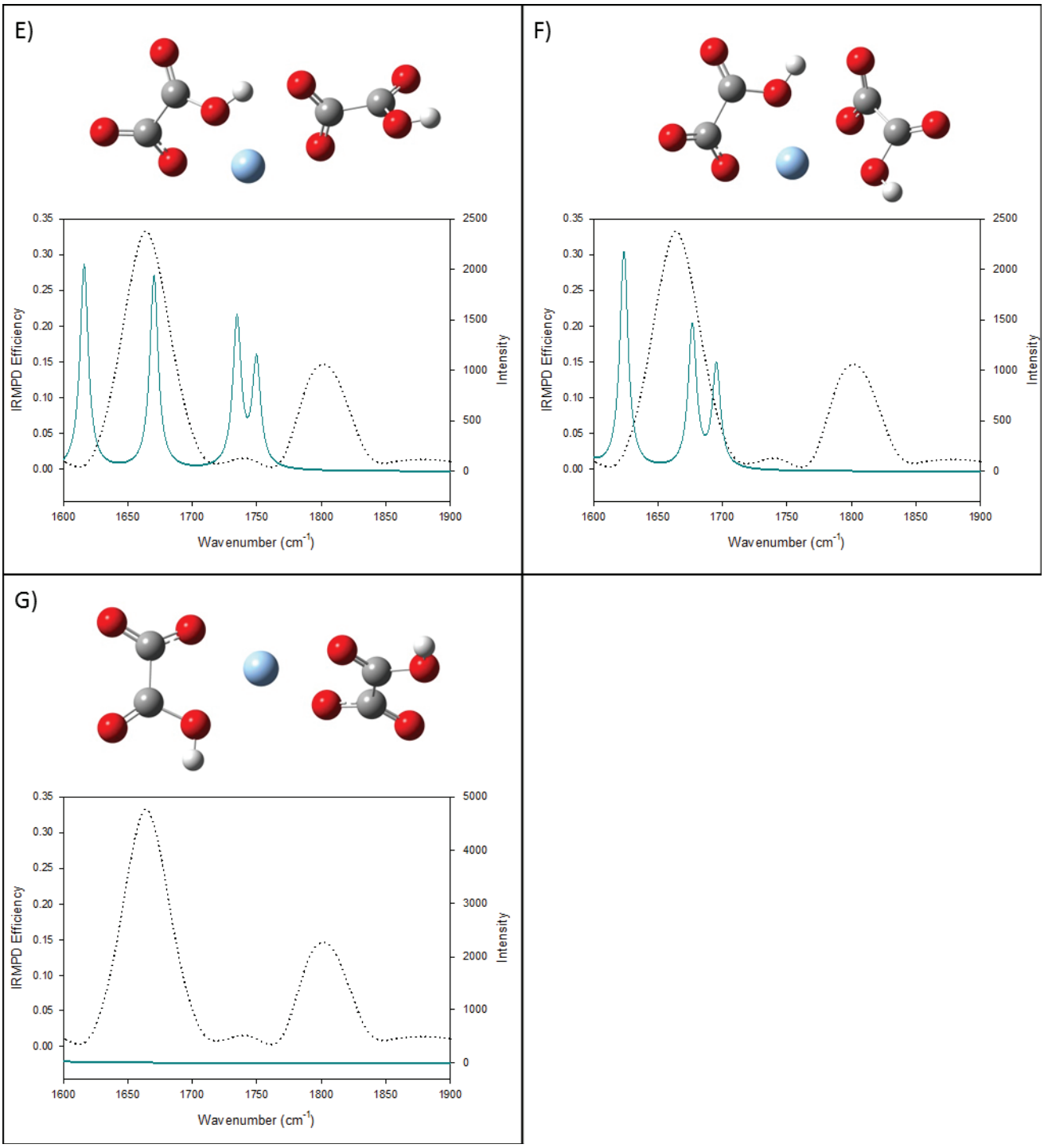


Figure 3-19: Theoretical Structures (basis set: lanl2dz) and Spectra for each unique $AgOx_2H_2^-$ structure. The IRMPD spectrum (dotted) overlaps each theoretical spectra (green). Parts A-D are the "X" structures for B98 ("Y" structures B3lyp, B98, Mpw1pw91 are identical), Bhandhlyp ("X" structure of M062x is identical), Mpw1pw91 ("X" structures of B3lyp, B3pw91 and

Pbe1pbe are identical), and MP2 respectively while Parts E-G are the "Y" structures for Bhandhlyp ("Y" structures of B3pw91 and Pbe1pbe are identical), M062x and MP2 respectively.

Like the previous two metal-oxalate species, a lot of structures have theoretical spectra too different compared to the IRMPD spectrum. When making the comparison, structures in Figure 3-19 parts A, C, D,F,G and H can be eliminated as potential plausible structures, leaving parts B and E as the closest matches in which both had theoretical peaks appearing in the 1650 cm^{-1} range where an IRMPD peak is present. All structures had no peaks around 1800 cm^{-1} where an IRMPD peak is present, however parts B and E were chosen as the best matching since there were theoretical peaks appearing close to the IRMPD peak at 1750 cm^{-1}, giving the Bhandhlyp level of theory the most promise to find a plausible structure.

3.2.3.2 1000-2100 cm^{-1} Range

The two theoretical structures matching the closest to the IRMPD spectrum were Figure 3-19 parts B and E for the range of 1600-1900 cm^{-1}. Even though these two are considered the closest matching, it is evident a plausible candidate has not been found due to absent peaks around 1800 cm^{-1}. When looking at the full spectrum range, for both structures as shown in Figure 3-20, it is obvious more structural exploration is needed. In both cases, there are peaks around and below 1200 cm^{-1} resulting from proton vibrational modes. Therefore other structures must be explored.

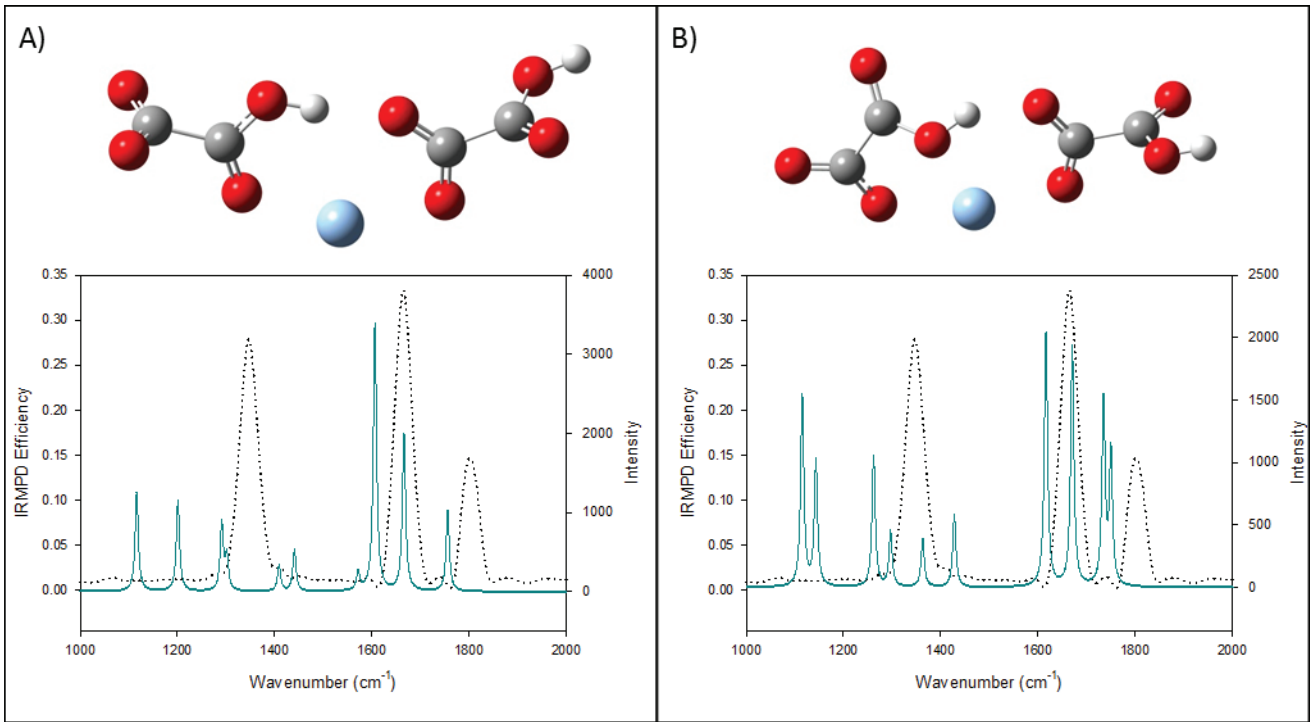


Figure 3-20: Theoretical spectra (basis set: lanl2dz) of the two best matching structures from the 1600-1900 cm^{-1} range (green) compared to the IRMPD spectrum (dotted) for the range of 1000-2100 cm^{-1}. Part A) is the "X" structure and part B) is the "Y" structure for the Bhandhlyp level of theory.

3.2.3.3 More attempts at structure determination for the 1000-2100 cm^{-1} range

At the first attempt at finding a plausible structure in the gas phase, the structures matching most closely to experimental results were the "X" and "Y" structures of Bhandhlyp and therefore this level of theory was used for exploring other structures. The vibrational modes corresponding to theoretical peaks around and below 1200 cm^{-1} were due to the protons and therefore new starting structures were created by moving the position of the protons to try and eliminate these peaks and to generate a peak in the 1800 cm^{-1} range.

There were eight new starting structures which had optimization and frequency calculations performed in attempt to find a structure whose theoretical spectrum matches the IRMPD spectrum. The starting structures can be seen in Figure 3-21 where part A) is similar to the optimized structure of "Y" Bhandhlyp however the positions of the protons have been changed, B) is the plausible structure for

$KOx_2H_2^{-1}$ but potassium switched for silver, C) and D) had a proton moved from the optimized structure of B), and E-H) had protons moved to different positions based on the optimized structure in part D). All optimized structures can be seen in the appendix.

After optimization and frequencies were performed on the starting structures, it is possible to compare their energies since they were calculated using the same level of theory. In theory, the lowest energy structure should be the one existing in the gas phase. The relative energies of all structures calculated using the Bhandhlyp level of theory are shown in Table 3-10 with D) being lowest in energy. Figure 3-22A) shows the lowest energy optimized structure along with its theoretical spectrum overlapping the IRMPD spectrum. The two spectra match closely to one another, however there a couple of discrepancies – the first being a peak around 1300 cm^{-1}, just below an IRMPD peak, and secondly, the peak around 1700 cm^{-1} being just above the IRMPD peak. Figure 3-21E) optimized to a structure extremely similar to the optimized structure of D) whose theoretical frequencies matched well with the IRMPD spectrum and Figure 3-22B) shows the optimized structure of E). Like the previous structure, there are two theoretical peaks in the 1300-1400 cm^{-1} range, however in this case, they both overlap the IRMPD peak and the peak around 1700 cm^{-1} matches nicely with the IRMPD peak. Therefore, even though this structure is higher in energy by 7 kJ/mol, it is the most probable structure existing in the gas phase.

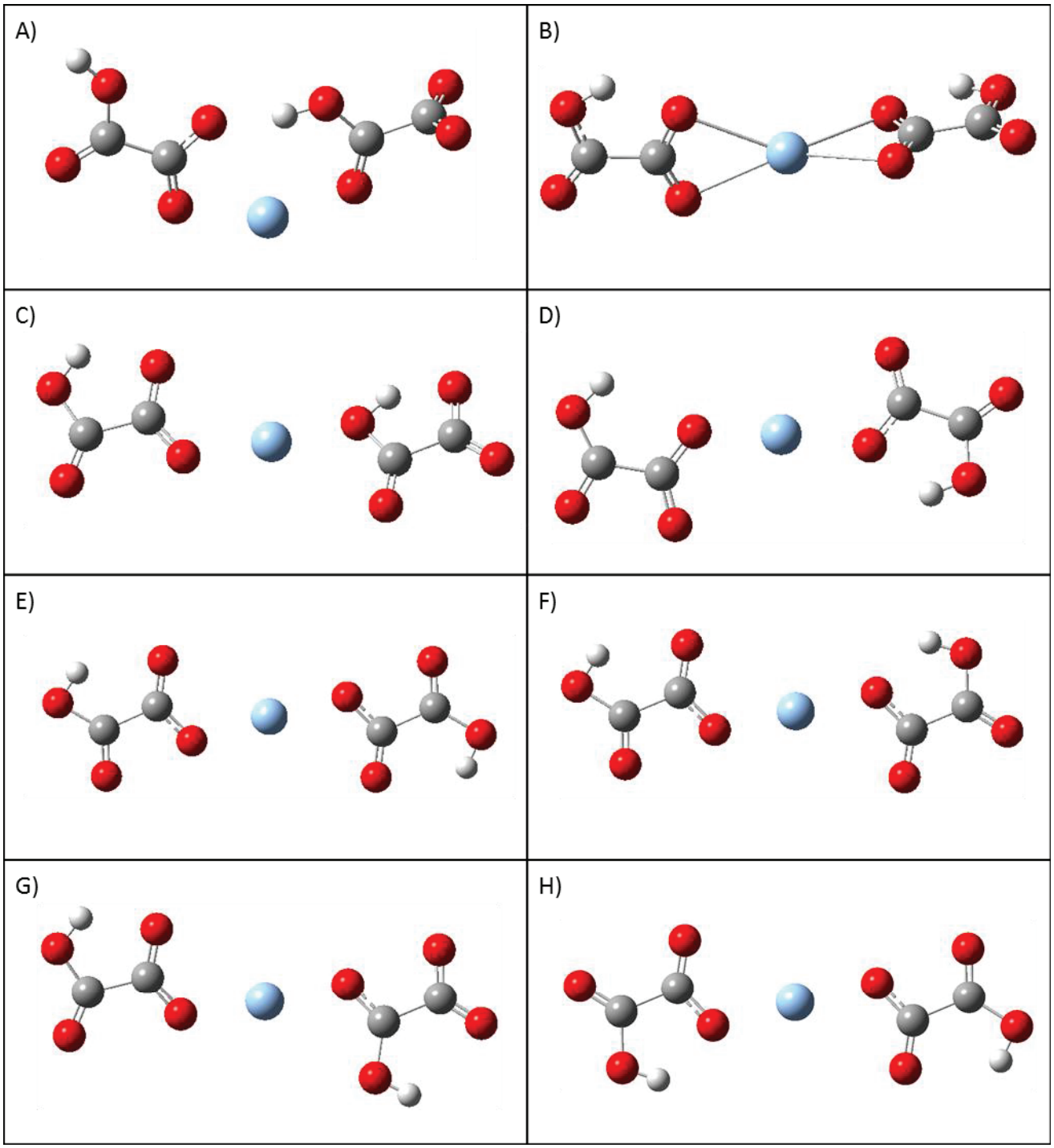


Figure 3-21: Modified starting structures using the Bhandhlyp level of theory.

Table 3-10: Relative energies (kJ/mol) of optimized structures the "X" and "Y" structures of the Bhandhlyp level of theory and optimized structures from Figure 3-21.

Structure	Relative Energy (kJ/mol)
"X"structure	123.81
"Y"structure	49.47
A)	123.82
B)	4.24
C)	123.82
D)	**0.00**
E)	7.48
F)	4.24
G)	52.39
H)	4.24

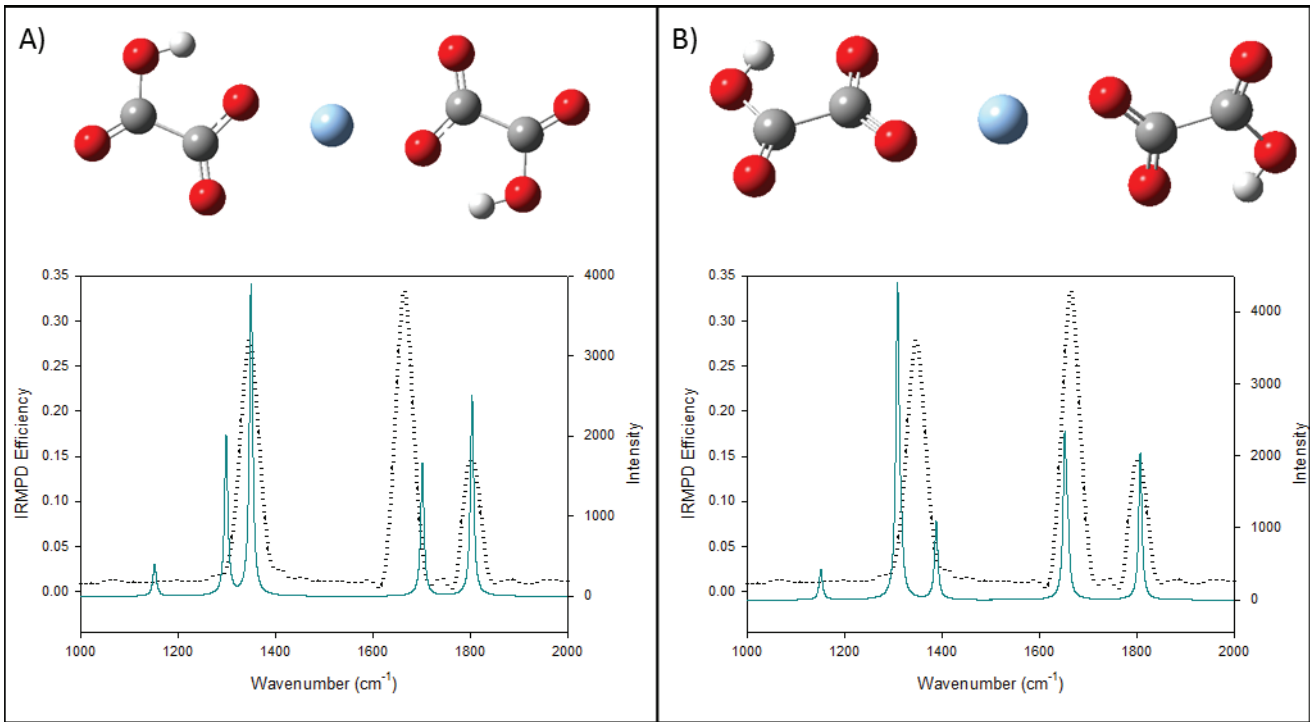


Figure 3-22: A) The optimized structure from Figure 3-21D). B) The optimized structure from Figure 3-21E).

3.2.3.4 $AgOx_2H_2^{-1}$ Conclusions

To summarize the process of determining a plausible structure for $AgOx_2H_2^{-1}$, two starting structures were created for each level of theory using the lanl2dz basis set. After optimization and frequency calculations were performed, the closest match ended up being the "X" and "Y" structures of the Bhandhlyp level of theory. Their theoretical spectra did not have a peak in the 1800 cm^{-1} range where an IRMPD peak was present, and there were peaks around and below 1200 cm^{-1} (caused by vibrational modes of protons) where there was none present in the IRMPD spectrum. Therefore further structural exploration was needed. After eight more structures were optimized, the structure with the best matching spectrum was the starting structure from Figure 3-21E with its optimized structure shown in Figure 3-22B) and its frequencies assigned in Table 3-11. In this case, it was not the lowest energy structure, but was higher by 5 kJ/mol and like in the case of $KOx_2H_2^{-1}$, proves computational chemistry is not always enough to determine structure alone so it is important to compare to computational results to experimental results.

Table 3-11: Vibrational assignments to corresponding frequencies. Note: Each vibration was doubly degenerate.

Theoretical Frequencies (cm^{-1})	Experimental Frequencies (cm^{-1})	Assignment
1150	--	• H-bonded CO Stretch •H-bonded COH Bend
1310	1350	• H-bonded COH Bend
1390	1350	• Symmetrical CO_2 stretch • H-bonded CO stretch •H-bonded COH bend
1650	1665	• Asymmetrical CO_2 stretch • CO Stretch •H-bonded COH bend
1800	1800	• CO Stretch • H-bonded COH bend

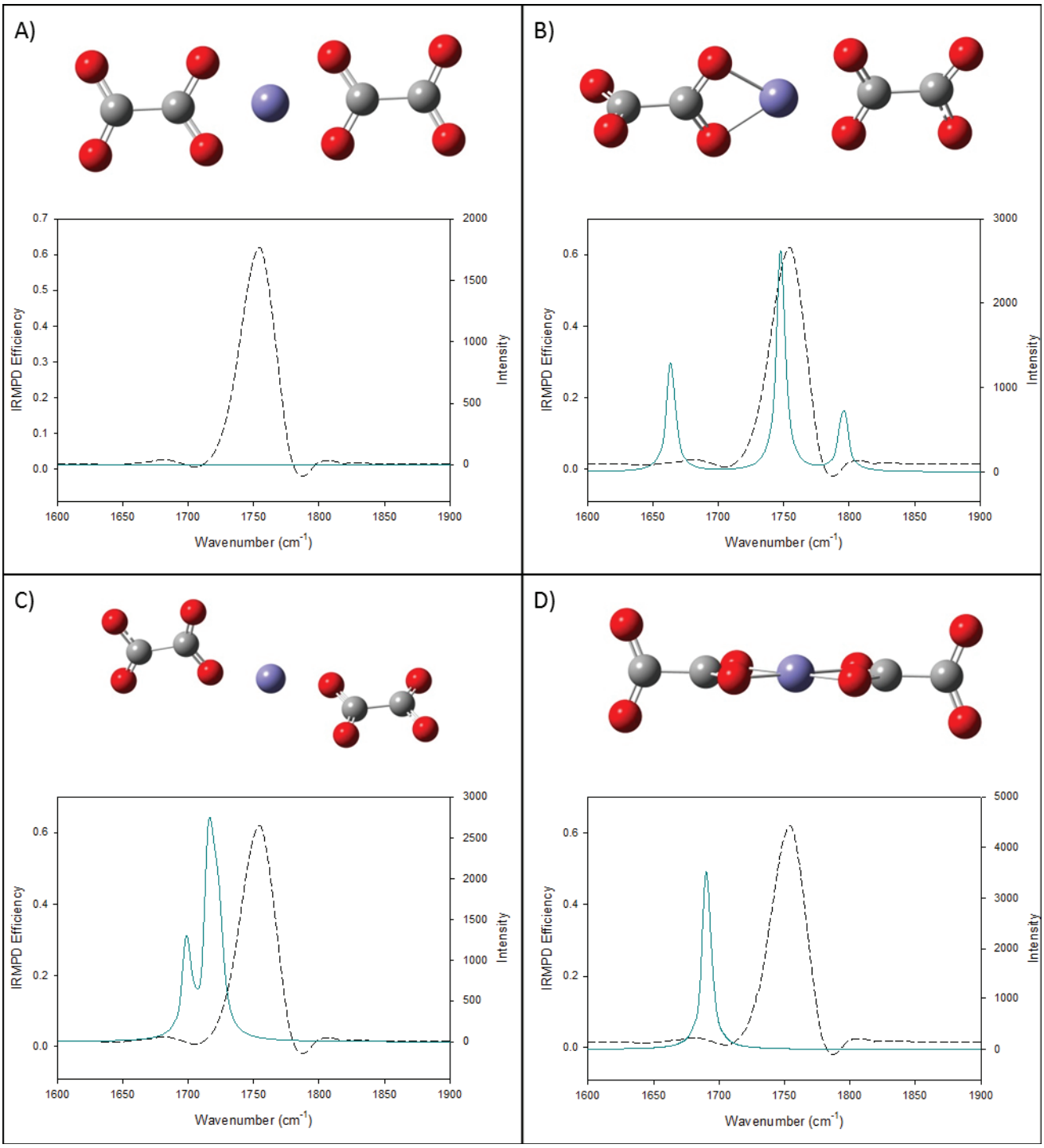
3.3 Metal – Ox_2^{-1} complexes

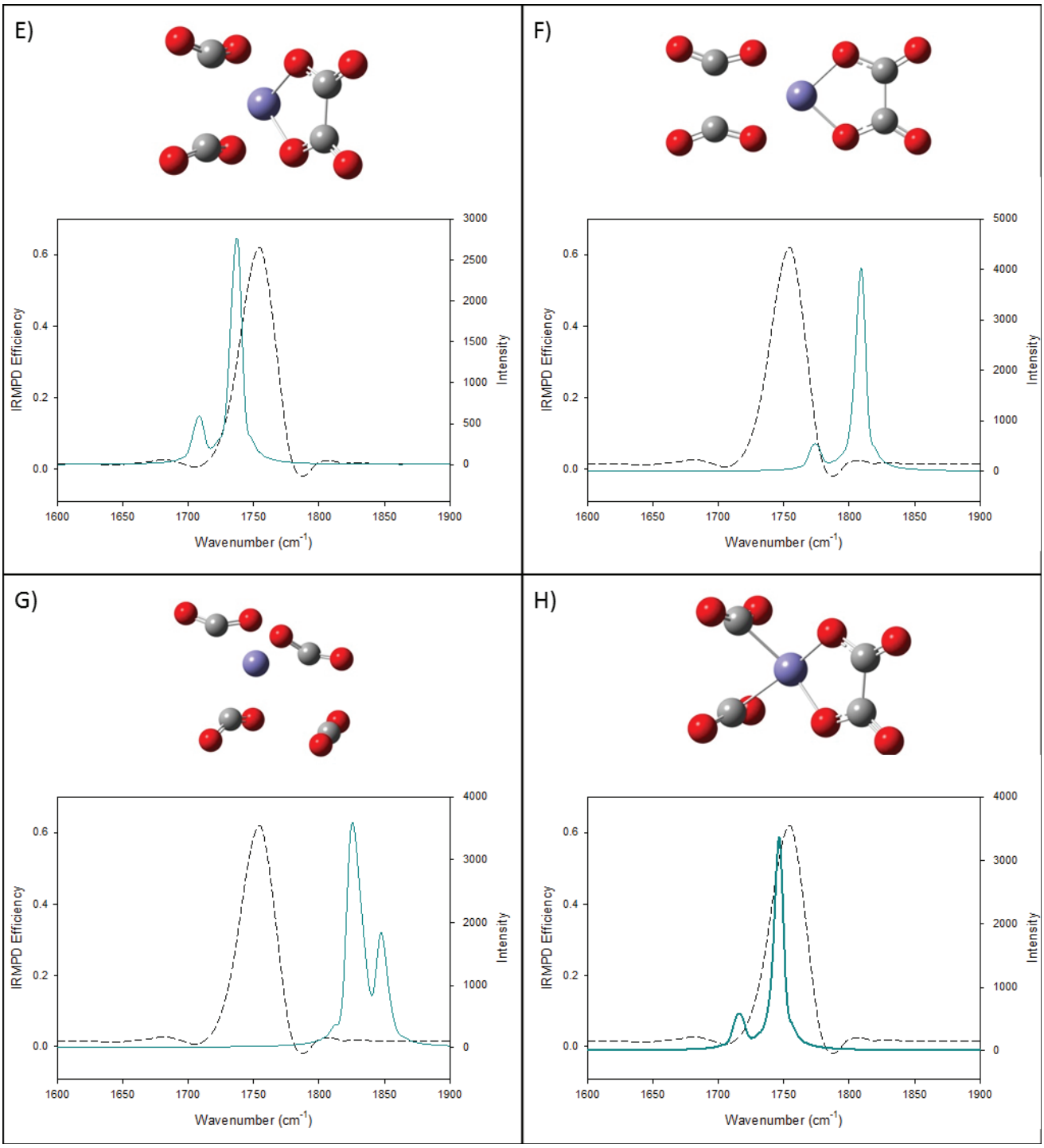
As mentioned previously, for optimization and frequency calculations there were two starting structures ("X" and "Y") generated per level of theory to start exploring different structural conformations. After optimization was performed, different levels of theory resulted in different low energy structures. This section will go through the process of determining a plausible structure for $FeOx_2^{-1}$ and once a plausible structure has been determined, frequencies will be assigned.

3.3.1 $FeOx_2^{-1}$

3.3.1.1 1600-1900 cm^{-1} Range

When optimization frequency calculations were performed on $FeOX_2^{-1}$, nine unique structures were generated. Each structure with its theoretical spectrum overlapped with the IRMPD spectrum can be seen in Figure 3-23. Structures whose theoretical peaks do not align with the IRMPD spectrum can be immediately eliminated as a plausible structure. Those too different from experimental results are Figure 3-23 parts A, C, D, E, F, G, and I since they do not have a peak overlapping with the IRMPD peak at 1750cm^{-1}. Thus, this leaves parts B ("X" structure of Bhandhlyp) and H ("Y" structure of Mpw1pw91), the two structures as possible candidates which have peaks at 1750 cm^{-1} overlapping with the IRMPD spectrum.


A)
B)
C)
D)
IRMPD Efficiency
Intensity
Wavenumber (cm-1)
1600
1650
1700
1750
1800
1850
1900


E)
F)
G)
H)
IRMPD Efficiency
Intensity
Wavenumber (cm-1)
1600
1650
1700
1750
1800
1850
1900
0.0
0.2
0.4
0.6
0
500
1000
1500
2000
2500
3000
4000
5000

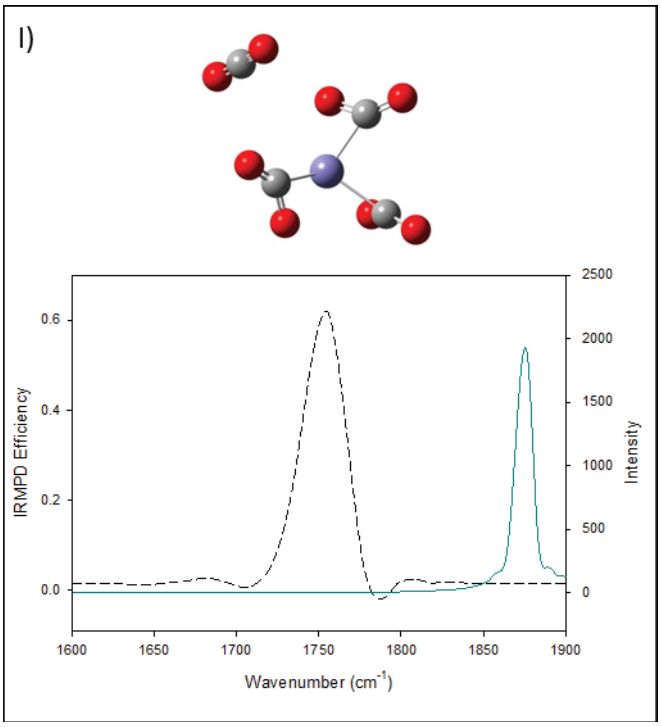


Figure 3-23: Theoretical Structures (basis set: 6-311+gd) and spectra for each unique $FeOx_2^{-1}$ structure. The IRMPD spectrum (dotted) overlaps each theoretical spectra (green). Parts A-D are the "X" structures for B98 ("X" structures of B3lyp, B3pw91, Mpw1pw91 and Pbe1pbe are identical), Bhandhlyp, M062x and MP2 respectively while E-I are the "Y" structures for B3pw91 ("Y" structures of B3lyp and B98 are identical), Bhandhlyp ("Y" structure of MP2 is identical), M062x, Mpw1pw91 and Pbe1pbe respectively.

3.3.1.2 1000-2000 cm^{-1} Range

The theoretical structures best matching the IRMPD spectrum for the range of 1600-1900cm^{-1} were Figure 3-23 parts B and H. However the IRMPD spectrum was observed from approximately 1000-2000 cm^{-1} range and the structures spectra can be seen in this range in Figure 3-24. In both theoretical spectra there are peaks that do not appear in the IRMPD spectrum due to vibrational modes of CO_2 groups. Therefore more structures must be explored.

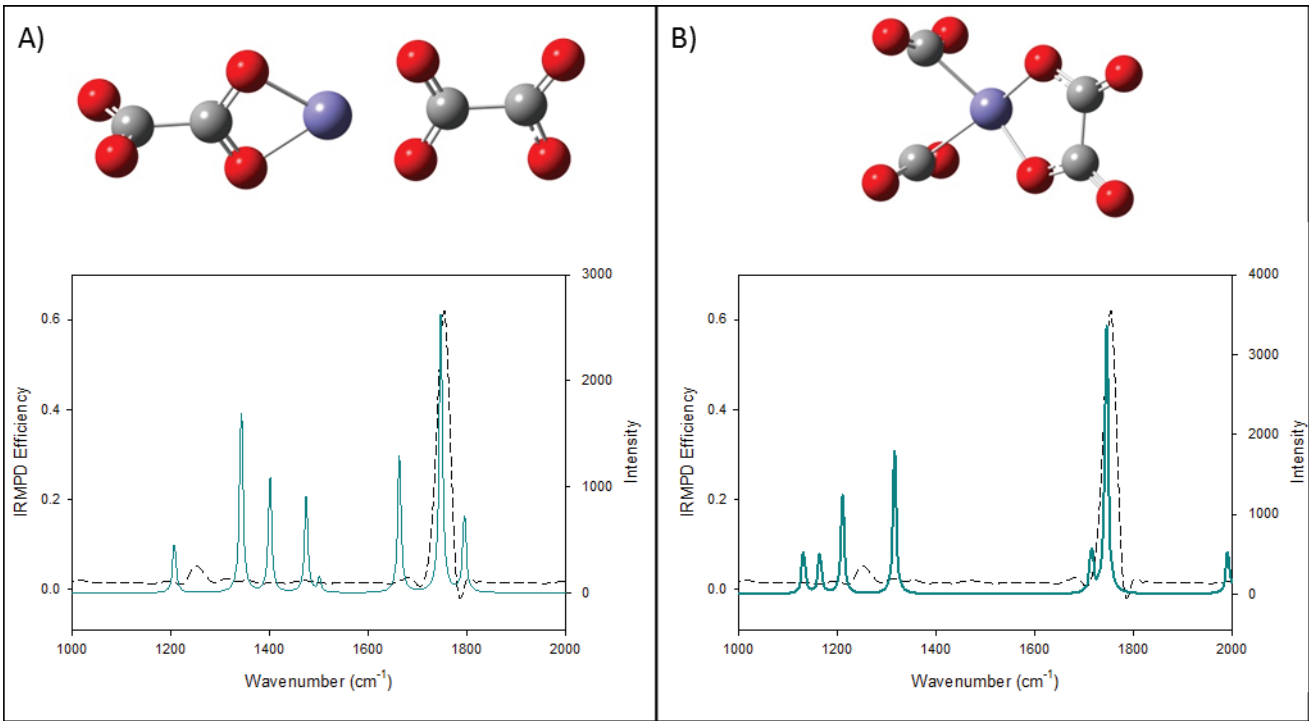


Figure 3-24: Theoretical spectra (basis set: 6-311+gd) of the two best matching structures from the 1600-1900 cm^{-1} range (green) compared to the IRMPD spectrum (dotted) for the range of 1000-2100 cm^{-1}. Parts A and B are the "X" structure of Bhandhlyp and "Y" structure of Mpw1pw91 respectively.

3.3.1.3 More attempts at structure determination for the 1000-2100 cm^{-1} range

In attempts at determining a plausible structure existing in the gas phase, both levels of theory, Bhandhlyp and Mpw1pw91 were used for further structural exploration. To try and eliminate the extra peaks, the oxalates had their CO_2 groups rotated. The first DFT method chosen was Bhandhlyp where nine different starting structures (Figure 3-25) had optimization and frequency calculations performed.

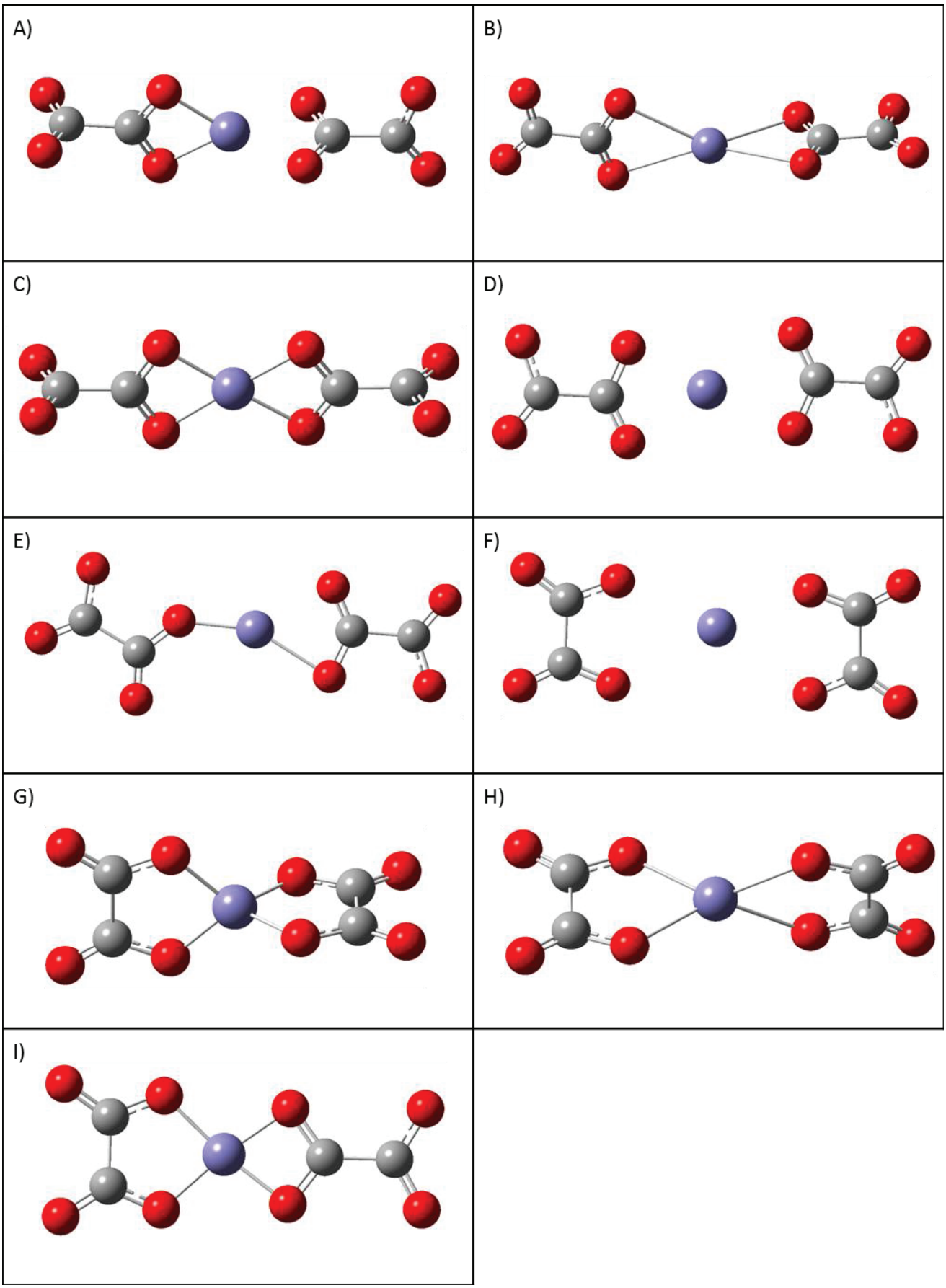


Figure 3-25: Modified starting structures starting from the "X" structure of Bhandhlyp.

None of the optimized structures aligned with the IRMPD, however the optimized structure resulting from Figure 3-25F) gave a spectrum similar to the experimental shown in Figure 3-26 with peaks shifted to higher wave numbers. Table 3-12 shows the energies of optimized structures and the structure of interest had a relative energy of 7 kJ/mol higher than the lowest energy structure. With Figure 3-25F) having a theoretical spectrum being similar to the IRMPD and being a lower energy structure, it has the potential to be a plausible structure, however Bhandhlyp is the wrong level of theory as the theoretical spectrum cannot align properly with the IRMPD spectrum.

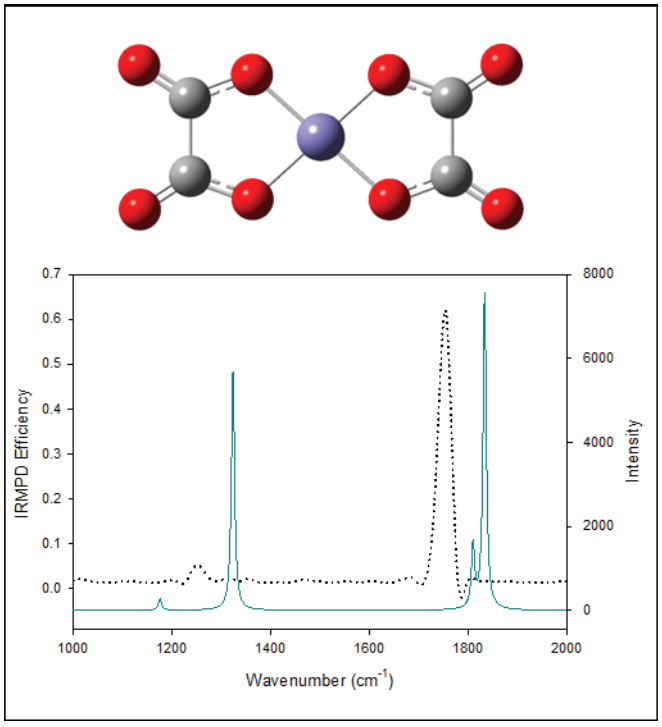


Figure 3-26: Theoretical spectrum (basis set: 6-311+gd) of the best Bhandhlyp modified structure (green) compared to the IRMPD spectrum (dotted) for the range 1000-2100cm^{-1}.

Table 3-12: Relative energies (kJ/mol) of optimized structures from Figure 3-25. Calculations were performed with a 6-311+gd basis set at a Bhandhlyp level of theory.

Structure	Relative Energy (kJ/mol)
"X"structure	218.33
A	218.33
B	312.41
C	218.33
D	312.41
E	312.41
F	6.68
G	204.80
H	**0.00**
I	151.10

In the next attempt at structure determination, the structure in Figure 3-26 was used as a starting structure with the Mpw1pw91 level of theory, the second DFT method for structural exploration. The optimized structure with its theoretical spectrum overlapping the IRMPD spectrum can be seen in Figure 3-27. The theoretical spectrum matches quite well with the experimental results making the structure a plausible structure in the gas phase. It is also important to mention the IRMPD spectrum of $FeOx_2^{-1}$ resembles the IRMPD spectrum of $FeOx^-$, and the plausible structure for $FeOx_2^{-1}$ has the oxalates in the same orientation as $FeOx^{-1}$. The plausible structure's frequencies are assigned in Table 3-1.

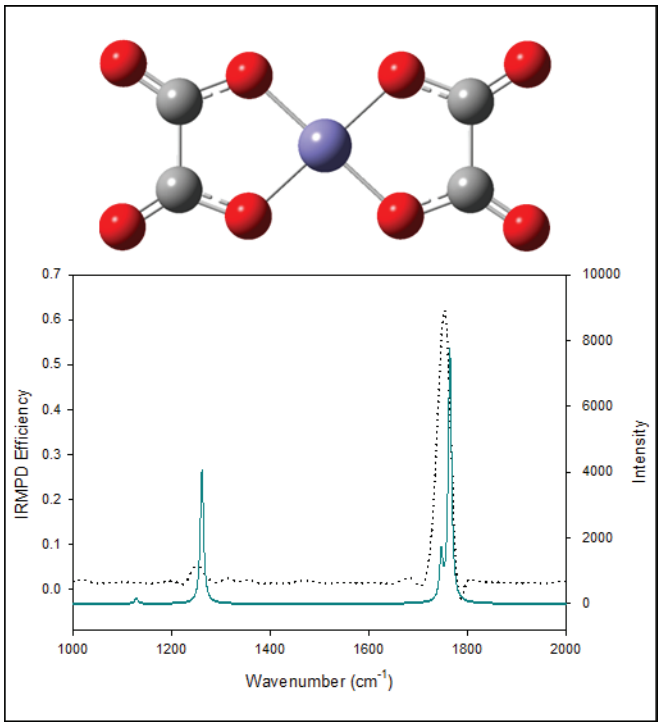


Figure 3-27: Theoretical spectrum (basis set: 6-311+gd) of the Mpw1pw91 modified structure (green) overlapping the IRMPD spectrum (dotted) for the range of 1000-2100 cm^{-1}.

Table 3-13: Vibrational assignments to corresponding frequencies. Note: Each vibration had four generate modes (two on each oxalate).

Theoretical Frequencies (cm^{-1})	Experimental Frequencies (cm^{-1})	Assignment
1265	1255	• Bound CO Stretch
1745	1755	• CO Stretch
1765	1755	• CO Stretch

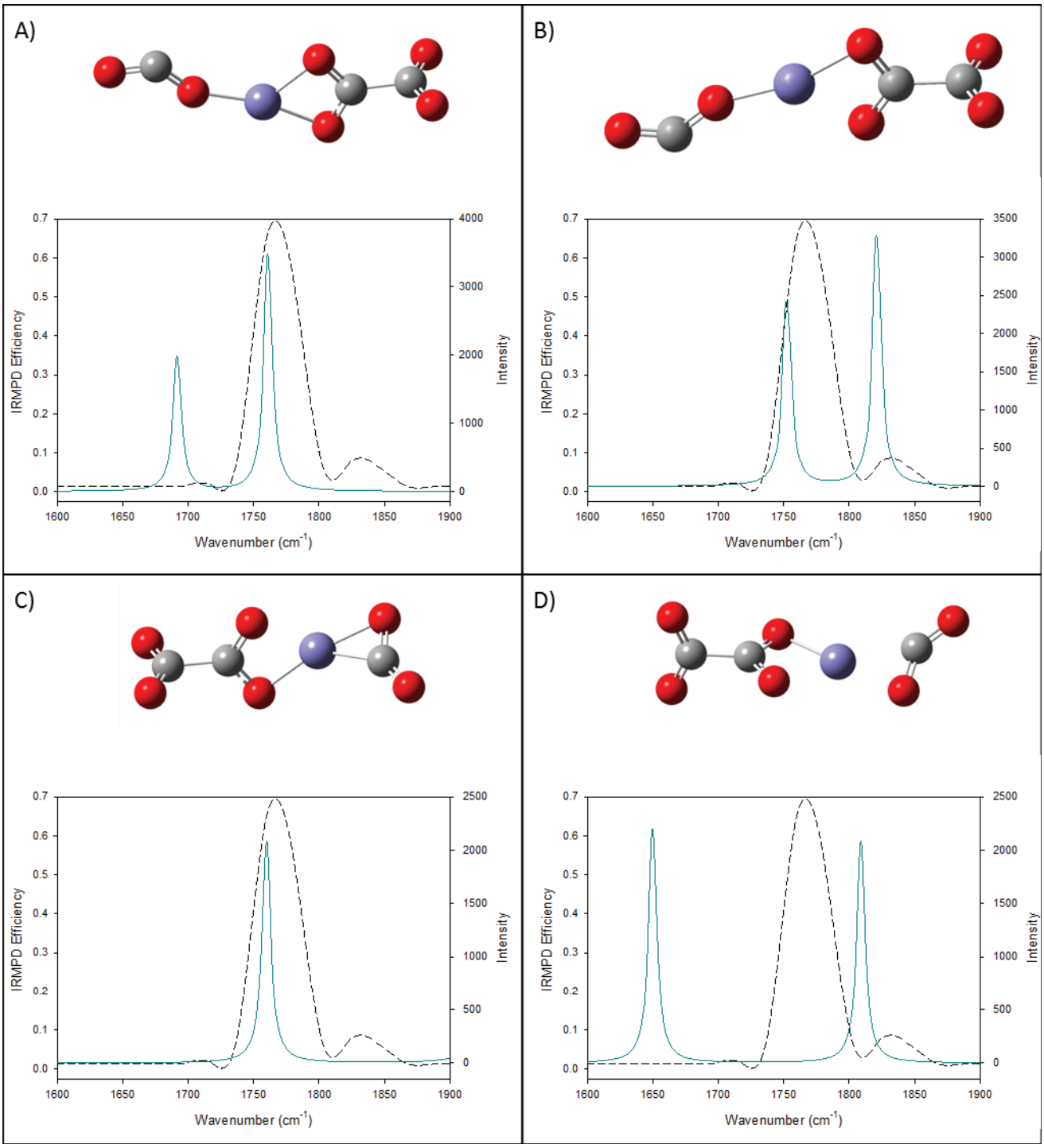
3.4 Metal – $OxCO_2^-$ complexes

Each level of theory had two starting structures ("X" and Y") which had optimization and frequency calculations performed to generate different structural conformations. This section will go through the process of determining a plausible structure existing in the gas phase for $FeOXCO_2^-$.

3.4.1 $FeOxCO_2^{-1}$

3.4.1.1 1600-1900 cm^{-1} Range

When optimization and frequency calculations were performed on $FeOxCO_2^-$, six unique structures were generated. Each structure with its theoretical spectrum overlapped with the IRMPD spectrum can be seen in Figure 3-28. Structures with theoretical spectra too different than the IRMPD spectrum are eliminated from becoming plausible structures (Figure 3-28 parts A, C, D and F). Structures in parts B ("X" structure of Bhandlhyp) and E ("Y" structure of M062x) have theoretical spectra with two peaks close to the IRMPD peaks in the range between 1700-1850 cm^{-1} making them decent matches for a first attempt.


A)
B)
C)
D)
IRMPD Efficiency
Intensity
Wavenumber (cm-1)

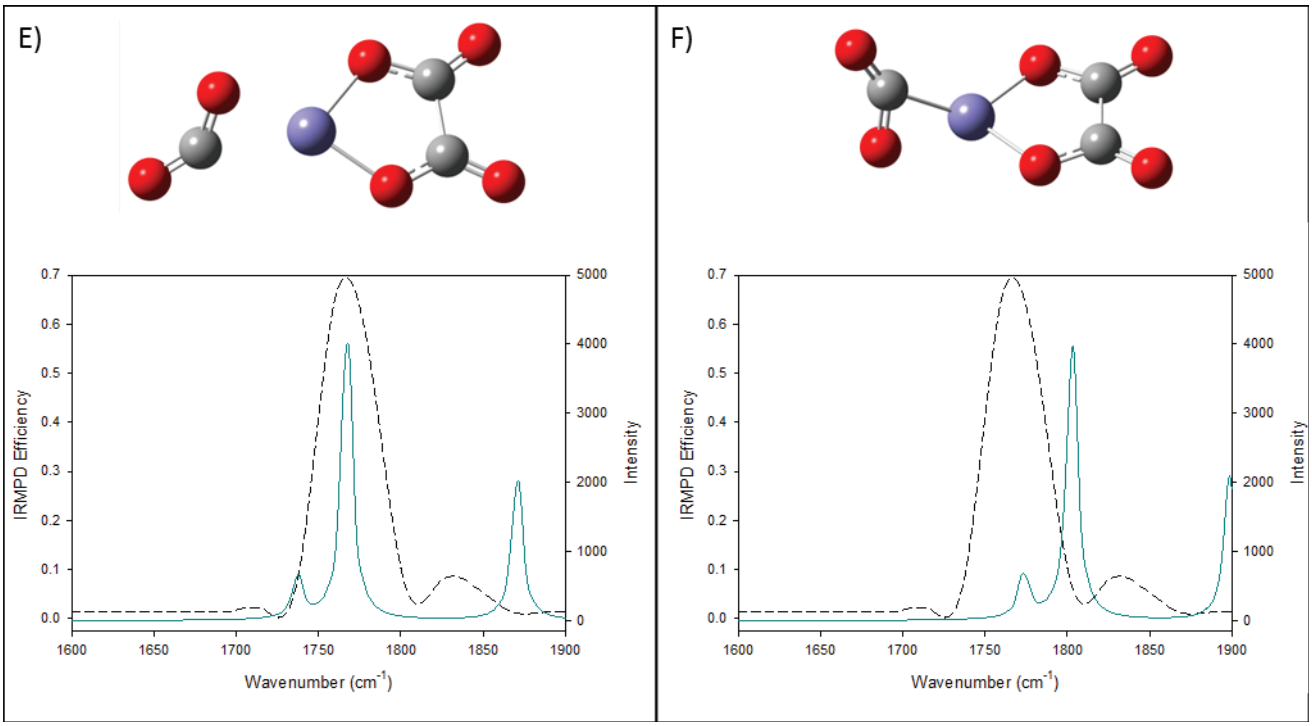


Figure 3-28: Theoretical Structures (basis set: 6-311+gd) and Spectra for each unique $FeOxCO_2^-$ structure. The IRMPD spectrum (dotted) overlaps each theoretical spectra (green). Parts A-D are the "X" structures of B3pw91, Bhandhlyp ("X" structure of M062x is identical), Pbe1pbe ("X" structures of B3lyp, B98 and Mpw1pw91 are identical), and MP2 respectively while parts E-F are the "Y" structures of M062x ("Y" structures of Bhandhlyp and MP2 are identical) and Pbe1pbe ("Y" structures of B3lyp, B3pw91, B98 and Mpw1pw91 are identical) respectively.

3.4.1.2 1000-2000 cm^{-1} Range

The theoretical structures that had spectra closest to the IRMPD spectrum for the range of 1600-1900 cm^{-1} were the "X" structure of Bhandhlyp and the "Y" structure of M062x. Both spectra can be seen overlapping the IRMPD spectrum for the full acquisition range in Figure 3-29. Part A shows the "X" structure of Bhandhlyp which has too many theoretical peaks and Part B shows the "Y" structure of M062x which has a theoretical spectrum matching nicely to the IRMPD spectrum. The optimized "Y" structure of M062x has all major theoretical peaks overlapping the IRMPD peaks making it a plausible structure. However, a couple more structures will be explored.

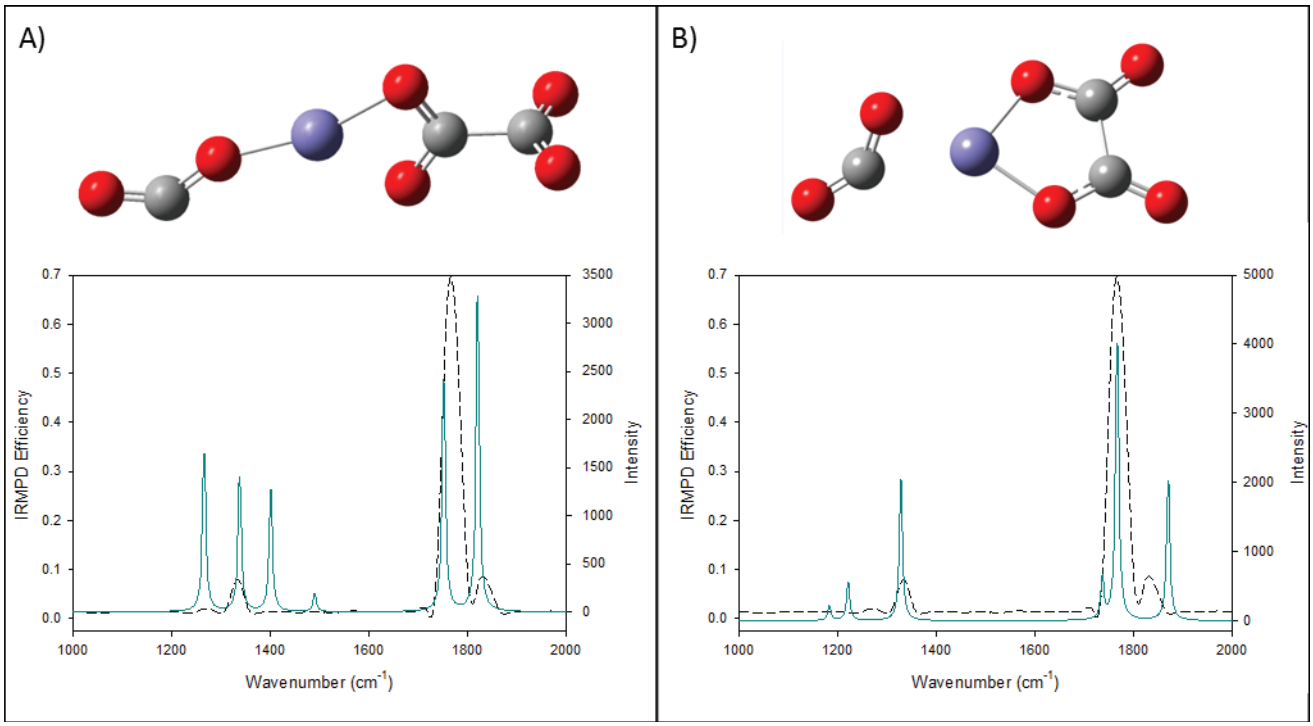


Figure 3-29: Theoretical spectra (basis set: 6-311+gd) for the two best matching structures from the 1600-1900 cm^{-1} range (green) compared to the IRMPD spectrum (dotted) for the range of 1000-2100 cm^{-1}. Part A is the "X" structure of Bhandhlyp and B is the "Y" structure for M062x.

3.4.1.3 More attempts at structure determination for the 1000-2100 cm^{-1} range

At the first attempt at finding a structure that could exist in the gas phase for $FeOXCO_2^-$, the optimized "Y" structure of M062x is deemed to be a plausible structure. However, there will be further exploration with the Mpw1pw91 level of theory. The other iron oxalate complexes had plausible structures found using the Mpw1pw91 level of theory and had spectra looking very similar to experimental spectra. Both their structures had oxalate(s) in the same plane with degenerate vibrational modes and therefore a starting structure for $FeOxCO_2^{-1}$ with similar orientation had optimization and frequency calculations performed. Figure 3-30A) shows a structure with the oxalates in a similar position to the other iron oxalate clusters. The optimized structure resulting from this starting structure was the same as Figure 3-29B), however at this level of theory; the frequencies did not match up to the IRMPD as well as the M062x level of theory. Figure 3-31A) shows the theoretical spectrum overlapping the IRMPD spectrum

for the plausible structure with the Mpw1pw91 level of theory. There is a peak in the theoretical spectrum around 1150 cm^{-1} which is absent in the IRMPD spectrum, and peaks around 1300 and 1750 cm^{-1} are slightly to the left of the IRMPD peaks. Whereas the M062x theoretical spectrum in Figure 3-29B) had those peaks overlapping the IRMPD spectrum but had the theoretical peak around 1850 cm^{-1} shifted to the right of the IRMPD peak. Therefore the M062x level of theory gave a better theoretical spectrum for this optimized structure.

Another starting structure had optimization and frequency calculations performed to see if another plausible structure existed. Figure 3-30B) shows the starting structure with the lone CO_2 group rotated 90°. The resulting structure gave a theoretical spectrum (Figure 3-31B) too different to the IRMPD spectrum making it not plausible.

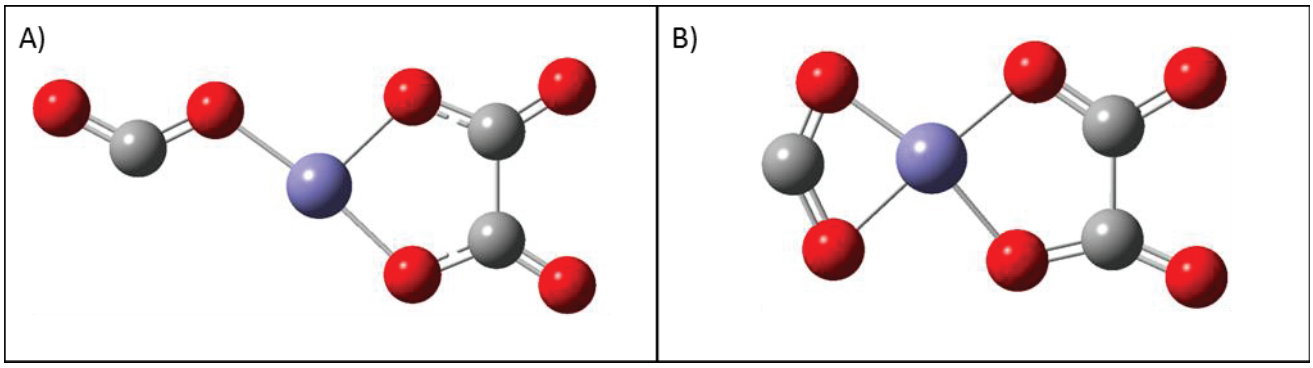


Figure 3-30: Modified starting structures using the Mpw1pw91 level of theory.

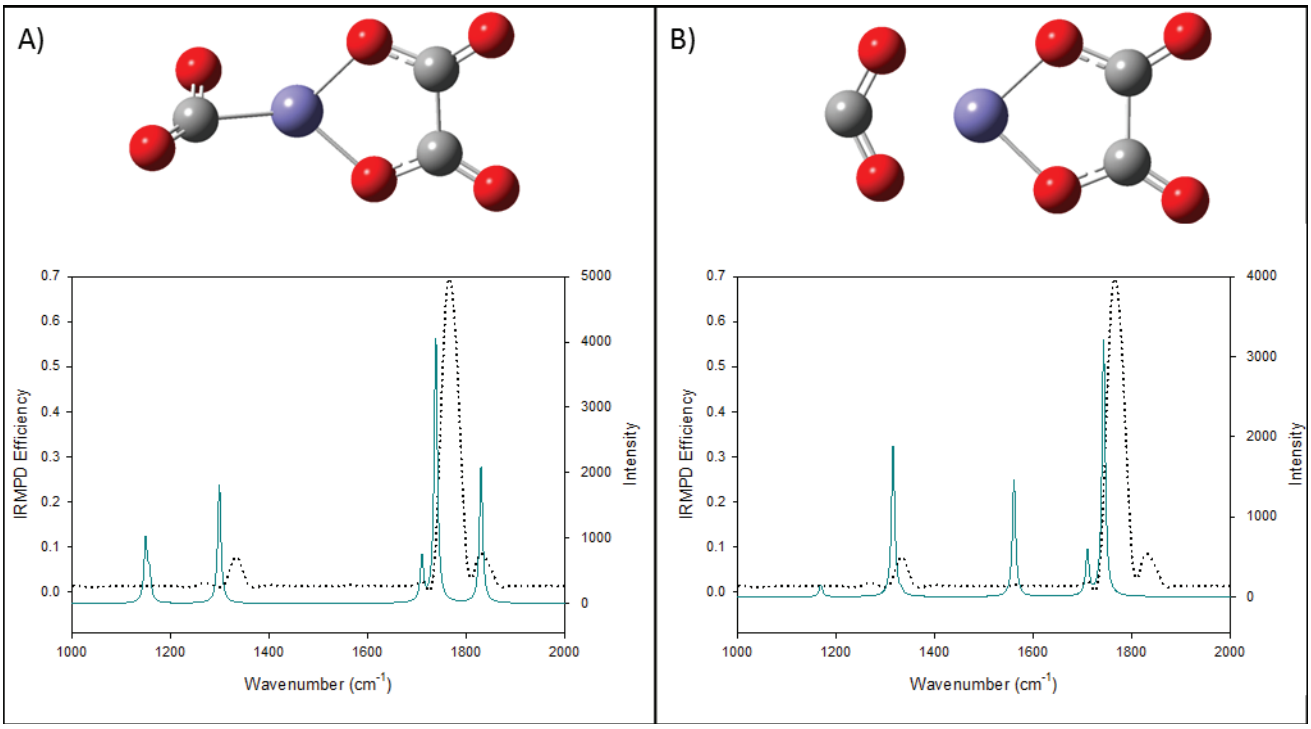


Figure 3-31: Theoretical spectra (basis set: 6-311+gd) of the modified structures (green) from Figure 3-30A and B compared to the IRMPD spectrum (dotted) for the range of 1000-2100 cm^{-1}.

3.4.1.4 $FeOxCO_2^-$ Conclusions

To summarize the process for structure determination of $FeOxCO_2^-$, two starting structures were generated per level of theory. After optimization and frequency calculations were performed with various levels of theory with the 6-311+gd basis set, a plausible structure was generated from the "Y" structure of the M062x level of theory. To ensure there were no other plausible structures, a couple of other starting structures were created with the Mpw1pw91 level of theory (which found plausible structures for other iron oxalate clusters). This level of theory generated the same plausible structure as the M062x level of theory; however the frequencies were not as good of a match as the M062x level of theory. Therefore, the plausible structure with the best level of theory is shown in Figure 3-29B with its frequencies assigned in Table 3-14.

Table 3-14: Vibrational assignments to corresponding frequencies. Note: vibrations denoted with a * are doubly degenerate.

Theoretical Frequencies (cm^{-1})	Experimental Frequencies (cm^{-1})	Assignment
1185	--	• Bound CO Stretch*
1220	--	• CO Stretch on lone CO_2 group
1325	1330	• Bound CO Stretch*
1740	1765	• Bound asymmetrical CO_2 Stretch *
1765	1765	• Bound asymmetrical CO_2 Stretch
1865	1835	• Asymmetrical CO_2 Stretch on lone CO_2 group

3.5 Metal $–Ox^-$ complexes

Like previous metal oxalate clusters, there were "X" and "Y" starting structures which had optimization and frequency calculations performed and compared to IRMPD spectra. This section will go through the process of determining plausible structures for KOx^-, $CsOx^-$, $AgOx^-$ and $FeOx^-$.

3.5.1 KOx^-

3.5.1.1 1550-1850 cm^{-1} Range

When optimization and frequency calculations were performed on KOx^-, two unique structures were generated. Both structures with their theoretical spectrum overlapped with the IRMPD spectrum can be seen in Figure 3-1. In both spectra there are theoretical peaks overlapping the IRMPD peak and thus neither structure can be eliminated as a plausible structure when looking at this range.

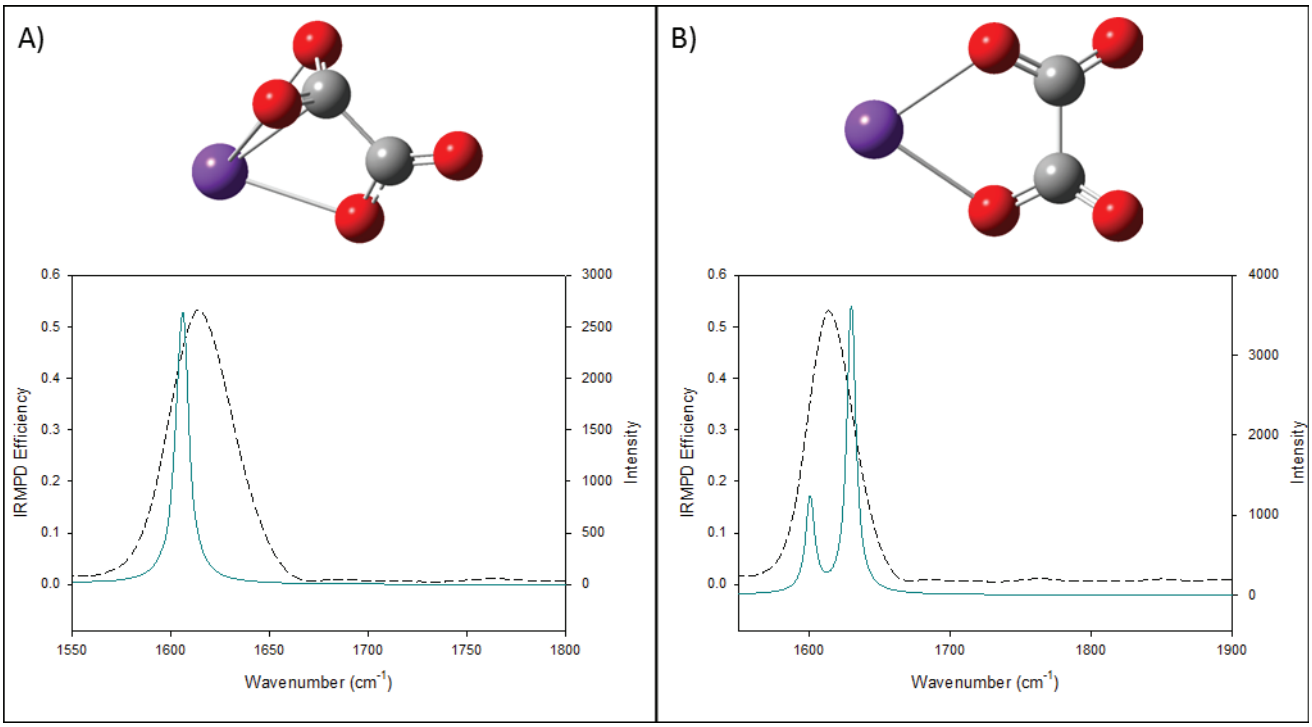


Figure 3-32: Theoretical Structures (basis set: 6-311+gd) and Spectra for each unique KOx^- structure. The IRMPD spectrum (dotted) overlaps each theoretical spectra (green). Part A is the "X" structure for B98 and all of the other "X" structures and the "Y" structure of M062x are identical. Part B is the "Y" structure for Mpw1p91 and all other remaining "Y" structures are identical.

3.5.1.2 1000-2000 cm^{-1} Range

Both theoretical structures in Figure 3-32 matched well with the IRMPD spectrum in the 1550-1850 cm^{-1} range. However the IRMPD spectrum was observed from the 1000-2000 cm^{-1} range and the full spectra can be seen in Figure 3-33. Part A has a few peaks occurring outside the IRMPD peak range eliminating the structure as a possibility whereas part B only has two peaks outside the IRMPD range allowing it to be more plausible. The two peaks outside the range are due to degenerate CO stretches with oxygen atoms bound to potassium. To try and eliminate these peaks, the oxalate had all atoms placed in the same plane. The structure optimized to the same structure where the oxalate had a bend resulting in the same theoretical peaks (appendix). The same calculation was performed with the M062x level of theory giving the same structure and theoretical spectrum (appendix).

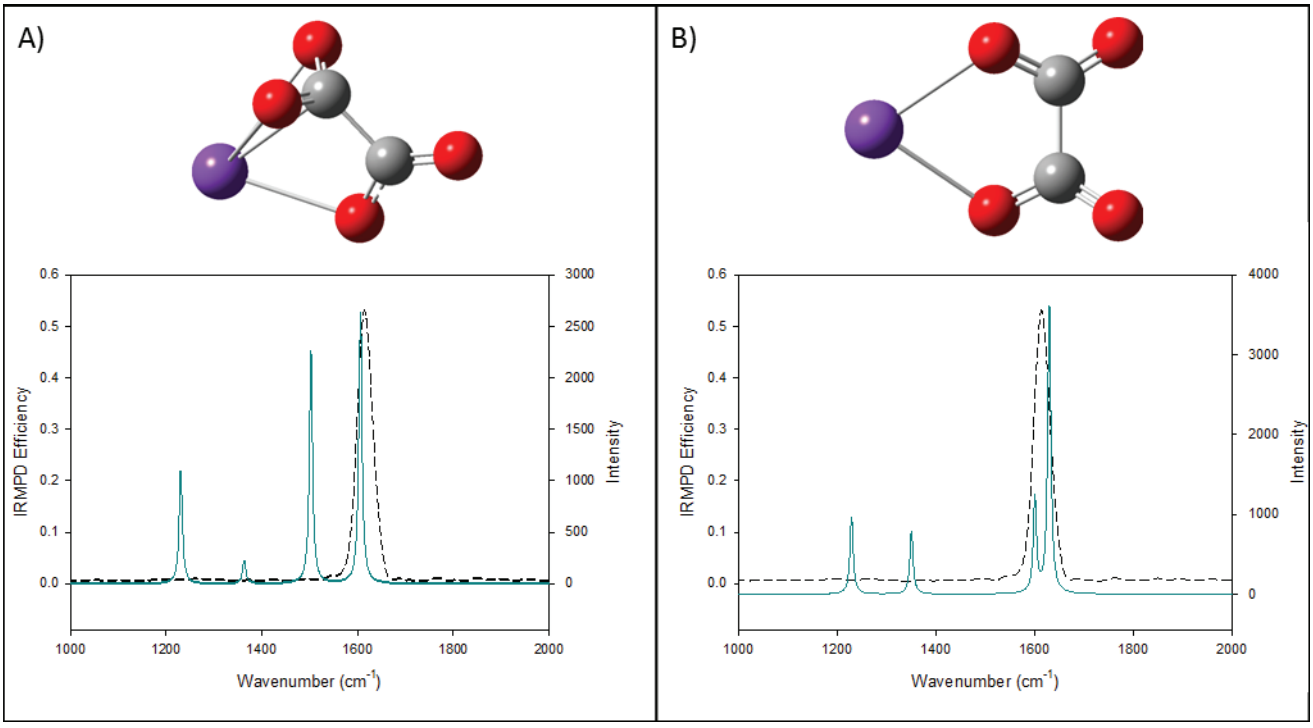


Figure 3-33: Theoretical spectra (basis set: 6-311+gd) of the two unique structures (green) compared to the IRMPD spectrum (dotted) for the range of 1000-2100 cm^{-1}. Part A is the "X" structure of B98 and part B is the "Y" structure of Mpw1pw91

3.5.1.3 KOx^- Conclusions

Unlike the other metal clusters discussed to date, the possibilities of structures are limited for metal and single oxalate structures as there are only so many positions a single oxalate and metal can have. An optimized structure could not be found without the removal of the two peaks, however all other metal oxalate clusters discussed to date had at least one peak in the 1200 cm^{-1} range. Therefore the structure in Figure 3-33B) is a plausible structure for KOx^- with its vibrational modes assigned in Table 3-15.

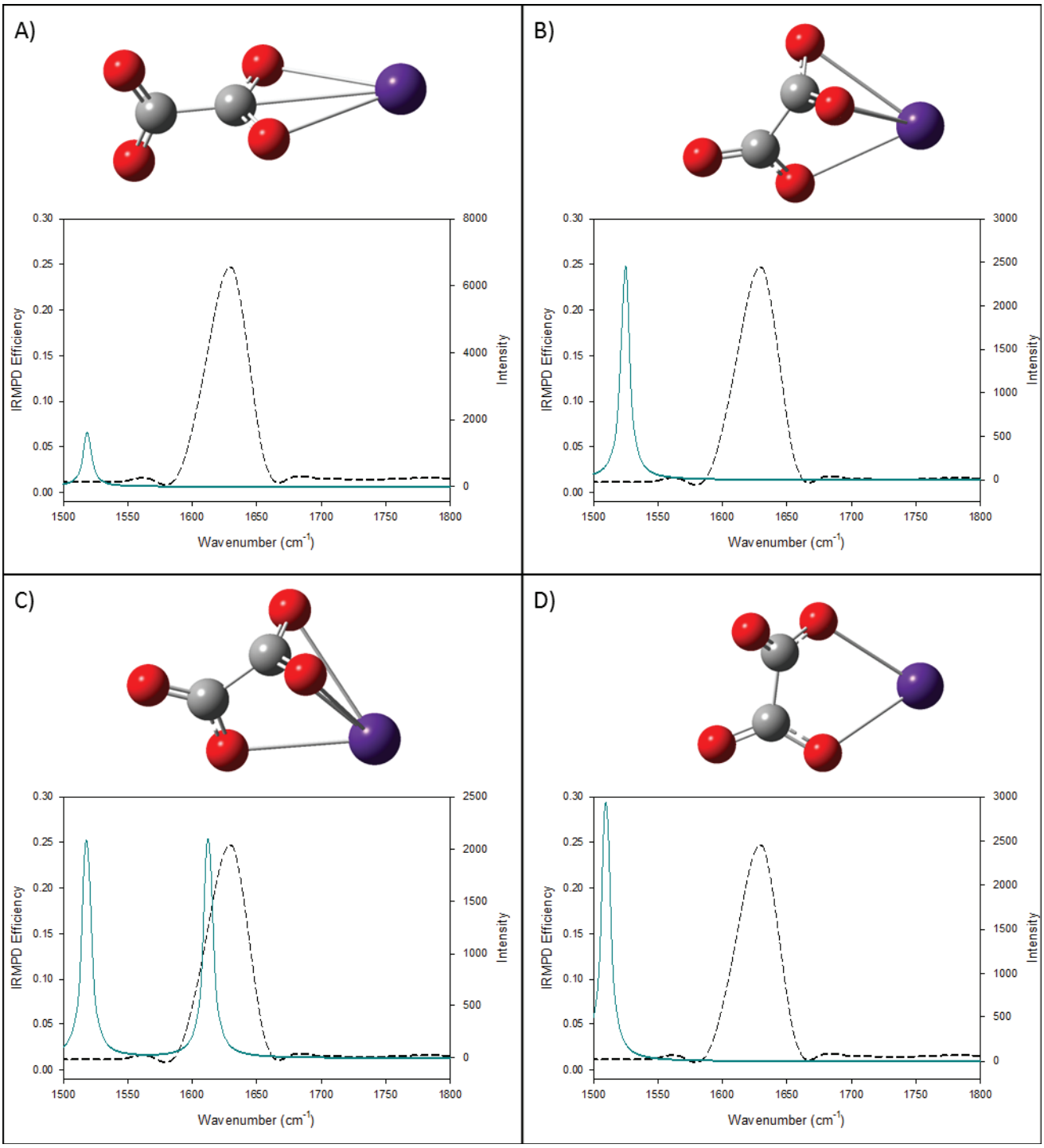
Table 3-15: Vibrational assignments to corresponding frequencies. Note: Each vibration was doubly degenerate.

Theoretical Frequencies (cm^{-1})	Experimental Frequencies (cm^{-1})	Assignment
1225	--	• Bound CO Stretch
1350	--	• Bound CO Stretch
1600	1615	• Bound asymmetrical CO_2 Stretch
1630	1615	• Bound asymmetrical CO_2 Stretch

3.5.2 $CsOx^-$

3.5.2.1 1500-1800 cm^{-1} Range

When optimization and frequency calculations were performed on different levels of theory for $CsOx^-$, five structures with unique spectra were generated and can be seen in Figure 3-34. The only structure in Figure 3-34 that has a peak overlapping the IRMPD peak is part C, corresponding to the "X" structure of Bhandhlyp. The other structures have theoretical spectra too different than that of IRMPD to be plausible structures. However, the structure resulting from parts D and E will also be considered because it is similar to the plausible structure for KOx^-.


A)
B)
C)
D)
IRMPD Efficiency
Intensity
Wavenumber (cm-1)
0.30
0.25
0.20
0.15
0.10
0.05
0.00
8000
6000
4000
2000
0
3000
2500
1500
1000
500
1500
1550
1600
1650
1700
1750
1800

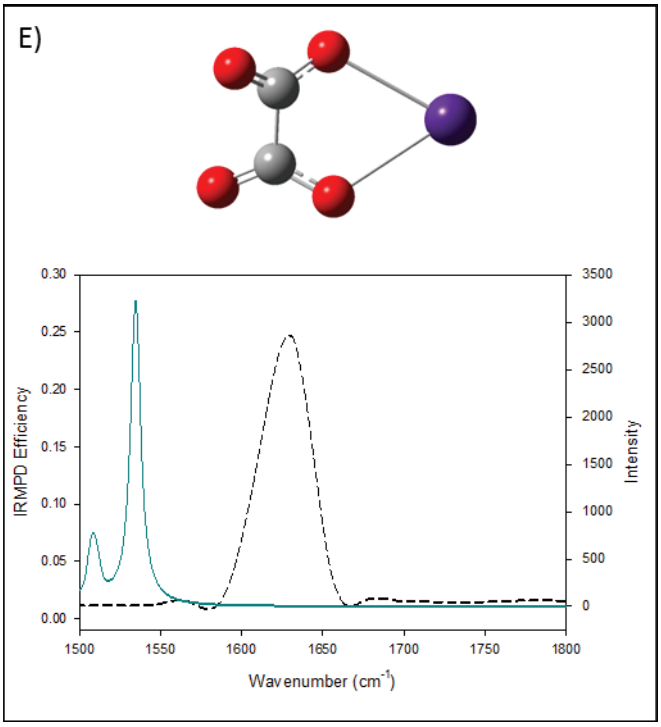


Figure 3-34: Theoretical Structures (basis set: lanl2dz) and Spectra for each unique $CsOx^-$ structure. The IRMPD spectrum (dotted) overlaps each theoretical spectra (green). Parts A-C are the "X" structures for B3lyp, B3pw91 ("X" structures B98, Mpw1pw91, Pbe1pbe and "Y" structure of B3pw91 are identical), and Bhandhlyp ("X" structures of M062x, Mp2 and "Y" structures of B98, Bhandhlyp, M062x and MP2 are identical) respectively. Parts D-E are the "Y" structures of B3lyp and Mpw1pw91 ("Y" structure of Pbe1pbe is identical) respectively.

3.5.2.2 1000-2100 cm^{-1} Range

The theoretical structure that had the closest frequencies to the IRMPD spectrum was Figure 3-34C corresponding to the "X" structure of Bhandhlyp and the two structures similar to the plausible structure of KOx^- are Figure 3-34D and E which are the "Y" structures of B3lyp and Mpw1pw91. The full spectrum range for the three structures is shown in Figure 3-35. Even though the "X" structure of Bhandhlyp had a peak overlapping the IRMPD peak, there are a couple of peaks outside the range making the structure unlikely to exist in the gas phase.

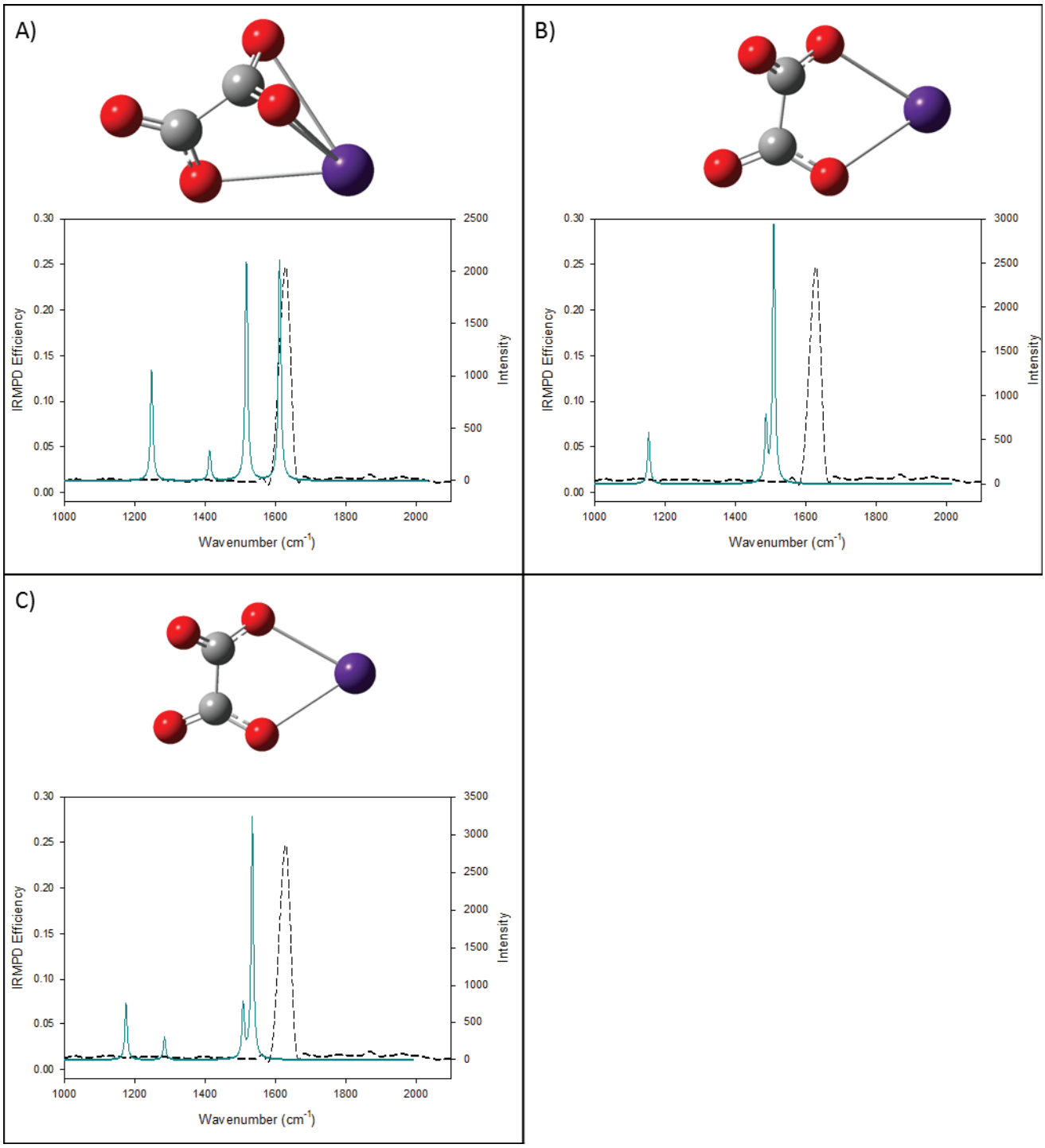


Figure 3-35: Theoretical spectra (basis set: lanl2dz) shown in green overlapping the IRMPD spectrum (dotted) for the 1000-2100 cm^{-1} range. Part A is the "X" structure of Bhandhlyp, B is the "Y" structure of B3lyp and C is the "Y" structure of Mpw1pw91.

The other structure with the two spectra for the B3lyp and Mpw1pw91 level of theories have only one major peak but not overlapping the IRMPD peak, thus these level of theories not reliable for this metal complex. Therefore, a plausible structure has not been found in the first attempt at structure determination.

3.5.2.3 Second attempt at structure determination for the 1000-2100 cm^{-1} range

At the first attempt of finding the correct structure existing in the gas phase, the structure that had theoretical peak overlapping the IRMPD was the "X" structure of Bhandhlyp (Figure 3-35A), however there were too many other peaks eliminating it from becoming a plausible structure. The optimized "Y" structures of B3lyp and Mpw1pw91 gave a similar structure to the plausible structure of KOx^- and both spectra had one major peak (Figure 3-35B and C) but did not overlap with the IRMPD peak. The next step in structural identification is to use the Bhandhlyp level of theory to re-optimize the structure from the B3lyp and Mpw1pw91 levels of theory. The reasoning behind this is the Bhandhlyp level of theory gave a peak overlapping the IRMPD peak while the other two levels of theory gave an optimized structure with one major peak. The hope is with the use of the Bhandhlyp level of theory, there will only be one theoretical peak and it will overlap with the IRMPD peak. The new optimized structure and theoretical spectrum can be seen in Figure 3-36 and its relative energy shown in Table 3-1. The optimized structure is the same as the previous two levels of theory but with the Bhandhlyp level of theory, the major peak overlaps with the IRMPD peak and is a low energy structure. Like KOx^-, there are two peaks with lower intensity between the 1200-1400 cm^{-1} range caused by doubly degenerate CO stretches. However, even with these peaks, the structure is still a plausible structure.

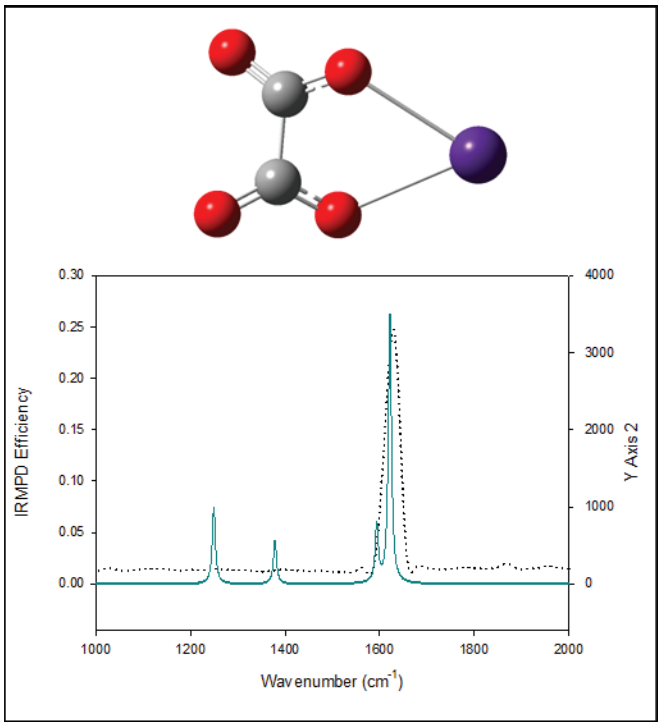


Figure 3-36: Theoretical spectrum (basis set: lanld2dz) of the optimized Bhandhlyp modified structure (green) overlapping the IRMPD spectrum (dotted) for the range 1000-2100 cm^{-1}.

Table 3-16: Relative energies (kJ/mol) of optimized structures of the Bhandhlyp of theory. Calculations were performed with the lanl2dz basis set.

Structure	Relative Energy (kJ/mol)
`X`Structure of Bhandhlyp	**0.00**
Modified Bhandhlyp	0.70

3.5.2.4 $CsOx^-$ Conclusions

To summarize the process of structure determination for $CsOx^-$, two starting structures were generated for each level of theory. After optimization and frequency calculations, the "X" structure of Bhandhlyp was the only structure having a theoretical peak overlapping the IRMPD peak but had too many other peaks making it highly unlikely to be a plausible structure to exist in the gas phase. The optimized structure resulting from the "Y" structures of B3lyp and Mpw1pw91 were the same as the plausible structure for KOx^-, however the theoretical peaks did not overlap with the experimental peaks. Further examination was needed and the optimized structure of those levels of theory was used as a starting structure for the Bhandhlyp level of theory. The structure yielding from the new optimization calculations gave a major theoretical peak overlapping the IRMPD peak as well as two peaks within the 1200-1400 cm^{-1} range. Even though these theoretical peaks are present, the structure is a plausible gas-phase structure. Therefore the best plausible gas phase structure for $CsOx^{-1}$ is shown in Figure 3-36 with its frequencies assigned in Table 3-17.

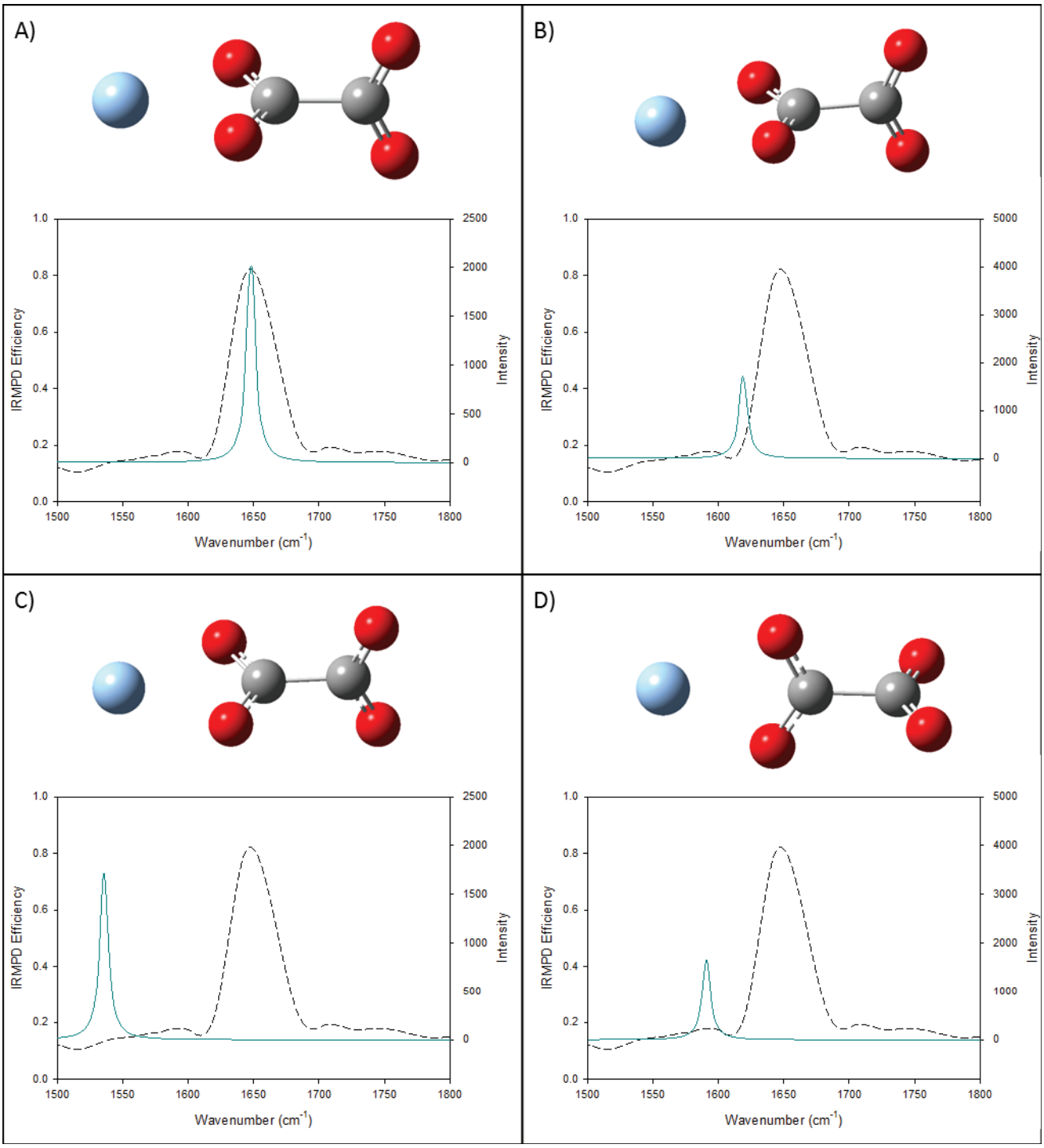
Table 3-17: Vibrational assignments to corresponding frequencies. Note: each vibration was doubly degenerate.

Theoretical Frequencies (cm^{-1})	Experimental Frequencies (cm^{-1})	Assignment
1245	--	• Bound CO Stretch
1375	--	• Bound CO Stretch
1590	1630	• Bound asymmetrical CO_2 Stretch
1620	1630	• Bound asymmetrical CO_2 Stretch

3.5.3 $AgOx^-$

3.5.3.1 1500-1800 cm^{-1} Range

When structures with various levels of theory had optimization and frequency calculations performed on them, six structures with unique frequencies were generated. Each structure with its theoretical spectrum overlapped with the IRMPD spectrum can be seen in Figure 3-37.


A)
B)
C)
D)
IRMPD Efficiency
Intensity
Wavenumber (cm-1)
1.0
0.8
0.6
0.4
0.2
0.0
2500
2000
1500
1000
500
0
5000
4000
3000
2000
1000
0
1500
1550
1600
1650
1700
1750
1800

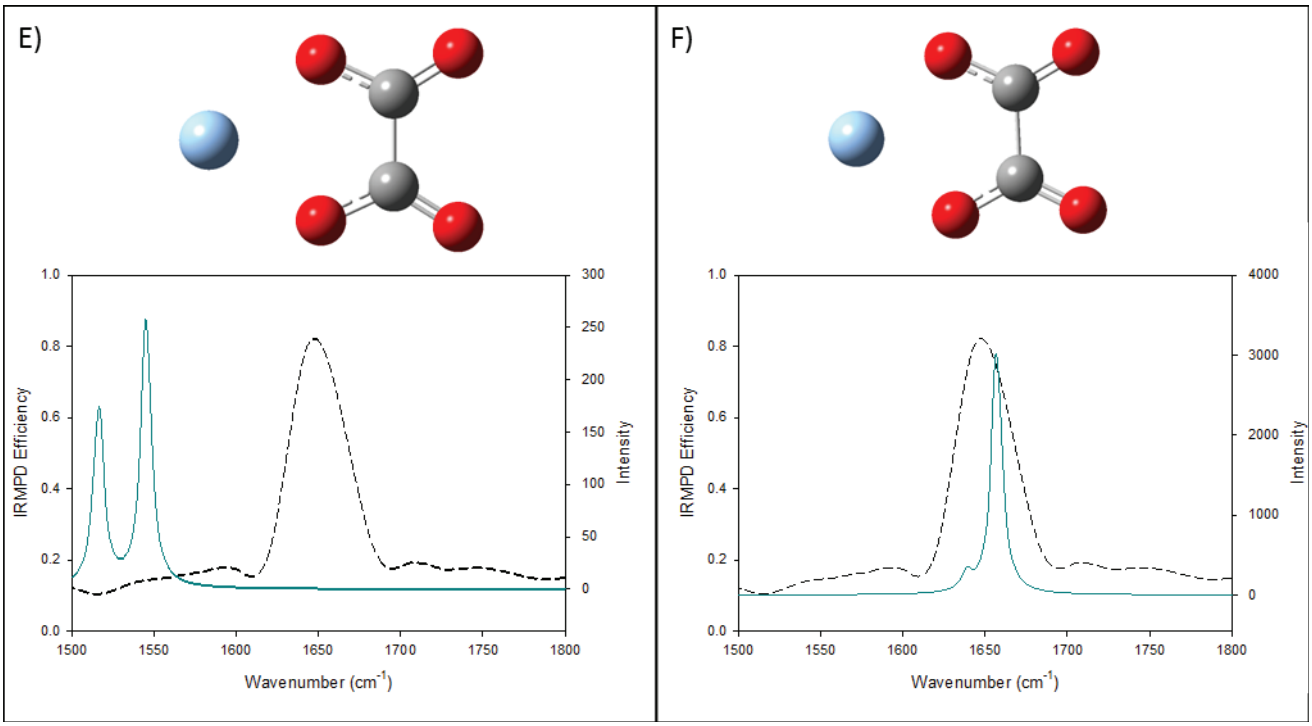


Figure 3-37: Theoretical structures (basis set: lanl2dz) and spectra for different $AgOx^-$ structures. The IRMPD spectrum (dotted) overlaps each theoretical spectrum (green). Parts A-C are the "X" structures of Bhandhlyp ("X" structure of M062x is identical), Pbe1pbe ("X" structures of B3lyp, B3pw91, B98 and Mpw1pw91 are identical) and MP2 respectively. Parts D-F are the "Y" structures of B3pw91, B98 and Bhandhlyp ("Y" structures of B3lyp, M062x, Mpw1pw91, Pbe1pbe and MP2 are identical) respectively.

Looking at the theoretical spectra in Figure 3-37, all spectra except parts A and F are too different than that of the IRMPD spectrum to be considered plausible spectra. Parts A and F have a theoretical peak overlapping the IRMPD peak making them a close match for the 1500-1800 cm^{-1} range.

3.5.3.2 1000-2000 cm^{-1} Range

The theoretical structures that best matched the experimental IRMPD spectrum were Figure 3-37 parts A ("X" structure of Bhandhlyp) and F ("Y" structure of Bhandhlyp) for the range of 1500-1800 cm^{-1}. The IRMPD spectrum however was acquired approximately from the 1000-2000 cm^{-1} range and the spectra for the full range are shown in Figure 3-38. The optimized "X" structure of Bhandhlyp (shown in part A) has a couple of peaks not overlapping the IRMPD peak making it unlikely to be a plausible structure, whereas the optimized structure of Bhandhlyp (shown in part B) matches nicely to the experimental spectrum and is the lower energy structure of the two (energies shown in Table 3-18).

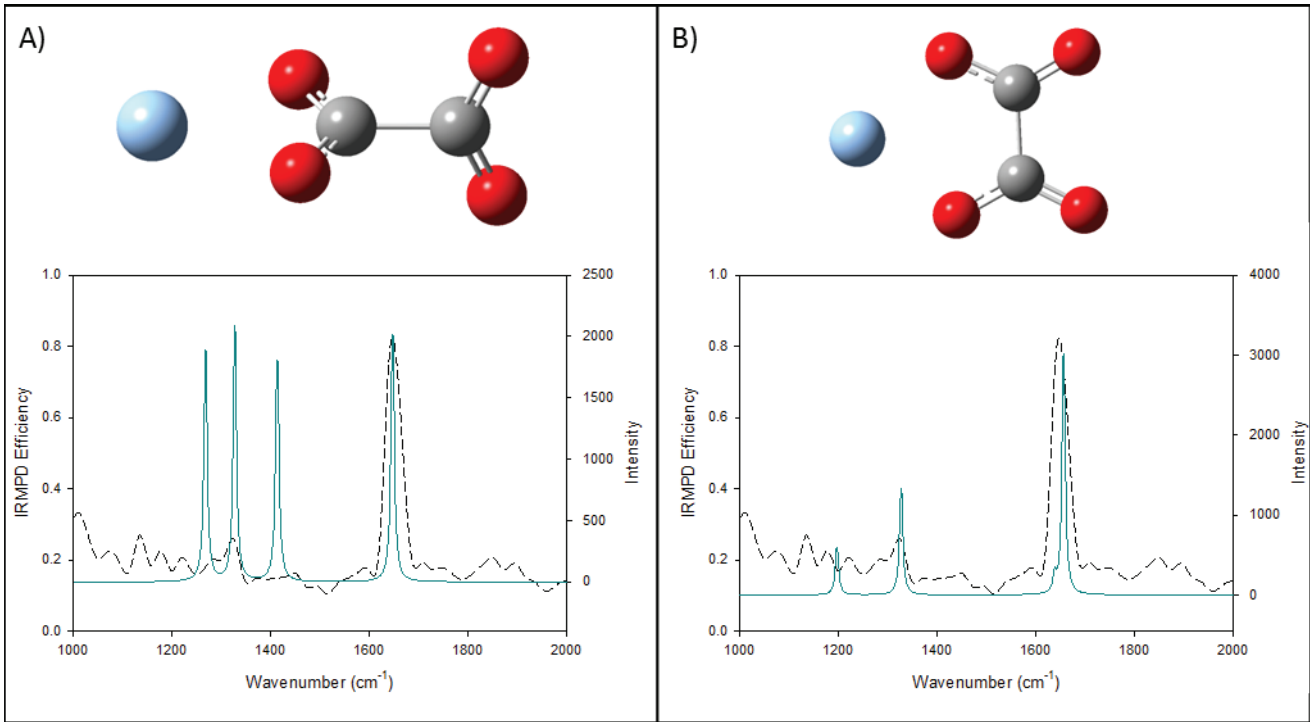


Figure 3-38: Theoretical spectra (basis set: lanl2dz) of the two best matching structures from the 1500-1800 cm^{-1} range (green) compared to the IRMPD spectrum (dotted) for the range 1000-2100 cm^{-1}. Part A is the optimized structure of "X" Bhandhlyp and part B is the optimized structure of "Y" Bhandhlyp.

Table 3-18: Relative energies (kJ/mol) of optimized structures of the Bhandhlyp of theory. Calculations were performed with the lanl2dz basis set.

Structure	Relative Energy (kJ/mol)
"X" Structure of Bhandhlyp	59.67
"Y" structure of Bhandhlyp	**0.00**

3.5.3.3 $AgOx^-$ Conclusions

To summarize the process of structure determination of $AgOx^{-1}$, two starting structures were generated for each level of theory. After optimization and frequency calculations both "X" and "Y" structures of Bhandhlyp ended up being the closest matching to the IRMPD spectrum for the 1500-1800 cm^{-1} range. However, the full acquisition range for the IRMPD spectrum was from approximately 1000-2000 cm^{-1} and the optimized "X" structure had too many theoretical peaks compared to the IRMPD spectrum and therefore was not a plausible gas phase structure. The optimized "Y" structure of the Bhandhlyp method overlapped the IRMPD quite well and was the lower energy structure of the two by 60 kJ/mol. Therefore it is a plausible structure with its frequencies assigned in Table 3-1.

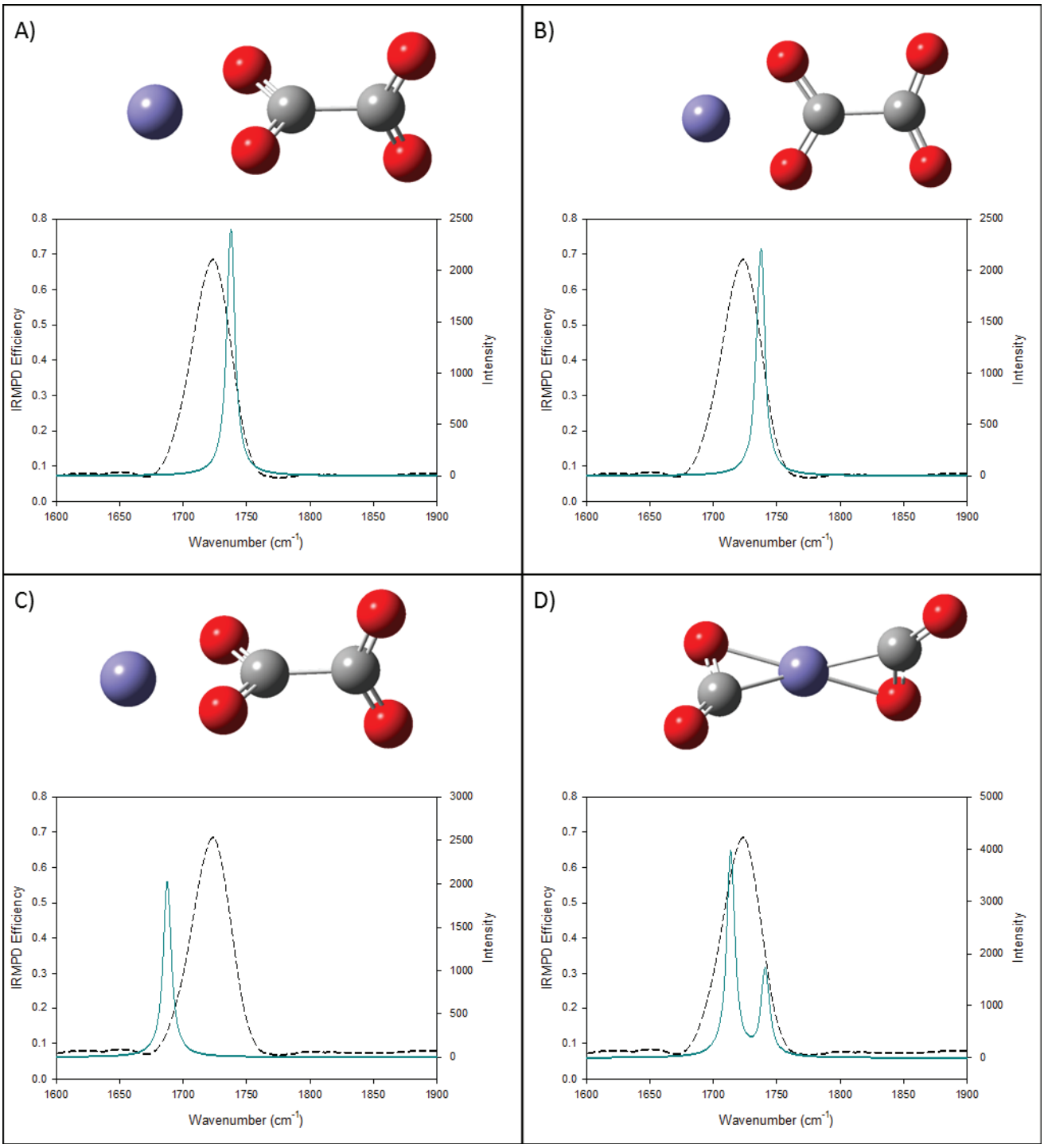
Table 3-19: Vibrational assignments to corresponding frequencies. Note: each vibration was doubly degenerate.

Theoretical Frequencies (cm^{-1})	Experimental Frequencies (cm^{-1})	Assignment
1200	--	• Bound CO Stretch
1325	1325	• Bound CO Stretch
1655	1645	• Bound asymmetrical CO_2 Stretch

3.5.4 $FeOx^-$

3.5.4.1 1600-1900 cm^{-1} Range

When optimization and frequency calculations were performed on $FeOx^-$, seven structures with unique spectra were generated. Each structure with its unique theoretical spectrum can be seen in Figure 3-39. Structures with theoretical peaks having good overlap to the IRMPD spectrum are A, B, D and F corresponding to the "X" structure of Bhandhlyp, "X" structure of M062x, "Y" structure of B3lyp and the "Y" structure of Mpw1pw91 respectively. Meanwhile structures in parts C, E and G have spectra too different than the IRMPD spectrum to be candidates for a plausible structure of $FeOx^-$ in the gas phase.


A)
B)
C)
D)
IRMPD Efficiency
Intensity
Wavenumber (cm-1)
0.0
0.1
0.2
0.3
0.4
0.5
0.6
0.7
0.8
0
500
1000
1500
2000
2500
3000
4000
5000
1600
1650
1700
1750
1800
1850
1900

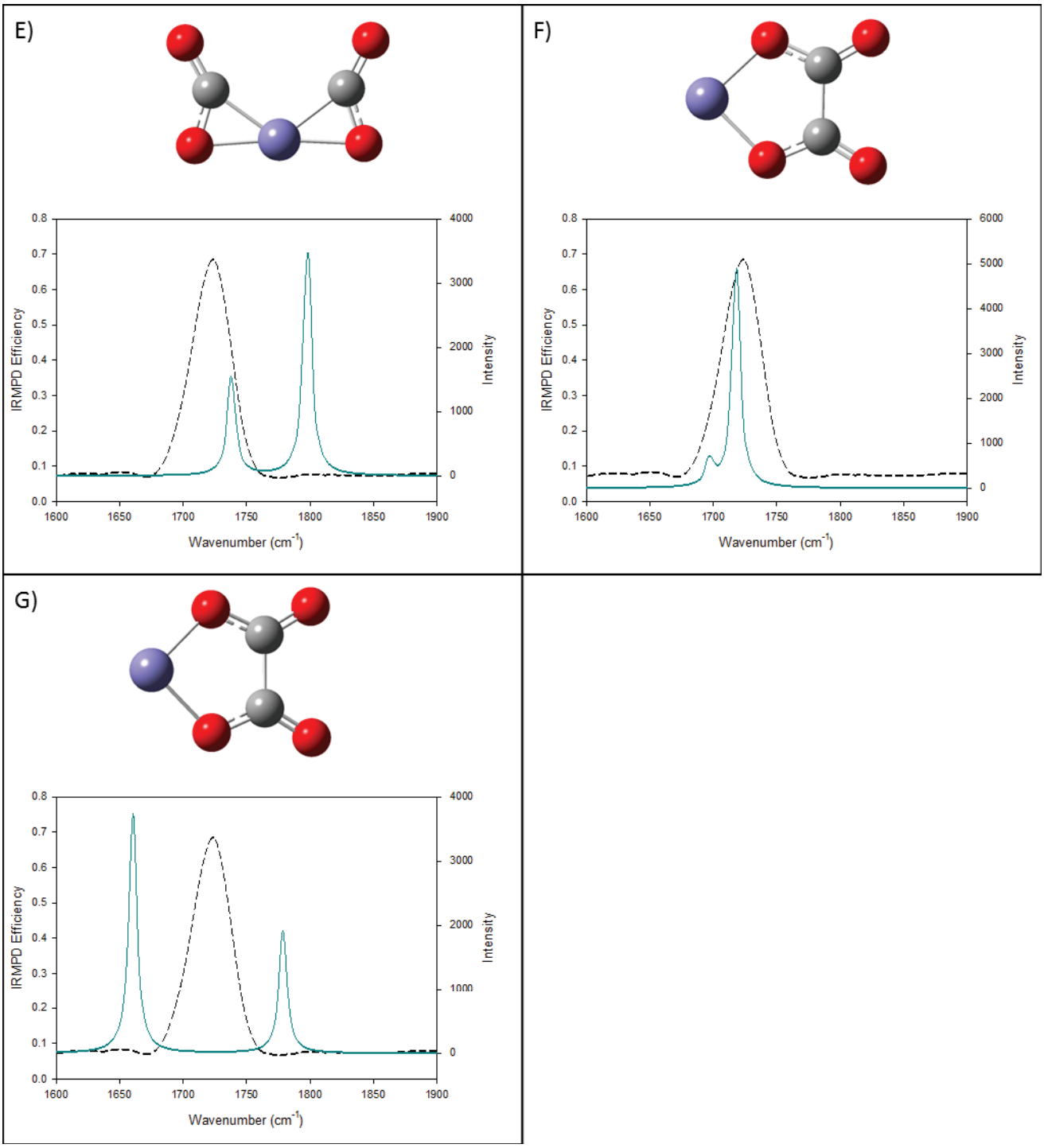


Figure 3-39: Theoretical Structures (basis set: 6-311+gd) and Spectra for each unique $FeOx^-$ spectra. The IRMPD spectrum (dotted) overlaps each theoretical spectra (green). Parts A-C are the "X" structures of Bhandhlyp, M062x ("X" structures of B3lyp, B3pw91, B98 and MP2 are identical) and Mpw1pw91 ("X" structure of Pbe1pbe is identical) respectively while parts

D-G are the "Y" structures of B3lyp, B3pw91 ("Y" structure of Pbe1pbe is identical), Mpw1pw91 ("Y" structures of B98, Bhandhlyp, M062x are identical) and MP2 respectively.

3.5.4.2 1000-2000 cm^{-1} Range

The theoretical structures with spectra having good overlap to the IRMPD spectrum were Figure 3-39 parts A,B, D and F for the range of 1600-1900 cm^{-1}. However, the full IRMPD spectrum was acquired from approximately 1000-2000 cm^{-1} and thus each spectrum overlapped to the IRMPD spectrum must be looked at for this range. Figure 3-40 shows the best matching theoretical structure and spectrum from the 1600-1900 cm^{-1} overlapping the IRMPD spectrum for the full acquisition range. Parts A through C all have a peak not overlapping the IRMPD spectrum, eliminating them as plausible structures. Part D shows the optimized "Y" structure of Mpw1pw91 which matches nicely to the IRMPD spectrum making it a plausible structure.

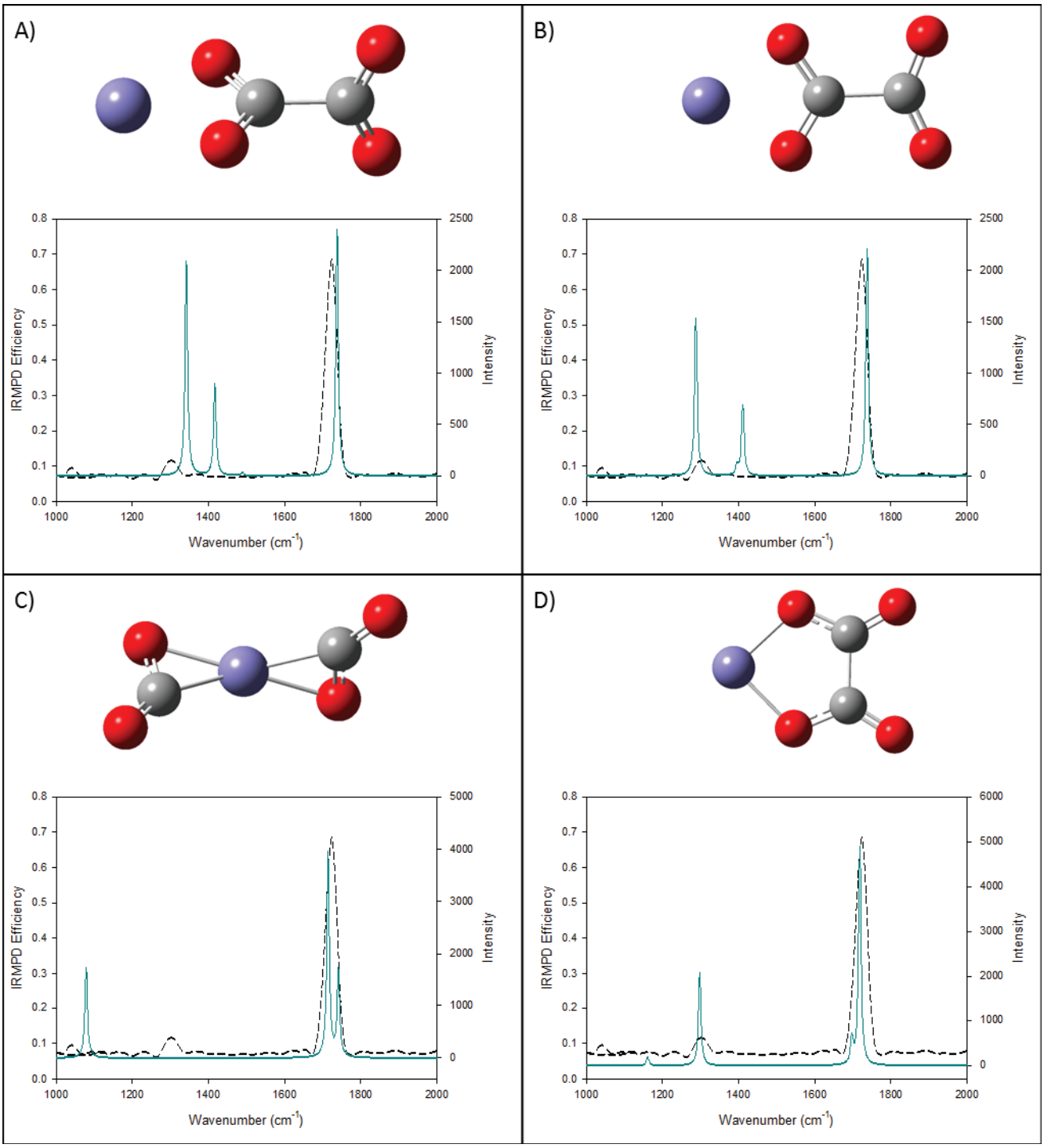


Figure 3-40: Theoretical spectra (basis set: 6-311+gd) of the three best matching structures from the 1600-1900 cm^{-1} range (green) compared to the IRMPD spectrum (dotted) for the range of 1000-2100 cm^{-1}. Parts A and B are the "X" structures of Bhandhlyp and M062x respectively while parts C and D are the "Y" structures of B3lyp and Mpw1pw91 respectively.

3.5.4.3 $FeOx^-$ Conclusions

To summarize the process of determining a plausible gas-phase structure of $FeOx^-$, two starting structures were generated for each level of theory. After optimization and frequency calculations were performed, the structures with the closest matching spectra were the "X" structures of Bhandhlyp and M062x and the "Y" structures of B3lyp and Mpw1pw91 for the 1600-1900 cm^{-1}. However, the IRMPD spectrum was acquired from approximately the 1000-2000 cm^{-1} range and when looking at the theoretical spectra for the full range, all except the optimized "Y" structure of Mpw1pw91 could be eliminated. The "Y" structure of Mpw1pw91 matched nicely to the IRMPD spectrum and is therefore a plausible structure with its frequencies assigned in Table 3-20.

Table 3-20: Vibrational assignments to corresponding frequencies. Note: each vibration was doubly degenerate.

Theoretical Frequencies (cm^{-1})	Experimental Frequencies (cm^{-1})	Assignment
1160	--	• Bound CO Stretch
1300	1300	• Bound CO Stretch
1700	1725	• Bound asymmetrical CO_2 Stretch
1720	1725	• Bound asymmetrical CO_2 Stretch

3.6 Conclusions

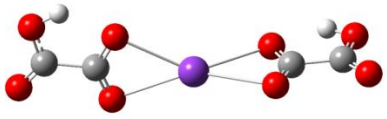
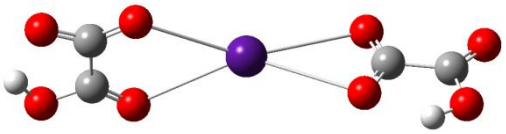
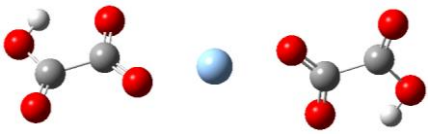
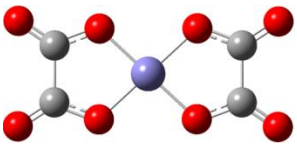
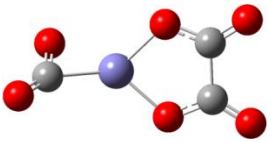
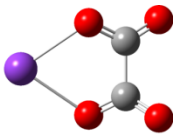
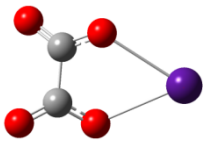
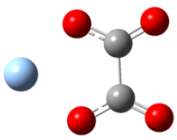
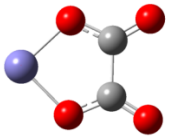
There were two starting structures per level of theory which had optimization and frequency calculations performed for $KOx_2H_2^-$, $CsOx_2H_2^-$, $FeOx_2^-$, $FeOxCO_2^-$, KOx^-, $CsOx^-$, $AgOx^-$ and $FeOx^{-1}$ in hopes of determining a plausible structure for these metal complexes in the gas phase. Different levels of theory gave different low energy structures making it difficult to assign a structural conformation for a metal complex with computational methods alone. Comparing theoretical frequencies to experimental IRMPD spectra allowed for elimination of some optimized structures. In many cases having only two starting structures per level of theory was only useful to determine what level of theory should be used for

structural exploration as opposed to determining a plausible low-energy gas-phase structure. The Metal-$Ox_2H_2^-$ complexes were the most difficult to assign a plausible structure. This is due to the effect hydrogen bonding can have on a structure. Depending on the placement of the protons, the structural conformation can change greatly. Therefore for these complexes it took many attempts to determine a plausible structure. Whereas the Metal-Ox^- complexes were the easiest to determine a plausible gas-phase structure since there are only so many orientations a single oxalate and metal can have. The difficulty of determining a plausible structure for the Metal-Ox_2^- and Metal-$OxCO_2^-$ complexes was moderately difficult as they can have more orientations than the Metal-Ox^- complexes but do not have the strong effect hydrogen bonding has on structural conformations.

3.6.1 Levels of Theory

The plausible structures of all metals can be seen in Table 3-21 along with the basis-set and level of theory used. DFT levels of theory were chosen as they were a nice compromise between speed and accuracy. The MP2 level of theory (which is more time-consuming) was also used to compare to the quicker DFT levels of theory. All MP2 structures had spectra too different than the IRMPD spectra and therefore this level of theory is not appropriate for structure determination of metal oxalate complexes. Before structural conformations were assigned, it was unknown which level of theory would give plausible structures, thus many were tried. After plausible structures have been found, it was shown only certain levels of theory find plausible structures – for structures calculated using the 6-311+gd basis set, the M series of DFT works best (i.e. M062x and Mpw1pw91) and for structures calculated using the Lanl2dz basis set, Bhandhlyp level of theory gave plausible structures. Therefore for future attempts at structural exploration only these basis sets need to be used instead of the many that were tried.

Table 3-21: Plausible structures of all metal-oxalate complexes.

Complex	Level of Theory	Basis-set	Plausible Structure
$KOx_2H_2^-$	M062x	6-311+gd	
$CsOx_2H_2^-$	Bhandhlyp	Lanl2dz	
$AgOx_2H_2^-$	Bhandhlyp	Lanl2dz	
$FeOx_2^-$	Mpw1pw91	6-311+gd	
$FeOxCO_2^-$	M062x	6-311+gd	
KOx^-	Mpw1pw91	6-311+gd	
$CsOx^-$	Bhandhlyp	Lanl2dz	
$AgOx^-$	Bhandhlyp	Lanl2dz	
$FeOx^-$	Mpw1pw91	6-311+gd	

3.7 References

1. M. J. Frisch, G. W. Trucks, H. B. Schlegel, G. E. Scuseria, M. A. Robb, J. R. Cheeseman, G. Scalmani, V. Barone, B. Mennucci, G. A. Petersson, H. Nakatsuji, M. Caricato, X. Li, H. P. Hratchian, A. F. Izmaylov, J. Bloino, G. Zheng, J. L. Sonnenberg, M. Hada, M. Ehara, K. Toyota, R. Fukuda, J. Hasegawa, M. Ishida, T. Nakajima, Y. Honda, O. Kitao, H. Nakai, T. Vreven, J. A. Montgomery Jr., J. E. Peralta, F. Ogliaro, M. J. Bearpark, J. Heyd, E. N. Brothers, K. N. Kudin, V. N. Staroverov, R. Kobayashi, J. Normand, K. Raghavachari, A. P. Rendell, J. C. Burant, S. S. Iyengar, J. Tomasi, M. Cossi, N. Rega, N. J. Millam, M. Klene, J. E. Knox, J. B. Cross, V. Bakken, C. Adamo, J. Jaramillo, R. Gomperts, R. E. Stratmann, O. Yazyev, A. J. Austin, R. Cammi, C. Pomelli, J. W. Ochterski, R. L. Martin, K. Morokuma, V. G. Zakrzewski, G. A. Voth, P. Salvador, J. J. Dannenberg, S. Dapprich, A. D. Daniels, Ö. Farkas, J. B. Foresman, J. V. Ortiz, J. Cioslowski, D. J. Fox. Gaussian, Inc.: Wallingford, CT, USA, 2013.

2. M. P. Andersson, P. Uvdal, New Scale Factors for Harmonic Vibrational Frequencies Using the B3LYP Density Functional Method with the Triple-ζ Basis Set 6-311+G(d,p). *The Journal of Physical Chemistry A* 2005, *109*. 2937-2941, DOI: 10.1021/jp045733a.

3. http://cccbdb.nist.gov/, Precomputed vibrational scaling factors. *NIST Standard Reference Database 101* 2013.

4 COLLISION CROSS-SECTIONS OF METAL OXALATE COMPLEXES

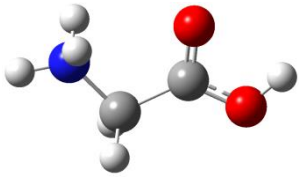
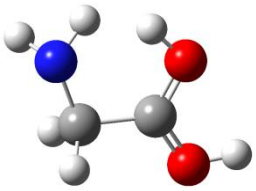
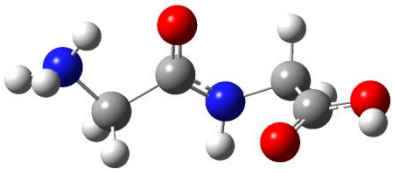
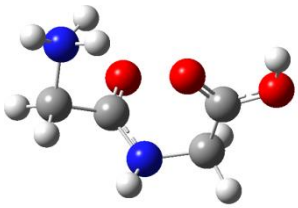
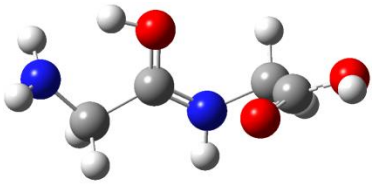
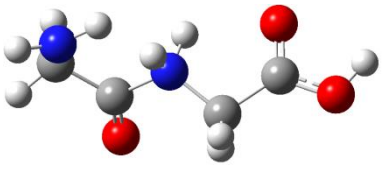
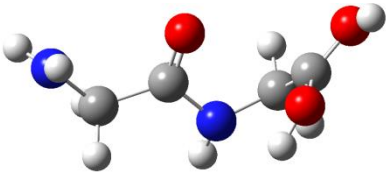
Comparing theoretical and experimental collision cross-sections is a technique that can allow for structural determination of ionic species with the use of mass spectrometry, ion mobility and computational methods.

4.1 Theoretical Collision Cross-Section Determination: Sigma or Mobcal?

There are two different programs that calculate theoretical collision cross-sections (Ω): Sigma which uses the projection method (Bowers *et al.*) and Mobcal which uses the trajectory method (Jarrold *et al.*).[1] To determine which program is more suitable for the small metal-oxalate clusters, protonated glycine and diglycine structures with known experimental cross-sections will have theoretical collision-cross sections calculated. By determining collision cross-sections for these structures, which are relatively the same size as the anionic metal complexes, it will shed light on which program is more appropriate for smaller ionic species.

Zhang *et al.* proposed two low energy structures for glycine and five low energy diglycine structures.[2] Collision cross-sections have previously been reported using IMS for the two cationic species – 46.6 $Å^2$ for glycine and 62 $Å^2$ for diglycine.[3] For both Sigma and Mobcal, fifty theoretical collision cross-sections were calculated per structure to get an average collision cross-section and compared to experimental results. Table 4-1 shows the relative energies, experimental collision cross-sections, and theoretical average collision cross-sections calculated using Sigma and Mobcal.

Table 4-1: Energies and collision cross-sections for proposed low energy structures of glycine and diglycine.

	Structure	Relative Energy (kcal/mol)	Exp. Ω (Å^2)	Sigma Ω (Å^2)	% Diff.	Mobcal Ω (Å^2)	% Diff.
A)		**0.00**	46.6	46.00 +/- 0.27	**-1%**	45.96 +/-1.19	**-1%**
B)		13.81	46.6	44.25 +/- 0.23	**-5%**	44.68 +/-1.01	**-4%**
C)		**0.00**	62	63.21 +/- 0.35	**2%**	63.59 +/-1.45	**3%**
D)		0.47	62	61.06 +/- 0.30	**-2%**	60.58 +/-1.47	**-2%**
E)		1.69	62	63.11 +/- 0.33	**2%**	62.91 +/- 1.36	**1%**
F)		18.10	62	63.75 +/-0.38	**3%**	64.15 +/- 1.42	**3%**
G)		26.90	62	63.41+/- 0.37	**2%**	62.42 +/- 1.21	**1%**

As discussed previously, the lowest energy structure in theory should be the structure existing in the gas phase. Therefore, the lowest energy structure proposed should have a theoretical collision cross-section closest to the experimental. For the protonated glycine structures, this was indeed the case for both Sigma and Mobcal calculated collision cross-sections in which both had collision cross-sections one percent smaller than experimental results. In the case of the protonated diglycine structures, all structures had theoretical collision cross-sections close to experimental results making it difficult to propose a single structure. However, it should be noted Mobcal gave collision cross-section values closer to experimental results compared to Sigma. Therefore, Mobcal will be used to calculated collision cross-sections of the Metal-Oxalate complexes.

4.2 Methods

4.2.1 Experimental

Solutions of metal oxalate complexes were prepared at a concentration of 10^{-5} M with deionized water for the stock solution and methanol for the diluted solutions. Experiments were performed on a Waters Synapt G1 where solutions were introduced into the mass spectrometer via electrospray ionization. CID experiments were performed to verify the identity of the ions, mobility times were recorded with the use of IMS and ions were detected using a TOF. α,ω-Dicarboxy Terminated Polystyrene (PS), purchased from Polymer source, under identical experimental conditions as the metal complexes was used as a calibrant to calculate collision-cross sections.[4] Calibrant drift-times and cross-sections were corrected for mass and charge effects and the natural logarithms were plotted to create a calibration set. Analyte collision cross-sections were calculated based on this set.

4.2.2 Computational

To determine collision cross-sections of metal-oxalic acid complexes, optimization and frequency calculations were performed with different density functional level of theory (B3lyp, B3pw91, B98,

Bhandhlyp, M062x, Mpw1pw91 and Pbe1pbe) with either a 6-311+gd (Fe, K) or Lanl2dz (Cs, Ag) basis set for each complex using the Gaussian 09 Suite of programs.[5] For each level of theory two starting structures were generated per complex (an "X" structure where the ligands are along the same plane as the metal and a "Y" structure where the ligands are above and below the plane). After the different structures were optimized, they had collision cross-sections calculated fifty times to obtain an average using the trajectory method of Mobcal and were compared to experimental collision cross-sections.[1c] Silver, potassium and cesium needed to be added to the Mobcal program and literature values of equilibrium bond length and energy were added from Weis *et al.* for silver were added to the program.[6] Gas-phase literature values could not be found for potassium and cesium, and were therefore determined using potentials derived by Viehland *et al.* and fitting them to a 12-6-4 potential with the nonlinear least-squares curving method.[7]

4.3 Iron – Oxalate Complexes

Iron (III) Oxalate hexahydrate purchased from Sigma-Aldrich was used to determine collision cross-sections of $FeOx_2^-$, $FeOxCO_2^-$, and $FeOx^-$. $FeOx_2^-$ loses a CO_2 group to form $FeOxCO_2^-$ which then in turn loses a CO_2 group to form $FeOx^-$. All three iron-oxalate complexes are singly charged species and to maintain the single charge, the oxidation state of iron changes (Figure 4-1). To confirm the iron oxalate species do exist in the mass spectrometer, collision induced dissociation experiments were performed.

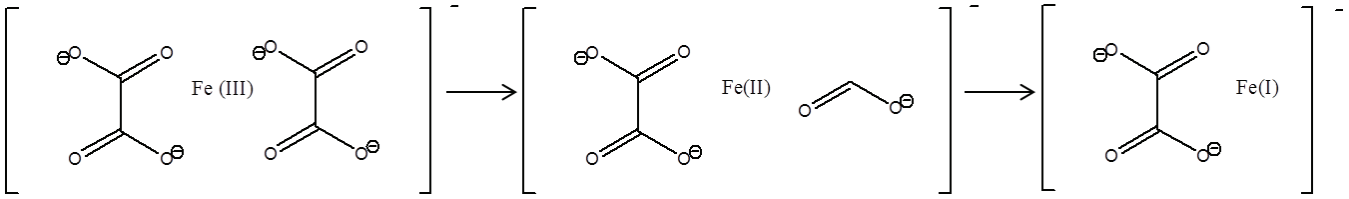


Figure 4-1: Schematic of $FeOx_2^-$ dissociating to $FeOx^-$.

Figure 4-2 shows a CID spectrum of iron (III) hexahydrate where m/z 232 was mass selected. The loss of CO_2 (m/z 44) is present in the spectrum confirming the chemical identity of the species and therefore collision cross-sections can be calculated based on their mobility times.

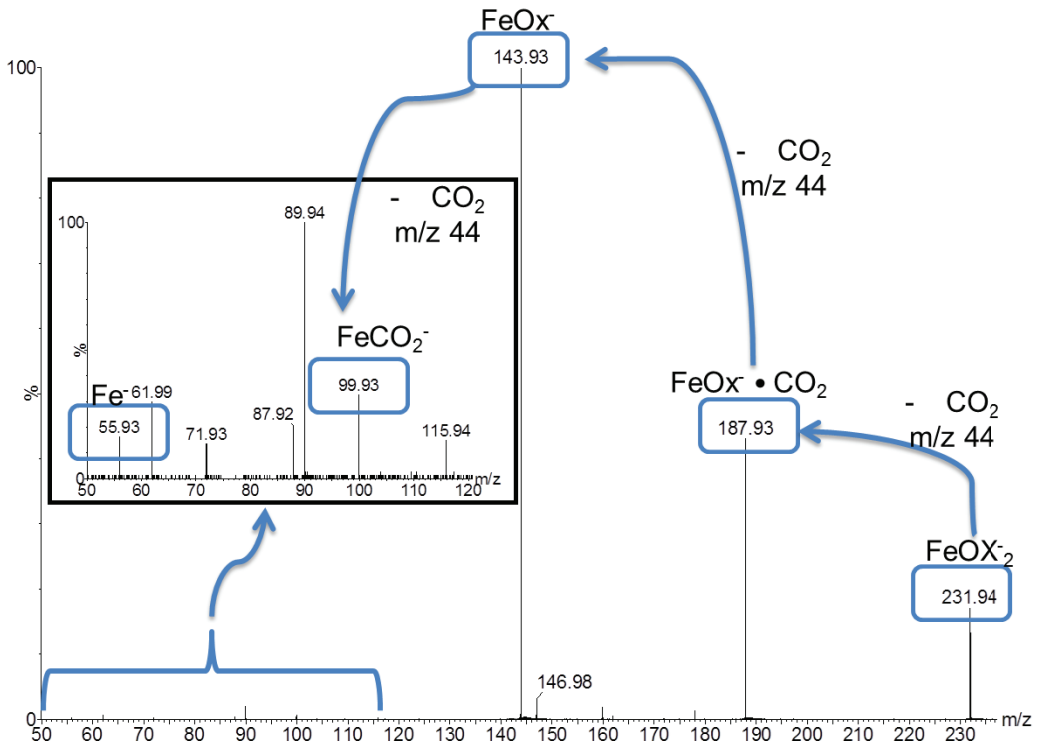


Figure 4-2: CID spectrum for iron (III) hexahydrate.

4.3.1 Helium as the buffer gas for IMS for collision cross-section determination

Typically helium or nitrogen gas is used as the neutral buffer gas for ion mobility. For the iron-oxalate complexes, collision cross-sections were determined using both gases and therefore both results will be shown. This section will go through the helium results. Firstly, the calibration set was built using drift times and literature collision cross-section values for PS with values shown in Table 4-2. After corrections were made for mass and charge effects, the natural logarithms were plotted and the constructed set can be seen in Figure 4-3.

Table 4-2: The drift times and cross-sections for polystyrene, used to build the calibration set[4]

Oligomer	m/z	Drift Time (ms)	Lit Ω ($Å^2$)
3	401.16	5.38	132
4	505.22	7.94	163
5	609.30	11.46	196
6	713.38	14.36	210
7	817.46	19.16	236
8	921.53	24.72	262
9	1025.86	29.80	276

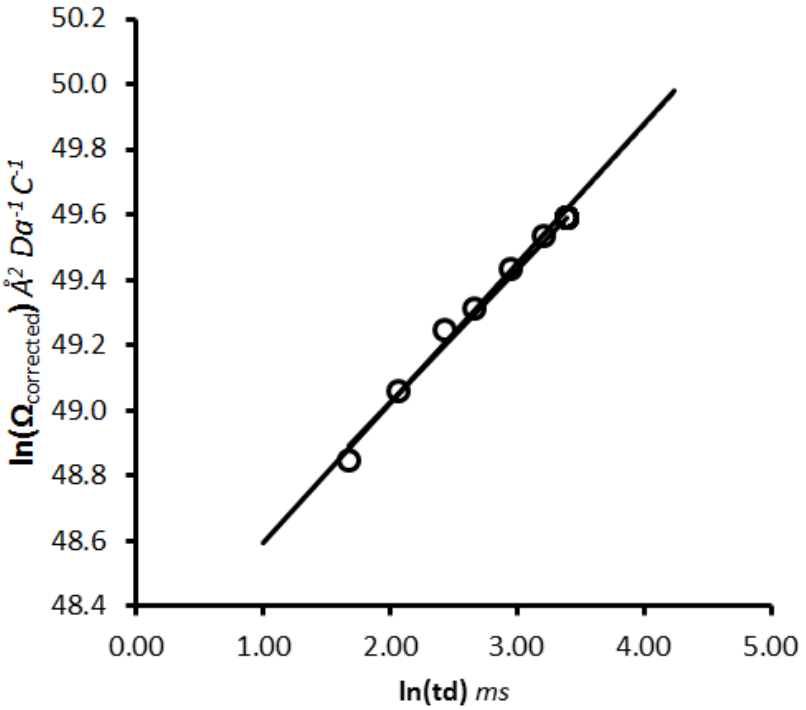


Figure 4-3: Calibration set constructed from corrected drift times and collision cross-sections for PS using helium as the buffer gas.

Collision cross-sections of iron oxalate complexes were then calculated using the calibration set and drift times measured. The experimental collision cross-sections are shown in Table 4-3. $FeOx_2^-$ has the largest drift time and the largest collision cross-section and is a reasonable observation since it is the larger of the iron oxalate species and therefore it should take longer to reach the end of the drift tube as it is experiencing more collisions with helium. The trend follows as it should (the smaller the ions get, the smaller the drift times and thus the smaller the collision cross-sections) except for the $FeCO_2^-$ species. It has the same drift-time and slightly larger collision cross-section (by 0.4Å^2) than $FeOx^-$. However, this is most likely due to both complexes being very small and therefore hard to separate.

Table 4-3: Drift times and experimental collision cross-sections for iron oxalate complexes with helium as the buffer gas

Cluster	m/z	Drift Time (ms)	Ω (Å^2)	+/- (Å^2)
$FeOX_2^-$	231.90	0.90	63.3	2.7
$FeOX^- \bullet CO_2$	187.91	0.70	56.9	2.4
$FeOX^-$	143.90	0.58	52.6	2.2
$FeCO_2^-$	99.92	0.58	53.0	2.2

4.3.2 Nitrogen as the buffer gas for IMS for collision cross-section determination

The process of the construction of the calibration set and determination of collision cross-sections for iron-oxalate complexes is the same as helium when nitrogen is the buffer gas. The calibration set was constructed (Figure 4-4) using the drift times and collision cross-sections shown in Table 4-4.

Table 4-4: The drift times and collision cross-sections for PS, used to build the calibration set with nitrogen as the buffer gas[4]

Oligomer	m/z	Drift Time (ms)	Lit Ω ($Å^2$)
3	401.26	5.95	132
4	505.38	8.06	163
5	609.48	10.18	196
6	713.59	12.35	210
7	817.70	14.18	236
8	921.79	16.62	262
9	1025.91	19.62	276

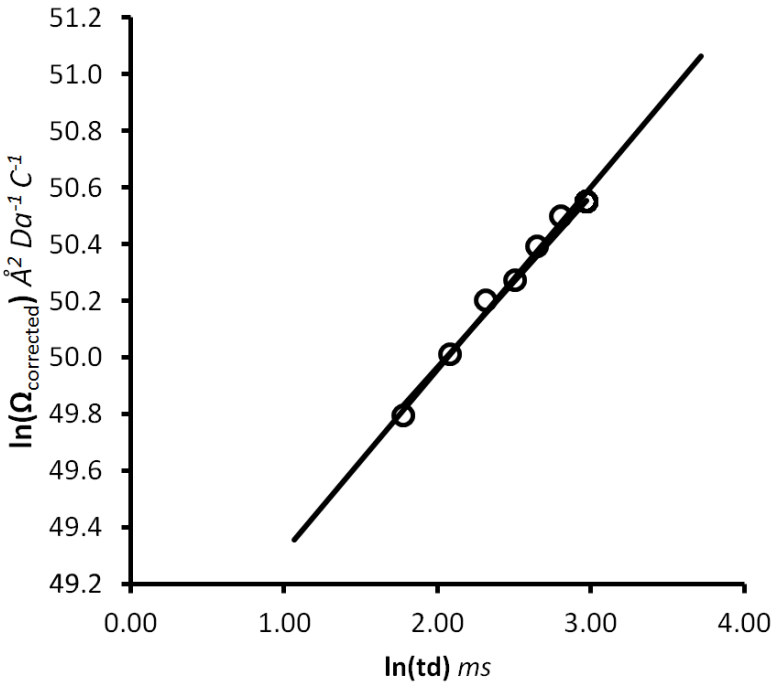


Figure 4-4: Calibration set constructed from corrected drift times and collision cross-sections for PS with nitrogen as the buffer gas.

Collision cross-sections were then calculated using the calibration set and drift times measured. Table 4-5 shows the experimental collision cross-sections. Unlike collision cross-sections calculated using helium, it appears nitrogen does not follow a trend. The drift time of $FeOx^-$ is larger than that of $FeOxCO_2^-$ resulting in a larger collision cross-section. $FeOx^-$ is smaller, so theoretically, it would experience fewer collisions with the buffer gas, arriving at the end of the drift tube earlier. However, it has a larger drift-time and collision cross-section and a plausible explanation is nitrogen, more reactive than helium, is sticking to the complex, making it larger than it really is and thus giving it a higher drift time. By the time the complex reaches the TOF, the nitrogen has evaporated and thus it appears at the correct m/z in the mass spectrum.

Table 4-5: Drift times and experimental collision cross-sections for iron oxalate complexes

Cluster	m/z	Drift Time (ms)	Ω (Å^2)	+/- (Å^2)
$FeOX_2^-$	231.9	1.22	49.3	2.3
$FeOX^- \bullet CO_2$	187.9	1.02	44.4	2.0
$FeOX^-$	143.9	1.09	47.4	2.1
$FeCO_2^-$	99.9	0.83	41.1	1.8

4.3.3 Comparing experimental and theoretical collision cross-sections

Experimental collision cross-sections varied depending on the buffer gas used, helium gave larger collision cross-sections, while nitrogen gave smaller ones. The comparison of theoretical collision cross-section versus helium can be seen in Table 4-6 and versus nitrogen can be seen in Table 4-7.

Table 4-6: Comparison of collision cross-sections (Ω) of experimental results using helium gas and theoretical results for different levels of theory.

Complex	Ω_{He} (Å^2)	Ω_{B3lhp} (Å^2)	Ω_{B3pw91} (Å^2)	Ω_{B98} (Å^2)	$\Omega_{Bhandhlyp}$ (Å^2)	Ω_{M062x} (Å^2)	$\Omega_{Mpw1pw91}$ (Å^2)	$\Omega_{Pbe1pbe}$ (Å^2)
"X" – $FeOx_2^-$	63.3 +/-2.7	77.08 +/- 1.76	77.87 +/- 1.78	77.82 +/- 1.77	78.26 +/- 1.83	81.31 +/- 1.90	78.08 +/- 1.79	77.83 +/- 1.78
% Diff	--	18%	19%	19%	19%	22%	19%	19%
"Y" – $FeOx_2^-$	63.3 +/-2.7	71.99 +/- 1.62	71.50 +/- 1.59	71.79 +/- 1.62	72.92 +/- 1.55	77.91 +/- 1.56	71.47 +/- 1.60	76.02 +/- 1.47
% Diff	--	12%	11%	12%	13%	19%	11%	17%
"X" – $FeOxCO_2^-$	56.9 +/- 2.4	65.95 +/- 1.36	67.88 +/- 1.58	66.05 +/- 1.41	68.22 +/- 1.48	68.44 +/- 1.58	66.02 +/- 1.40	65.96 +/- 1.36
% Diff	--	14%	16%	14%	17%	17%	14%	14%
"Y" – $FeOxCO_2^-$	56.9 +/- 2.4	63.14 +/- 1.36	62.97 +/- 1.39	63.06 +/- 1.37	63.45 +/- 1.42	63.61 +/- 1.50	62.99+/- 1.36	62.98 +/- 1.39
% Diff	--	10%	10%	10%	10%	11%	10%	10%
"X" – $FeOx^-$	52.6 +/- 2.2	53.85 +/- 1.30	53.69 +/- 1.31	53.84	54.20 +/- 1.35	53.09 +/- 1.37	53.70 +/- 1.29	53.89 +/- 1.36
% Diff	--	2%	2%	2%	3%	1%	2%	2%
"Y" – $FeOx^-$	52.6 +/- 2.2	53.04 +/- 1.32	52.22 +/- 1.27	51.03 +/- 1.25	51.05 +/- 1.25	51.16 +/- 1.25	51.01 +/- 1.25	52.61 +/- 1.28
% Diff	--	1%	-1%	-3%	-3%	-3%	-3%	0%
"X" – $FeCO_2^-$	53.0 +/- 2.2	41.39 +/- 1.11	41.26 +/- 1.08	41.34 +/- 1.05	43.33 +/- 1.10	42.22 +/- 1.12	41.40 +/- 1.11	41.39 +/- 1.11
% Diff	--	-28%	-28%	-28%	-22%	-26%	-28%	-28%
"Y" – $FeCO_2^-$	53.0 +/- 2.2	41.39 +/- 1.11	40.00 +/- 1.10	40.00 +/- 1.09	40.21 +/- 1.12	40.30 +/- 1.12	39.95 +/- 1.11	39.93 +/- 1.11
% Diff	--	-28%	-33%	-33%	-32%	-32%	-33%	-33%

Table 4-7: Comparison of collision cross-sections (Ω) of experimental results using nitrogen gas and theoretical results for different levels of theory.

Complex	Ω_{N2} (Å^2)	Ω_{B3lhp} (Å^2)	Ω_{B3pw91} (Å^2)	Ω_{B98} (Å^2)	$\Omega_{Bhandhlyp}$ (Å^2)	Ω_{M062x} (Å^2)	$\Omega_{Mpw1pw91}$ (Å^2)	$\Omega_{Pbe1pbe}$ (Å^2)
"X" – $FeOx_2^-$	49.3 +/- 2.3	77.08 +/- 1.76	77.87 +/- 1.78	77.82 +/- 1.77	78.26 +/- 1.83	81.31 +/- 1.90	78.08 +/- 1.79	77.83 +/- 1.78
% Diff	--	36%	37%	37%	37%	39%	37%	37%
"Y" – $FeOx_2^-$	49.3 +/- 2.3	71.99 +/- 1.62	71.50 +/- 1.59	71.79 +/- 1.62	72.92 +/- 1.55	77.91 +/- 1.56	71.47 +/- 1.60	76.02 +/- 1.47
% Diff	--	32%	31%	31%	32%	37%	31%	35%
"X" – $FeOxCO_2^-$	44.4 +/- 2.0	65.95 +/- 1.36	67.88 +/- 1.58	66.05 +/- 1.41	68.22 +/- 1.48	68.44 +/- 1.58	66.02 +/- 1.40	65.96 +/- 1.36
% Diff	--	33%	35%	33%	35%	35%	33%	33%
"Y" – $FeOxCO_2^-$	44.4 +/- 2.0	63.14 +/- 1.36	62.97 +/- 1.39	63.06 +/- 1.37	63.45 +/- 1.42	63.61 +/- 1.50	62.99+/- 1.36	62.98 +/- 1.39
% Diff	--	30%	29%	30%	30%	30%	30%	30%
"X" – $FeOx^-$	47.4 +/- 2.1	53.85 +/- 1.30	53.69 +/- 1.31	53.84	54.20 +/- 1.35	53.09 +/- 1.37	53.70 +/- 1.29	53.89 +/- 1.36
% Diff	--	12%	12%	12%	13%	11%	12%	12%
"Y" – $FeOx^-$	47.4 +/- 2.1	53.04 +/- 1.32	52.22 +/- 1.27	51.03 +/- 1.25	51.05 +/- 1.25	51.16 +/- 1.25	51.01 +/- 1.25	52.61 +/- 1.28
% Diff	--	11%	9%	7%	7%	7%	7%	10%
"X" – $FeCO_2^-$	41.1 +/- 1.8	41.39 +/- 1.11	41.26 +/- 1.08	41.34 +/- 1.05	43.33 +/- 1.10	42.22 +/- 1.12	41.40 +/- 1.11	41.39 +/- 1.11
% Diff	--	1%	0%	1%	5%	3%	1%	1%
"Y" – $FeCO_2^-$	41.1 +/- 1.8	41.39 +/- 1.11	40.00 +/- 1.10	40.00 +/- 1.09	40.21 +/- 1.12	40.30 +/- 1.12	39.95 +/- 1.11	39.93 +/- 1.11
% Diff	--	1%	-3%	-3%	-2%	-2%	-3%	-3%

Using helium as a buffer gas compared to nitrogen gave different results in collision cross-sections. Helium gave larger experimental collision cross-sections compared to nitrogen. However, it was previously explained that nitrogen could be attaching to the metal complexes giving larger collision cross-sections to some complexes. Even though nitrogen gave overall smaller collision cross-sections, this phenomenon is still possible as separation of ions is not solely based on their size. Different settings of wave height, velocity and amount of buffer gas were needed for helium compared to nitrogen since separation of ions was more difficult using helium.

When comparing theoretical collision cross-sections to experimental ones when using helium as a buffer gas, all levels of theory for $FeOx_2^-$ and $FeOxCO_2^-$ gave collision cross-sections too big compared to experimental, and thus no plausible structures were found. $FeOx^-$ had theoretical values agree within experimental error, however all levels of theory were in agreement and therefore no decision on structure could be made whereas $FeCO_2^-$ had theoretical collision cross-sections too small compared to experimental making it impossible to assign a structure.

Using nitrogen as the buffer gas gave similar to results as helium when it comes to comparing collision cross-sections. The first three iron-oxalate complexes had theoretical collision cross-sections too big relative to experimental to be able to assign a plausible gas-phase structure and $FeCO_2^-$ had all levels of theory within agreement of experimental error making it not possible to assign a structure.

In both cases there was a trend with the percentage difference of collision cross-sections: the smaller the complex, the smaller the percent difference to experimental results. For helium, the complex with collision cross-sections closest to experimental was $FeOx^-$ and $FeCO_2^-$ had smaller values, whereas with nitrogen, $FeCO_2^-$ had the best agreeing results. Theoretical collision cross-sections decreased roughly by $10Å^2$ when losing CO_2, whereas with experimental collision cross-sections, the decrease in $Å^2$ was less

significant. Since helium had larger collision cross-sections than nitrogen, it makes sense the best agreeing complex was $FeOx^-$ whereas for nitrogen it was $FeCO_2^-$.

The large difference in errors in collision cross-sections can be accounted for. The PS calibrant, the smallest available for the negative mode of ion mobility, is too big compared to the metal oxalate clusters to give reliable results. The calibration set looks linear and at a first glance it looks like the calibrant should give reliable results. Figure 4-5 shows the iron oxalate complexes lining up nicely compared to the calibration set.

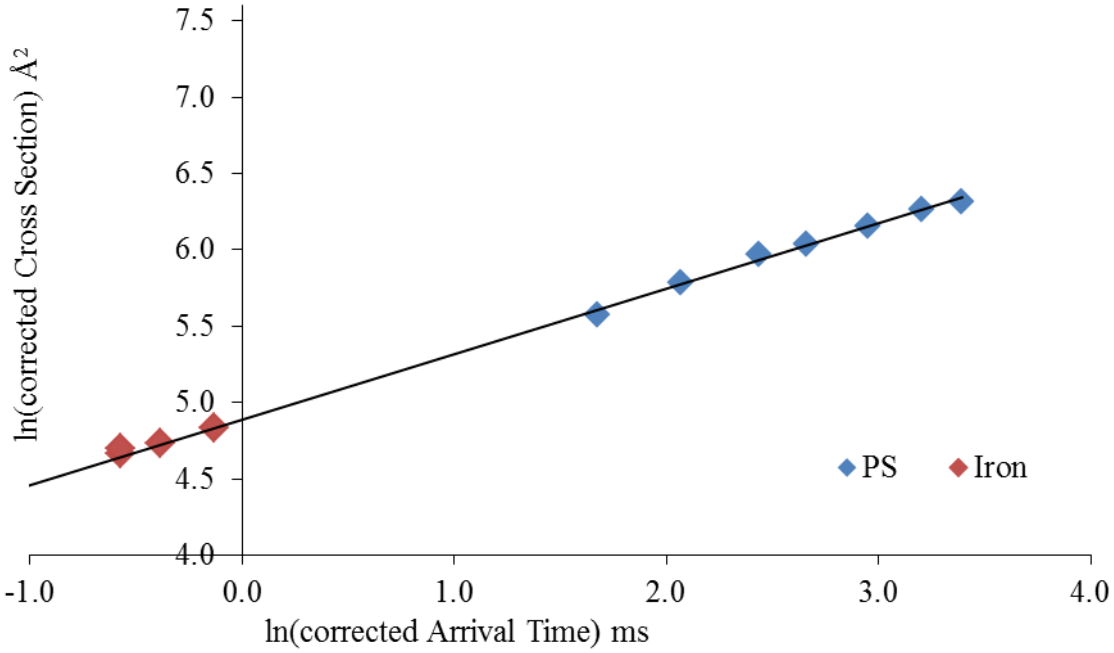


Figure 4-5: Calibration set with iron oxalate complexes. (Helium is the buffer gas).

However to achieve linearity, natural logarithms of corrected collision cross-sections and drift times were taken. When the natural logarithms are removed from the calibration set, it is evident there is a curve and PS is too large of a calibrant to be used with the small iron-oxalate clusters. Figure 4-6 shows the calibration set and iron oxalate clusters with the natural logarithms removed where the iron species

are too far from the line of best fit of the calibrant. Therefore PS is a poor choice for a calibrant for the iron-oxalate species. Unfortunately it is the smallest calibrant available for the negative mode and until there is a smaller available calibrant, reliable collision cross-sections of metal-oxalate species cannot be found. To demonstrate iron-oxalate clusters are not an anomaly, collision cross-sections of the other metal oxalate clusters will briefly be analyzed to show collision cross-sections of metal-oxalate clusters cannot be determined with accuracy.

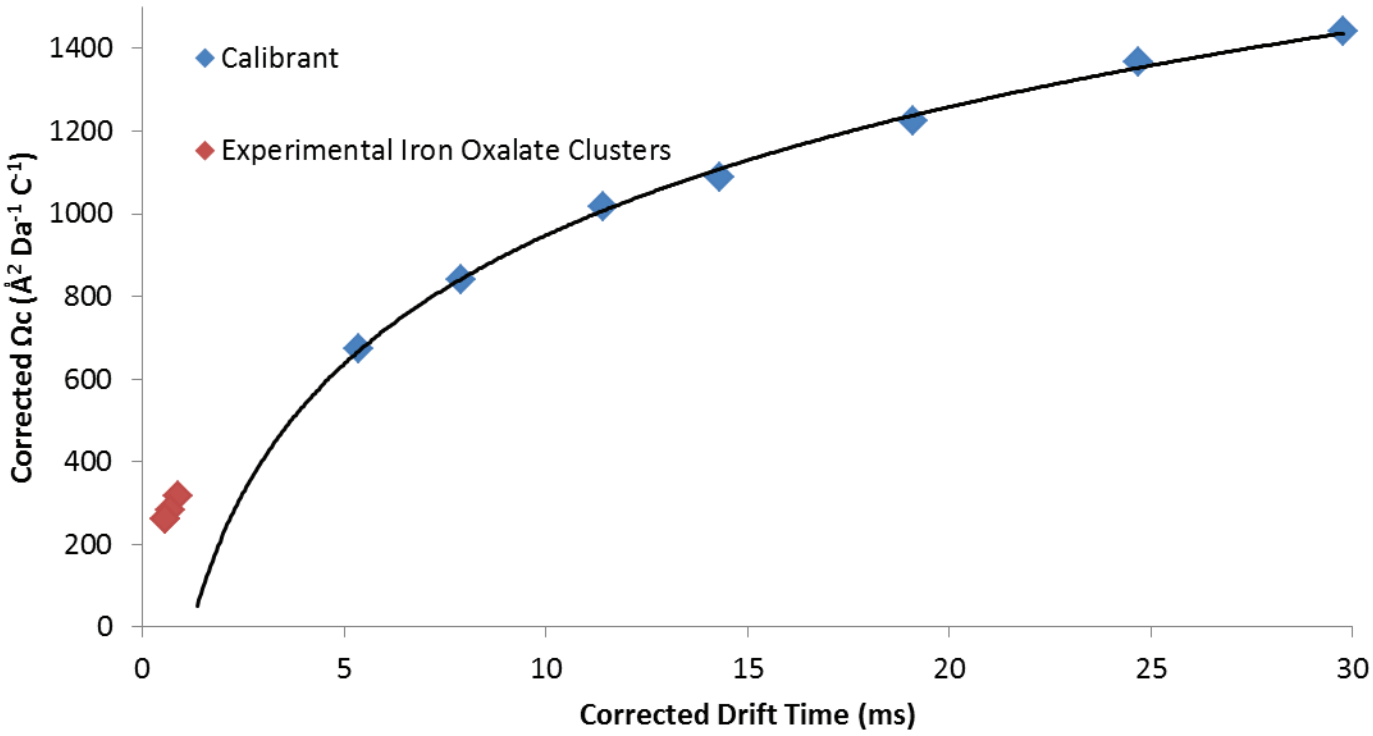


Figure 4-6: Calibration set and iron oxalate complexes with natural logarithms removed. (Helium is the buffer gas).

4.4 Silver-Oxalate Complexes

Silver acetate and oxalic acid, both purchased from Sigma Aldrich, were used to determine collision cross-sections of $AgOx_2H_2^-$ and $AgOx^-$. Both species were singly charged with silver having a +1 oxidation state. Before drift-times were determined, a CID experiment was performed to confirm the identities of the silver-oxalate species. Silver has two dominant isotopes, 107 and 109. Figure 4-7 shows the CID spectrum of silver-oxalate species with the 107 isotope. (CID spectra of the 109 isotope and for mass selections of $AgOx^-$ can be seen in the appendix). Both silver-species of interest and the atomic silver anion are shown, confirming their identities and therefore collision cross-sections can be determined based on their measured mobility times.

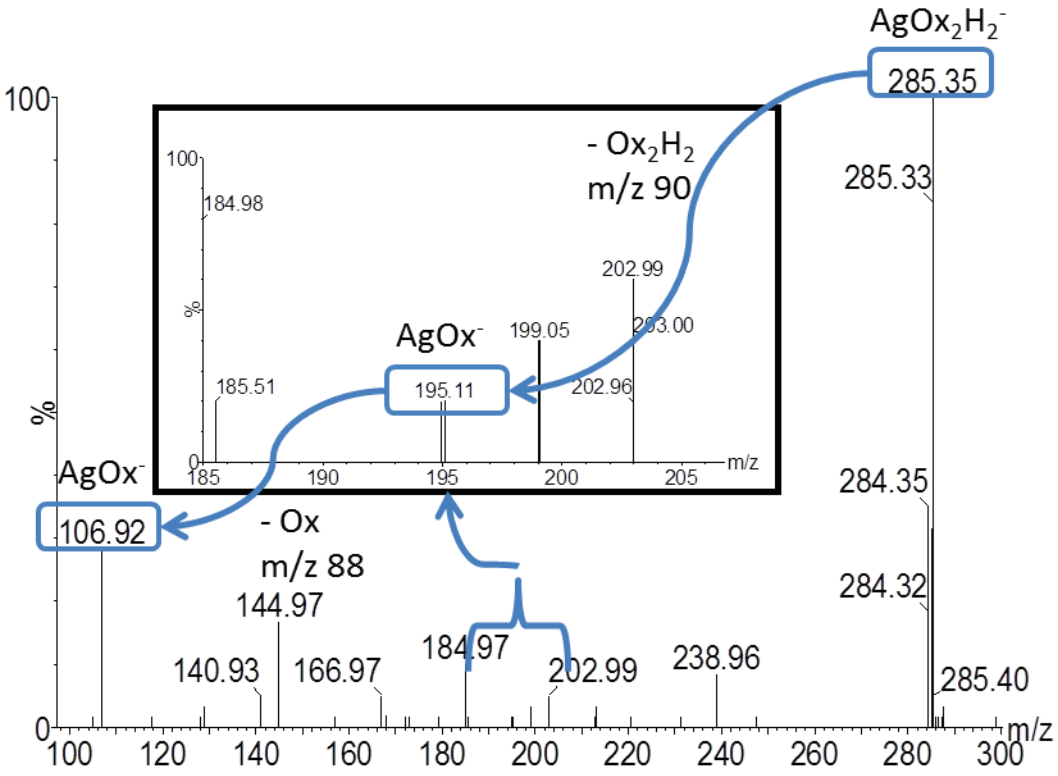


Figure 4-7: CID spectrum for silver oxalate.

4.4.1 Nitrogen as the buffer gas for IMS collision cross-section determination

The calibration set was constructed using drift-times and literature collision cross-sections for PS with values shown in Table 4-8. After corrections were made for mass and charge effects, the natural logarithms were plotted and the constructed set can be seen in Figure 4-8.

Table 4-8: The drift times and collision cross-sections for polystyrene, used to build the calibration set [4]

Oligomer	m/z	Drift Time (ms)	Lit Ω (Å^2)
3	401.22	5.57	132
4	505.29	7.87	163
5	609.36	9.73	196
6	713.46	11.52	210
7	817.54	13.73	236
8	921.63	15.77	262
9	1025.73	18.14	276

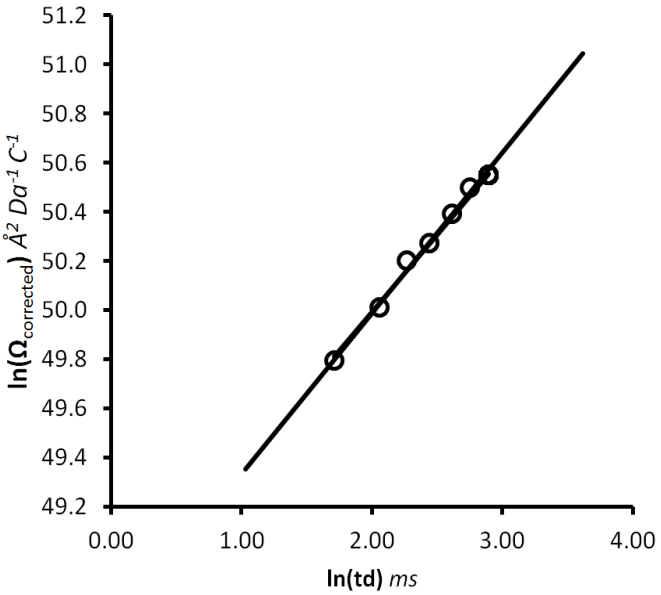


Figure 4-8: Calibration set constructed from corrected drift times and cross-sections for PS

Collision cross-sections of silver-oxalate complexes were then calculated using the calibration set and their drift times with experimental collision cross-sections shown in Table 4-9. Each silver complex had their collision cross-sections calculated twice, based on which isotope was present for silver. However, the different isotopes did not have an effect on collision-cross section as they yielded the same result. In the case of silver-oxalate, it is not possible to determine if nitrogen was attaching itself to the complexes in the ion mobility cell as there were only two complexes with collision cross-sections calculated, compared to the four different iron-oxalates.

Table 4-9: Drift times and experimental collision cross-sections for silver oxalate complexes.

Cluster	m/z	Drift Time (ms)	Ω (Å^2)	+/- (Å^2)
$AgOx_2H_2^-$	286.97	2.37	76.8	3.3
$AgOx_2H_2^-$	284.94	2.37	76.8	2.6
$AgOx^-$	196.90	1.47	57.2	1.9
$AgOx^-$	195.06	1.47	57.2	1.9

4.4.2 Comparing experimental and theoretical collision cross-sections

Silver-oxalate clusters only had their experimental collision cross-sections calculated only using nitrogen as the buffer gas. The comparison between experimental and theoretical results can be seen in Table 4-10. The same observations are made for silver-oxalate clusters as they were for iron-oxalate clusters. The smaller the complex, the smaller the percent difference is compared to theoretical results. $AgOx_2H_2^-$ had theoretical collision cross-sections agreeing with experimental, however they were all within experimental error and therefore no plausible structure could be found, whereas with $AgOx^-$, all theoretical structures had collision cross-sections too small compared to experimental and thus no plausible structure could be found.

Table 4-10: Comparison of collision cross-sections (Ω) of experimental results using nitrogen gas and theoretical results for different levels of theory.

Complex	Ω_{N2} (Å^2)	Ω_{B3lhp} (Å^2)	Ω_{B3pw91} (Å^2)	Ω_{B98} (Å^2)	$\Omega_{Bhandhlyp}$ (Å^2)	Ω_{M062x} (Å^2)	$\Omega_{Mpw1pw91}$ (Å^2)	$\Omega_{Pbe1pbe}$ (Å^2)
"X" – $AgOx_2H_2^-$	76.80 +/- 2.6	79.94 +/- 1.68	79.71 +/- 1.67	76.64 +/- 1.59	79.42 +/- 1.66	79.82 +/- 1.63	79.55 +/- 1.66	79.55 +/-1.66
% Diff	--	4%	4%	0%	3%	4%	3%	3%
"Y" – $AgOx_2H_2^-$	76.80 +/- 2.6	76.52 +/- 1.61	77.53 +/- 1.72	76.61 +/- 1.61	77.29 +/- 1.57	75.44 +/- 1.59	76.14 +/- 1.60	77.39 +/- 1.59
% Diff	--	0%	1%	0%	1%	-2%	-1%	1%
"X" – $AgOx^-$	57.2 +/- 1.90	52.46 +/- 1.38	52.18 +/- 1.49	52.30 +/- 1.50	52.40 +/- 1.49	52.60 +/- 1.49	52.18 +/- 1.46	52.14 +/- 1.50
% Diff	--	-9%	-10%	-9%	-9%	-9%	-10%	-10%
"Y" – $AgOx^-$	57.2 +/- 1.90	50.38 +/- 1.33	52.18 +/- 1.49	50.14 +/- 1.30	50.38 +/- 1.34	50.33 +/- 1.43	50.29 +/- 1.33	50.09 +/- 1.41
% Diff	--	-14%	-10%	-14%	-14%	-14%	-14%	-14%

4.5 Potassium-Oxalate Complexes

Potassium oxalate hydrate was purchased from Sigma-Aldrich and was used to determine collision cross-sections of $KOx_2H_2^-$ and KOx^-. Both complexes are singly charged species with potassium have a +1 oxidation state. To confirm $KOx_2H_2^-$ and KOx^- are present in the gas phase, CID experiments must be performed. Figure 4-9 shows a CID spectrum of potassium oxalate monohydrate where m/z 217 was mass selected. The loss of OxH_2 is present (m/z 90) confirming the chemical identity of the potassium species and therefore collision cross-sections can be calculated based on their mobility times.

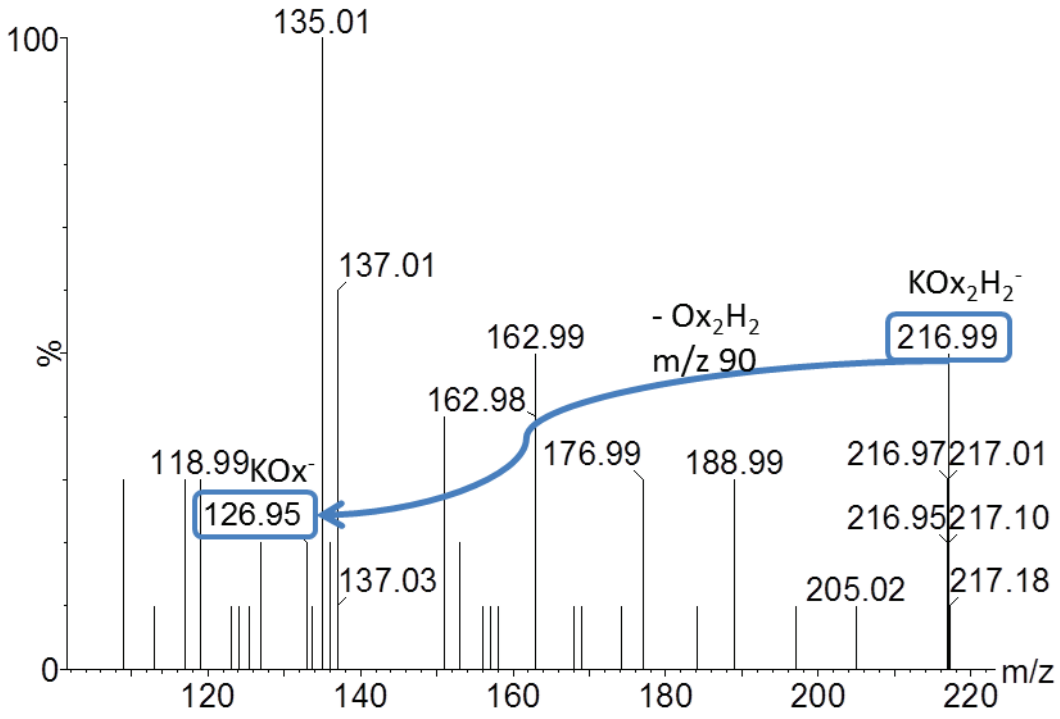


Figure 4-9: CID spectrum for potassium oxalate.

4.5.1 Nitrogen as the buffer gas for IMS for collision cross-section determination

For potassium oxalate species, collision cross-sections were determined using nitrogen. The calibration set was built using drift times and literature collision cross-section values for PS with its values shown in

Table 4-11. After mass and charge effect corrections were made, the natural logarithms were plotted and the constructed calibration set can be seen in Figure 4-10.

Table 4-11: The drift-times and cross-sections for polystyrene, used to build the calibration set.[4]

Oligomer	m/z	Drift Time (ms)	Lit Ω (Å^2)
3	401.18	5.63	132
4	505.24	7.81	163
5	609.32	10.11	196
6	713.41	11.52	210
7	817.47	13.79	236
8	921.52	16.09	262
9	1025.61	18.97	276

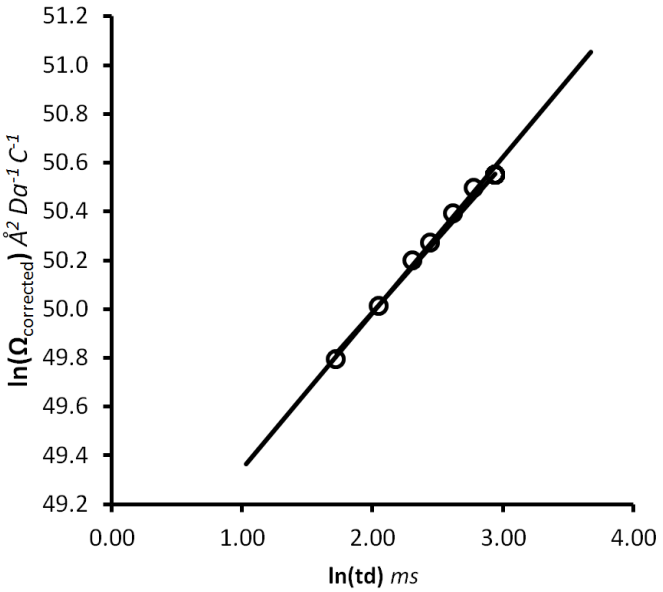


Figure 4-10: Calibration set constructed from corrected drift-times and cross-sections for PS

Experimental collision cross-sections of potassium oxalate complexes were then calculated using this calibration set and the drift times measured. The collision cross-sections are shown in Table 4-12. Like in the case of the silver oxalate species, it is not possible to determine if nitrogen is attaching itself to the complexes since only two complexes had their collision cross-sections calculated.

Table 4-12: Drift times and experimental collision cross-sections for potassium oxalate complexes.

Cluster	m/z	Drift Time (ms)	Ω (Å^2)	+/- (Å^2)
$KOx_2H_2^-$	216.97	2.05	71.8	3.3
KOx^-	126.88	0.77	36.6	1.3

4.5.2 Comparing experimental and theoretical collision cross-sections

Experimental collision cross-sections versus theoretical can be seen in Table 4-13. For both complexes, no plausible structure can be determined based on comparison of collision cross-sections. In the case of metals previously discussed, the smaller the complex, the smaller the percent difference between theoretical and experimental results. In the case of potassium, the opposite is true as KOx^- has theoretical collision cross-sections much larger than experimental compared to the percent difference of collision cross-sections of $KOx_2H_2^-$. This difference is most likely caused by errors in experimental collision cross-section calculations due to using an inappropriate calibrant. The similarity between potassium and other metal oxalate species is it is impossible to determine a plausible structure using collision cross-sections.

Table 4-13: Comparison of collision cross-sections (Ω) of experimental results using nitrogen gas and theoretical results for different levels of theory.

Complex	Ω_{N2} (Å^2)	Ω_{B3lhp} (Å^2)	Ω_{B3pw91} (Å^2)	Ω_{B98} (Å^2)	$\Omega_{Bhandhlyp}$ (Å^2)	Ω_{M062x} (Å^2)	$\Omega_{Mpw1pw91}$ (Å^2)	$\Omega_{Pbe1pbe}$ (Å^2)
"X" – $KOx_2H_2^-$	71.8 +/- 3.3	85.08 +/- 1.87	85.99 +/- 1.87	86.30 +/- 2.06	84.69 +/- 1.83	85.47 +/- 2.03	79.59 +/- 1.51	81.95 +/- 1.64
% Diff	--	16%	17%	17%	15%	16%	10%	12%
"Y" – $KOx_2H_2^-$	71.8 +/- 3.3	79.95 +/- 1.48	83.18 +/- 1.86	83.14 +/- 1.80	82.41 +/- 1.88	80.95 +/- 1.59	79.72 +/- 1.56	82.80 +/- 1.87
% Diff	--	10%	14%	14%	13%	11%	10%	13%
"X" – KOx^-	36.6 +/- 1.3	58.93 +/- 1.38	58.84 +/- 1.38	58.97 +/- 1.39	58.73 +/- 1.39	58.68 +/- 1.38	58.78 +/- 1.38	58.73 +/- 1.42
% Diff	--	38%	38%	38%	38%	38%	38%	38%
"Y" – KOx^-	36.3 +/- 1.3	60.58 +/- 1.47	60.48 +/- 1.35	60.59 +/- 1.35	60.46 +/- 1.36	58.63 +/- 1.41	60.44 +/- 1.35	60.45 +/- 1.35
% Diff	--	40%	39%	40%	39%	38%	39%	39%

4.6 Cesium-Oxalate Complexes

Cesium hydroxide monohydrate and oxalic acid were purchased from Sigma-Aldrich and used to determine collision cross-sections of $CsOx_2H_2^-$ and $CsOx^-$. Both complexes are singly charged species with cesium having a +1 oxidation state. To confirm the identity of the cesium complexes, CID experiments were performed. The CID spectrum where m/z 311 ($CsOx_2H_2^-$) is mass selected is shown in Figure 4-11. The cesium-oxalate species was very stable and only a peak at m/z of 133 appeared (the mass of the atomic metal anion). Performing a CID experiment for m/z of 133 proved it is in fact cesium as no dissociation occurred therefore confirming m/z 311 is $CsOx_2H_2^-$. To confirm the identity of $CsOx^-$, a CID experiment was performed and m/z 221 was mass selected as shown in Figure 4-12. A peak at m/z 133 was observed corresponding to Cs^-, providing evidence the peak at m/z 221 is $CsOx^-$. Therefore experimental collision cross-sections can be determined.

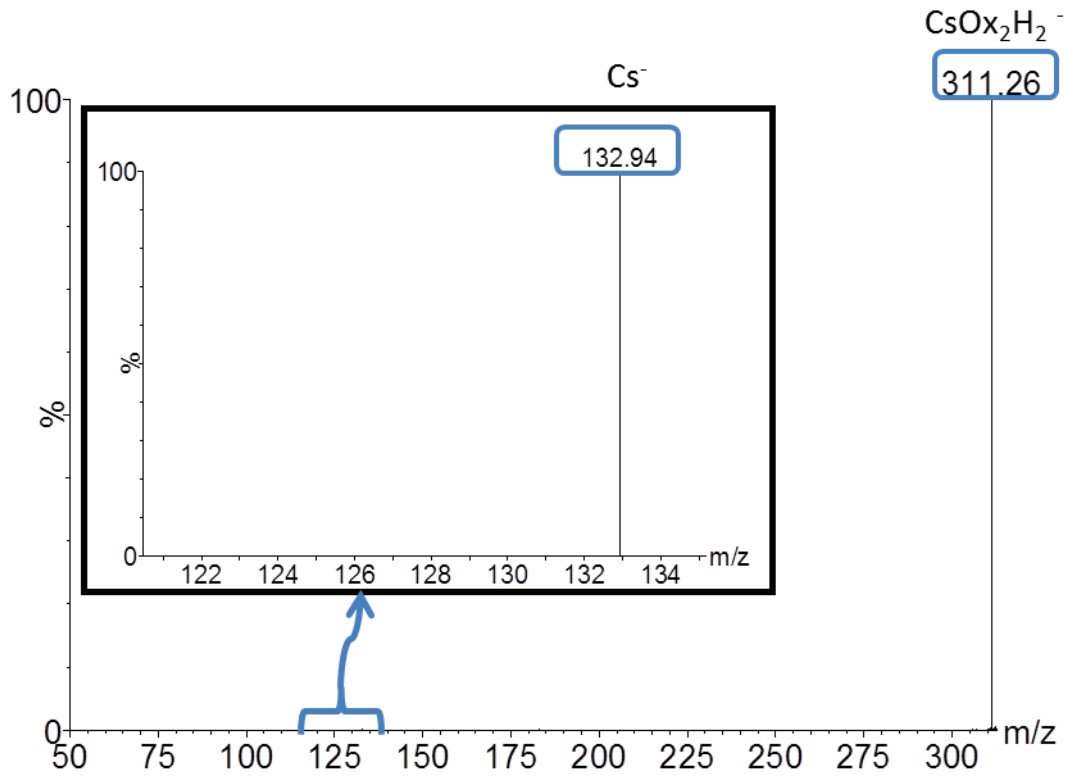


Figure 4-11: CID spectrum for $CsOx_2H_2^-$.

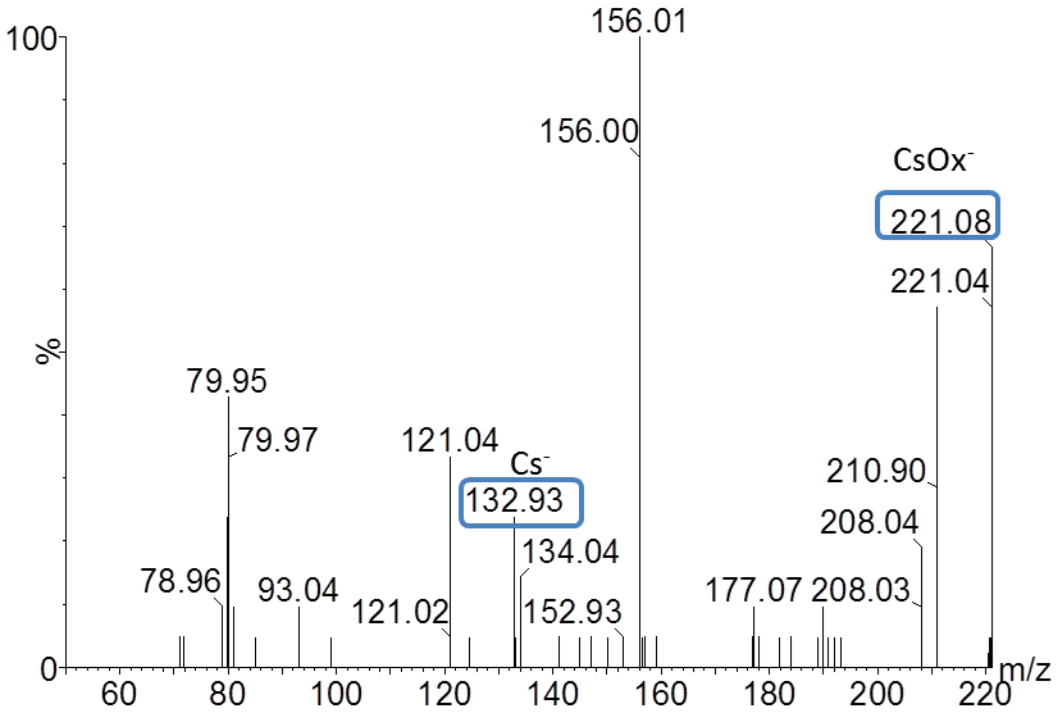


Figure 4-12: CID spectrum for $CsOx^-$.

4.6.1 Nitrogen as the buffer gas for IMS for collision cross-section determination

The calibration set needed to determine collision cross-sections for cesium-oxalate complexes was constructed using drift times and literature cross-sections of PS, shown in Table 4-14. After corrections were made for mass and charge effects, the natural logarithms were plotted and the constructed calibration set can be seen in Figure 4-12.

Table 4-14: The drift times and cross-sections for polystyrene, used to build the calibration set [4]

Oligomer	m/z	Drift Time (ms)	Lit Ω ($Å^2$)
3	401.32	5.63	132
4	505.42	7.74	163
5	609.55	9.98	196
6	713.71	11.65	210
7	817.77	13.79	236
8	921.87	16.22	262
9	1026.03	19.04	276

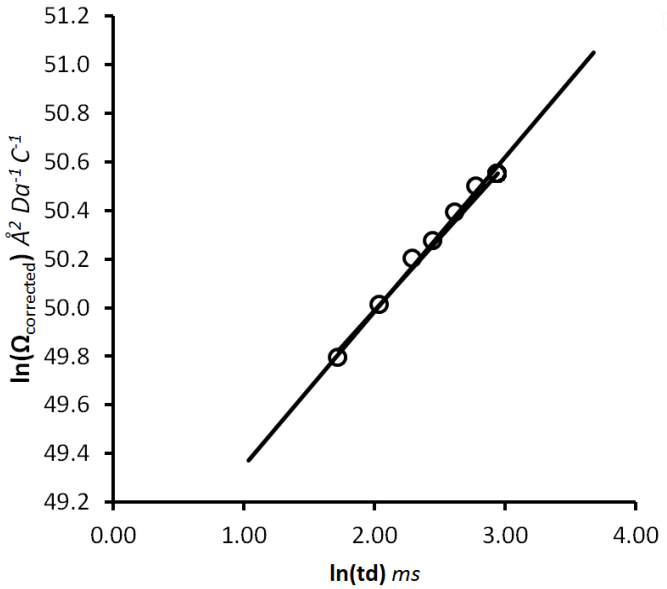


Figure 4-13: Calibration set constructed from correct drift times and cross-sections for PS

Collision cross-sections of cesium oxalate were then calculated using the calibration set and drift times measured. The experimental collision cross-sections are shown in Table 4-15

Table 4-15: Drift times and experimental collision cross-sections for cesium oxalate complexes

Cluster	m/z	Drift Time (ms)	Ω (Å^2)	+/- (Å^2)
$CsOx_2H_2^-$	310.91	2.30	76.6	3.8
$CsOx^-$	220.95	1.98	70.8	2.5

4.6.2 Comparing experimental and theoretical collision cross-sections

The comparison of theoretical collision cross-sections versus experimental collision cross-sections using nitrogen as the buffer gas can be seen in Table 4-16. $CsOx_2H_2^-$ had theoretical collision cross-sections much larger than experimental and $CsOx^-$ had the theoretical values agreeing well with the experimental collision cross-section. However, all structures, with the exception of the "X" structure of B3lyp agreed well with experimental results, and thus no plausible structure can be determined.

Table 4-16: Comparison of collision cross-sections (Ω) of experimental results using nitrogen gas and theoretical results for different levels of theory.

Complex	Ω_{N2} (Å^2)	Ω_{B3lhp} (Å^2)	Ω_{B3pw91} (Å^2)	Ω_{B98} (Å^2)	$\Omega_{Bhandhlyp}$ (Å^2)	Ω_{M062x} (Å^2)	$\Omega_{Mpw1pw91}$ (Å^2)	$\Omega_{Pbe1pbe}$ (Å^2)
"X" – $CsOx_2H_2^-$	76.6 +/- 3.8	92.17 +/- 1.57	92.62 +/- 1.87	91.92 +/- 1.85	93.20 +/- 1.74	94.70 +/- 2.03	89.20 +/- 1.70	89.13 +/- 1.70
% Diff	--	17%	17%	17%	18%	19%	14%	14%
"Y" – $CsOx_2H_2^-$	76.6 +/- 3.8	90.10 +/- 1.78	89.98 +/- 1.81	91.92 +/- 1.81	87.06 +/- 1.80	88.85 +/- 1.80	89.42 +/- 1.76	89.18 +/- 1.68
% Diff	--	15%	15%	17%	12%	14%	14%	14%
"X" – $CsOx^-$	70.8 +/- 2.5	75.70 +/- 1.82	69.93 +/- 1.74	70.00 +/- 1.74	69.88 +/- 1.74	69.88 +/- 1.71	69.84 +/- 1.74	69.82 +/- 1.74
% Diff	--	6%	-1%	-1%	-1%	-1%	-1%	-1%
"Y" – $CsOx^-$	70.8 +/- 2.5	72.51 +/- 1.75	69.93 +/- 1.74	70.08 +/- 1.71	69.97 +/- 1.71	69.88 +/- 1.71	72.47 +/- 1.75	72.45 +/- 1.75
% Diff	--	2%	-1%	-1%	-1%	-1%	2%	2%

4.7 Collision cross-section conclusions

Experimental collision cross-sections were determined for different metal-oxalate species using nitrogen (all metals) and helium (iron-oxalate clusters) as the buffer gases and compared to theoretical collision cross-sections. When using nitrogen gas, it is possible nitrogen is attaching itself to the complexes, resulting in larger collision cross-sections, but evaporating before hitting the TOF. Whereas, with helium there is no evidence this occurs. Iron-oxalate complexes were the only metal species calculated using helium due to instrument malfunction for the last three months of the project. Regardless, it was not possible to determine plausible gas-phase structures using collision cross-sections. To further prove this is the case, a last attempt at using collision cross-sections is shown in Table 4-17. The theoretical collision cross-sections were calculated for the plausible gas-phase structures determined by IRMPD. These collision cross-sections are very similar to ones previously calculated and therefore no distinction can be made.

Determining plausible gas phase structures for metal-oxalate clusters is not possible using collision cross-sections due to unsuitable calibrants. Polystyrene is the smallest available calibrant for the negative mode of ion mobility, but unfortunately is too large to use for the small metal-oxalate clusters. Until a new calibrant is made available for the smaller range of the negative mode, collision cross-sections are an inappropriate tool for determining structural conformations.

Table 4-17: Comparison of collision cross-sections (Ω) of experimental results and theoretical results for the IRMPD determined plausible structures.

Ω (Å^2)	$FeOx_2^-$	$FeOxCO_2^-$	$FeOx^-$	$AgOx_2H_2^-$	$AgOx^-$	$KOx_2H_2^-$	KOx^-	$CsOx_2H_2^-$	$CsOx^-$
Theor.	71.71 +/- 1.57	63.01 +/- 1.44	51.01 +/- 1.28	82.42 +/- 1.78	50.38 +/- 1.34	84.18 +/- 2.01	60.44 +/- 1.35	92.97 +/- 2.20	72.51 +/- 1.65
He	63.3 +/- 2.70	56.9 +/- 2.4	52.6 +/- 2.2	--	--	--	--	--	--
% Diff	**11%**	**10%**	**-3%**	**--**	**--**	**--**	**--**	**--**	**--**
N_2	49.3 +/- 2.3	44.4 +/- 2.0	47.4 +/- 2.1	76.8 +/- 2.6	57.2 +/- 1.9	71.8 +/- 3.3	36.6 +/- 1.3	76.6 +/- 3.8	70.8 +/- 2.5
% Diff	**31%**	**30%**	**7%**	**9%**	**-14%**	**15%**	**39%**	**18%**	**2%**

4.8 References

1. (a) G. von Helden, M. T. Hsu, N. Gotts, M. T. Bowers, Carbon cluster cations with up to 84 atoms: structures, formation mechanism, and reactivity. *The Journal of Physical Chemistry* 1993, *97*. 8182-8192, DOI: 10.1021/j100133a011; (b) T. Wyttenbach, G. von Helden, J. Batka, D. Carlat, M. Bowers, Effect of the long-range potential on ion mobility measurements. *J Am Soc Mass Spectrom* 1997, *8*. 275-282, DOI: 10.1016/s1044-0305(96)00236-x; (c) A. A. Shvartsburg, M. F. Jarrold, An exact hard-spheres scattering model for the mobilities of polyatomic ions. *Chemical Physics Letters* 1996, *261*. 86-91, DOI: http://dx.doi.org/10.1016/0009-2614(96)00941-4.
2. K. Zhang, D. M. Zimmerman, A. Chung-Phillips, C. J. Cassady, Experimental and ab initio studies of the gas-phase basicities of polyglycines. *Journal of the American Chemical Society* 1993, *115*. 10812-10822, DOI: 10.1021/ja00076a044.
3. (a) A. A. Shvartsburg, *Differential ion mobility spectrometry : nonlinear ion transport and fundamentals of FAIMS*. Boca Raton : CRC Press, c2009.: Boca Raton, 2009; (b) T. Wyttenbach, J. E. Bushnell, M. T. Bowers, Salt Bridge Structures in the Absence of Solvent? The Case for the Oligoglycines. *Journal of the American Chemical Society* 1998, *120*. 5098-5103, DOI: 10.1021/ja9801238.
4. J. V. Hamilton, J. B. Renaud, P. M. Mayer, Experiment and theory combine to produce a practical negative ion calibration set for collision cross-section determinations by travelling-wave ion-mobility mass spectrometry. *Rapid Communications in Mass Spectrometry* 2012, *26*. 1591-1595, DOI: 10.1002/rcm.6266.
5. M. J. Frisch, G. W. Trucks, H. B. Schlegel, G. E. Scuseria, M. A. Robb, J. R. Cheeseman, G. Scalmani, V. Barone, B. Mennucci, G. A. Petersson, H. Nakatsuji, M. Caricato, X. Li, H. P. Hratchian, A. F. Izmaylov, J. Bloino, G. Zheng, J. L. Sonnenberg, M. Hada, M. Ehara, K. Toyota, R. Fukuda, J. Hasegawa, M. Ishida, T. Nakajima, Y. Honda, O. Kitao, H. Nakai, T. Vreven, J. A. Montgomery Jr., J. E. Peralta, F. Ogliaro, M. J. Bearpark, J. Heyd, E. N. Brothers, K. N. Kudin, V. N. Staroverov, R. Kobayashi, J. Normand, K. Raghavachari, A. P. Rendell, J. C. Burant, S. S. Iyengar, J. Tomasi, M. Cossi, N. Rega, N. J. Millam, M. Klene, J. E. Knox, J. B. Cross, V. Bakken, C. Adamo, J. Jaramillo, R. Gomperts, R. E. Stratmann, O. Yazyev, A. J. Austin, R. Cammi, C. Pomelli, J. W. Ochterski, R. L. Martin, K. Morokuma, V. G. Zakrzewski, G. A. Voth, P. Salvador, J. J. Dannenberg, S. Dapprich, A. D. Daniels, Ö. Farkas, J. B. Foresman, J. V. Ortiz, J. Cioslowski, D. J. Fox. Gaussian, Inc.: Wallingford, CT, USA, 2013.
6. P. Weis, O. Welz, E. Vollmer, M. M. Kappes, Structures of mixed gold-silver cluster cations (AgmAun+,m+n<6): Ion mobility measurements and density-functional calculations. *The Journal of Chemical Physics* 2004, *120*. 677-684, DOI: doi:http://dx.doi.org/10.1063/1.1630568.
7. L. A. Viehland, Interaction potentials for the alkali ion—rare-gas systems. *Chemical Physics* 1984, *85*. 291-305, DOI: http://dx.doi.org/10.1016/0301-0104(84)85040-5.

5 CONCLUSIONS

It is possible to generate bare metal anions with metal-oxalate complexes in the gas phase with the use of mass spectrometry. These atomic metal anions are then able to undergo reactions with other species. Different properties of the metal-oxalate complexes are currently being studied in the Mayer lab and in order to get a complete picture, an attempt at structure determination was made. To determine plausible structures, two different experimental methods were compared to optimized computed structures for $KOx_2H_2^-$, KOx^-, $CsOx_2H_2^-$, $CsOx^-$, $FeOx_2^-$, $FeOxCO_2^-$, $FeOx^-$, $AgOx_2H_2^-$, and $AgOx^-$.

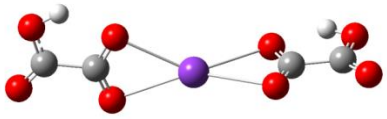
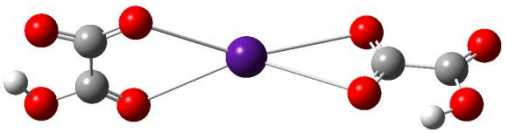
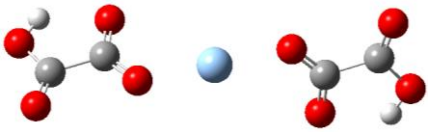
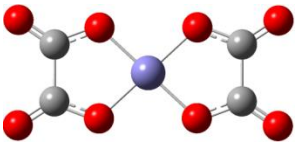
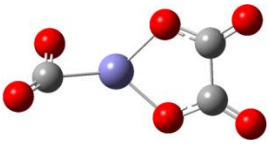
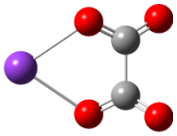
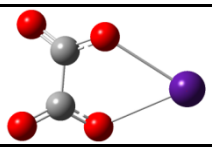
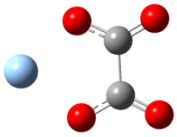
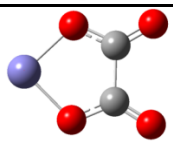
Theoretical structures had optimization and frequencies calculations performed for different levels of theory (B3lyp, B3pw91, B98, Bhandhlyp, M062x, Mpw1pw91, Pbe1pbe and MP2). To begin the process of structural exploration, each level of theory had two different starting structures, an "X" structure where the ligands were on the same plane as the metal, and a "Y" structure where the ligands were above and below the plane of the metal. After optimization, different low energy structures resulted from different levels of theory. To determine which of the low energy structures were plausible, they were compared to experimental results.

IRMPD experiments were performed at the CLIO facility in France and the frequencies were compared to theoretical frequencies. For the $M\text{-}Ox_2H_2^-$ complexes, the optimized structures resulting from the "X" and "Y" structures only gave an idea of which level of theory was appropriate. These complexes were the most difficult to find a plausible structure due to the effect hydrogen bonding has on structure. After many attempts, plausible structures were found. The $M\text{-}Ox^-$ complexes were the easiest to find due to the limited positions the single oxalate and metal can have and the iron complexes, $FeOx_2^-$ and $FeOxCO_2^-$ were more difficult to determine plausible structures than the $M\text{-}Ox^-$ complexes and easier than the $M\text{-}Ox_2H_2^-$ complexes. Before structure determination, it was unknown which level of theory would give plausible structures. However, after plausible structures have been found (Table 5-1), different levels of

theory were more appropriate for the different basis-sets used. For the 6-311+gd basis set, the M series of DFT gave plausible structures and for the lanl2dz, Bhandhlyp was a good level of theory to determine plausible structures.

Experimental collision cross-sections were calculated using drift times determined from ion mobility with the help of the calibrant, PS. Theoretical collision cross-sections were calculated for the optimized "X" and "Y" structures for the levels of theory previously mentioned using the Mobcal program. For all metal-oxalate complexes, no plausible structures were determined using this method. The calibrant used (the smallest available for the negative mode of ion mobility) was too large for the small metal-oxalate complexes resulting in collision-cross sections not agreeing with theoretical. In the cases were complexes did have experimental results agreeing, all complexes were within the same margin of error and thus no decision could be made. Until there is a smaller calibrant made available, collision cross-sections are an inappropriate method to determine plausible structures for metal oxalate complexes.

Table 5-1: Plausible structures of all metal-oxalate complexes

Complex	Level of Theory	Basis-set	Plausible Structure
$KOx_2H_2^-$	M062x	6-311+gd	
$CsOx_2H_2^-$	Bhandhlyp	Lanl2dz	
$AgOx_2H_2^-$	Bhandhlyp	Lanl2dz	
$FeOx_2^-$	Mpw1pw91	6-311+gd	
$FeOxCO_2^-$	M062x	6-311+gd	
KOx^-	Mpw1pw91	6-311+gd	
$CsOx^-$	Bhandhlyp	Lanl2dz	
$AgOx^-$	Bhandhlyp	Lanl2dz	
$FeOx^-$	Mpw1pw91	6-311+gd	

6 CLAIM TO ORIGINAL RESEARCH

1) Theory was evaluated using IRMPD
2) Determined plausible gas-phase structures for anionic metal-oxalate complexes
3) Deduced which level of theories are suitable to study anionic metal-oxalate complexes
4) Deemed collision cross-sections an insufficient method to determine plausible structures using available calibrants

7 APPENDIX

7.1 Optimized “X” and “Y” structures for all levels of theory

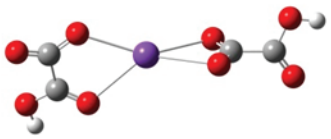
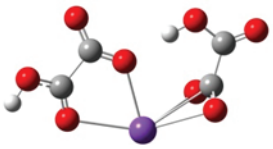
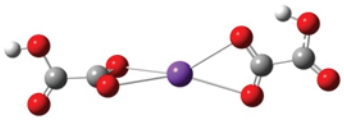
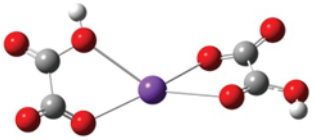
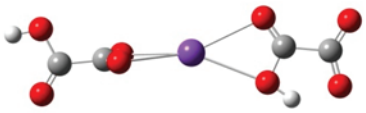
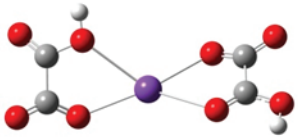
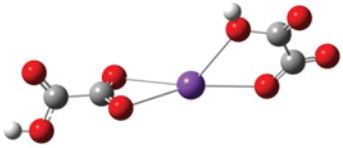
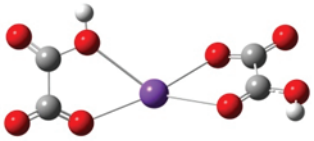
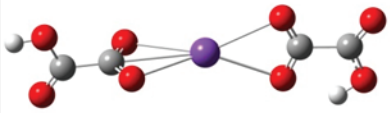
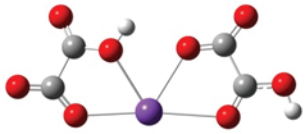
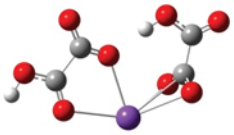
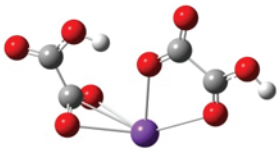
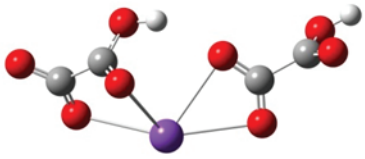
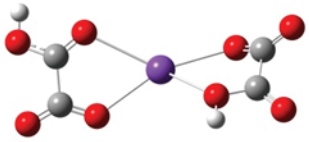
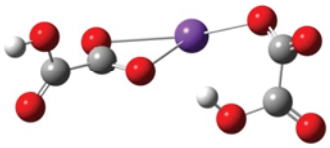
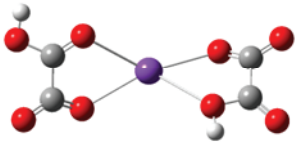
Level of Theory	"X" Structure	"Y" Structure
B3lyp		
B3pw91		
B98		
Bhandhlyp		
M062x		
Mpw1pw91		
Pbe1pbe		
MP2		

Figure 7-1: Optimized structures for $KOx_2H_2^-$.

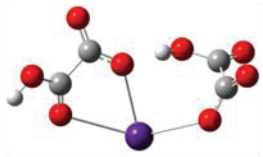
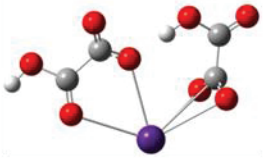
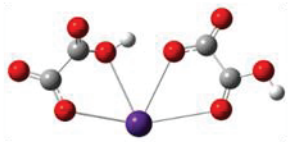
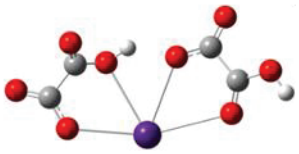
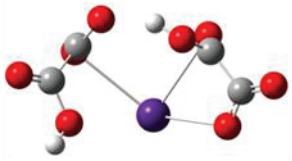
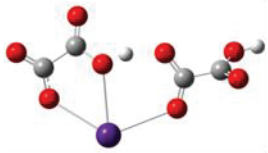
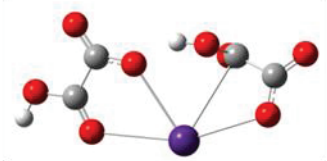
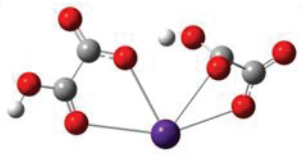
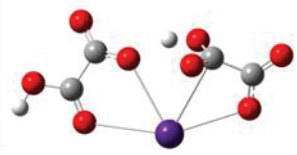
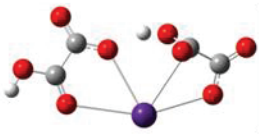
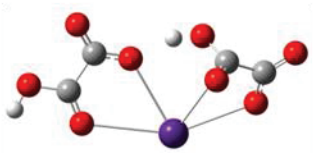
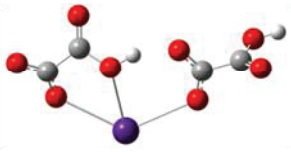
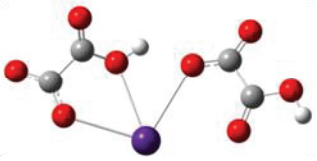
Level of Theory	"X" Structure	"Y" Structure
B3lyp		
B3pw91		
B98		
Bhandhlyp		
M062x		
Mpw1pw91		
Pbe1pbe		
MP2		

Figure 7-2: Optimized structures for $CsOx_2H_2^-$.

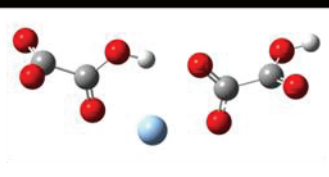
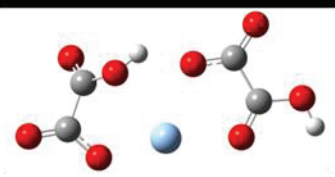
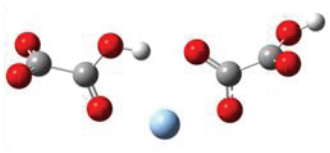
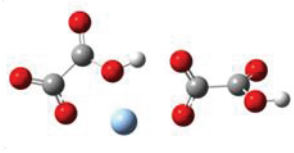
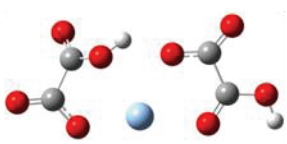
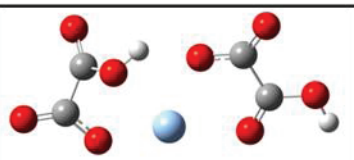
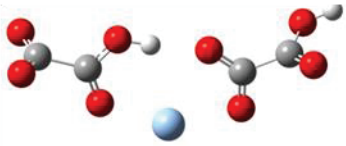
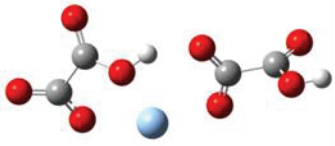
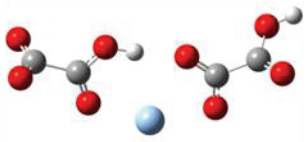
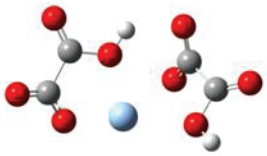
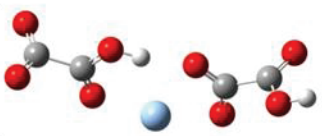
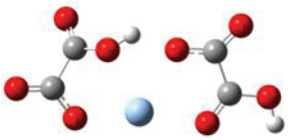
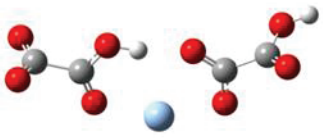
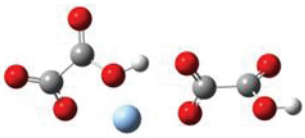
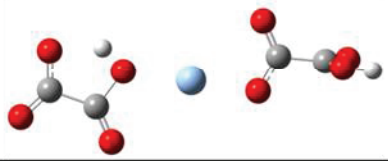
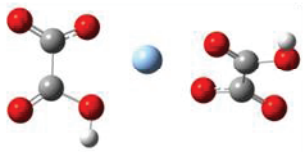
Level of Theory	"X" Structure	"Y" Structure
B3lyp		
B3pw91		
B98		
Bhandhlyp		
M062x		
Mpw1pw91		
Pbe1pbe		
MP2		

Figure 7-3: Optimized structures for $AgOx_2H_2^-$.

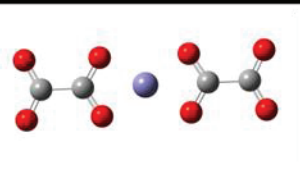
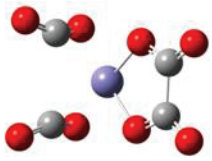
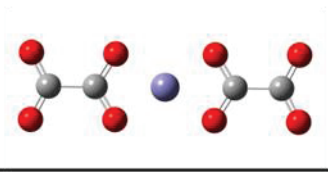
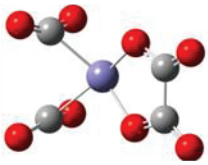
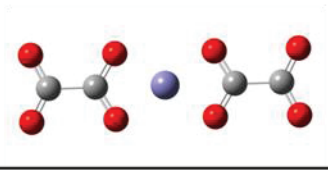
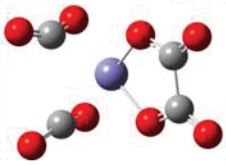
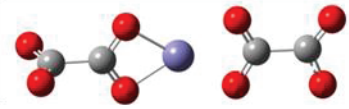
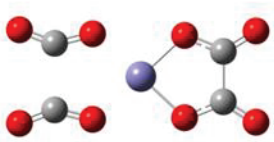
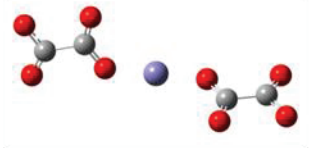
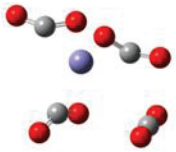
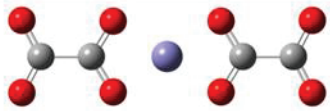
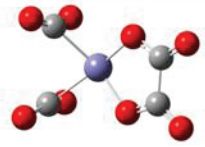
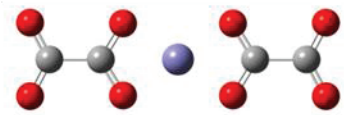
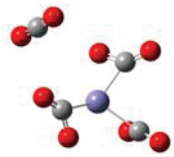
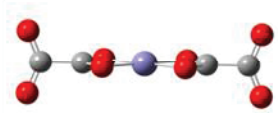
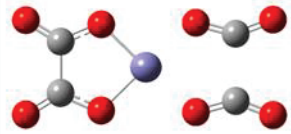
Level of Theory	"X" Structure	"Y" Structure
B3lyp		
B3pw91		
B98		
Bhandhlyp		
M062x		
Mpw1pw91		
Pbe1pbe		
MP2		

Figure 7-4: Optimized structures for $FeOx_2^-$.

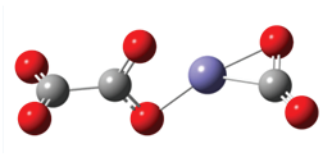
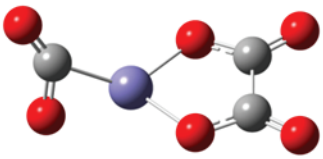
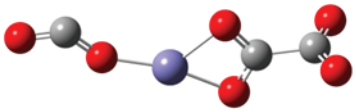
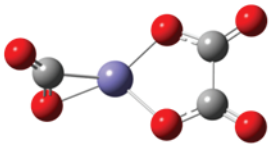
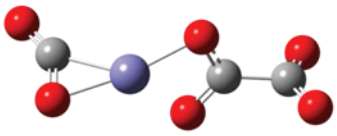
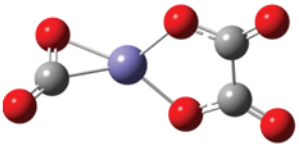
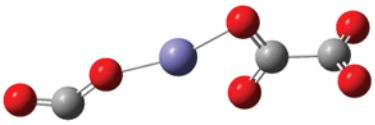
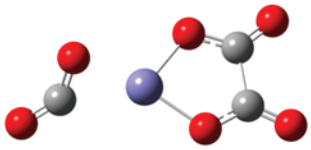
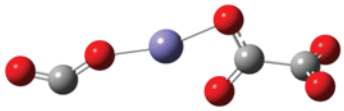
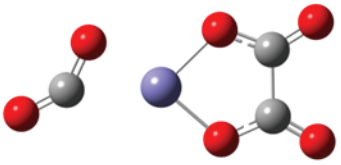
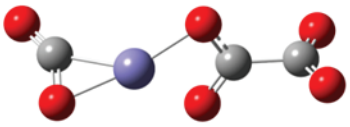
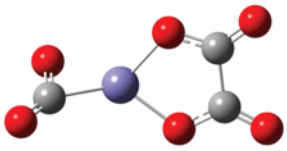
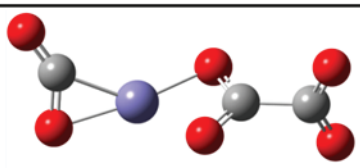
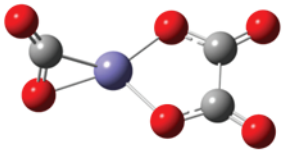
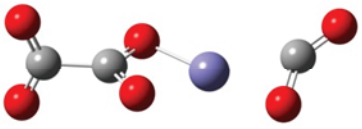
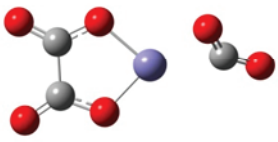
Level of Theory	"X" Structure	"Y" Structure
B3lyp		
B3pw91		
B98		
Bhandhlyp		
M062x		
Mpw1pw91		
Pbe1pbe		
MP2		

Figure 7-5: Optimized structures for $FeOxCO_2^-$.

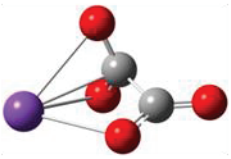
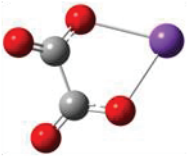
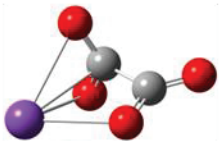
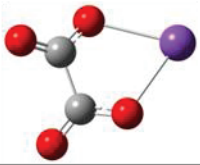
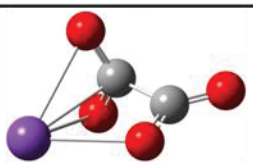
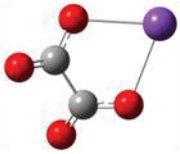
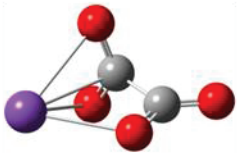
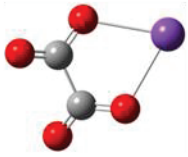
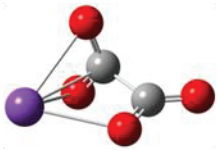
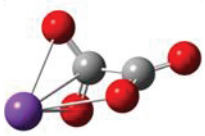
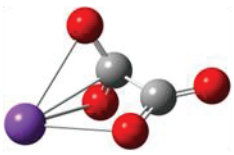
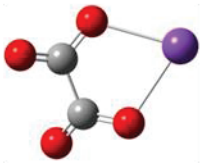
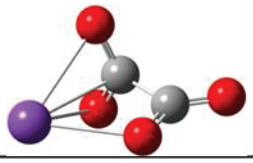
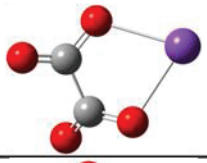
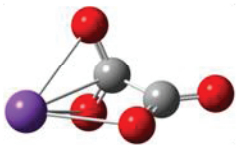
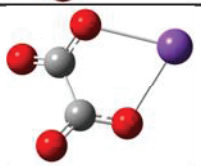
Level of Theory	"X" Structure	"Y" Structure
B3lyp		
B3pw91		
B98		
Bhandhlyp		
M062x		
Mpw1pw91		
Pbe1pbe		
MP2		

Figure 7-6: Optimized structures for KOx^-.

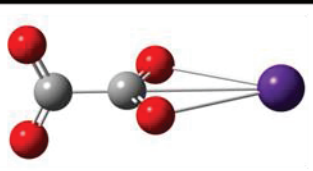
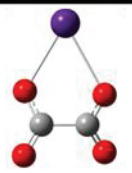
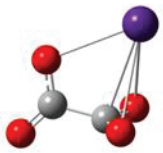
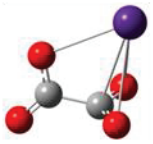
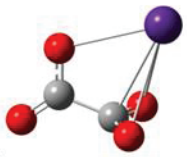
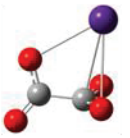
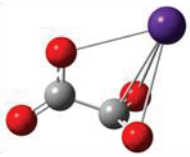
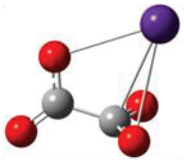
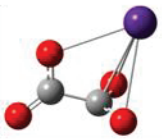
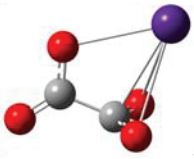
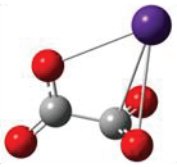
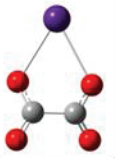
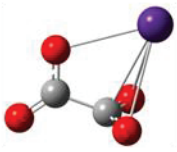
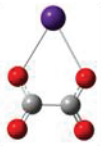
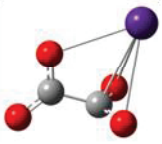
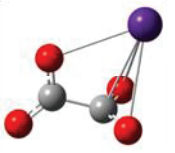
Level of Theory	"X" Structure	"Y" Structure
B3lyp		
B3pw91		
B98		
Bhandhlyp		
M062x		
Mpw1pw91		
Pbe1pbe		
MP2		

Figure 7-7: Optimized structures for $CsOx^-$.

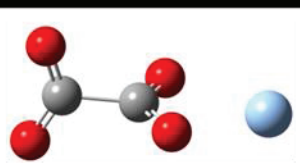
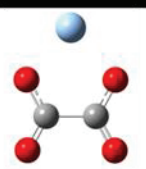
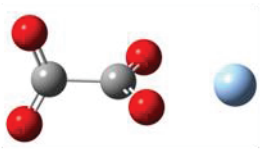
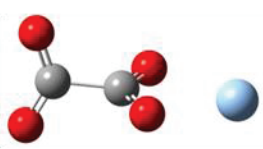
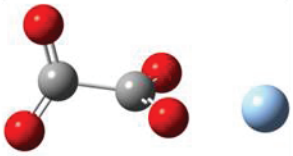
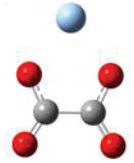
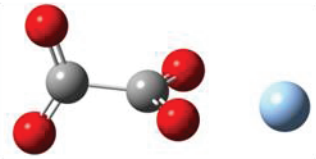
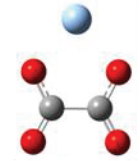
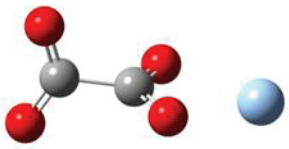
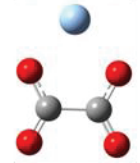
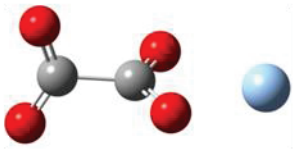
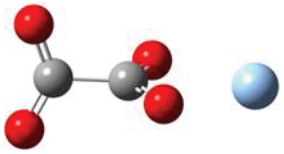
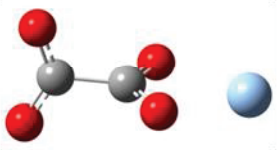
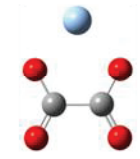
Level of Theory	"X" Structure	"Y" Structure
B3lyp		
B3pw91		
B98		
Bhandhlyp		
M062x		
Mpw1pw91		
Pbe1pbe		
MP2		

Figure 7-8: Optimized structures for $AgOx^{-}$.

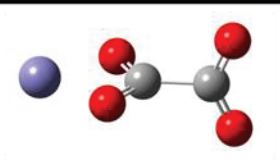
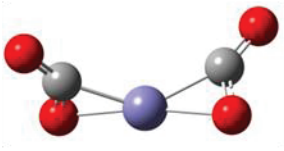
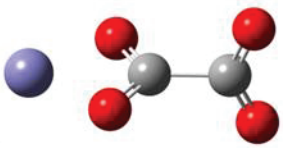
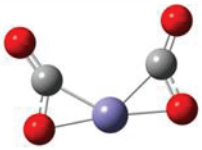
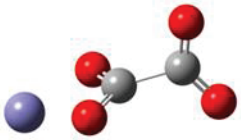
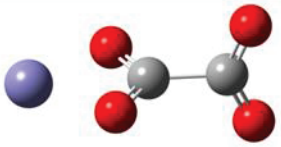
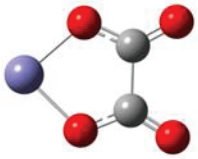
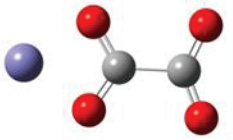
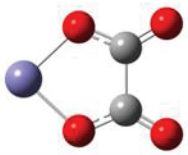
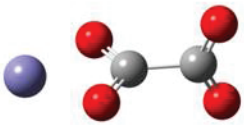
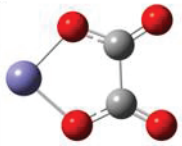
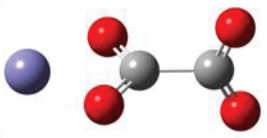
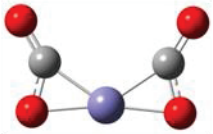
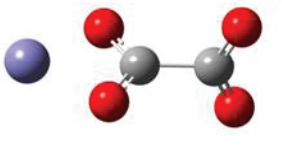
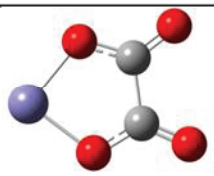
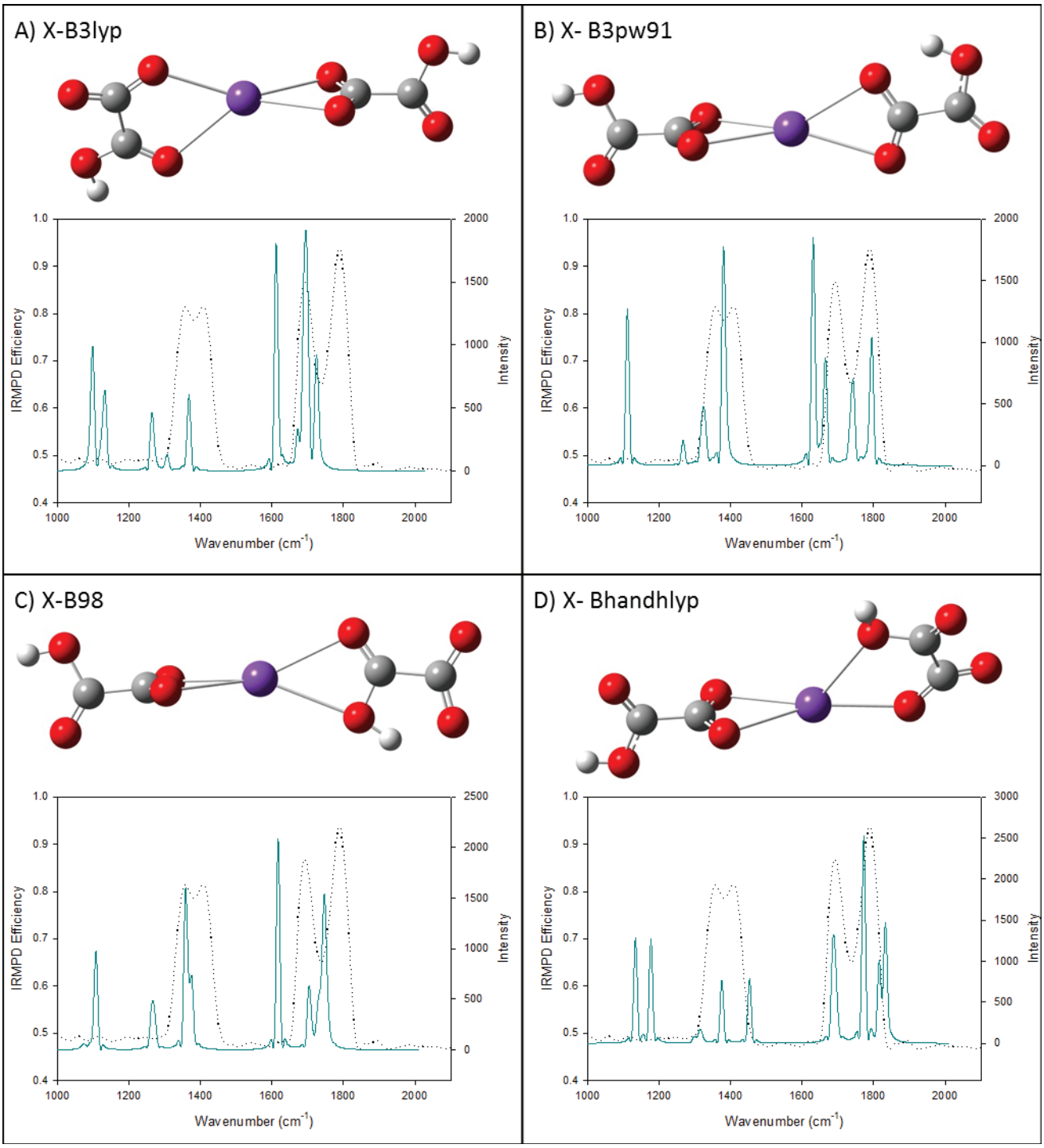
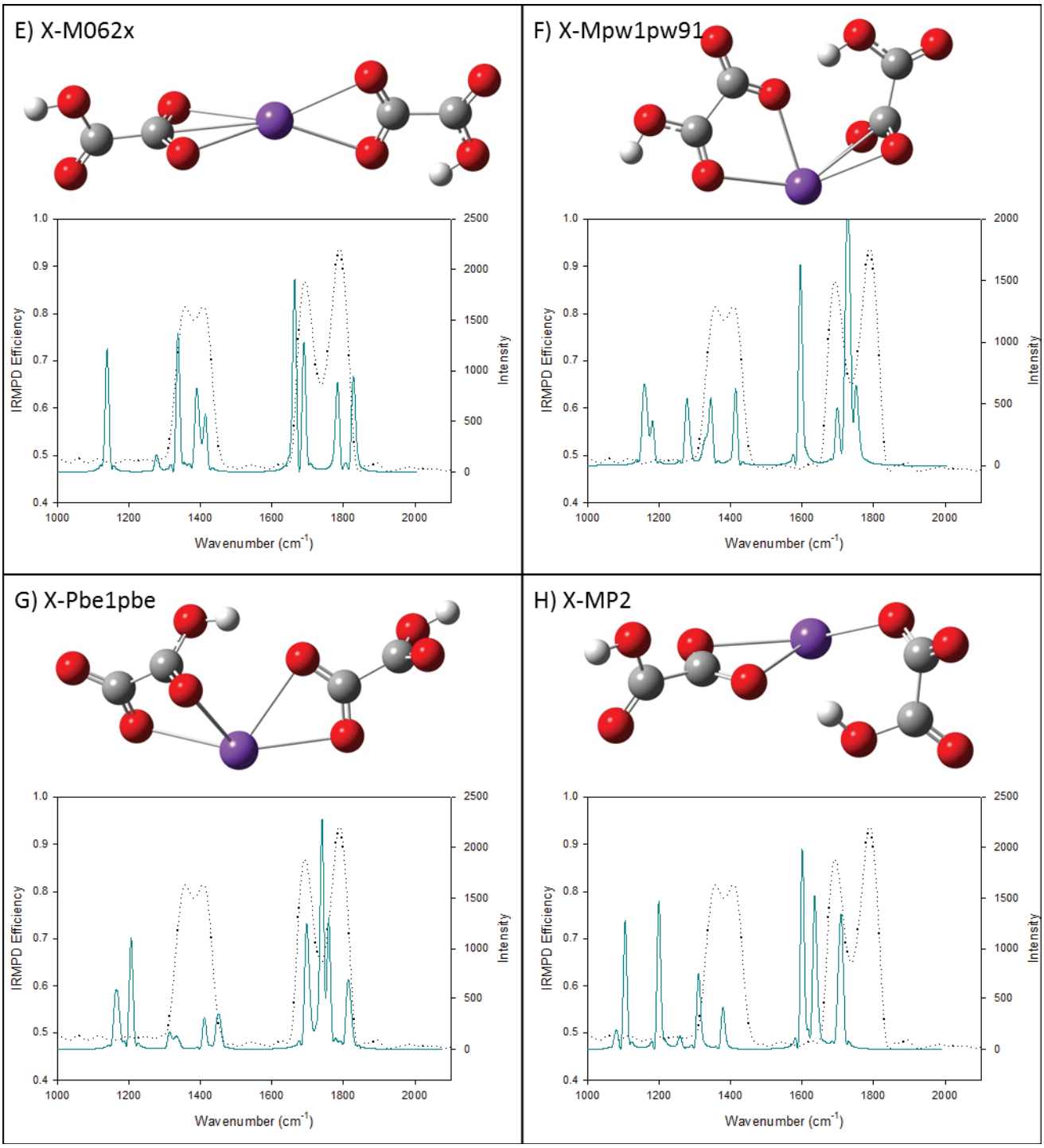
Level of Theory	"X" Structure	"Y" Structure
B3lyp		
B3pw91		
B98		
Bhandhlyp		
M062x		
Mpw1pw91		
Pbe1pbe		
MP2		

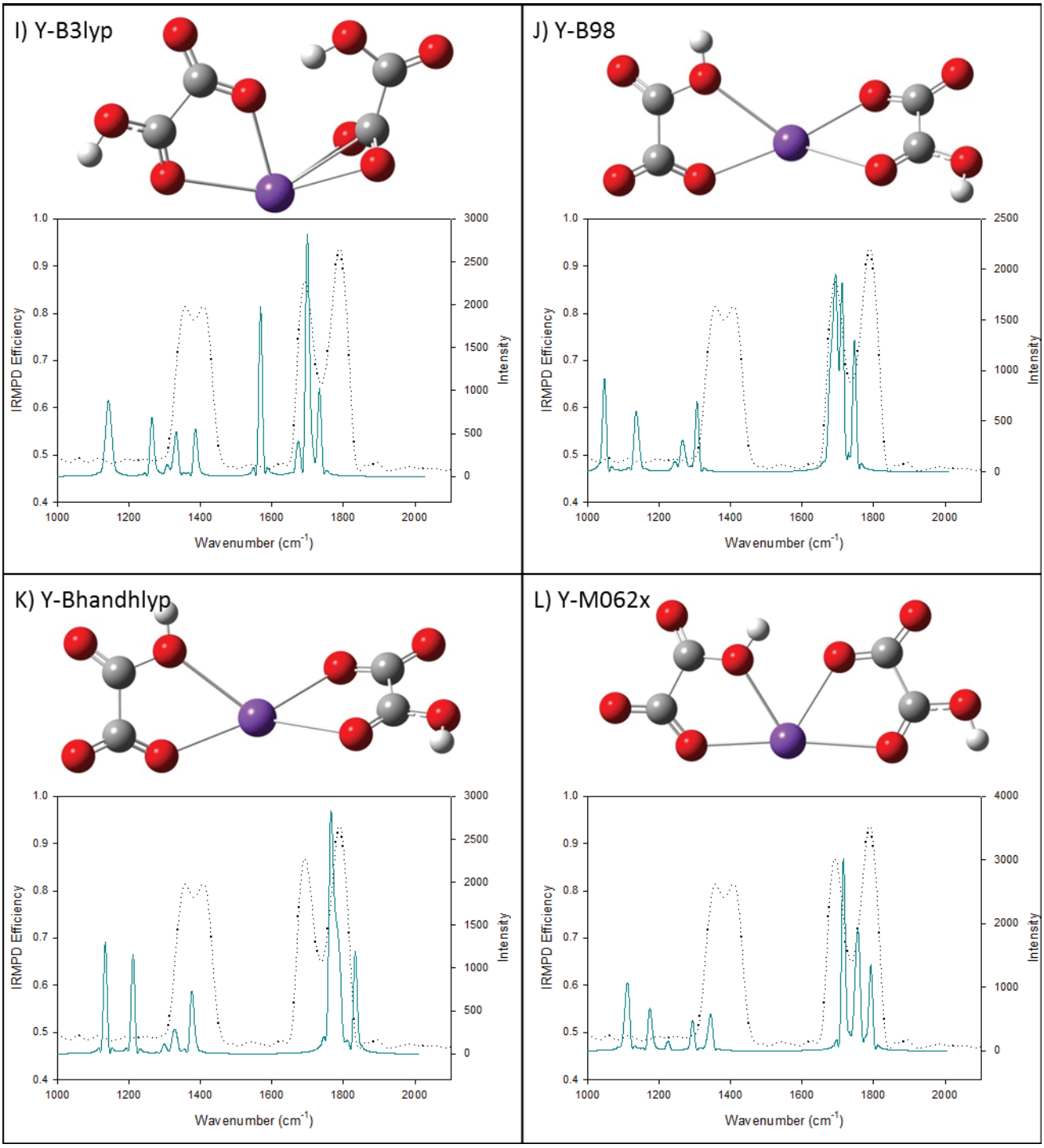
Figure 7-9: Optimized structures for $FeOx^-$.

7.2 IRMPD Results

7.2.1 $KOx_2H_2^-$: Unique "X" and "Y" structures




E) X-M062x
F) X-Mpw1pw91
G) X-Pbe1pbe
H) X-MP2
IRMPD Efficiency
Intensity
Wavenumber (cm-1)


I) Y-B3lyp
J) Y-B98
K) Y-Bhandhlyp
L) Y-M062x
IRMPD Efficiency
Intensity
Wavenumber (cm-1)

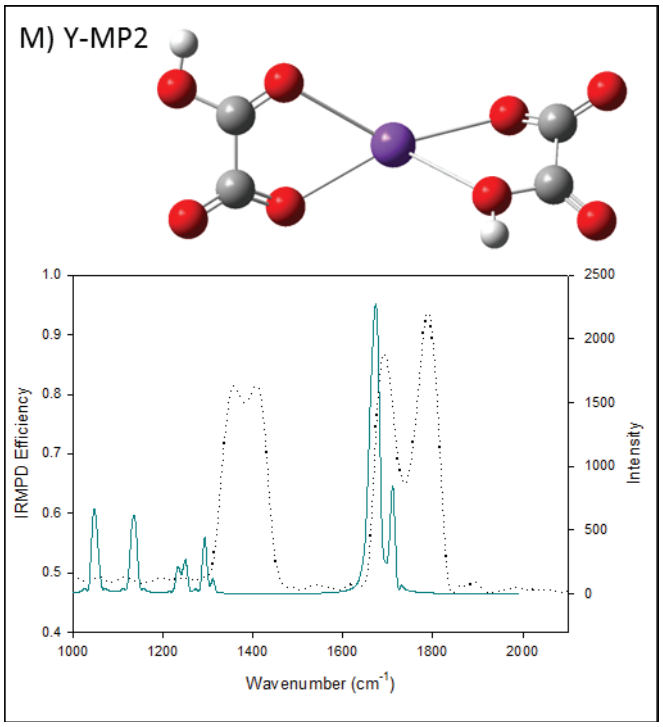


Figure 7-10: All unique optimized structures and theoretical spectra overlapping the IRMPD spectrum for the 1000-2000cm^{-1} range.

7.2.2 $KOx_2H_2^-$: Second attempt at structure determination

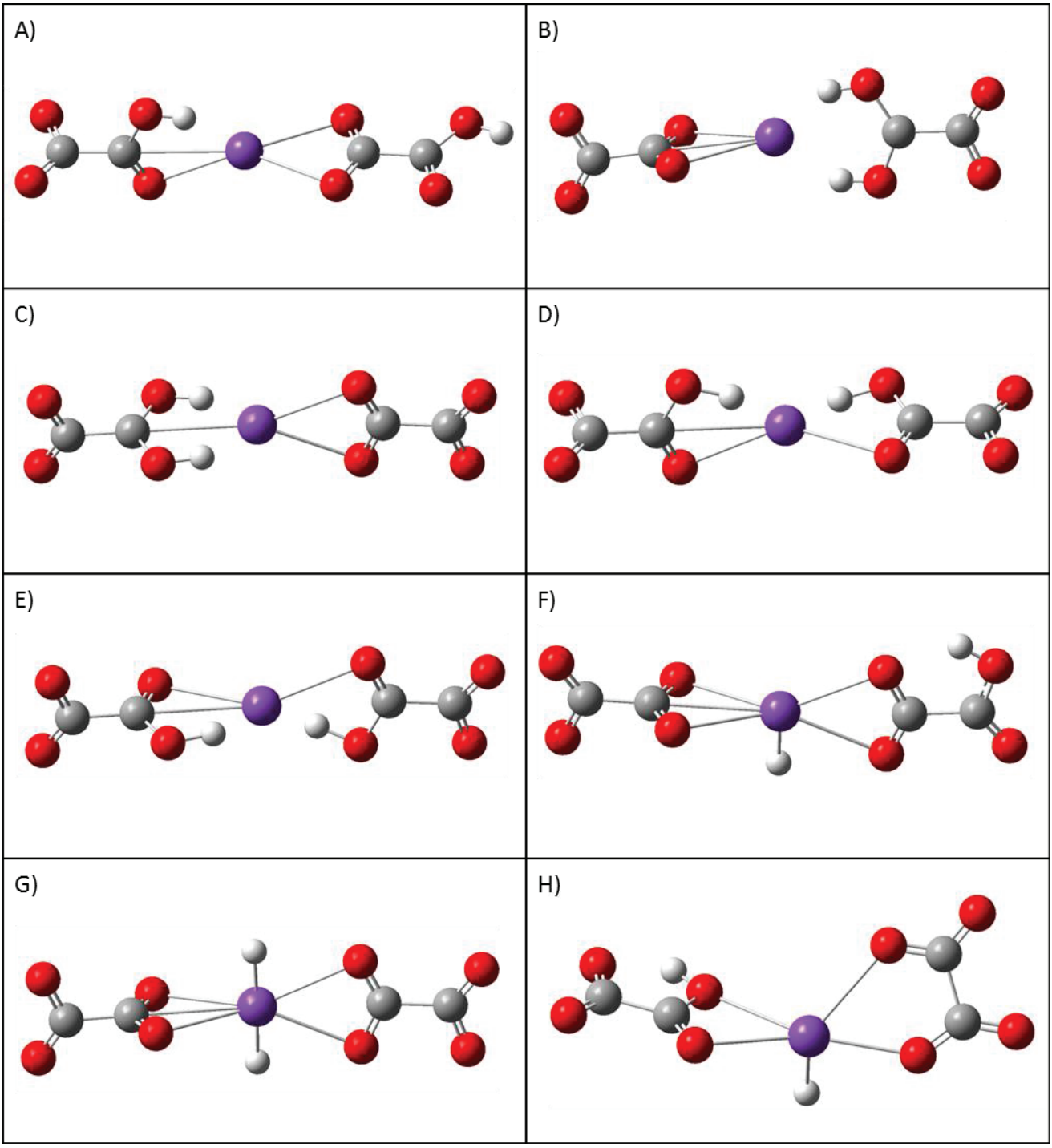
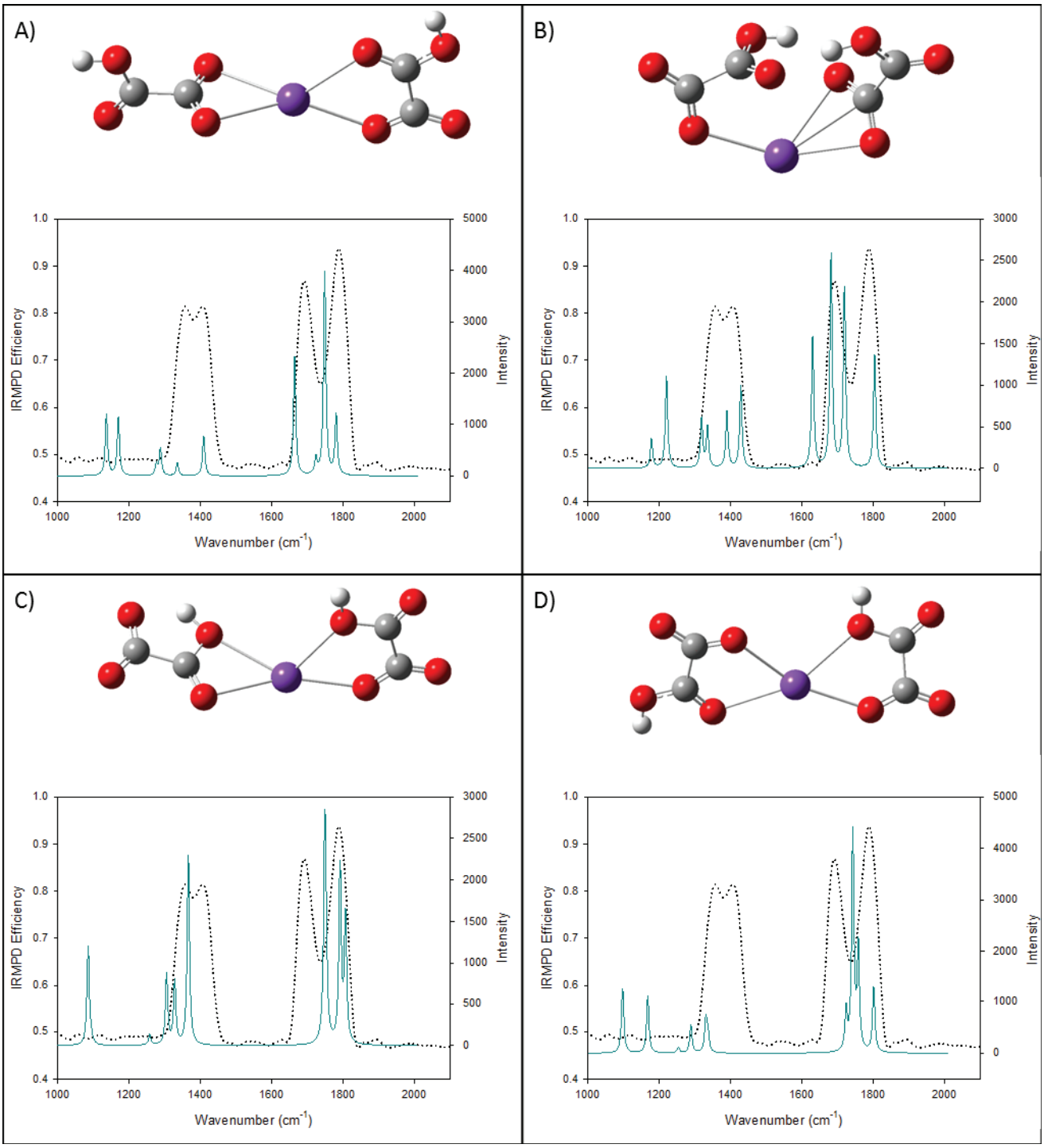


Figure 7-11: Starting structures for the second attempt at determining a plausible structure.


A)
B)
C)
D)
IRMPD Efficiency
Intensity
Wavenumber (cm-1)

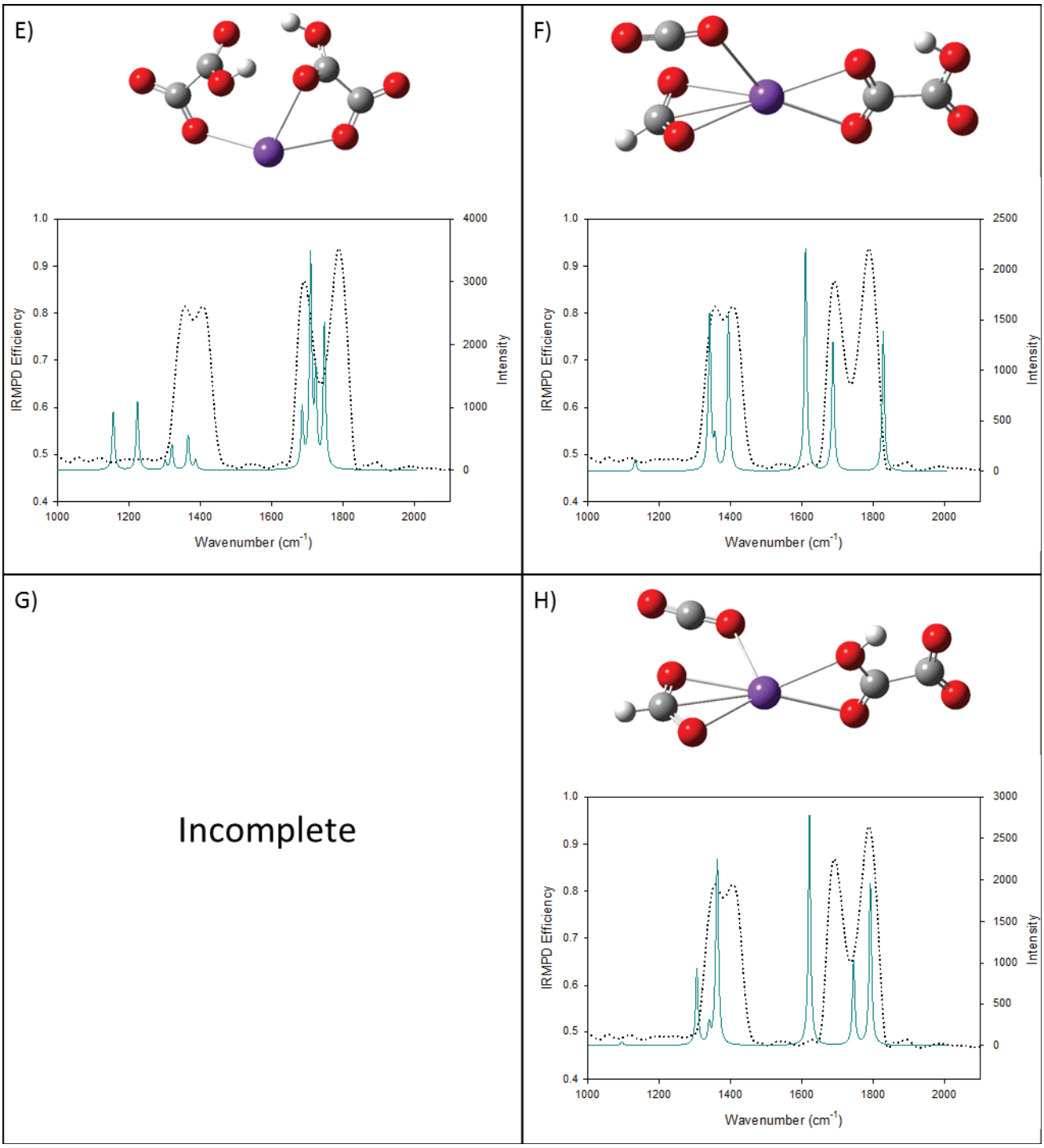


Figure 7-12: Optimized structures and spectra resulting from structures in Figure 7-11.

7.2.3 $KOx_2H_2^-$: Third attempt at structure determination

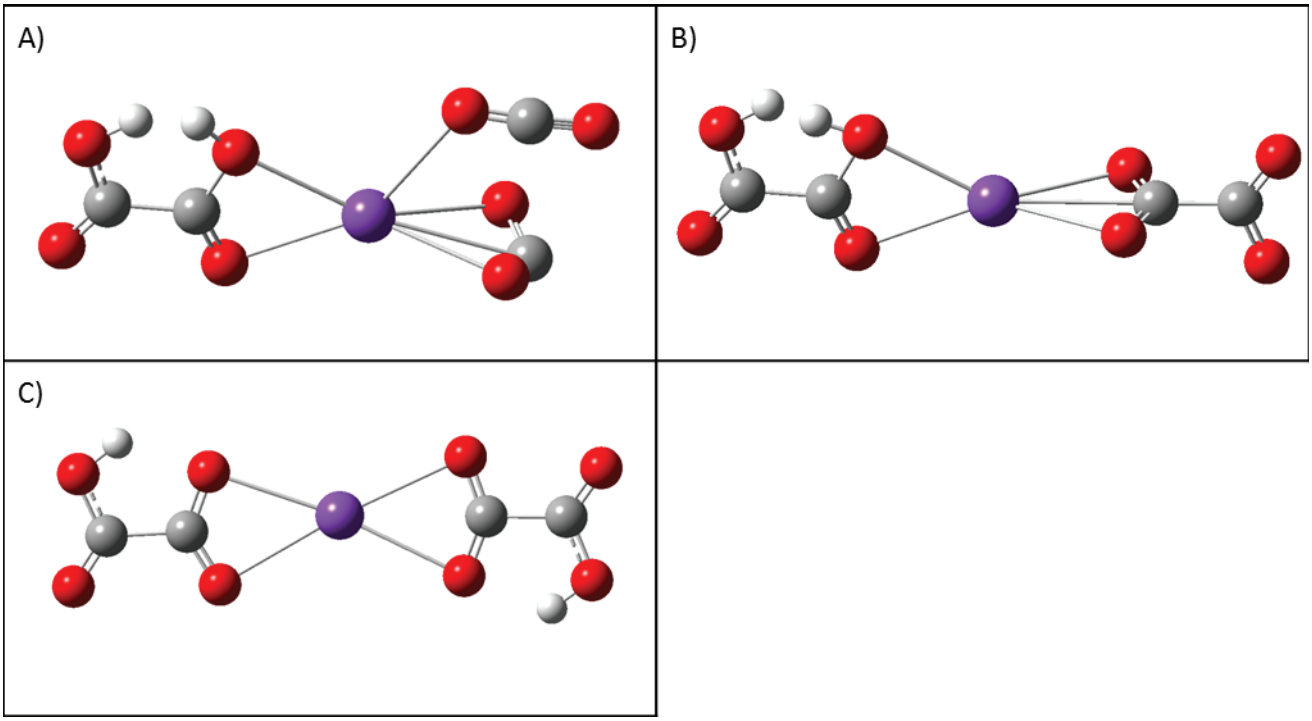


Figure 7-13: Starting structures for the third attempt at determining a plausible structure.

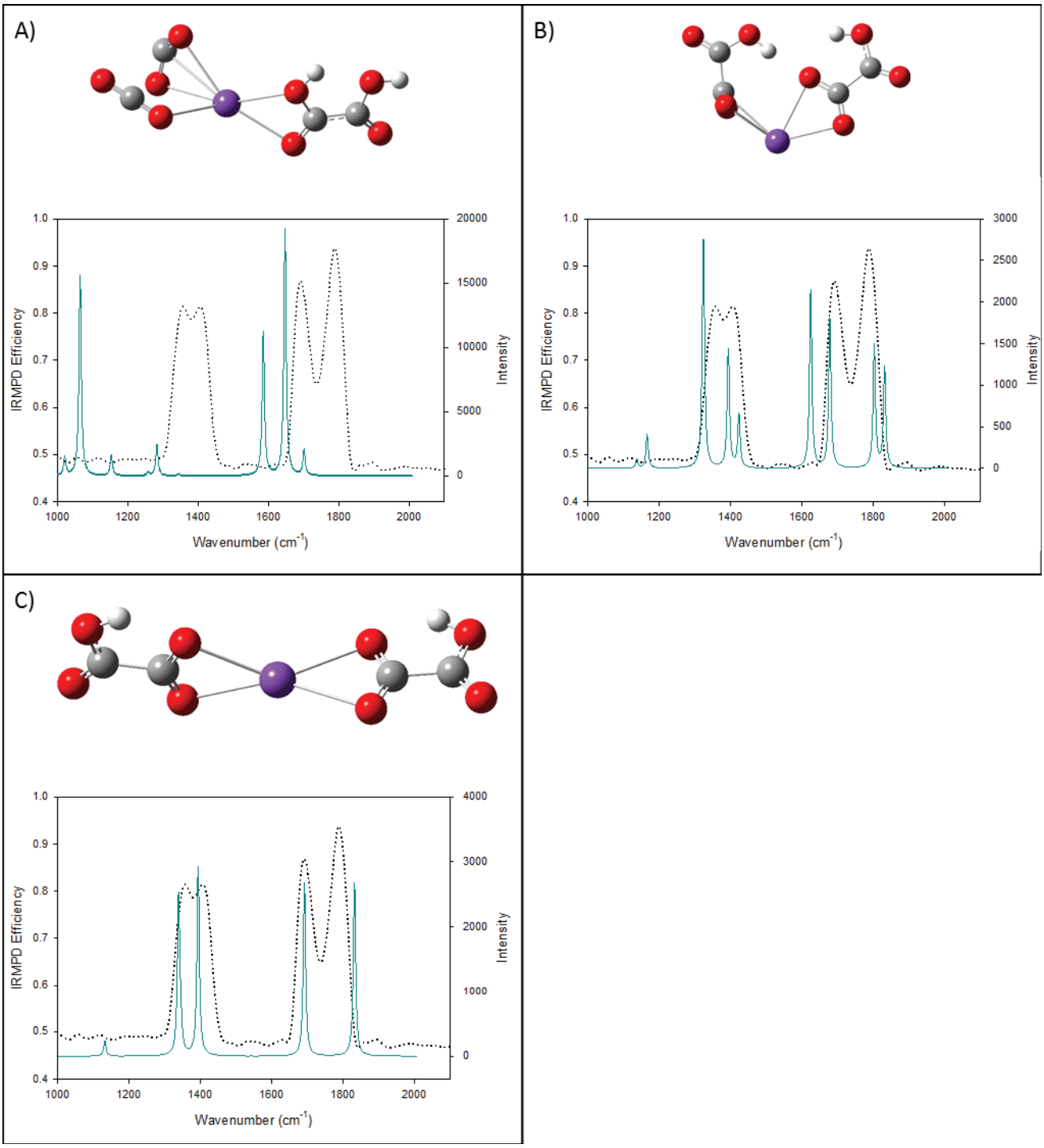
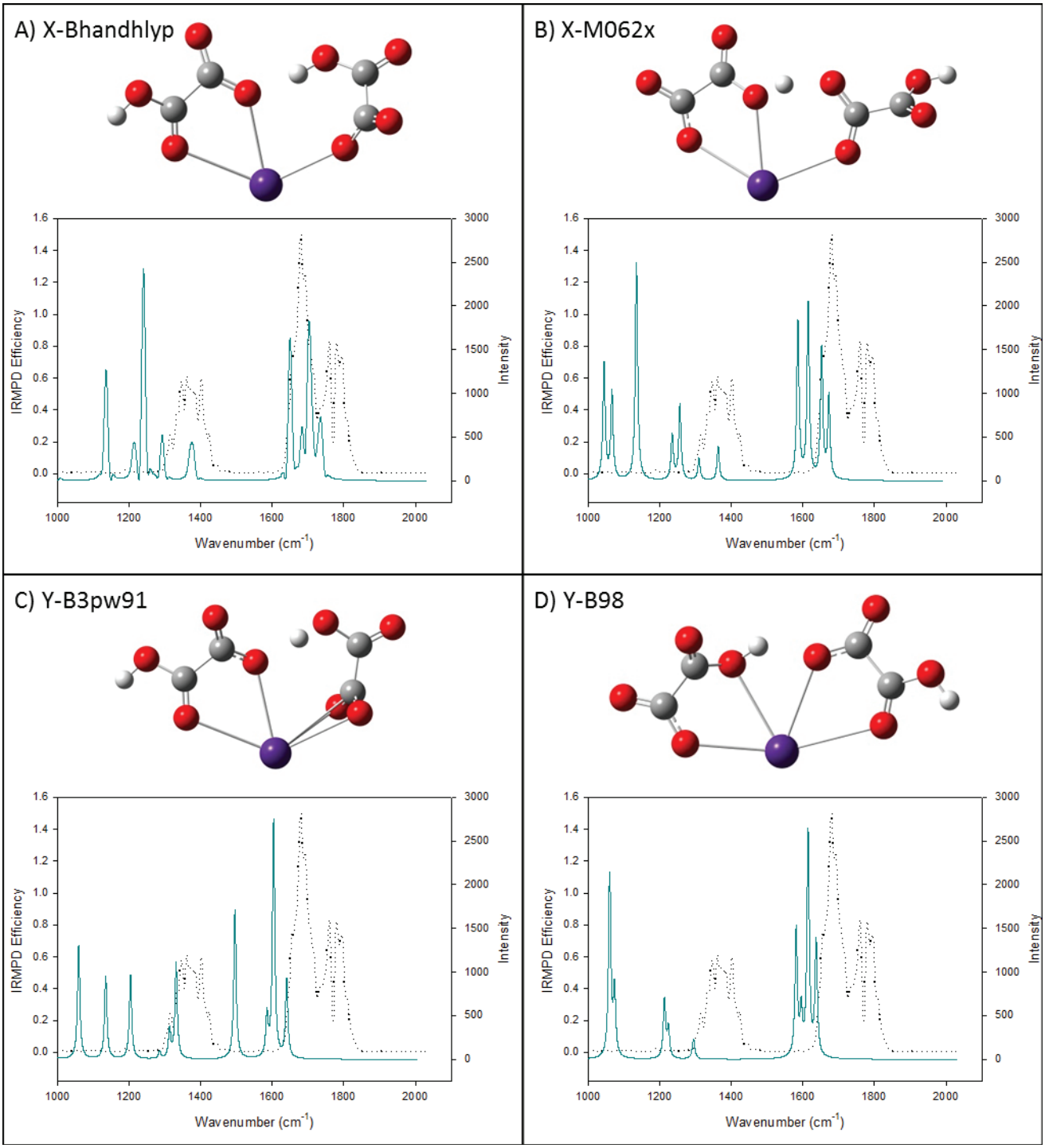


Figure 7-14: Optimized structures and spectra resulting from structures in Figure 7-13.

7.2.4 $CsOx_2H_2^-$: Unique "X" and "Y" structures



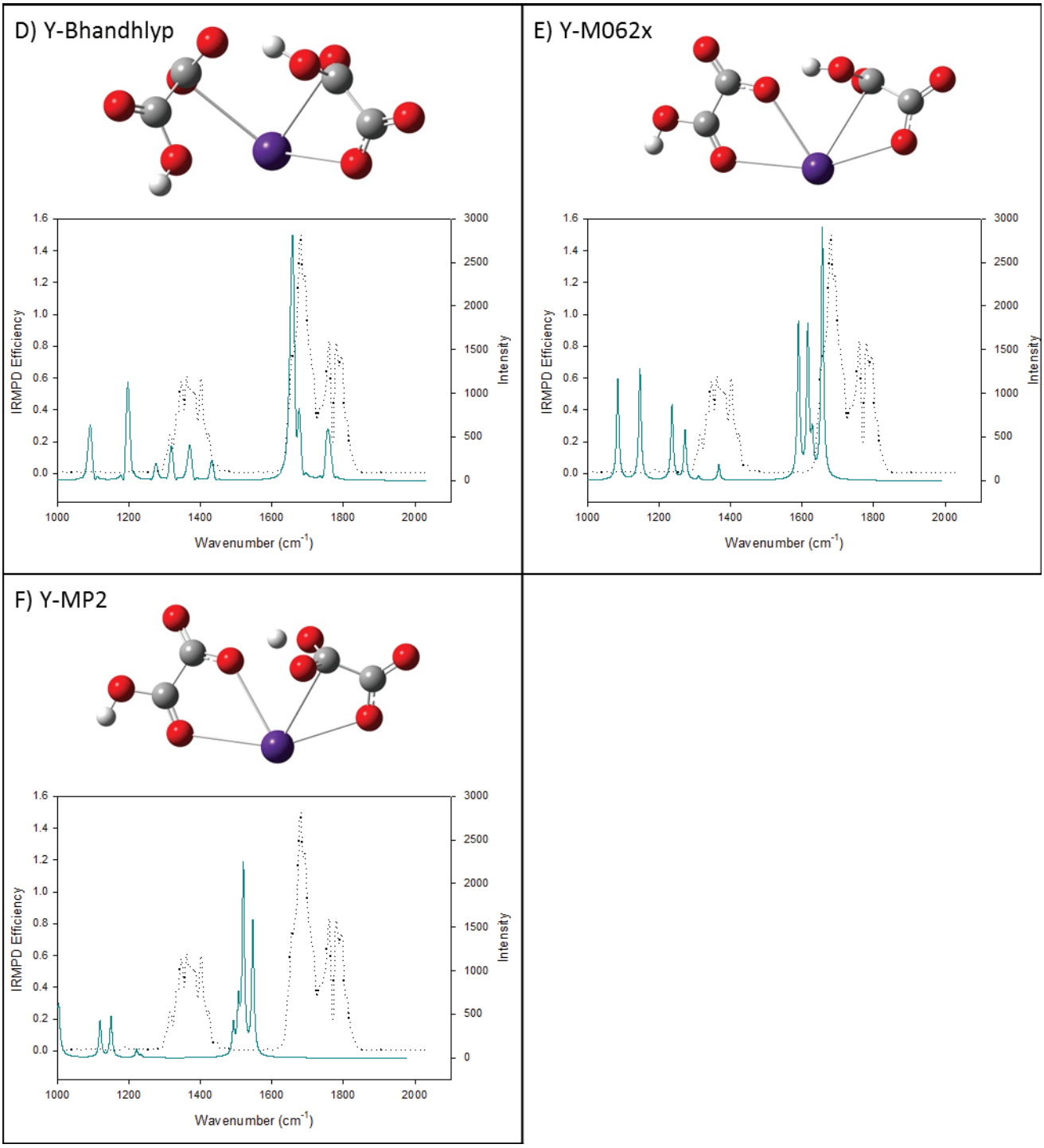


Figure 7-15: All unique optimized structures and theoretical spectra overlapping the IRMPD spectrum for the 1000-2000cm-1 range.

7.2.5 $CsOx_2H_2^-$: More attempts at structure determination

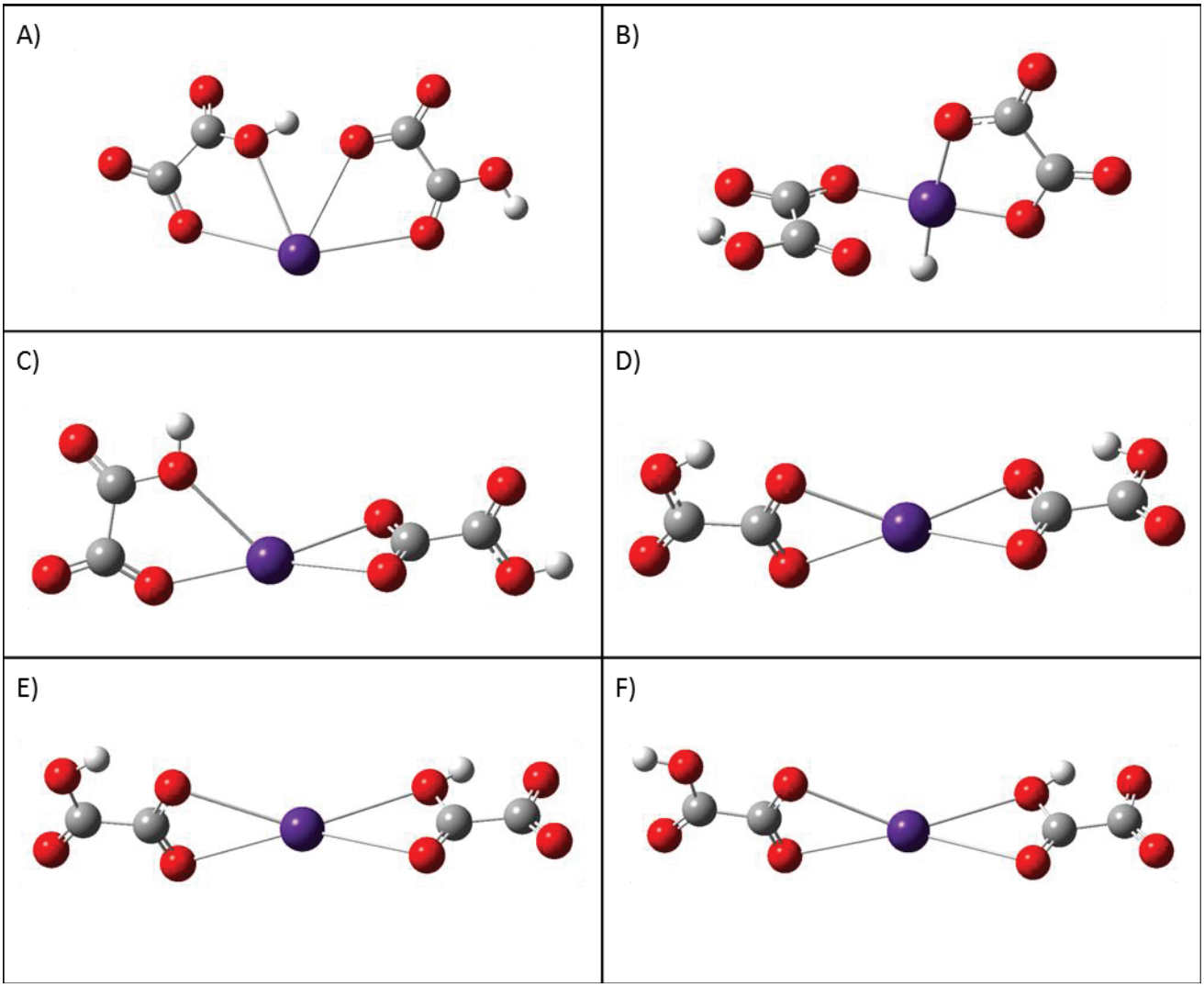


Figure 7-16: Starting structures for the second attempt at determining a plausible structure.

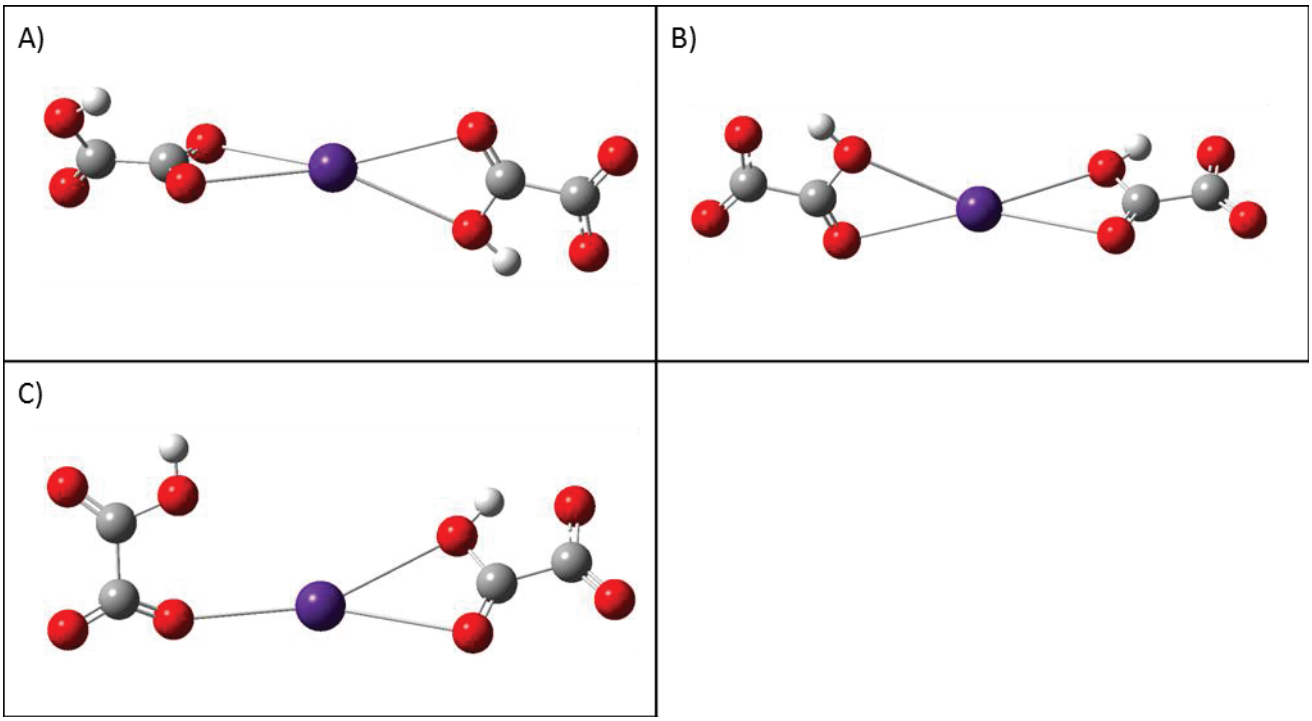


Figure 7-17: Starting structures for the third attempt at determining a plausible structure.

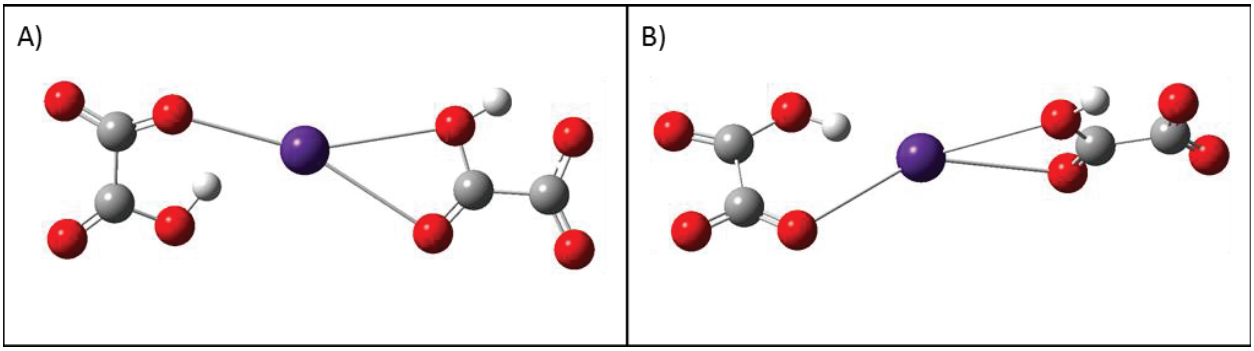
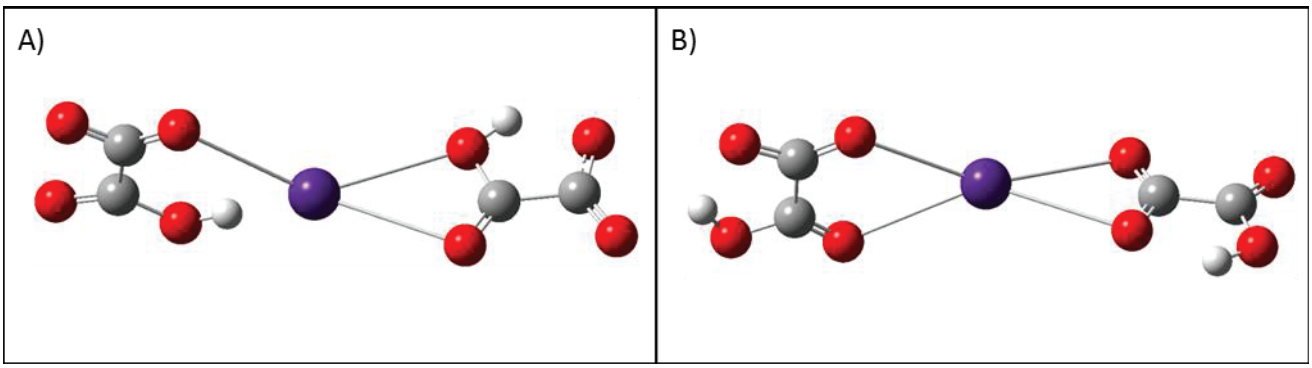
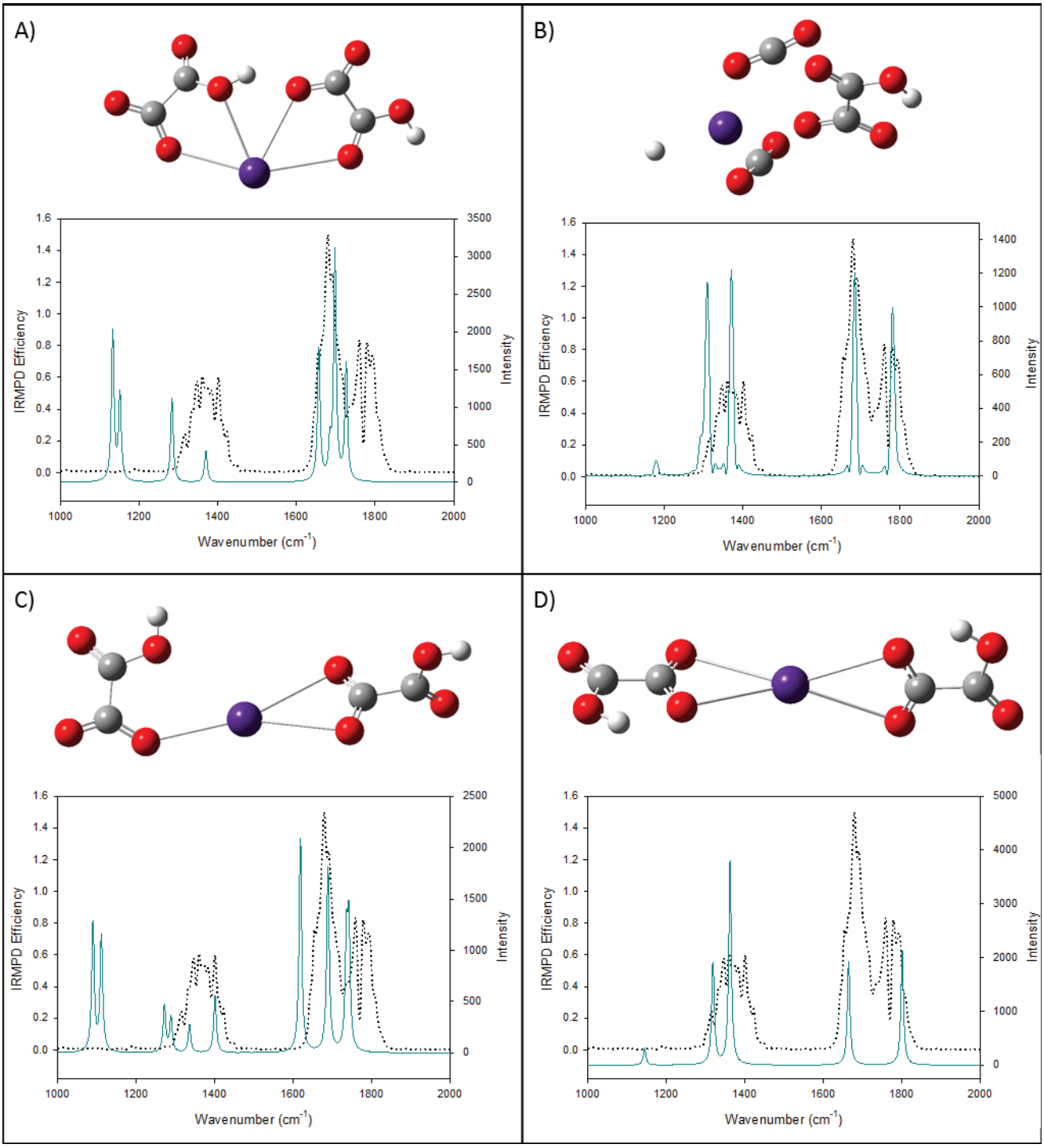


Figure 7-18: Starting structures for the fourth attempt at determining a plausible structure.

Figure 7-19: Starting structures for the fifth attempt at determining a plausible structure.




A)
B)
C)
D)
IRMPD Efficiency
Intensity
Wavenumber (cm-1)

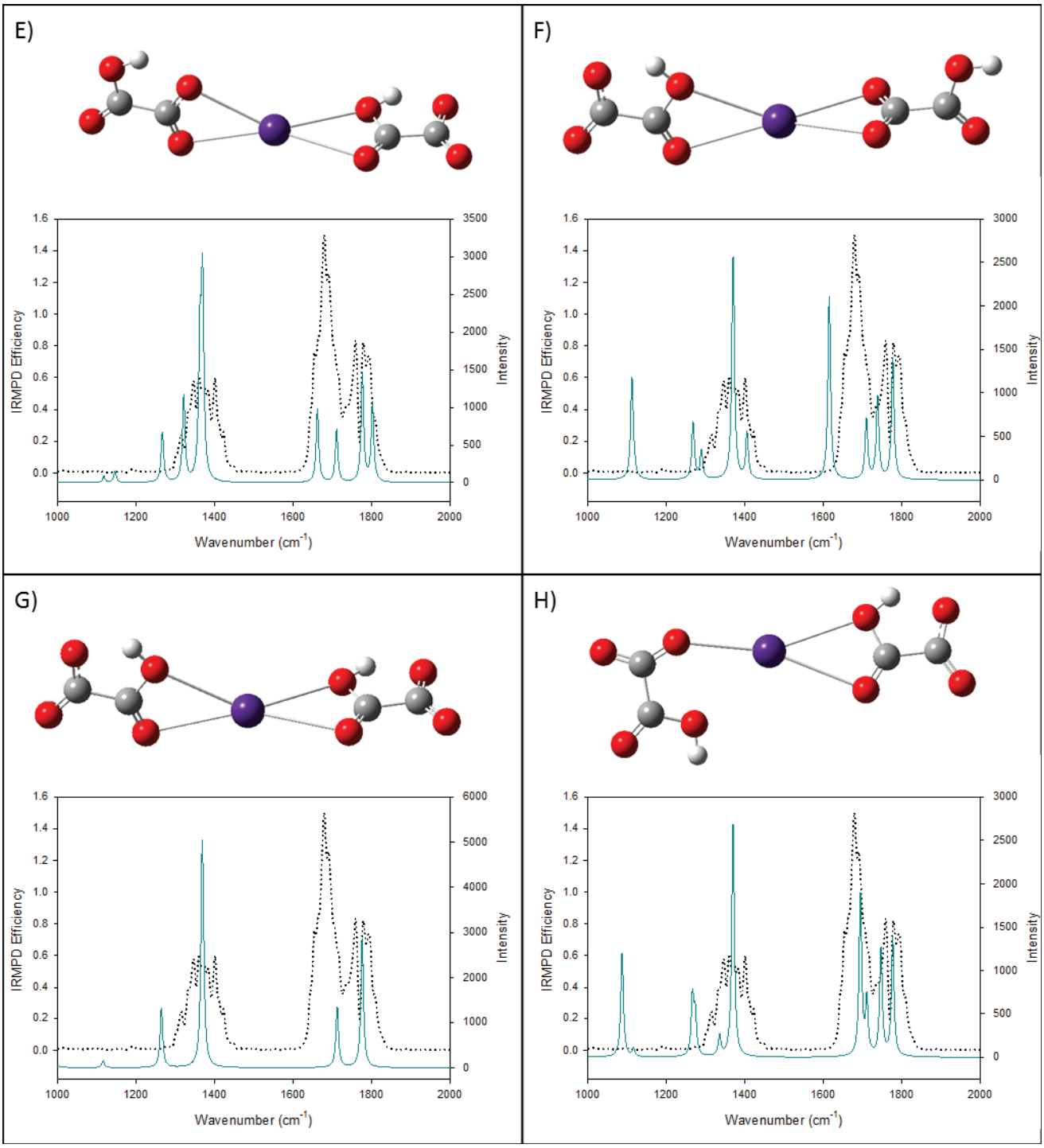
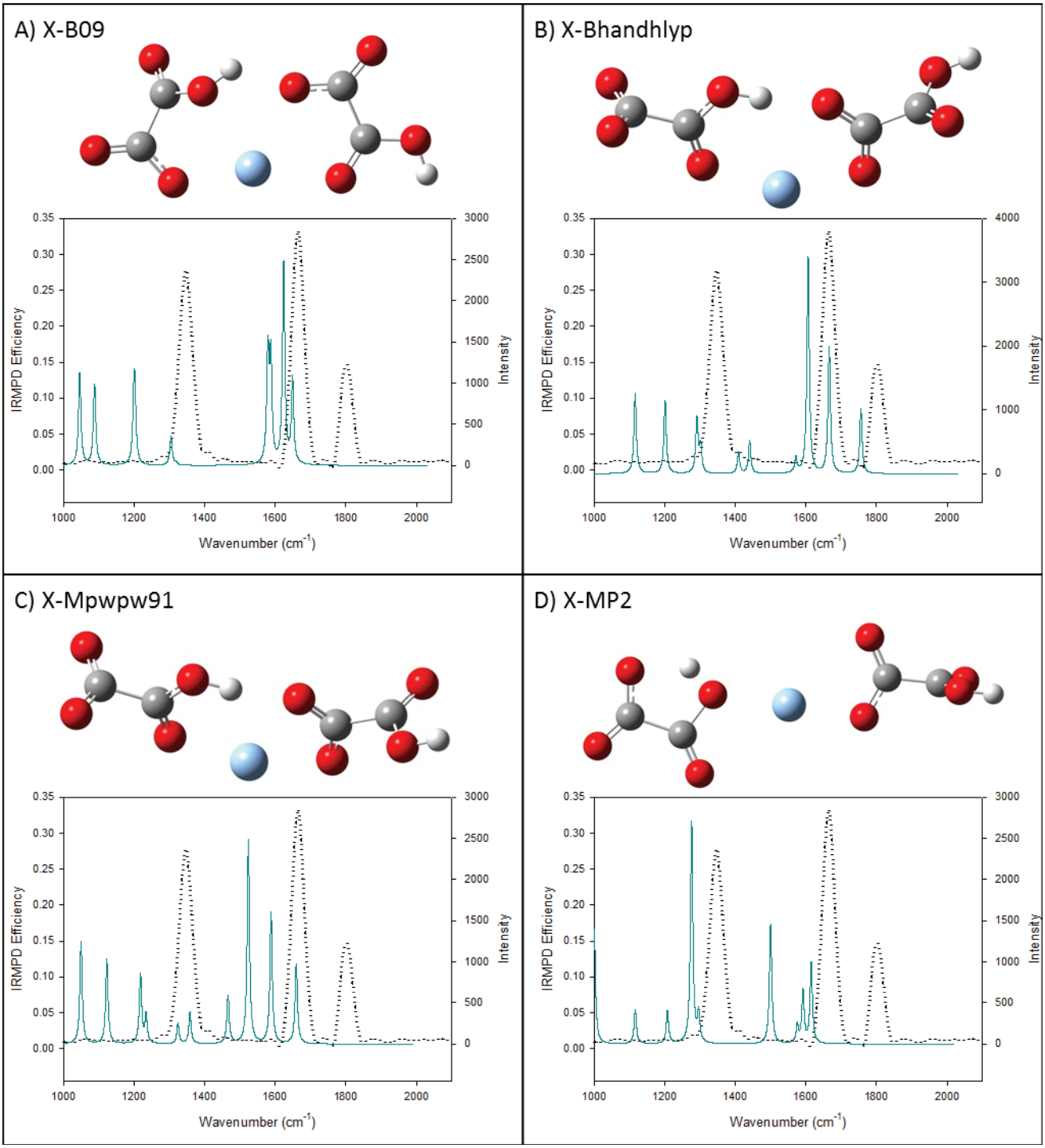


Figure 7-20: Optimized structures and spectra. Parts A-F are resulting from starting structures in Figure 7-16 respectively. Part E also resulted from Figure 7-17A, Figure 7-18A and Figure 7-19A. Parts G and H are the result from Figure 7-17B and C, while I and J are the results from Figure 7-18B and Figure 7-19B respectively.

7.2.6 $AgOx_2H_2^-$: Unique "X" and "Y" structures



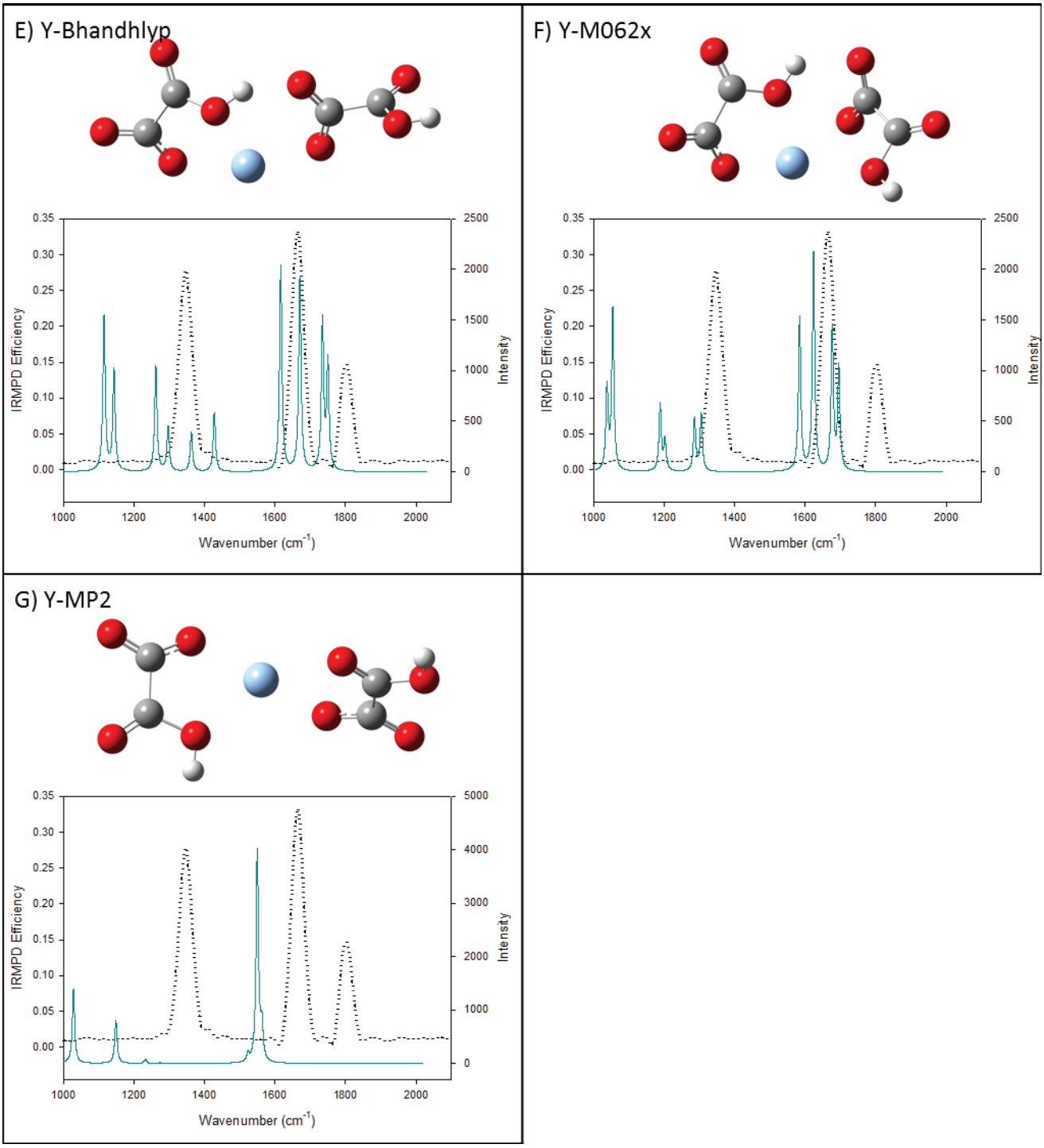


Figure 7-21: All unique optimized structures and theoretical spectra overlapping the IRMPD spectrum for the 1000-2000cm-1 range.

7.2.7 $AgOx_2H_2^-$: More attempts at structure determination

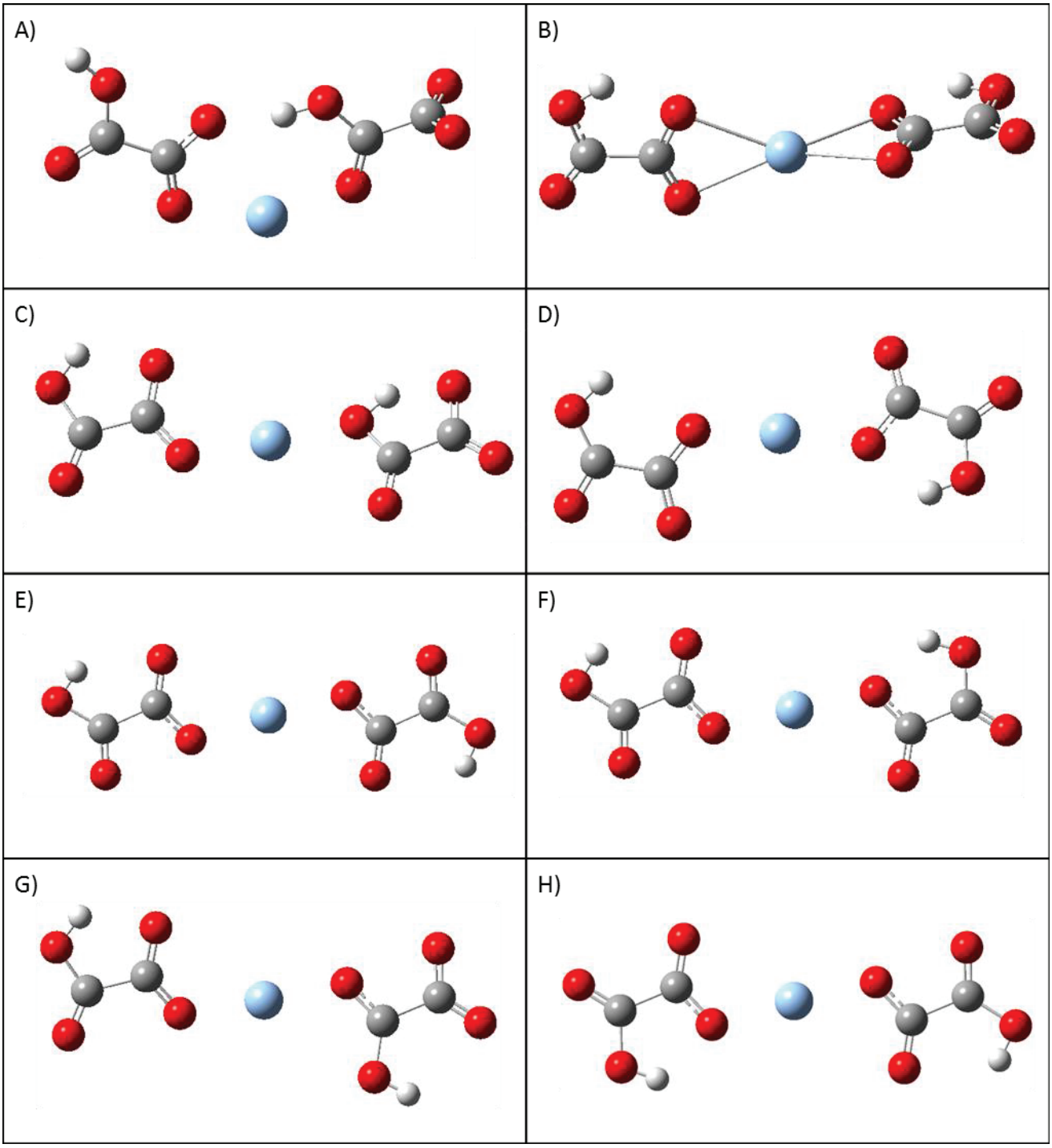
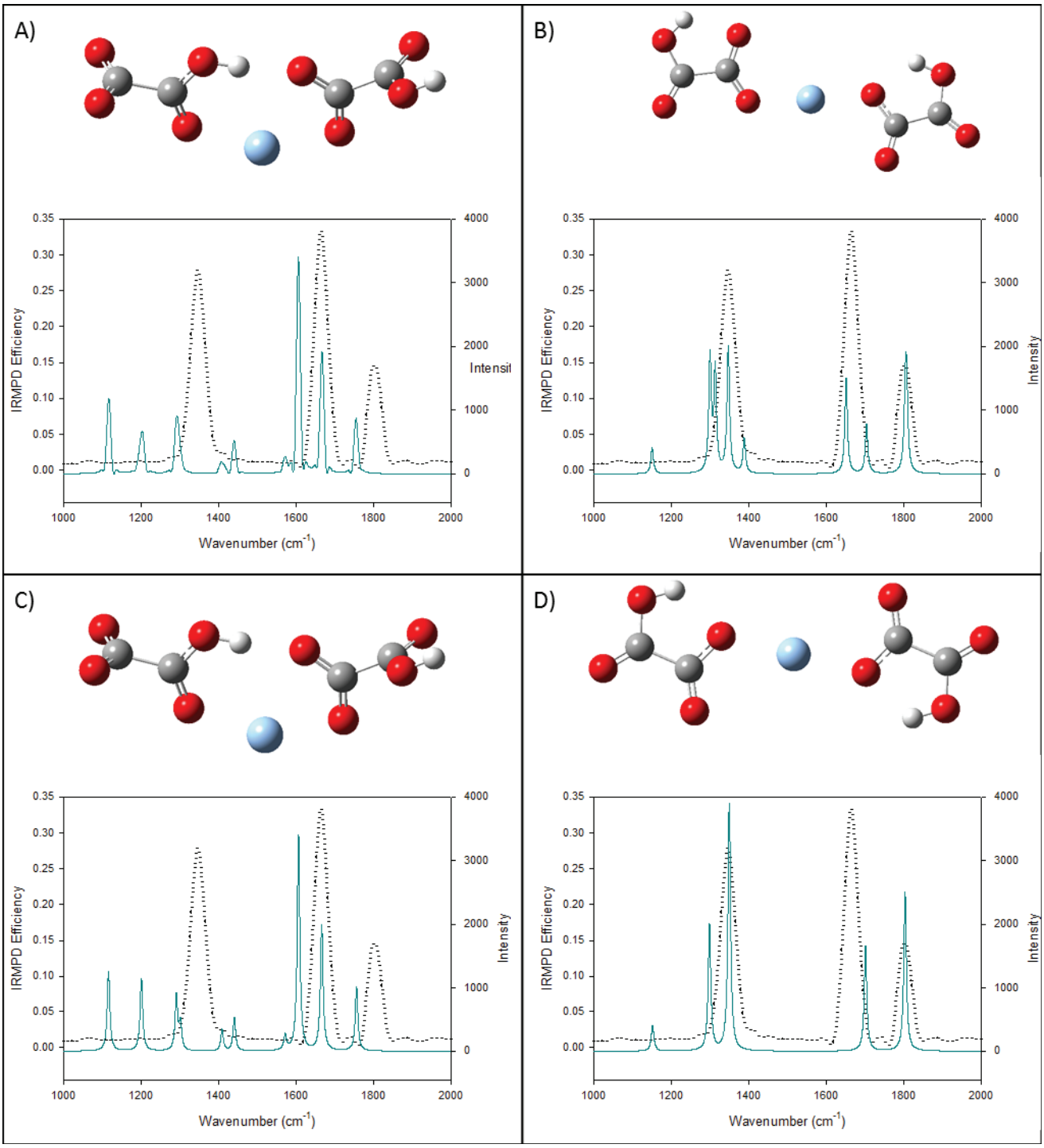


Figure 7-22: Starting structures for more attempts at determining a plausible structure.


A)
B)
C)
D)
IRMPD Efficiency
Intensity
Wavenumber (cm-1)
0.35
0.30
0.25
0.20
0.15
0.10
0.05
0.00
4000
3000
2000
1000
0
1000
1200
1400
1600
1800
2000

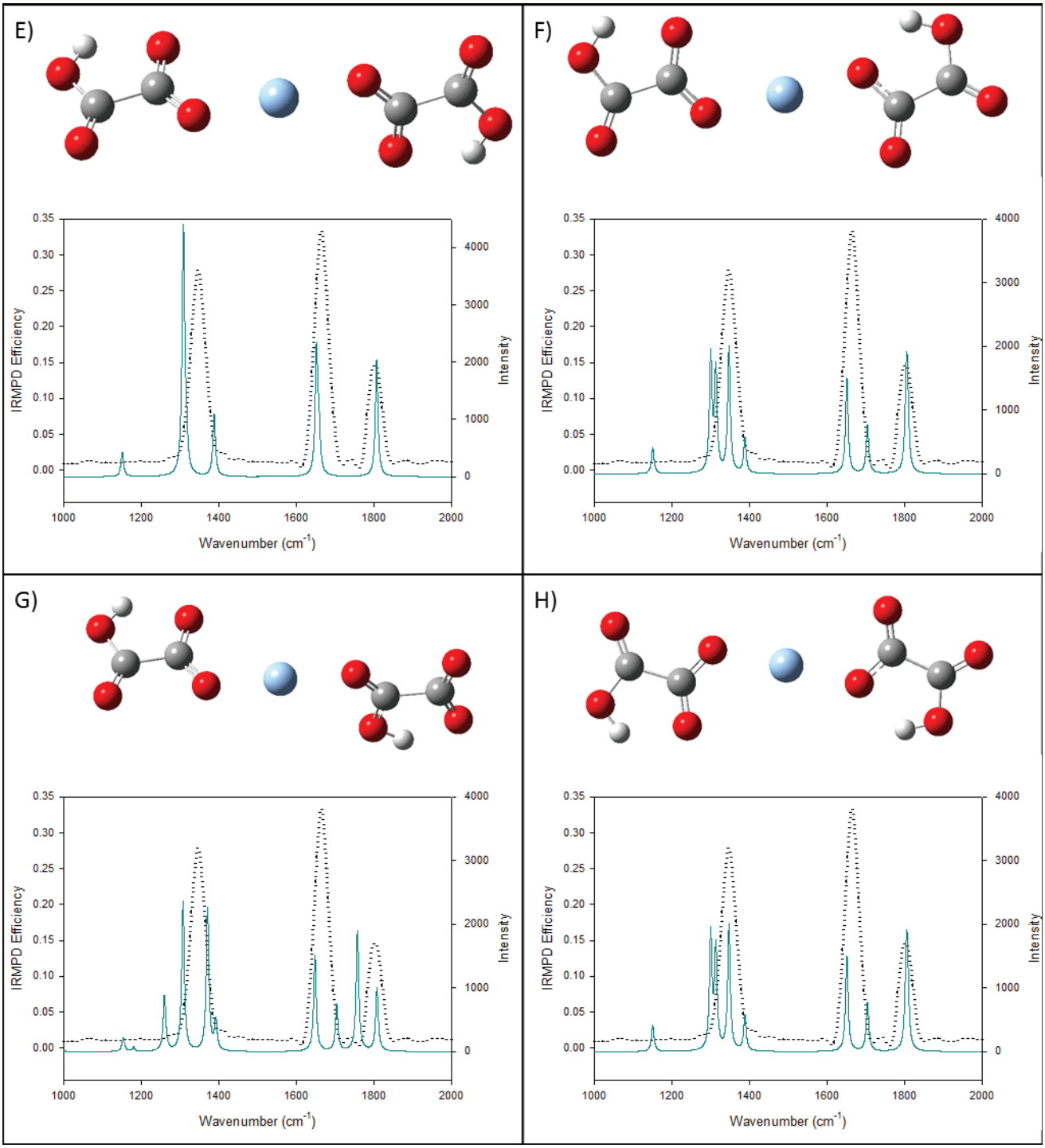
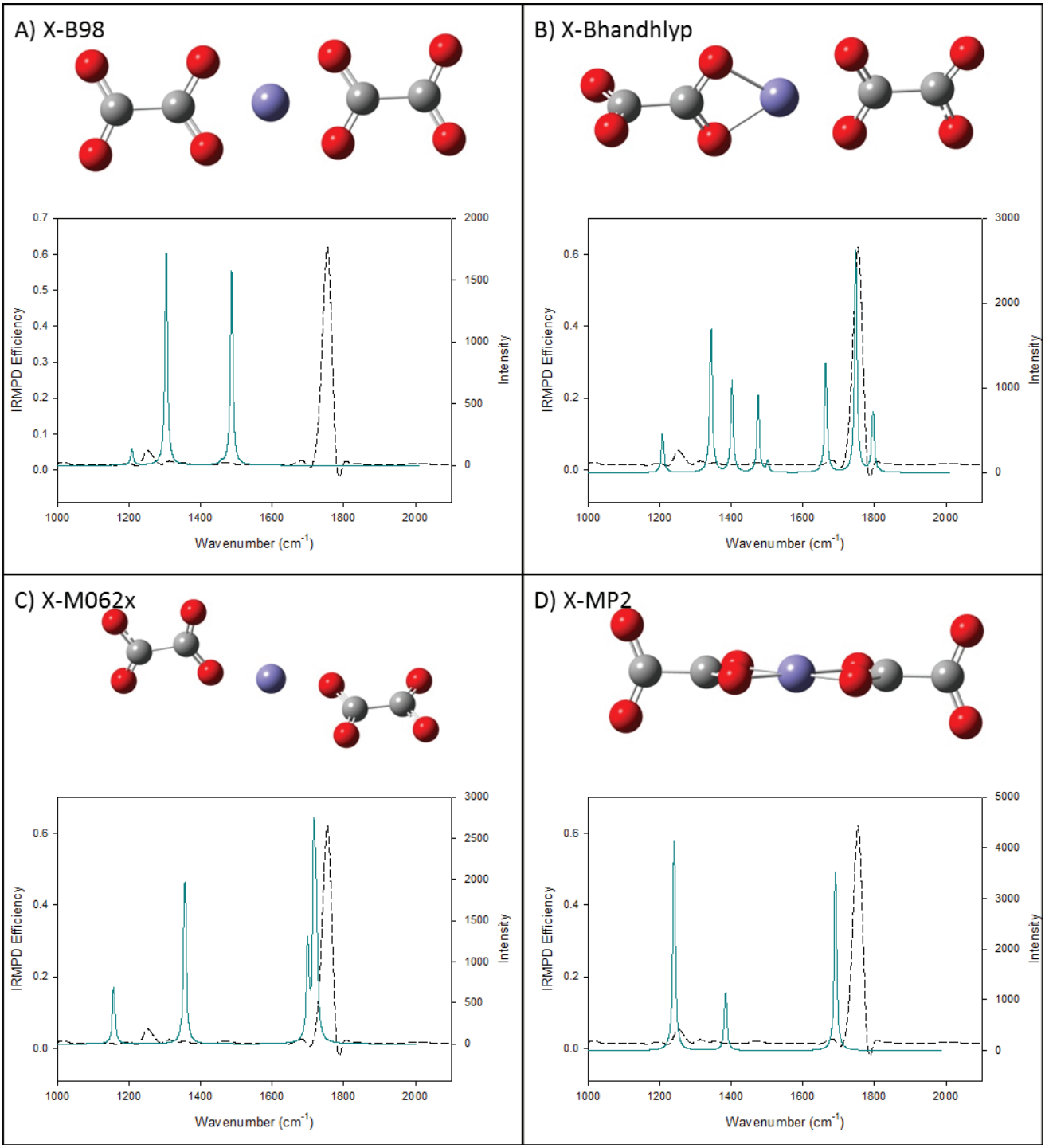
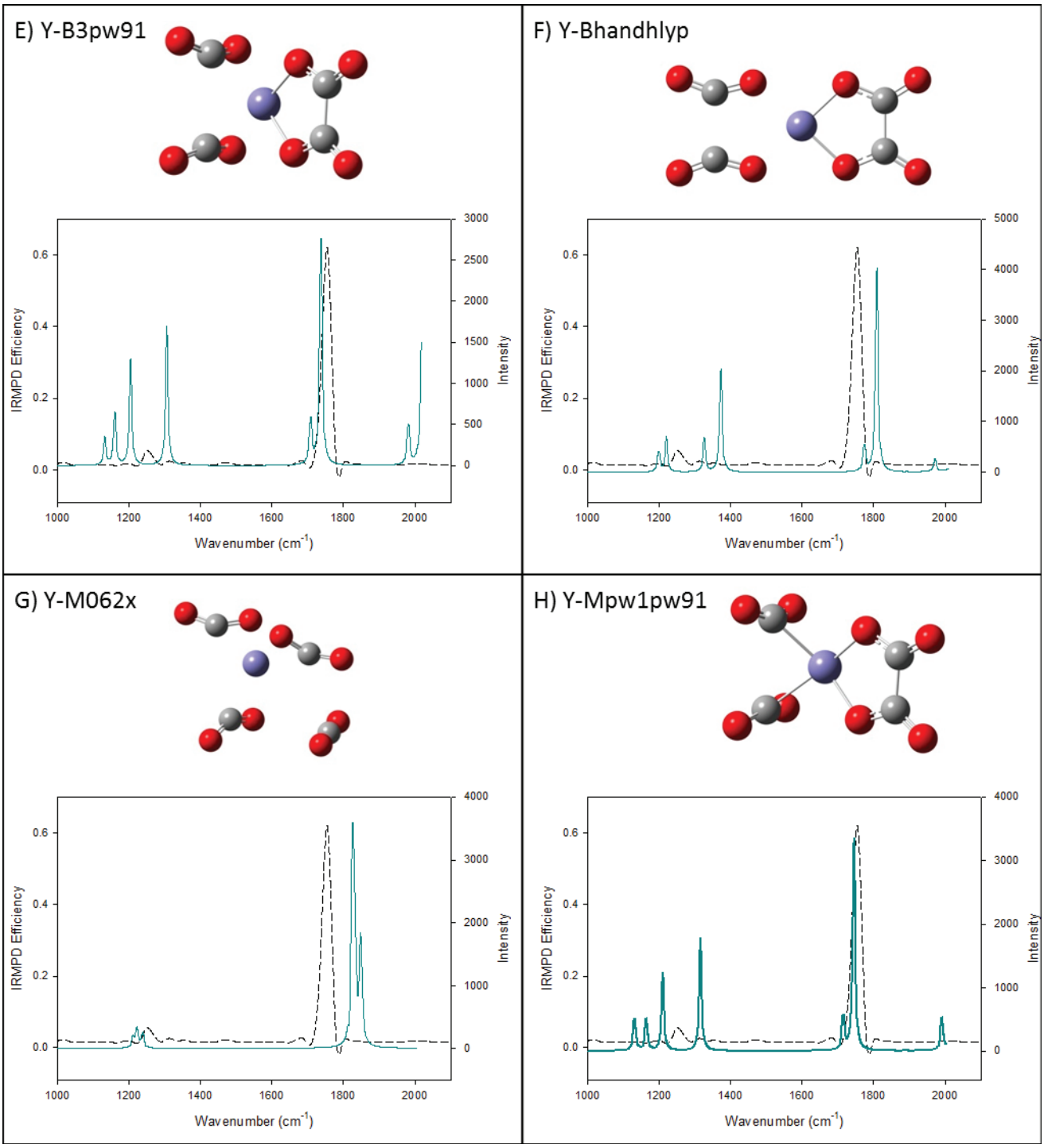


Figure 7-23: Optimized structures and spectra resulting from structures in Figure 7-22.

7.2.8 $FeOx_2^-$: Unique "X" and "Y" structures




E) Y-B3pw91
IRMPD Efficiency
Intensity
Wavenumber (cm-1)
F) Y-Bhandhlyp
IRMPD Efficiency
Intensity
Wavenumber (cm-1)
G) Y-M062x
IRMPD Efficiency
Intensity
Wavenumber (cm-1)
H) Y-Mpw1pw91
IRMPD Efficiency
Intensity
Wavenumber (cm-1)

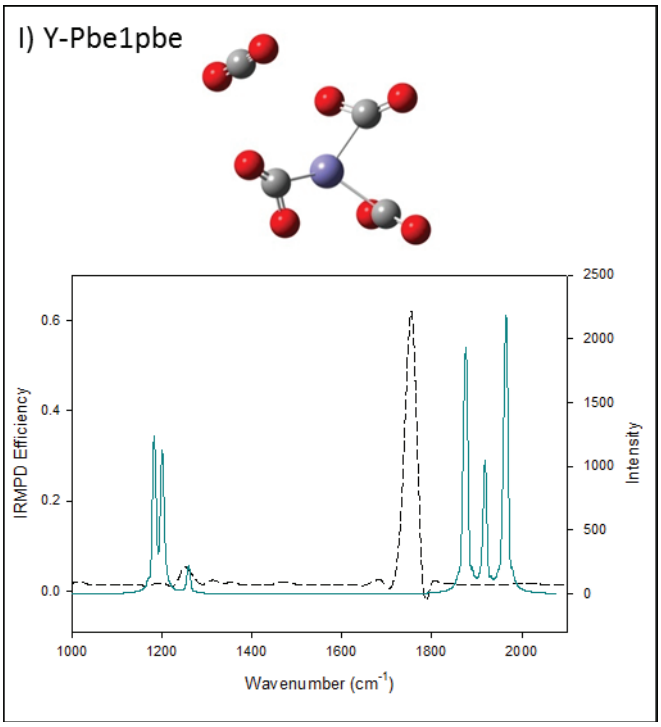


Figure 7-24: All unique optimized structures and theoretical spectra overlapping the IRMPD spectrum for the 1000-2000cm-1 range.

7.2.9 $FeOx_2^-$: More attempts at structure determination

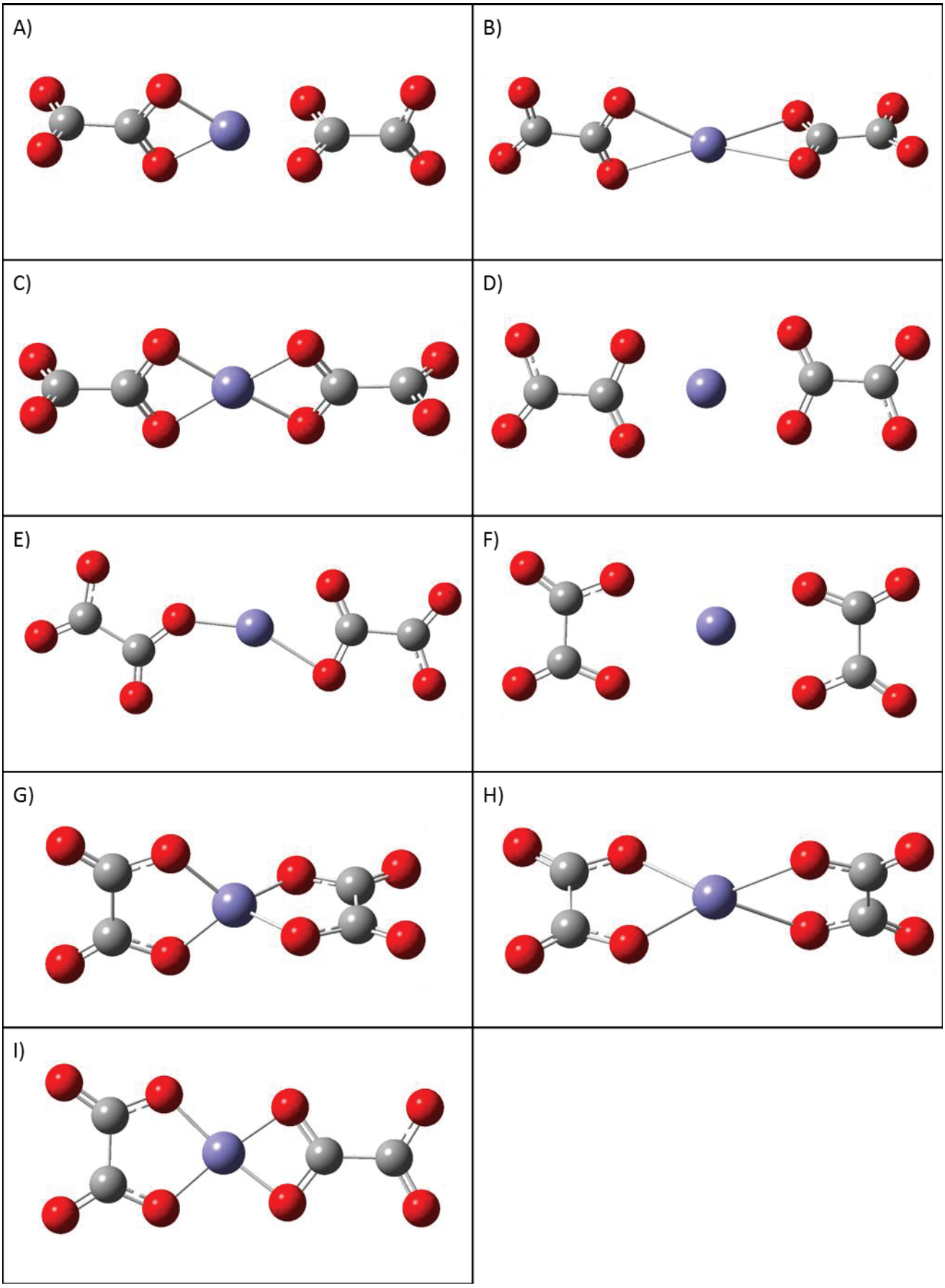
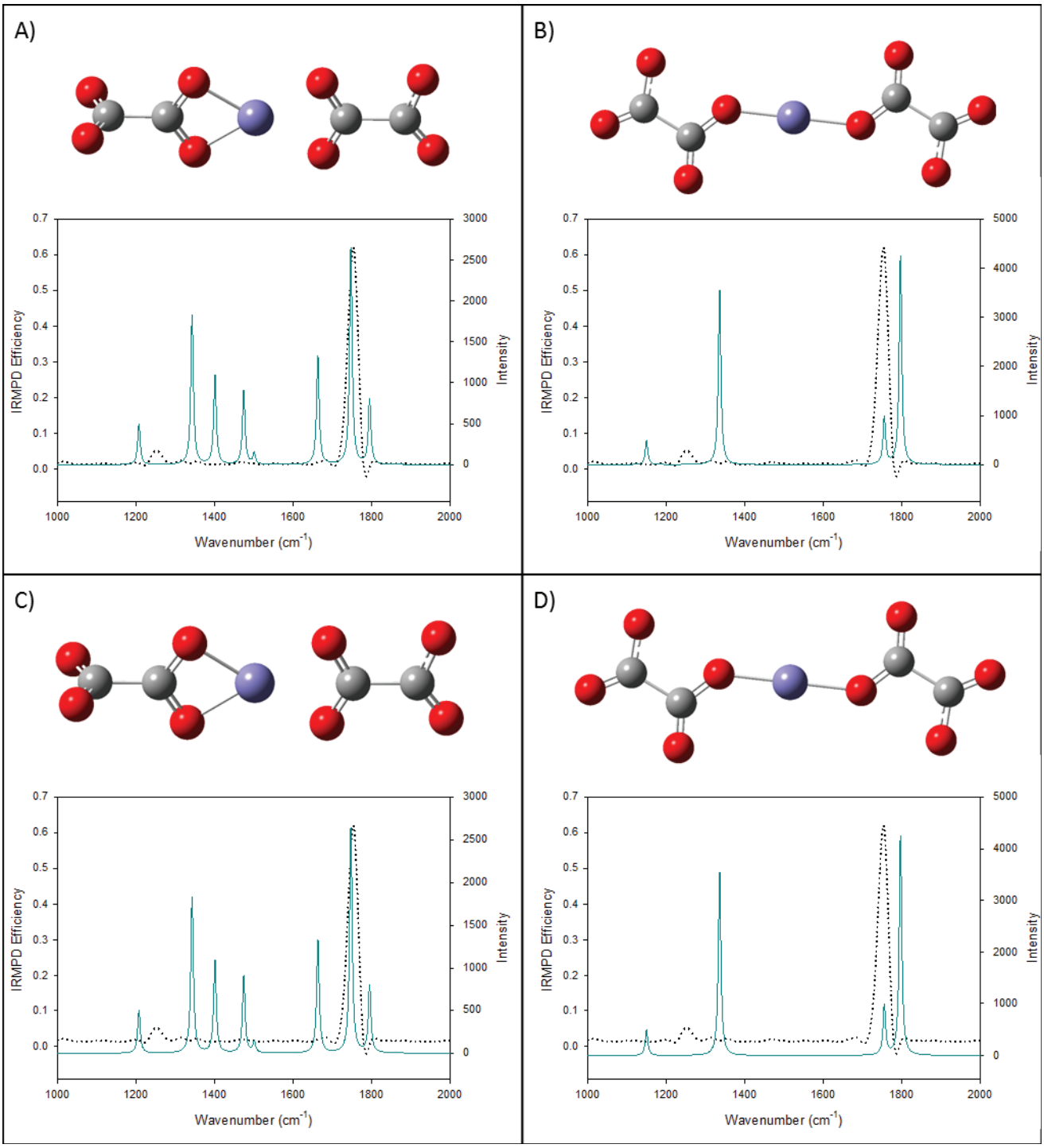
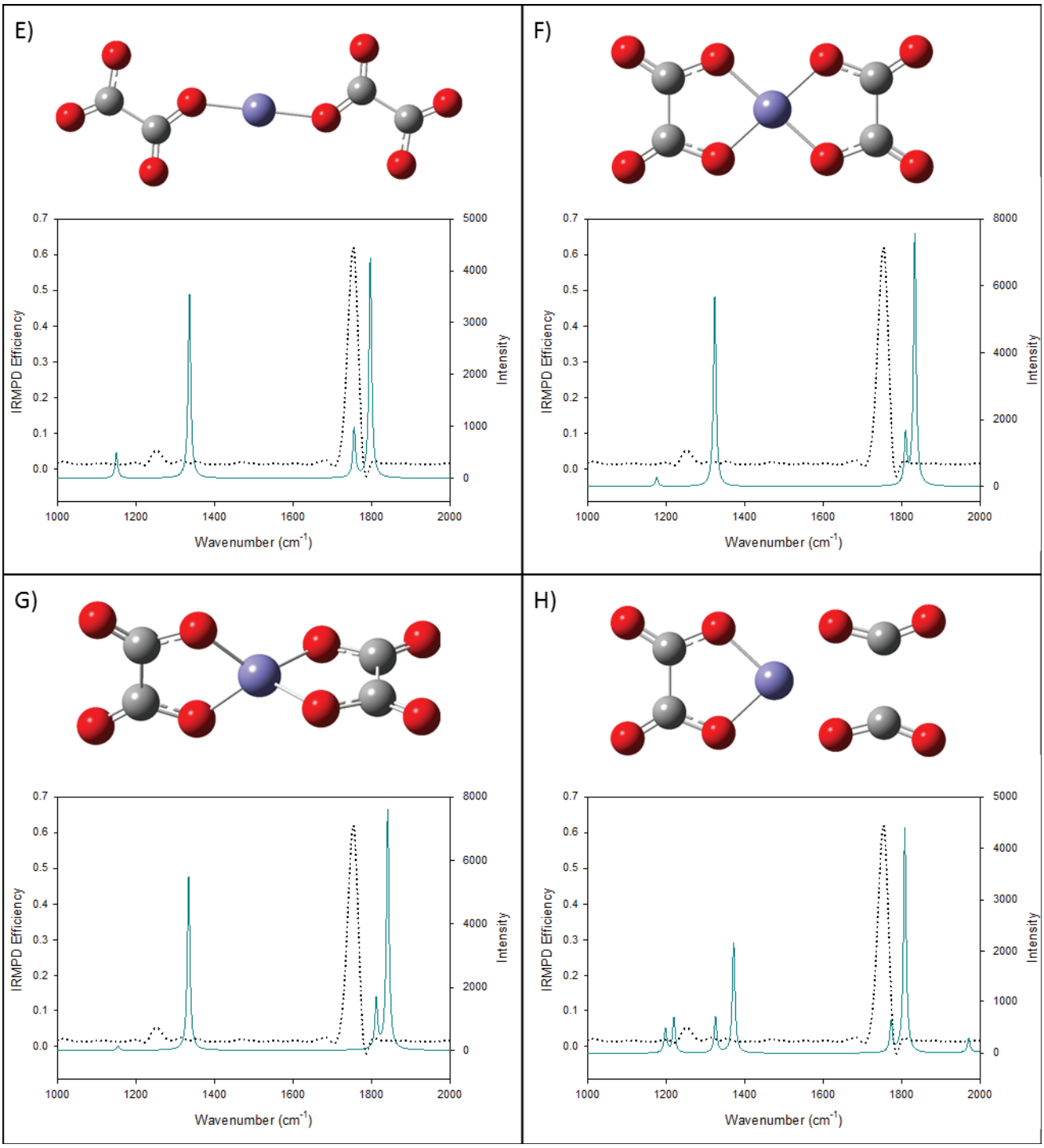


Figure 7-25: Starting structures for more attempts at determining a plausible structure.


A)
B)
C)
D)
IRMPD Efficiency
Intensity
Wavenumber (cm-1)
0.0
0.1
0.2
0.3
0.4
0.5
0.6
0.7
0
500
1000
1500
2000
2500
3000
4000
5000
1000
1200
1400
1600
1800
2000


E)
F)
G)
H)
IRMPD Efficiency
Intensity
Wavenumber (cm-1)

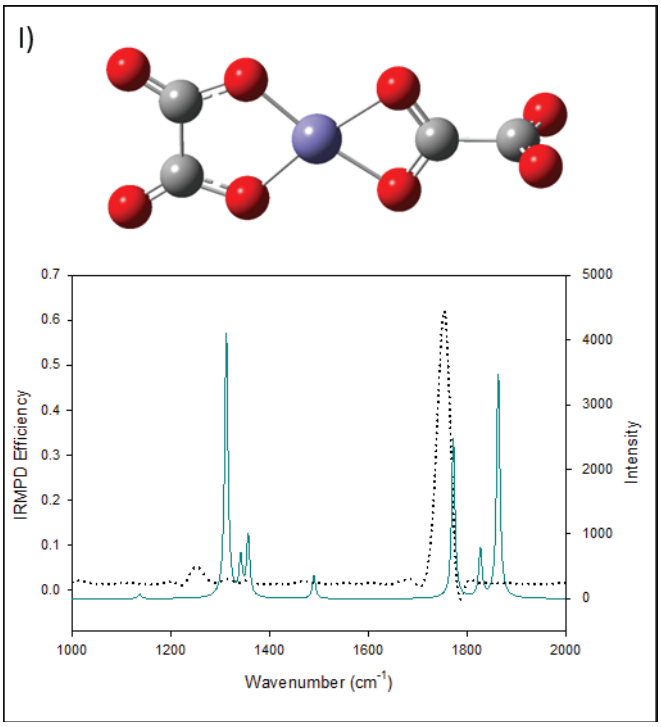
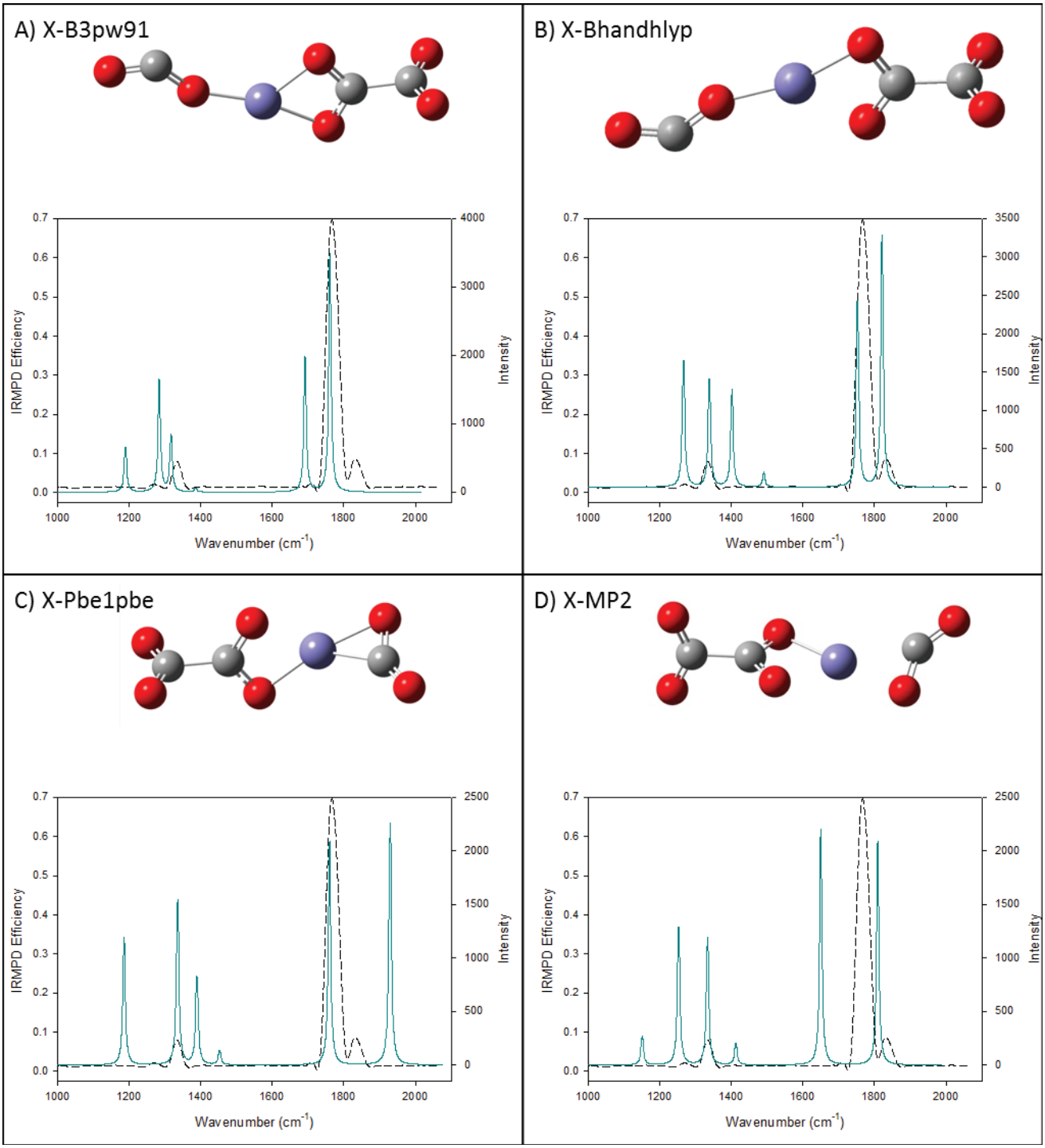


Figure 7-26: Optimized structures and spectra resulting from structures in Figure 7-25.

7.2.10 $FeOxCO_2^-$: Unique "X" and "Y" structures



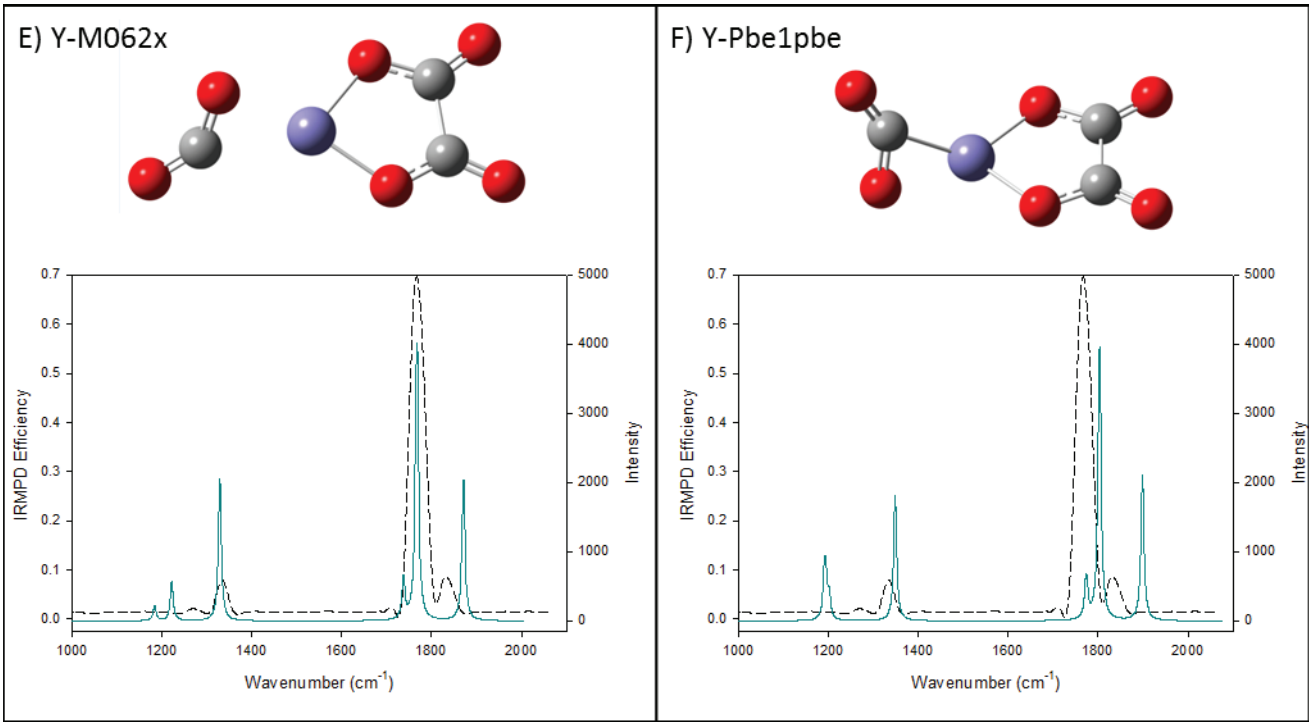
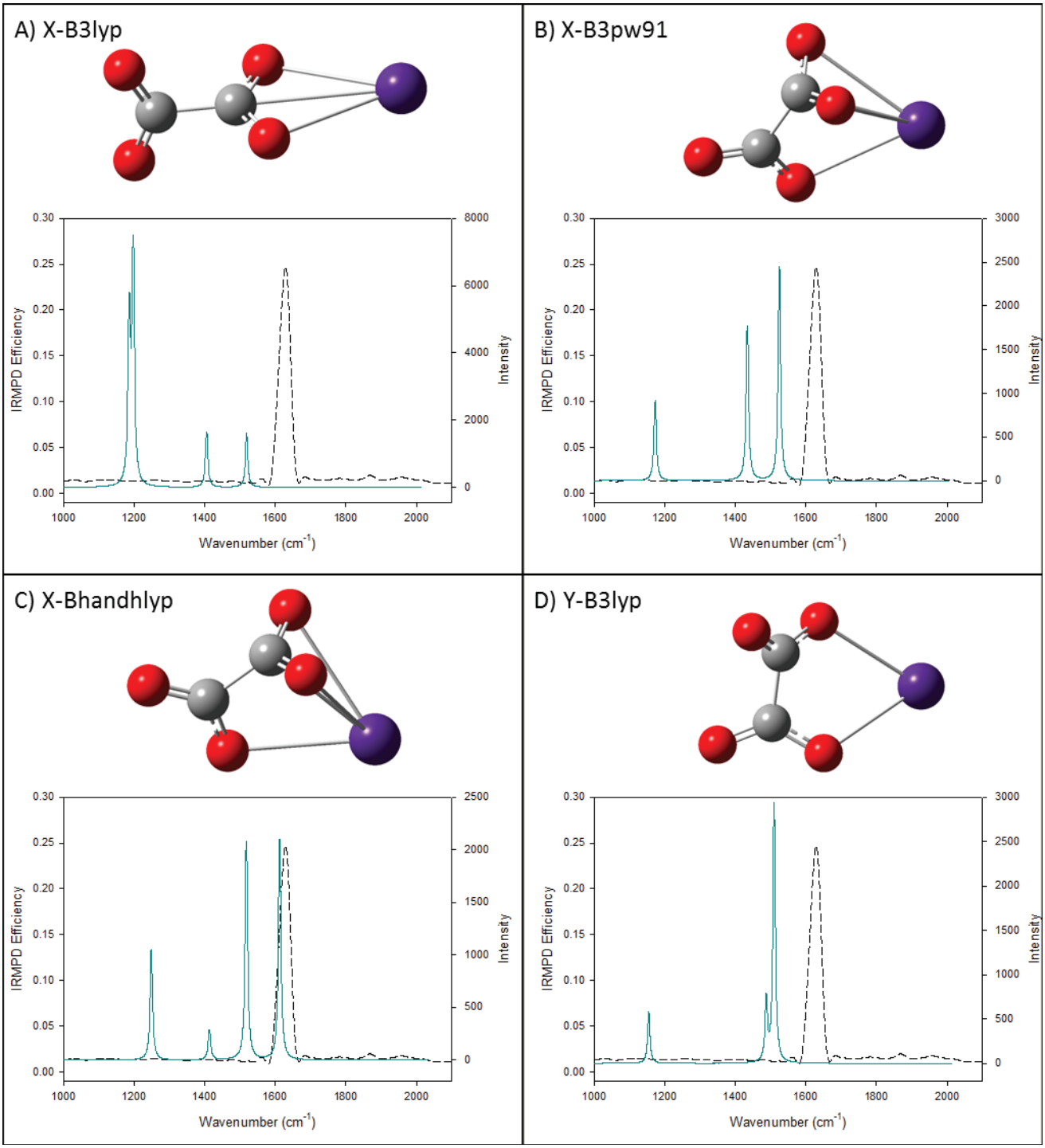


Figure 7-27: All unique optimized structures and theoretical spectra overlapping the IRMPD spectrum for the 1000-2000cm-1 range.

7.2.11 $CsOx^-$: Unique “X” and “Y” structures



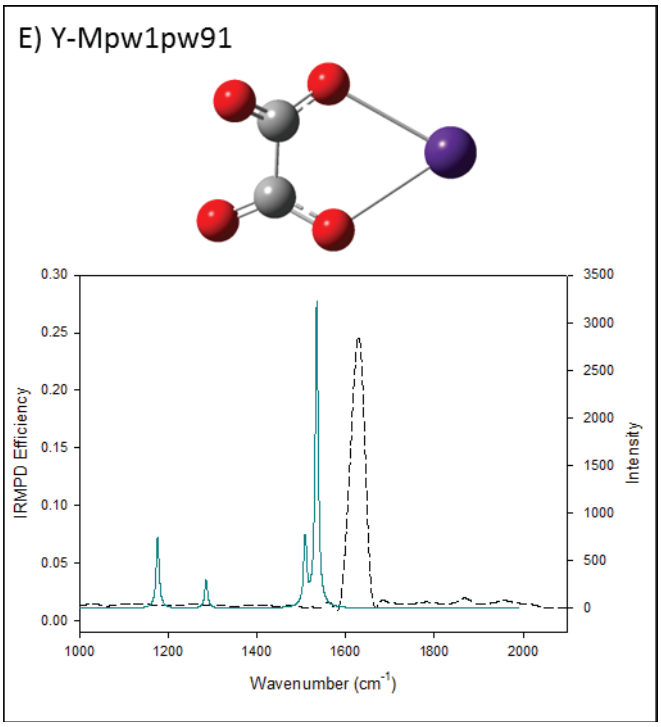
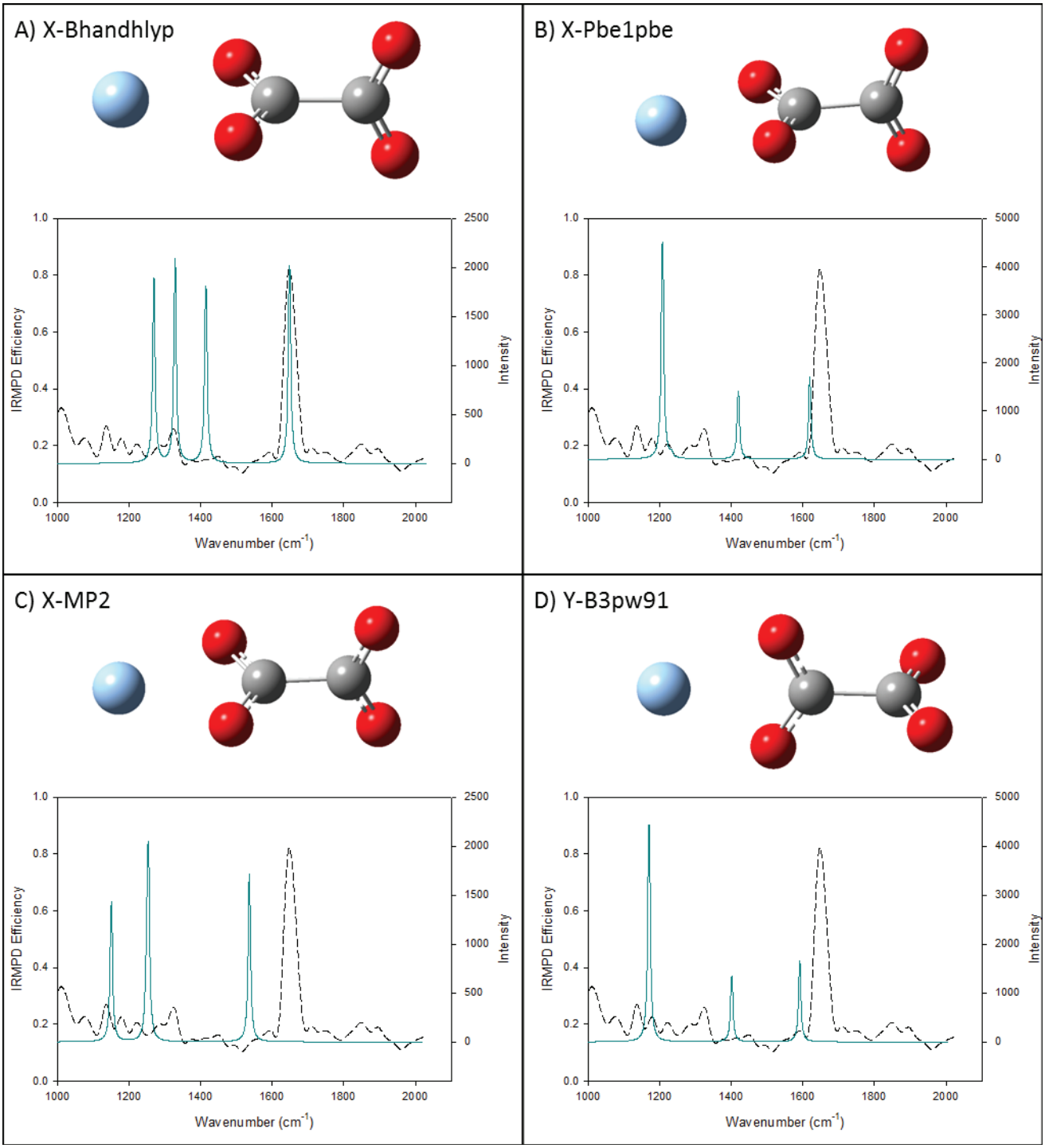


Figure 7-28: All unique optimized structures and theoretical spectra overlapping the IRMPD spectrum for the 1000-2000cm-1 range.

7.2.12 $AgOx^-$: Unique "X" and "Y" structures



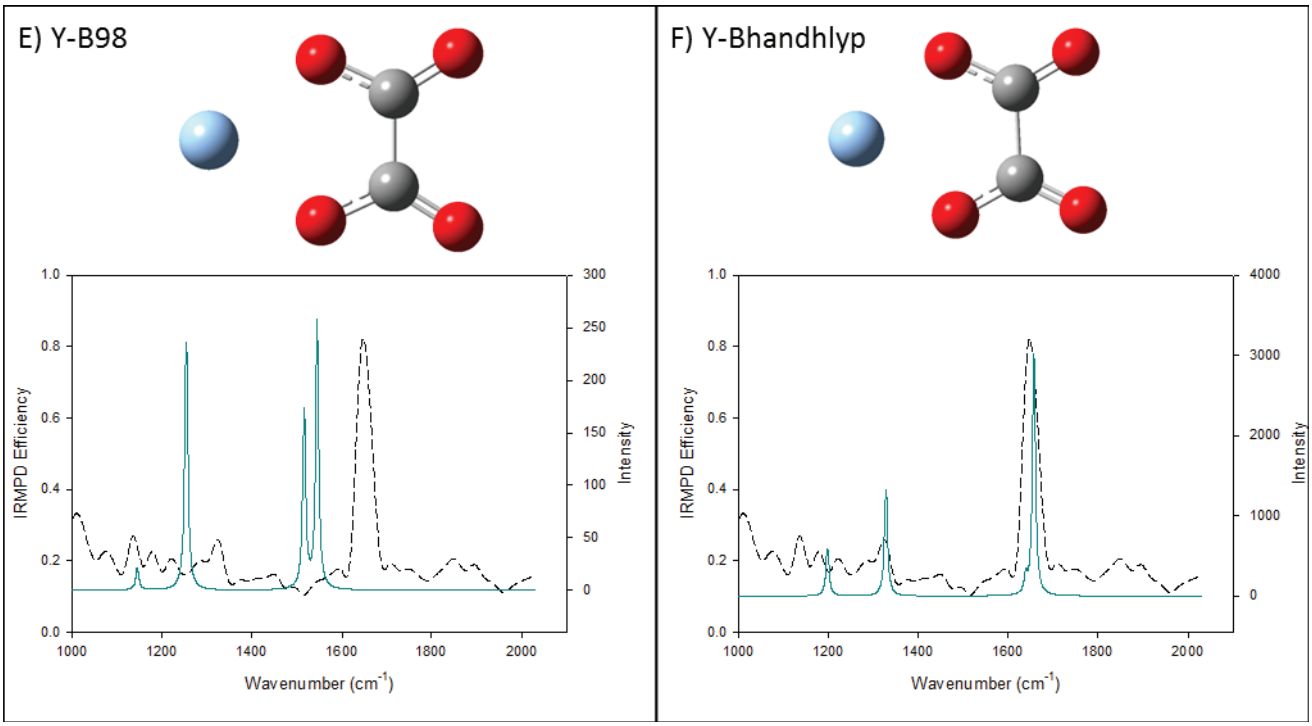
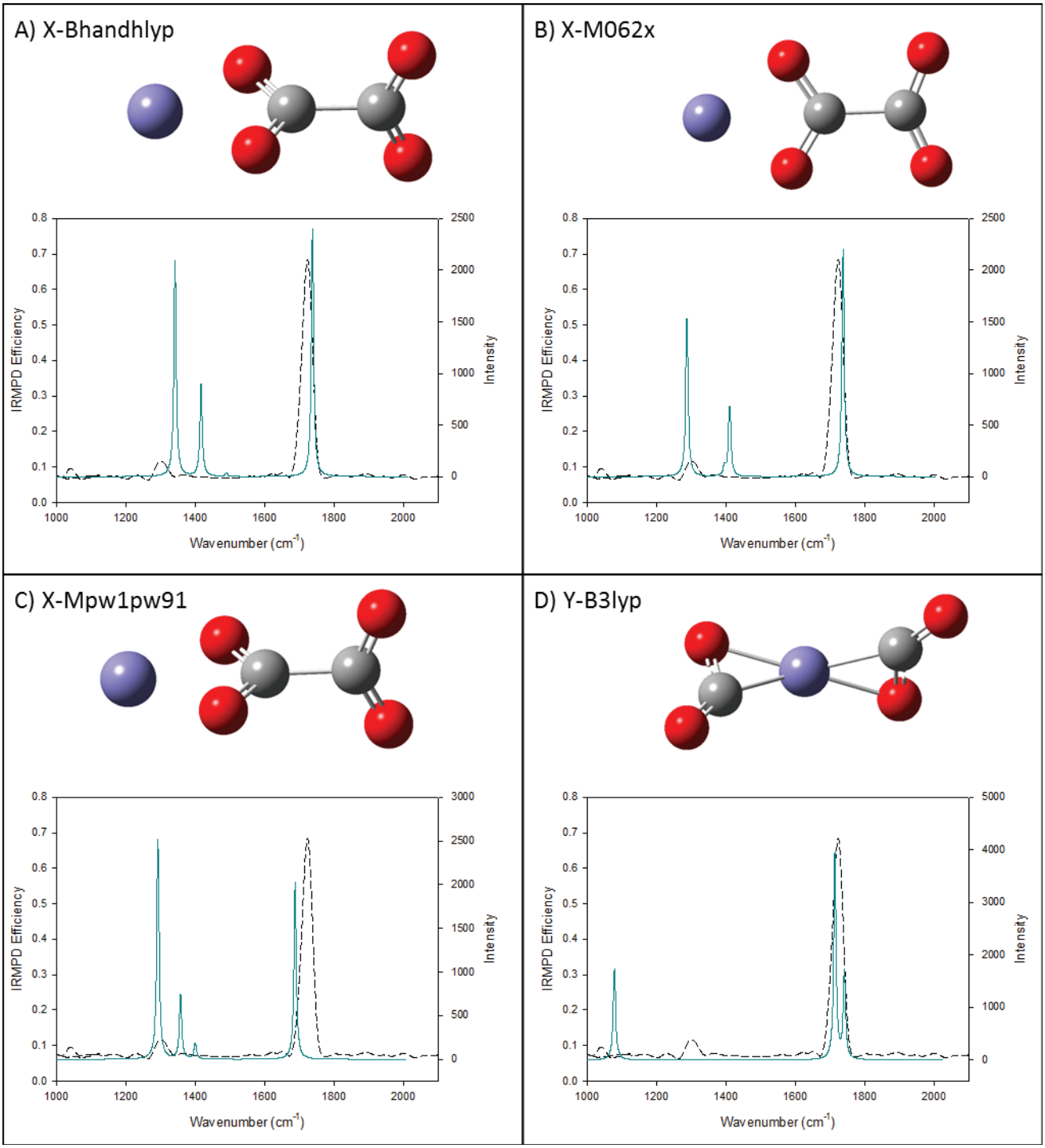


Figure 7-29: All unique optimized structures and theoretical spectra overlapping the IRMPD spectrum for the 1000-2000cm-1 range.

7.2.13 $FeOx^-$: Unique "X" and "Y" structures



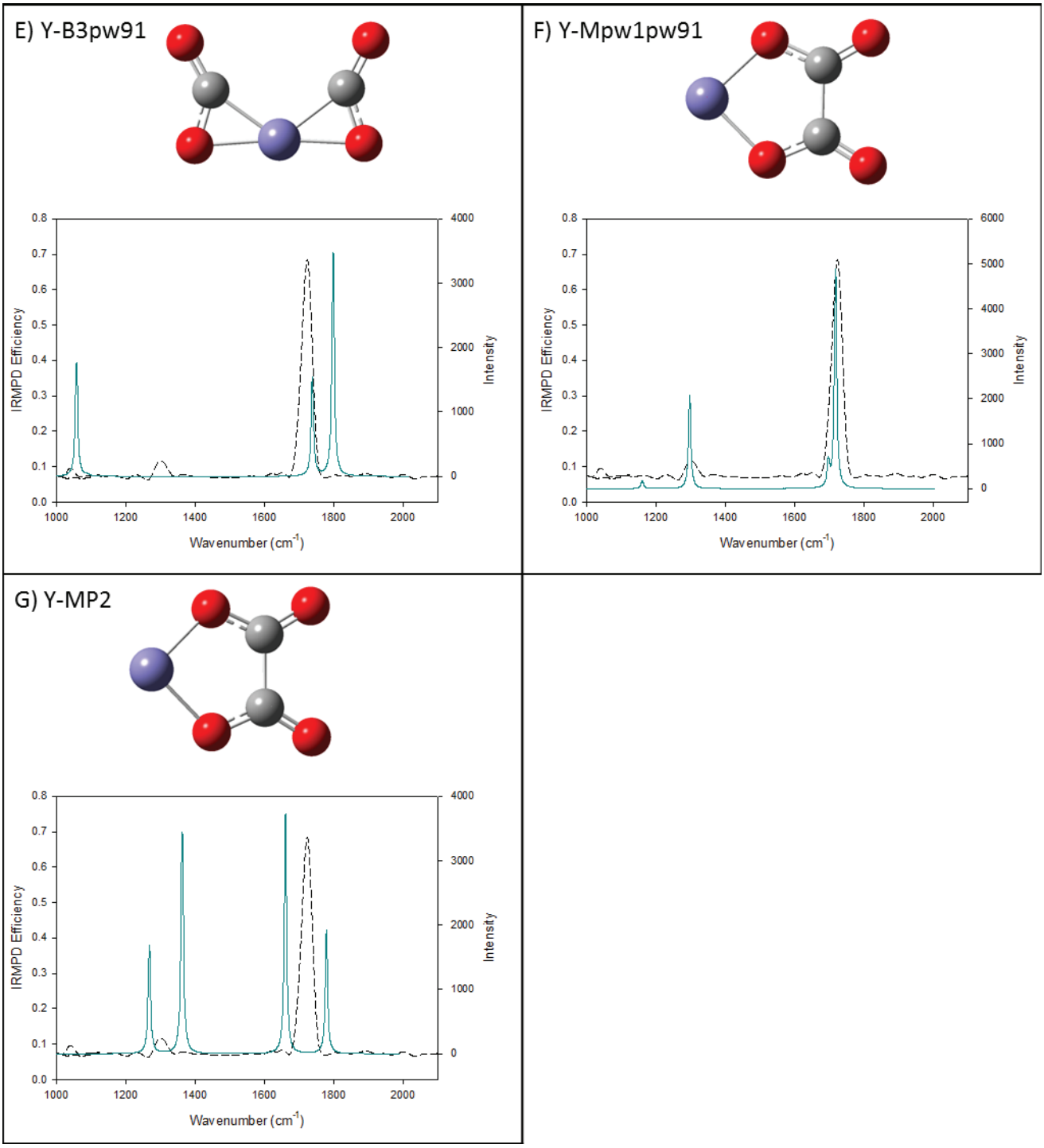


Figure 7-30: All unique optimized structures and theoretical spectra overlapping the IRMPD spectrum for the 1000-2000cm-1 range.

7.3 CID spectra to confirm species for collision cross-section determination

7.3.1 Silver

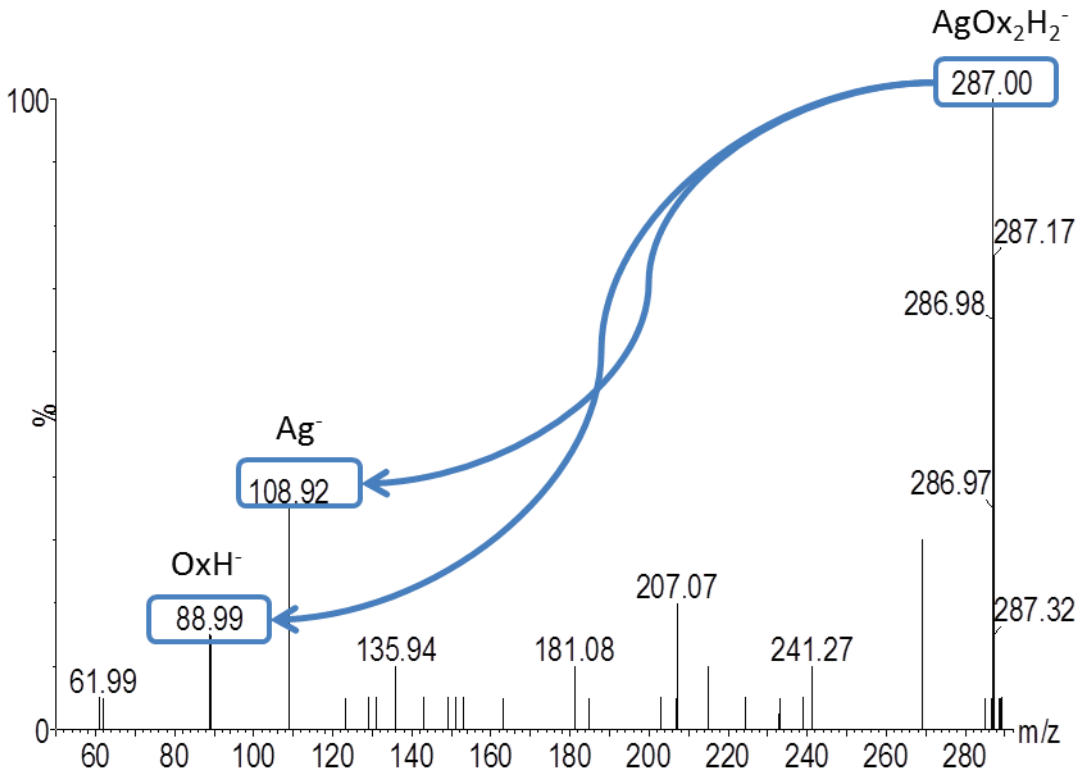


Figure 7-31: CID spectrum of m/z 287

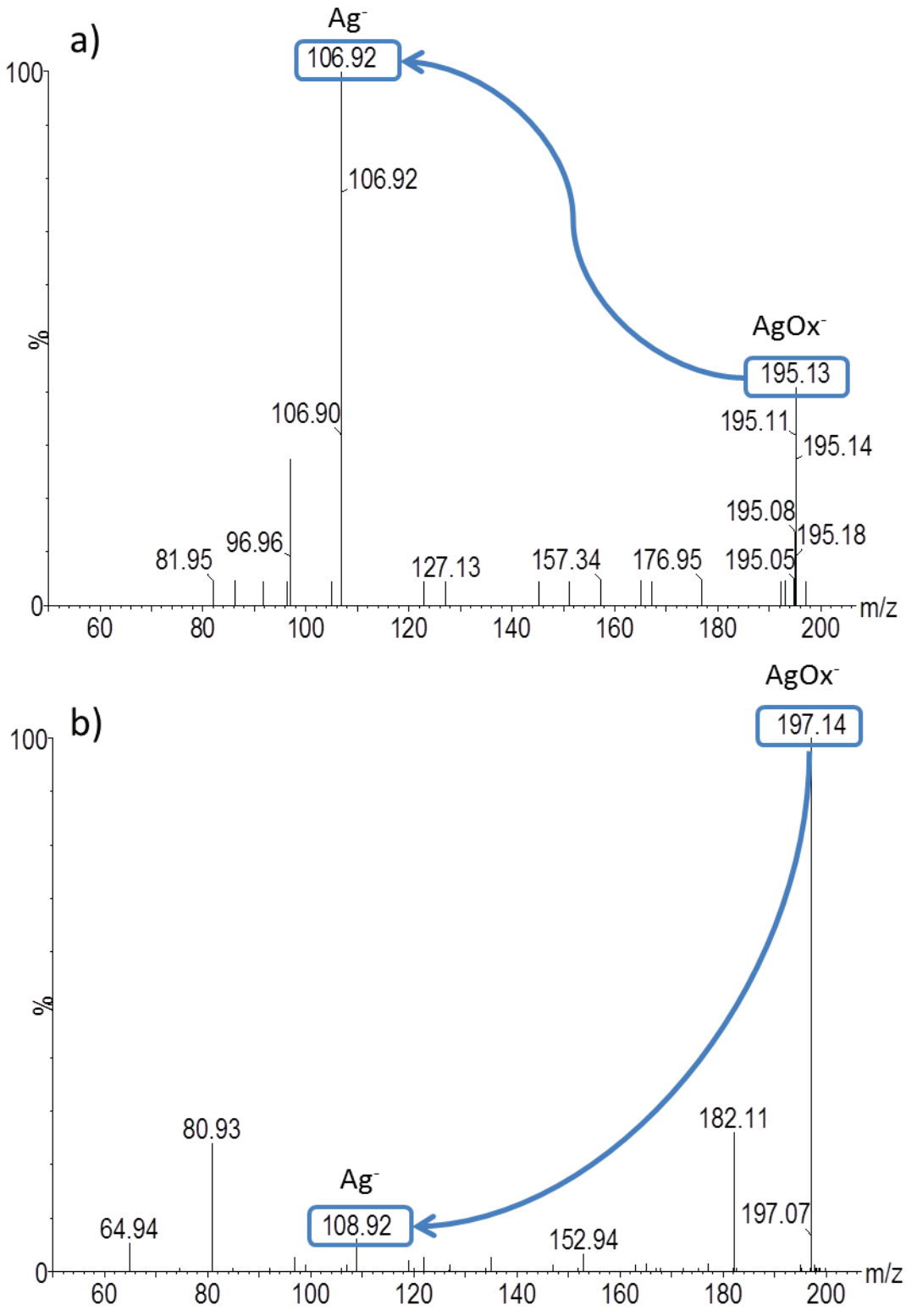


Figure 7-32: CID spectra of A) m/z 195 and B) m/z 197.

7.3.2 Cesium

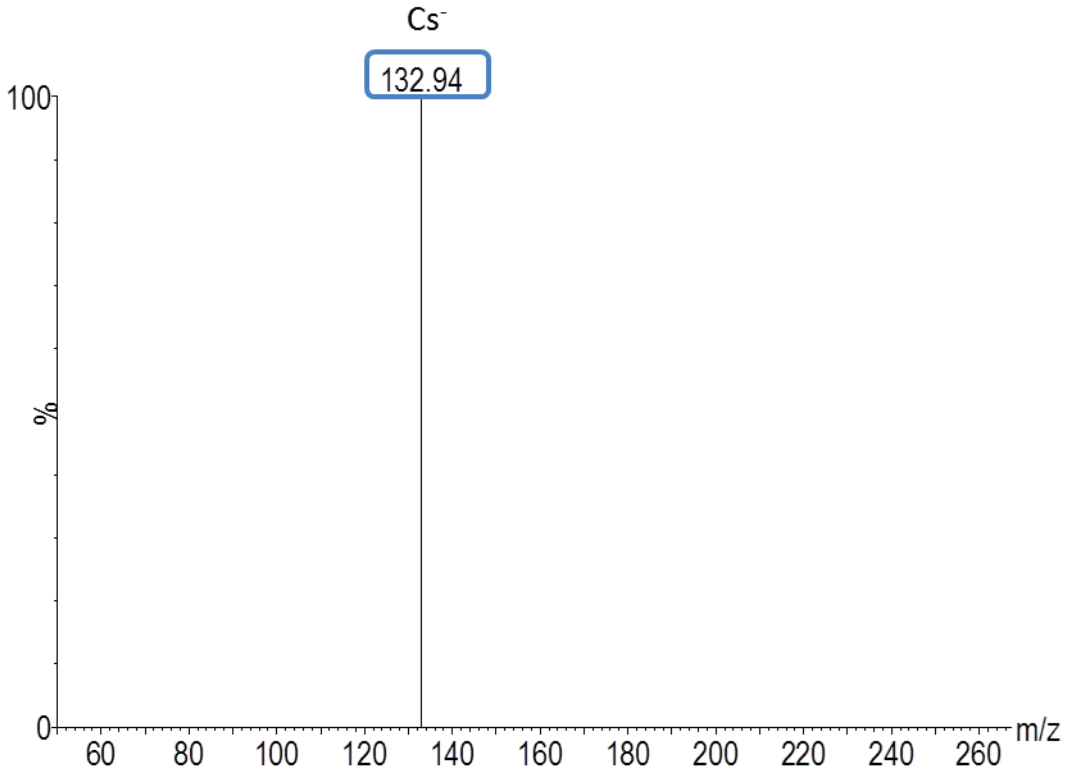


Figure 7-33: CID of m/z 133.